

The first generations of stars in the Local Group

Présentée le 21 mars 2022

Faculté des sciences de base
Laboratoire d'astrophysique
Programme doctoral en physique

pour l'obtention du grade de Docteur ès Sciences

par

Romain Ely Roland LUCCHESI

Acceptée sur proposition du jury

Prof. J.-Ph. Ansermet, président du jury
Prof. P. Jablonka, Prof. J.-P. R. Kneib, directeurs de thèse
Dr C. Hansen, rapporteuse
Prof. S. Feltzing, rapporteuse
Dr R. Anderson, rapporteur

Acknowledgements

During this thesis I benefited from the help and the experience of many people.

First of all, I would like to thank my PhD supervisor Pascale Jablonka for her support, her help and patience during the whole time. Jean-Paul Kneib for offering me the opportunity to conduct my thesis at Laboratory of Astrophysics (LASTRO).

I would also like to thank Francesca Primas, my co-supervisor for my stay at the European Southern Observatory (ESO) in Garching, who helped me a lot to start in this whole new environment.

My thanks also go to Pierre North and Carmela Lardo who followed my work, transmitted their knowledge and many useful advises. I extend these thanks to all my colleagues both from LASTRO and Geneva Observatory, the professors, secretaries, PhD students and postdocs, for all the very interesting discussions during the meetings, the lunches or the ping-pong games.

A special thank to all the Pristine collaboration members, for all the interesting discussions that we had during our meetings and the helpful comments on my papers.

Finally I would like to thank my family for their support during the last 4 years, but also during the whole duration of my studies.

Abstract

The different projects of this thesis contribute to improving our understanding of the early chemical evolution of the galaxies. The standard cosmological model states an hierarchical formation of the galaxies, the dwarf galaxies being the first stellar systems to form in the early Universe, merging to build larger galaxies over time. Observing the oldest stars in different environments can therefore answer many questions for the models of galaxy formation. Do the old stellar populations of the dwarf galaxies share the same chemical abundance patterns as the Milky Way halo ? These oldest and extremely metal-poor stars (EMP, $[\text{Fe}/\text{H}] \leq -3$) are challenging to find and to observe, especially outside our own Galaxy. Less than 10 EMP stars have very detailed chemical analysis within each of the closest dwarf galaxies, the Sculptor, Fornax, Carina and Sextans dwarf spheroidal galaxies (dSphs).

During a part of this thesis, detailed spectroscopic analyses have been carried at high resolution for different sets of stars observed with the Very Large Telescope in 3 dwarf spheroidal galaxies : Sextans, Fornax and Carina. I derived the abundances of a large set of chemical elements, providing the very first overview for some of them. I showed that Sextans presents an α -rich plateau in its early history, compatible with the Milky Way (MW) halo composition, contrary to what was previously suggested. Fornax and Carina barely explored in their EMP regime have now their α -plateau identified.

Another part of this thesis focused on the analysis of a sample of 132 candidate metal-poor stars, observed by the *Pristine* survey in the Milky Way. Only 1/2000 star is expected to be extremely metal-poor if observations are done blindly, and the statistics become much lower for the ultra metal-poor stars (UMP, $[\text{Fe}/\text{H}] \leq -4$). During the last decades, few hundreds of EMP stars, and ~ 40 UMP stars, have been found by dedicated surveys mainly in the Southern hemisphere. The *Pristine* survey was created few years ago to cover the Northern hemisphere, and has already proved the very high efficiency of its photometric calibration in finding these rare targets. A first large sample of the brightest metal-poor candidates has been analysed at high resolution. I delivered the first general view on the chemical evolution of the MW as witnessed by the *Pristine* survey.

Key words : galaxy evolution, dwarf galaxies, Sextans, Fornax, Carina, spectroscopy, chemical abundances

Résumé

Cette thèse se place dans le contexte de l'étude de la formation des galaxies et de leur évolution chimique. Les modèles cosmologiques prédisent qu'au début de l'Univers, les petites galaxies (appelées galaxies naines) ont été les premières à se former. Au cours du temps, elles se sont agglomérées par attraction gravitationnelle et ont formé les galaxies plus massives, comme notre Voie Lactée.

Cependant, beaucoup de questions sur ces modèles restent ouvertes. Les simulations ne reflètent pas parfaitement les observations, et beaucoup de processus physiques restent mal connus. L'univers à sa création n'étant composé que d'hydrogène, d'hélium et de lithium en très faible quantité, tous les autres éléments chimiques connus à ce jour ont été synthétisés par les étoiles. L'univers s'est donc enrichi en éléments chimiques au cours des différentes générations d'étoiles. La découverte d'une étoile de toute première génération (population III) n'a pas encore eu lieu, et ne sera peut être jamais possible. Ces étoiles étaient probablement très massives et avaient donc une durée de vie très courte. Cependant, leur directe signature peut être observée dans la composition chimique de la seconde génération d'étoiles, formées très tôt dans l'histoire de l'univers mais toujours observables à ce jour car moins massives. À ce jour, quelques centaines d'étoiles avec une métallicité de $[\text{Fe}/\text{H}] = -3$ (i.e. des métaux 1000 fois moins abondants que dans le Soleil) sont connues dans notre galaxie. Et seulement quelques unes ont été étudiées en détail dans les galaxies naines en orbite autour de la Voie Lactée (moins de 10 étoiles à $[\text{Fe}/\text{H}] = -3$ par galaxie naine).

Une partie de cette thèse a porté sur l'étude chimique détaillée par spectroscopie à haute résolution, d'échantillons de ce type d'étoiles dans 3 galaxies naines : Sextans, Fornax et Sculptor. De nombreuses abondances chimiques ont été dérivées, avec entre autres les éléments alphas (α : Mg, Ca, Ti), éléments produits par les supernova de type II. Le niveau d'enrichissement des éléments α dans les galaxies observées est bien compatible au début de leur histoire avec le niveau d'enrichissement du halo de la Voie Lactée, suggérant des conditions de formations communes. Alors qu'à plus haute métallicité, toutes les galaxies présentent des évolutions chimiques très différentes due à leurs caractéristiques et leurs histoires de formation d'étoiles très différentes.

Une autre partie de cette thèse s'est portée sur un échantillon de 132 étoiles, observées dans la Voie Lactée par le relevé *Pristine*, une collaboration internationale récemment créée spécialement

pour la recherche de ces étoiles extrêmement pauvres en métaux dans le ciel de l'hémisphère nord, très peu exploré jusqu'à maintenant.

Pristine a développé une calibration photométrique très efficace : en mesurant l'intensité lumineuse reçue dans une très courte bande spectrale autour de 2 raies d'absorption du calcium (Figure 4.3), une estimation de la métallicité peut être estimée avec une bonne fiabilité. Ainsi, seules les étoiles avec la plus haute probabilité d'être pauvres en métaux sont observées en spectroscopie à haute résolution. Ce premier échantillon de *Pristine*, à haute résolution et statistiquement significatif a été analysé en détail. Alors que la moitié des étoiles de l'échantillon sont confirmées comme étant pauvres en métaux, l'analyse chimique de l'échantillon complet a permis de produire la première vision globale de l'évolution chimique de la Voie Lactée par des observations de *Pristine*. Elle a également permis l'identification d'un possible biais dans la sélection photométrique des étoiles, en effet aucune des étoiles géantes pauvres en métaux identifiées ne sont enrichies en carbone. Or, en comparant avec d'autres études, environ 30% de ces étoiles devraient l'être. Enfin, cette analyse a aussi permis l'identification de quelques étoiles avec des compositions particulières, qui devraient être étudiées plus en détail dans le futur.

Mot clefs : évolution des galaxies, galaxies naines, Sextans, Fornax, Carina, spectroscopie, abondances chimiques

Contents

Acknowledgements	i
Abstract (English/Français)	iii
1 Introduction	1
1.1 Dwarf galaxies in the context of the Λ CDM paradigm and galaxy formation . . .	1
1.2 The first generations of stars	3
1.3 Objectives and structure of this thesis	4
2 Derivation of chemical abundances from stellar spectra	7
2.1 Selection of the absorption lines	7
2.2 Main steps of abundance determination	7
3 The low metallicity tail of 3 classical dwarfs spheroidal galaxies	13
3.1 Context in the DART survey	13
3.2 Firsts chemical evolution overviews	14
3.3 Publication : Homogeneity in the early chemical evolution of the Sextans dwarf spheroidal galaxy	17
3.4 Publication in preparation : Extremely metal-poor stars in the Fornax and Carina dwarf spheroidal galaxies	34
4 A Milky Way chemical evolution view from the <i>Pristine</i> survey	49
4.1 The <i>Pristine</i> survey : overview and its photometric calibration	49
4.2 Publication : The <i>Pristine</i> survey – XV. A CFHT ESPaDOnS view on the Milky Way halo and disc populations	52
5 Conclusions and outlooks	71
Analytical tools	71
Dwarf galaxies	71
Milky Way and the <i>Pristine</i> survey	72
A Improved data reduction of CFHT/ESPaDOnS spectra	75
B Acronyms	77

Contents

Bibliography	84
Curriculum Vitae	85

1 Introduction

1.1 Dwarf galaxies in the context of the Λ CDM paradigm and galaxy formation

The currently favoured model which describes the structure of the universe, is the cold dark matter (Λ CDM) paradigm, assuming a formation by hierarchical clustering of the matter ([White & Rees 1978](#)). According to the Planck collaboration ([Planck Collaboration et al. 2016](#)), the Universe is composed of ~ 70 % of dark energy that drives its expansion, 25 % of Dark Matter (DM), and only ~ 5 % of baryonic matter. Very small inhomogeneities of the matter distribution (over- and under-densities) were present at the begin of the Universe. The origin of these inhomogeneities is beyond the standard cosmology model, their characterisation sit at the very early times, when the Universe was dense enough that quantum effects were playing an important role (see Chapter 4 of [Mo et al. \(2010\)](#) for a description). These inhomogeneities were however critical to form the Universe as observed now, they made the DM, along with the baryonic gas, to slowly gravitationally collapse to form DM halos and the first structures of the Universe. This gravitational collapse eventually triggered the formation of the first stars in the denser regions, that would themselves assemble to produce the first galaxies.

The DM halos merged with one another, along with their gas and stellar content, forming larger and larger systems, ending in the galaxies as we observe them now, such as the Milky Way (MW) and larger galaxies ([White & Rees 1978](#); [Springel et al. 2006](#); [Mo et al. 2010](#)). In this scenario, small galaxies are the building blocks of larger ones.

Large scale (Gpc to Mpc) properties of our Universe are successfully reproduced by the Λ CDM scenario. Studies of the anisotropies in the Cosmic Microwave Background (CMB) have shown good agreement with the predictions ([Spergel et al. 2007](#); [Planck Collaboration et al. 2014, 2016](#)). The Big Bang nucleosynthesis and the predicted primordial abundances of light elements (helium and deuterium) are also in excellent agreement with observational data from *Planck* ([Planck Collaboration et al. 2016](#)).

There are however some limitations to this model at smaller scale (Mpc to kpc) when compared to the observations. One of them is known as the "Missing satellite problem" ([Moore et al. 1999](#)),

high resolution simulations (DM only) of MW-like halos ([Springel et al. 2008](#)) are predicting many more dwarf galaxies of all sizes (~ 500 , see Figure 1.1) compared to the actual known MW satellites (~ 30). Moreover, the brightest observed dwarf galaxies around the MW reside in only medium sized dark matter halos. The predicted most massive DM subhalos are not found in observations, otherwise known as the "Too-big-to-fail" problem ([Boylan-Kolchin et al. 2011](#)). The anisotropic distribution of MW satellites is an other limitation to the Λ CDM model ([Kroupa et al. 2005](#); [Metz et al. 2007](#)), indeed, dwarf galaxies seem to be confined and co-orbiting inside a thin "plane-of-satellites". This configuration is also observed for the Andromeda galaxy (M31, [Ibata et al. \(2013\)](#)) but not expected from the standard cosmological model which predicts isotropically distributed dwarfs with random motions.

Some of these limitations (e.g. missing satellite or the too-big-to-fail problems) are being solved with a better understanding of the baryonic processes in the galaxies (e.g. including the supernova feedback, UV-background heating ([Revaz & Jablonka 2018](#); [Sawala et al. 2016](#), and references therein)), while others limitations remain today more challenging (e.g. plane of satellite problem, see [Pawlowski \(2018\)](#) for an overview).



Figure 1.1 – Dark matter distribution from high-resolution simulation for a MW-like halo, in a box size of 1Mpc with the Λ CDM model. Image from the [Aquarius Project](#).

The exact details of the cosmological models and their limitations are however beyond the project of this thesis. This simplified picture is given to show the importance of dwarf galaxies in our understanding of the formation and evolution of the Universe. What is important to note is the fact that as observed in the Local Group, most galaxies are arranged in groups, with a massive central galaxy, and less massive fainter ones orbiting around them. While orbiting around the central galaxy, these small satellites lose energy and some of them eventually merge with the massive galaxy, while others remain gravitationally bound. The merging satellites contribute

to the build-up of the galaxy halo and leave their imprints in its stellar populations. Therefore, dwarf galaxies as they are observed in the Local Universe are the relics of the very first stages of galaxy formation. As such they are crucial probes for our understanding of galaxy formation and evolution. The study of the closest examples can provide the keys needed to link theory and observation, providing the constraints for the simulations.

More specifically, studying the abundance patterns of the stellar populations allows us to understand in detail the evolutionary processes that shape the galaxies. Thus looking at individual stars in dwarf galaxies in the Local Group is an important component in understanding the big picture of galaxy formation and evolution throughout the Universe.

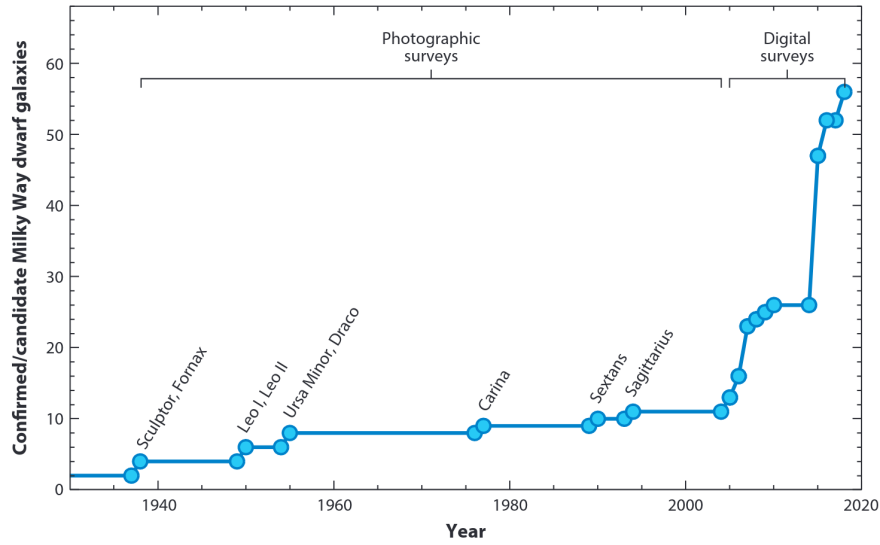


Figure 1.2 – Evolution of the discovery of dwarf MW satellites in function of time. Figure from [Simon \(2019\)](#)

More and more fainter systems are discovered over the years (Figure 1.2, more than 50 dwarf galaxies are known around the MW, see [Mateo \(1998\)](#); [McConnachie \(2012\)](#); [Simon \(2019\)](#) for an overview) thanks to the advent of deeper surveys such as the Sloan Digital Sky Survey (SDSS, [York et al. \(2000\)](#)). However, while we barely start to draw detailed chemical evolution for a few systems (presented in Section 3.1), the 8 most luminous satellites, denominated as "classical dwarf spheroidal" galaxies (dSph) remains very little explored and badly constrain in their very early stages of formation. For each system, only few stars of their oldest population have very detailed investigations, leaving many open questions.

1.2 The first generations of stars

At the beginning of the Universe, during the Big Bang, only hydrogen (H), helium (He) and a very small amount of lithium (Li) have been produced. All the heavier elements have been produced later, by stellar nucleosynthesis during stellar evolution or explosion.

The very first generation of stars that formed few million years after the Big Bang are called the population III (Pop III), they were totally free of metals¹. None of these stars have been detected yet, and it would be surprising that some of them could have survived until now. They were most likely very massive stars, from 10 solar masses (M_{\odot}) to more than 100 M_{\odot} due to inefficient cooling (Bromm & Larson 2004), and therefore had a short life of the order of a few million years (Abel et al. 2000; Hirano et al. 2014). After their death, the Pop III stars were the first objects that enriched the interstellar medium (ISM) with heavier chemical elements. Thus their signature can be directly observed in the chemical composition of the oldest stars that formed from this enriched ISM, few hundreds million of years after the Big Bang, and which had a mass low enough ($\sim 0.8 M_{\odot}$) to survive until today.

Since stars are enriched through the successive life and death of their predecessors, the ones with the lowest metal content should also be among the oldest, providing a unique way to probe the earliest times of the Universe. They host clues on the supernova (SNe) feedback, the level of homogeneity and the mixing efficiency (Revaz & Jablonka 2012) of the interstellar medium, the galaxy star formation histories, but also the identification of stellar nucleosynthesis sites. Therefore, detecting and studying those extremely metal-poor stars in different environment is extremely important.

1.3 Objectives and structure of this thesis

The aim of this thesis is the detailed spectroscopic chemical analysis of the oldest stars that we can observe.

Chapter 2 introduces the different steps of the derivation of chemical abundances from stellar spectra. I present the tools used and developed over the years to perform the analysis. Since stellar spectra contain thousands of absorption lines corresponding to dozens of various chemical elements, an efficient workflow is critical to perform a complete analysis of large samples of stars.

In Chapter 3 I first focus on the old population of 3 classical dSphs : Sextans, Carina and Fornax. The extremely metal-poor regime (EMP, $[\text{Fe}/\text{H}] = -3$) is barely explored in these galaxies, with at most 6 EMP stars known in Sextans, a single one in Fornax and none of them in Carina. Nevertheless, the study of EMP stars in dwarf galaxies can yield an efficient method of constraining early nucleosynthesis sites in the universe : the mixing processes, which homogenize the ejecta of different SNe, are expected to be less efficient in low mass systems. They can give clues on which processes dominated the earliest chemical enrichment, and what types of stars produced the first heavy elements, and on which timescales. The comparison of their abundance patterns with the Milky Way halo can tell us if early versions of today's dwarf satellites could

¹The term "metals" refers to all the chemical elements heavier than helium. The metallicity is used to inform on the metal content of a star. The metallicity is a on logarithm scale, and usually uses iron as reference, meaning that a metallicity of $[\text{Fe}/\text{H}] = -3$ corresponds to a content of metals a thousand times less abundant than in the Sun. With $[\text{Fe}/\text{H}] = \log(N_{\text{Fe}}/N_{\text{H}}) - \log(N_{\text{Fe}}/N_{\text{H}})_{\odot}$

be the building blocks of the MW halo. In this chapter I first present the ESO large program DART (Dwarf galaxy Abundances and Radial-velocities Team) from which the new EMP stars candidates were identified. Two papers are then presented : the first one dedicated to the study of the Sextans dSph is accepted in the Astronomy and Astrophysics (A&A) journal ([Lucchesi et al. 2020](#)). The second paper presented in this chapter is the last project conducted during this thesis. It is focused on the Fornax and Carina dSphs. At the time of writing it is close to be submitted to A&A.

Between the two projects dedicated to dwarf galaxies, I conducted the project presented in Chapter 4, focused on the analysis of stars in the Milky Way. In the Milky Way and its halo, few hundreds of EMP stars have been discovered during the last decades, by chance, or by dedicated large surveys. The community is continuously trying to increase this sample and to lower its metallicity limit. In the ultra metal-poor regime (UMP, $[\text{Fe}/\text{H}] < -4$) only ~ 40 UMP stars are known in the Milky Way halo (see [Sestito et al. \(2019\)](#) for a review), while only one is known in dwarf galaxies. The dedicated large photometric surveys are the most likely to detect these extremely rare objects.

I first introduce the recent photometric survey *Pristine*, dedicated to the search of metal-poor stars in the Northern hemisphere, and then I present the work that I realized on a large sample of candidates MP stars observed at high resolution. This last paper presented is actually the second paper that I conducted and was published in the journal Monthly Notices of the Royal Astronomical Society (MNRAS) ([Lucchesi et al. 2022](#)).

2 Derivation of chemical abundances from stellar spectra

2.1 Selection of the absorption lines

The analysis of high resolution spectra is a very meticulous and time consuming work. As presented in Figure 2.1, a complete VLT/UVES spectrum of RGB star ranging from 3400 to 6800 Å contains hundreds of absorption lines, even in the extremely metal-poor regime ($[\text{Fe}/\text{H}] = -2.94$ in that case).

Some automatic tools are used to detect and measure the lines of interest, such as DAOSPEC (Stetson & Pancino 2008). Once the continuum level is fitted (red line on Figure 2.1) and the spectrum normalized, DAOSPEC computes the radial velocity by matching observed lines with a given line list, measuring the Doppler shifts. Each of the detected lines are then fitted with Gaussian profiles in order to measure their equivalent widths (EW). In this study, a typical list of measured EWs contains ~300 lines for a single star. While around two thirds of the lines are Fe I lines only, about a hundred of lines correspond to other elements. If large samples, as presented in Chapter 4, are processed blindly, the resulting abundances can be biased from many reasons. Lines can be blended, they can have a non-Gaussian shape, they can be affected by a continuum level badly fitted, by an order merging issue, or by too high a level of noise. Thus, having a very efficient workflow is critical to select the lines, optimize the stellar parameters and compute robust abundances.

2.2 Main steps of abundance determination

The stellar atmospherical models used for this work are the MARCS models (Gustafsson et al. 2008), associated with the interpolation tool of Thomas Masseron available on the MARCS website. Abundances are computed with the 1D LTE code Turbospectrum (Plez 2012). The Python tool developed is used as a wrapper to link the 2 above mentioned codes, but also to present and shape the results in an efficient way. The main steps are :

1. Stellar parameters are first assumed from photometric data. The effective temperature

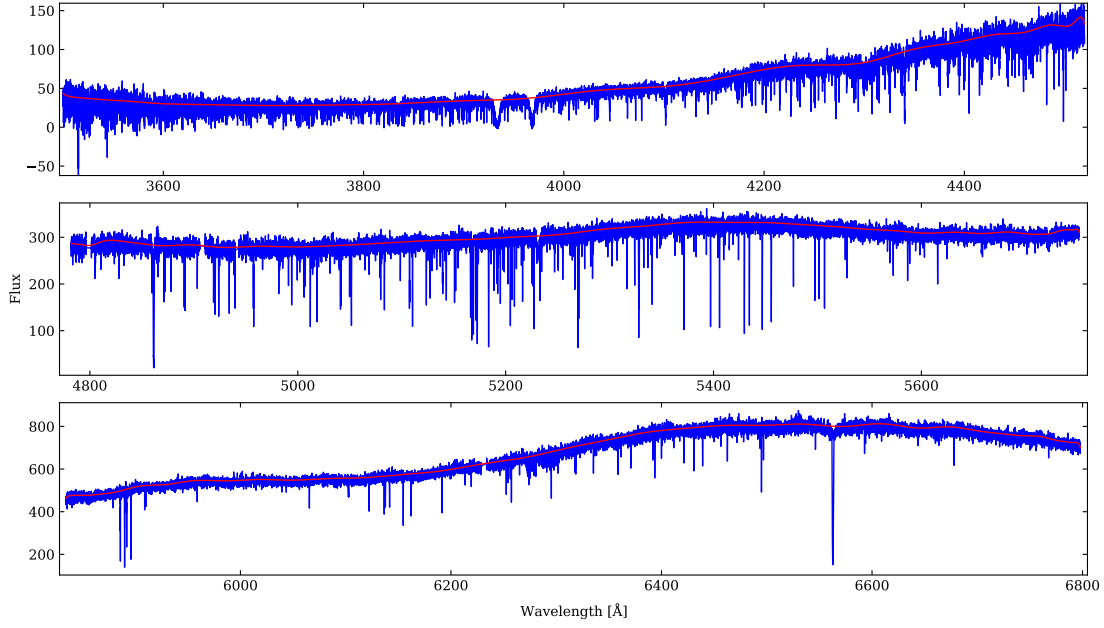


Figure 2.1 – VLT/UVES observed spectrum of S04-130 in Sextans. The red line is the continuum level fitted by DAOSPEC.

T_{eff} is computed using the calibration of [Alonso et al. \(1999\)](#) and the V-I, V-J, V-H, V-K, colours. The metallicity of the star is first taken as the DART $[\text{Fe}/\text{H}]_{\text{CaT}}$ estimate or the Pristine $[\text{Fe}/\text{H}]_{\text{CaHK}}$ estimations (see detailed explanations in Chap. 3 and 4 respectively).

2. A first abundance derivation is performed from the DAOSPEC EW measurements and the photometric parameters.
3. Diagnostics plots (Figure 2.3) are produced from the individual abundances of iron lines in function of the properties of the lines, allowing for the spectroscopic stellar parameters optimisation :
 - T_{eff} is adjusted by requiring no trend on the abundances in function of the excitation potential (χ_{exc}) of the lines.
 - Microturbulence velocity (v_t) is adjusted by requiring no trend between the abundances and the predicted EWs.
 - Surface gravity $\log(g)$ can be adjusted from the ionisation equilibrium between Fe I and Fe II. However, at low metallicity ($[\text{Fe}/\text{H}] < -2.5$), non-local thermodynamic equilibrium (NLTE) can affect Fe I leading to an abundance difference $\Delta(\text{Fe II}-\text{Fe I})$ up to +0.2 dex ([Mashonkina et al. 2017](#)). Therefore photometric $\log(g)$ (eq. 1 in Sec. 3.3) is preferred when possible. This is generally the case for dwarf galaxies members, when distances are known and used for the bolometric correction. When no reliable estimate of the distances are available, surface gravities are adjusted from the iron ionisation equilibrium modulo the NLTE $\Delta(\text{Fe II}-\text{Fe I})$, as in Sec 4.
 - Each adjustment on a parameter induces a change on the derived mean iron abundance.

2.2. Main steps of abundance determination

Thus, for each iteration, the stellar model metallicity is adjusted to the mean Fe I abundance obtained at the previous iteration.

4. When the final stellar parameters are determined, the abundances of other elements than iron can be obtained from their EW measurements or from spectral synthesis. When required, the observed spectrum is compared with synthetic spectra computed on the fly by *Turbospectrum* to obtain abundances. Spectral synthesis is required for strong lines, blended lines, elements presenting hyperfine structure (HFS), or abundances derived from molecular bands such as carbon in the region of the CH band at 4324 Å (see Figure 2.2). The parameters of the synthesis are adjusted for each cases, the abundance of an element X is varied between $-2.0 \leq [X/Fe] \leq +2.0$ dex, the resolution of the synthetic spectra can be adjusted in wide ranges of convolution starting from the nominal instrumental resolution. Small residual radial velocity shifts can also be corrected if needed. A second minimisation is then performed starting from the best χ^2 obtained in smaller ranges and smaller steps to refine the results.

Figure 2.5 illustrates a problem that can be encountered. The Mg 5172 Å and 5183 Å lines predict abundances strongly underestimated compared to Mg 5528 Å when derived with the EW measurement from DAOSPEC using a Gaussian fit. They are strong and start to deviate from Gaussian profile, they are not in the linear range of the curve of growth and require a spectral synthesis.

5. For each individual line, the DAOSPEC Gaussian fit or the best synthetic spectrum, associated with the derived abundance, are shown in summary tables (Figure 2.4), allowing fast selection or rejection of lines.
6. The final mean abundances and uncertainties are computed, the parameters and the results can be saved in an usable table format.

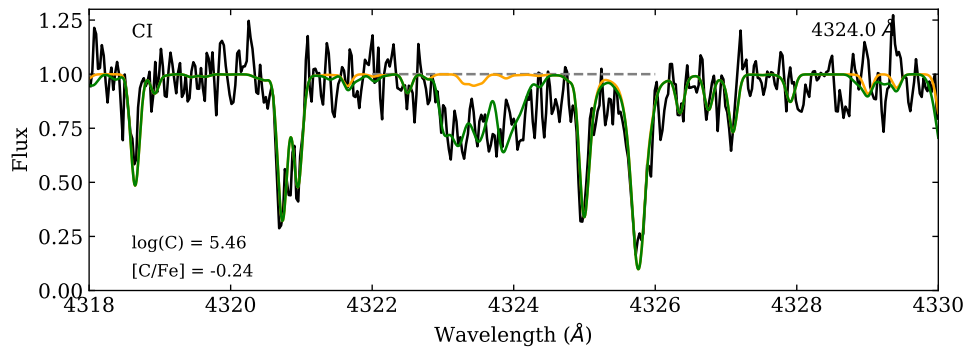


Figure 2.2 – Observed spectrum of the star fnx0579x-1 (in black) in the region of the CH molecular absorption band. In orange a synthetic spectrum is computed without carbon, allowing to identify the carbon contribution. The best synthetic spectrum obtained after the χ^2 minimisation is shown in green.

Chapter 2. Derivation of chemical abundances from stellar spectra

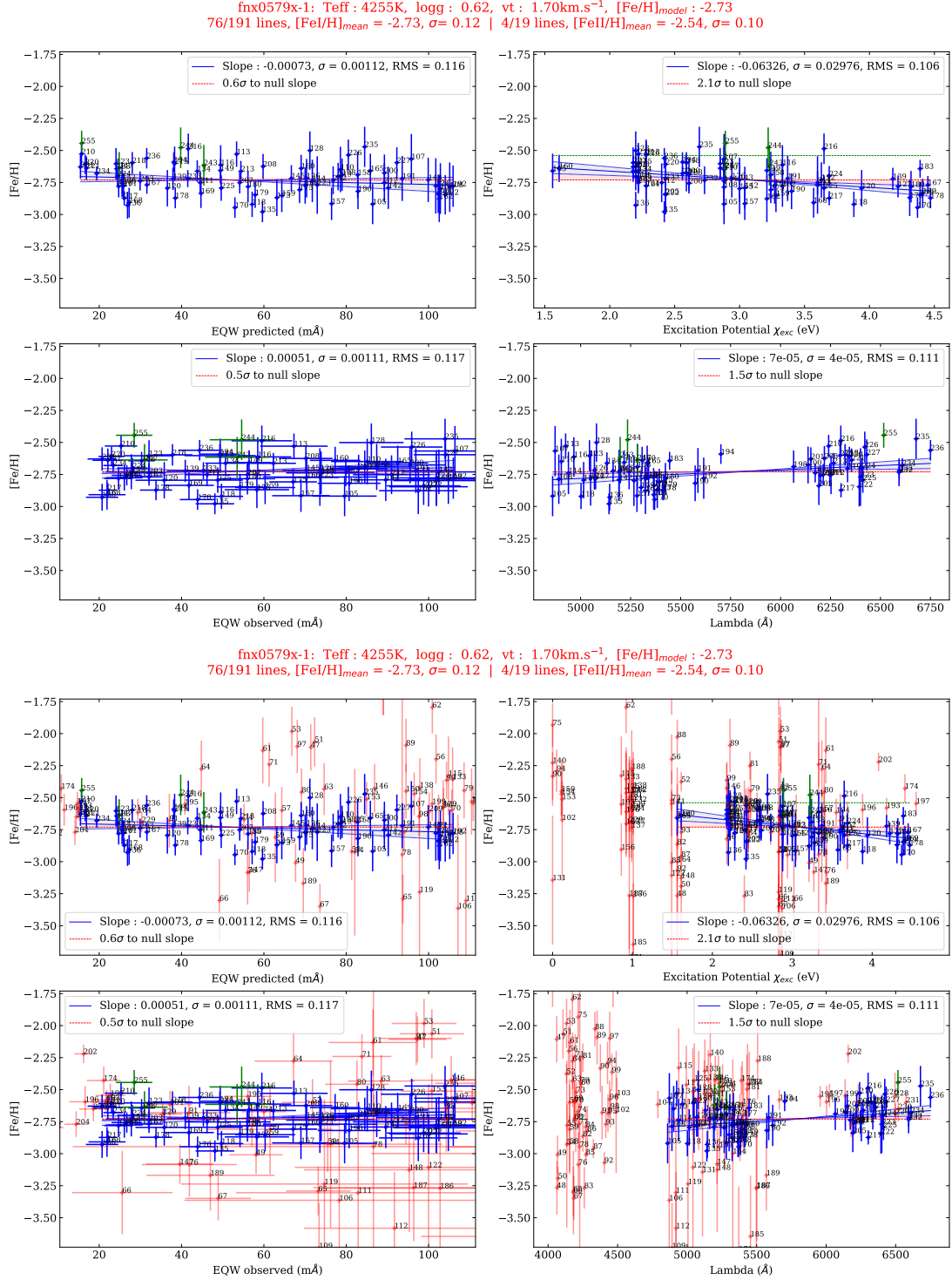


Figure 2.3 – Top: Final diagnostics plots for star fnx0579x-1 in Fornax.

Bottom: Final diagnostics showing in red the iron lines automatically excluded by the routine with : $\lambda < 4400 \text{ \AA}$, $110 \text{ m\AA} < \text{EW} < 20 \text{ m\AA}$, or $\chi < 1.4 \text{ eV}$.

2.2. Main steps of abundance determination

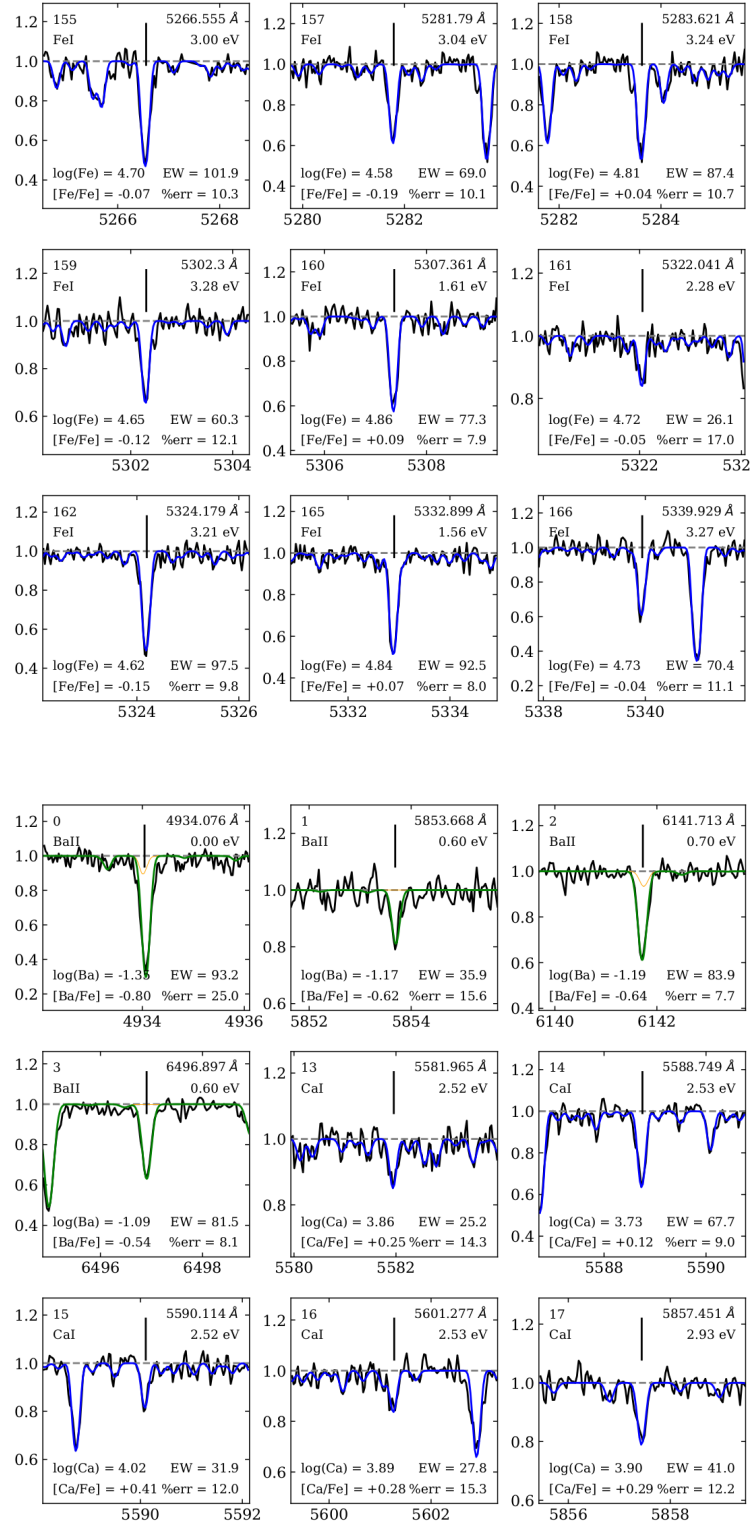


Figure 2.4 – Example of summary tables of individual lines measured in a spectrum (fnx0579x–1 in that case). Abundances are derived from their EWs (in blue) or from spectral synthesis (in green).

Chapter 2. Derivation of chemical abundances from stellar spectra

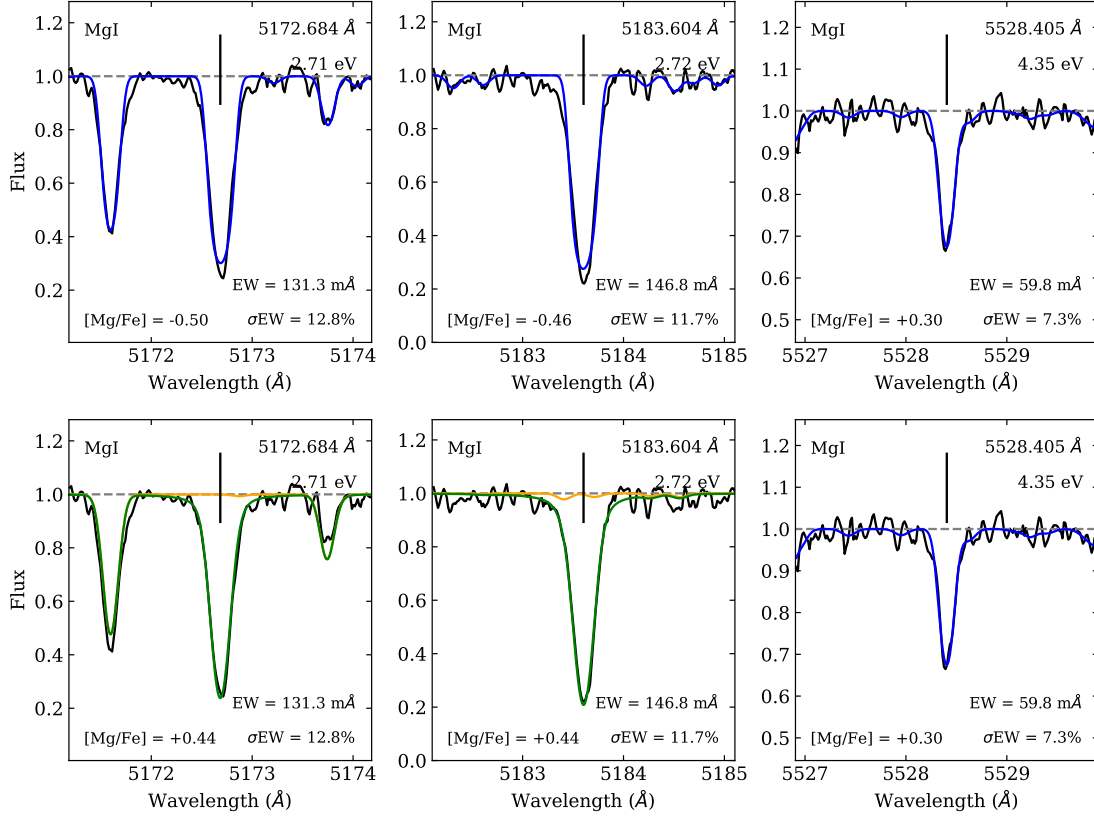


Figure 2.5 – Comparison of three Mg lines (5172.684, 5183.604, 5528.405 Å) measured in the star S04-130 in Sextans. The observed spectrum is in black, the blue line is the fitted spectrum by DAOSPEC with Gaussian profiles, the green line is the best synthetic spectrum obtained from spectral synthesis. The corresponding derived abundances are indicated at the bottom of each panels.

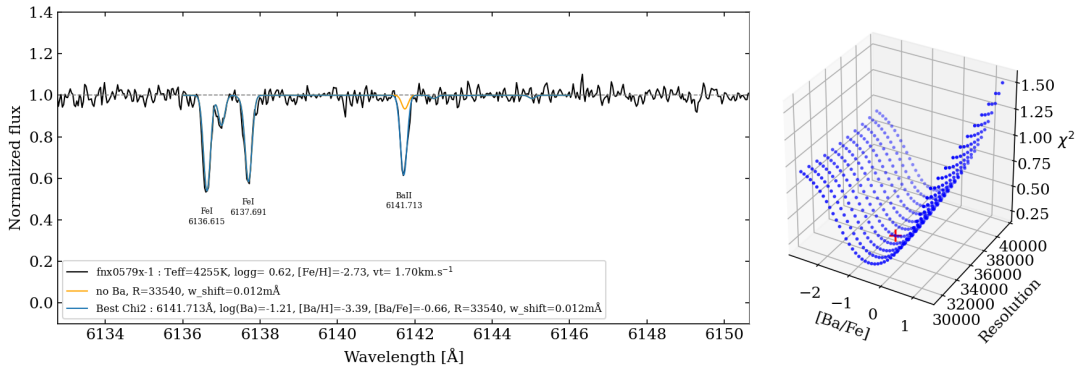


Figure 2.6 – Example of a spectral synthesis by χ^2 minimisation for the Ba II 6141 Å line in star fnx0579x-1. The barium abundance is varied between $-2.0 \leq [\text{Ba}/\text{Fe}] \leq +2.0$ dex. The resolution of the synthetic spectrum is optimised between $30,000 < R < 40,000$.

3 The low metallicity tail of 3 classical dwarfs spheroidal galaxies

3.1 Context in the DART survey

The Dwarf galaxy Abundances and Radial-velocities Team (DART) is a ESO large program (171.B-0588, PI: Tolstoy, [Tolstoy et al. \(2003\)](#)) focused on the study of 4 classical dwarf galaxies : Sculptor, Fornax, Sextans and Carina. Thanks to the advent of 8m-class telescopes such as the ESO Very Large Telescope (VLT) associated with efficient multi-object spectrograph, spectroscopic study of large samples of stars within dwarf galaxies became possible.

DART used the multi-object spectrograph FLAMES/GIRAFFE at the VLT with the low resolution mode LR 8 ($R = 6500$) covering the region of the Ca II triplet (CaT) in the near-infrared region at $\sim 6500 \text{ \AA}$. The CaT is known to be a very good indicator of the metallicity (noted $[\text{Fe}/\text{H}]_{\text{CaT}}$) thanks to an empirical relation with the strength of the lines (i.e. their equivalent width).

[Battaglia et al. \(2008\)](#) proved the robustness of classical CaT calibration from globular clusters, applied to RGB stars in the metallicity range of $-2.5 < [\text{Fe}/\text{H}] < -0.5$. The GIRAFFE observations covered the dwarfs galaxies from their centre to their tidal radius, it allowed to compute metallicities, radial velocities, and to identify hundreds of probable members : around 200 in Sextans (their spatial distribution is presented on Figure 1 of Publication in Section 3.3), ~ 900 in Fornax and ~ 300 in Carina (Figure 2 of Publication in Section 3.4), and 500 in Sculptor.

The first CaT results of DART have shown that dwarf galaxies are not as simple systems as they have been considered for a long time. [Battaglia et al. \(2006\)](#) identified 3 different stellar populations in Fornax, with different ages, metallicity distribution and spatial distribution. In a same way [Tolstoy et al. \(2004\)](#) demonstrated the existence of two different populations in Sculptor, a metal-poor spatially extended population, and a more metal-rich population ($[\text{Fe}/\text{H}] > -1.7$) more centrally concentrated. As observed in Fornax and Sculptor, the metal-poor population of Sextans is more spatially extended than its central metal-rich population ([Battaglia et al. 2011](#)).

It was initially thought that dwarf galaxies were missing stars with $[\text{Fe}/\text{H}] < -2.9$ from the large CaT sample observed by DART, as reported by [Helmi et al. \(2006\)](#); [Helmi \(2006\)](#). They statistically compared the low metallicity tail of the 4 dSphs with the MW Halo distribution

from the Hamburg/ESO survey HES, which had already identified hundreds of EMP (Beers & Christlieb 2005), but also stars below $[\text{Fe}/\text{H}] = -4$ (Christlieb et al. 2002), concluding that some EMPs should have been detected in the dSphs.

Later Starkenburg et al. (2010) showed that the CaT calibration was significantly deviating from the linear regime for metallicities below $[\text{Fe}/\text{H}] < -2$. They provided an updated calibration valid down to $[\text{Fe}/\text{H}] = -4.5$ associated with new $[\text{Fe}/\text{H}]_{\text{CaT}}$ estimations for the stars observed by DART.

In parallel, high resolution spectroscopy in large wavelength ranges (3800–6500 Å), at high signal to noise ratios (SNR) of 30–100, were conducted on the most promising candidates : e.g. Tafelmeyer et al. (2010) observed in Sculptor a star with $[\text{Fe}/\text{H}] = -3.96$, the most metal-poor star studied in a dwarf galaxy, but also the single EMP studied in Fornax so far. Since then Jablonka et al. (2015) have doubled the number of EMPs known in Sculptor, reaching 10 stars, the most studied dSph in its extremely metal-poor regime. Moreover Aoki et al. (2009) observed 6 stars with metallicities $[\text{Fe}/\text{H}] < -2.5$ in Sextans. Eventually, the dSphs were not totally lacking of EMPs, and their observation opened new insights on the very early stages of the dSphs formation.

3.2 Firsts chemical evolution overviews

In addition to this meticulous works on the most interesting stars, and to the general view provided by the CaT spectroscopy, observations were conducted in intermediate wavelength ranges (5300–6700 Å) with the multi-object spectrograph FLAMES/GIRAFFE (HR10, HR13, HR14 modes, $R = 20,000$) for a single pointing in the central region of each dSph.

Eighty to 100 stars, among the probable members identified by DART, were observed in the centre of Fornax (Letarte et al. 2010), Sculptor (Hill et al. 2019), Sextans (Theiler et al. 2020), and by Norris et al. (2017); Lemasle et al. (2012); Venn et al. (2012) in Carina. The wavelength range associated with a decent resolution and SNR, allowed to derive reliable metallicities and abundance of up to 10 chemical elements. These statistically significant samples opened insights on the chemical evolution of the three dSphs for the first time.

One of the most striking result is summarized in Figure 3.1. This figure shows the abundances of three α -elements derived : magnesium, calcium and titanium, for Sextans, Sculptor and Fornax compared to the MW halo distribution. The three dSphs and the halo, have very different abundance patterns. At low metallicity ($[\text{Fe}/\text{H}] < -1$) in the MW halo, an α -rich plateau is observed at a mean level of $[\alpha/\text{Fe}] \sim +0.4$ dex. This plateau has a very small level of dispersion ($\sigma \sim 0.2$ dex), and very few outliers ($[\alpha/\text{Fe}] \leq 0.0$ dex) are observed. This is suggesting a very well mixed ISM and homogeneous conditions of formation. At higher metallicity, when the contribution of SNeIa which produces large quantity of iron starts to dominate the production of α -elements from the SNeII, we observe the so-called "knee", a fast decrease in the $[\alpha/\text{Fe}]$ ratios from +0.4 to the solar ratio $[\alpha/\text{Fe}] = 0.0$. The knee is located at around $[\text{Fe}/\text{H}] = -0.8$ in the MW halo, in Sextans the knee is located at a much lower metallicity, around $[\text{Fe}/\text{H}] = -2$ and has very steep slope. This is explained by the fact that Sextans had a very short star formation history (SFH) which stopped after only a few Gyrs (Bettinelli et al. 2018; Lee et al. 2009). As seen on

Figure 3.2, Lee et al. (2009) showed that the star formation almost totally stopped after ~ 5 Gyrs in Sextans. They computed the SFHs in 4 different regions from the centre of Sextans and also revealed the presence of a gradient in the spatial distribution of the Sextans members, with the more spatially extended regions having the shortest SFH, resulting in a more metal-poor stellar population than the inner regions.

Fornax on the other hand, has a more extended star formation history with a population dominated by star of intermediate ages of 1–10 Gyr (as seen on Figure 3.3, taken from de Boer et al. (2012)), resulting in an overall metallicity of $\langle [\text{Fe}/\text{H}] \rangle = -0.8$ and a knee at higher metallicity than Sextans. Finally in a similar way as in Sextans, a gradient with increasing metallicity is also present towards the centre of Fornax.

Carina, unlike Sextans and Fornax, presents a more complex SFH. de Boer et al. (2014) showed the evidence for 4 different bursts of star formation that occurred during the evolution of Carina, as seen in Figure 3.4. This complex SFH is reflected in its chemical composition, in Section 3.4, Figure 4 of the publication, we can see that Carina has a very scattered chemical composition, with a large dispersion in the $[\alpha/\text{Fe}]$ distribution down to $[\text{Fe}/\text{H}] = -2.5$.

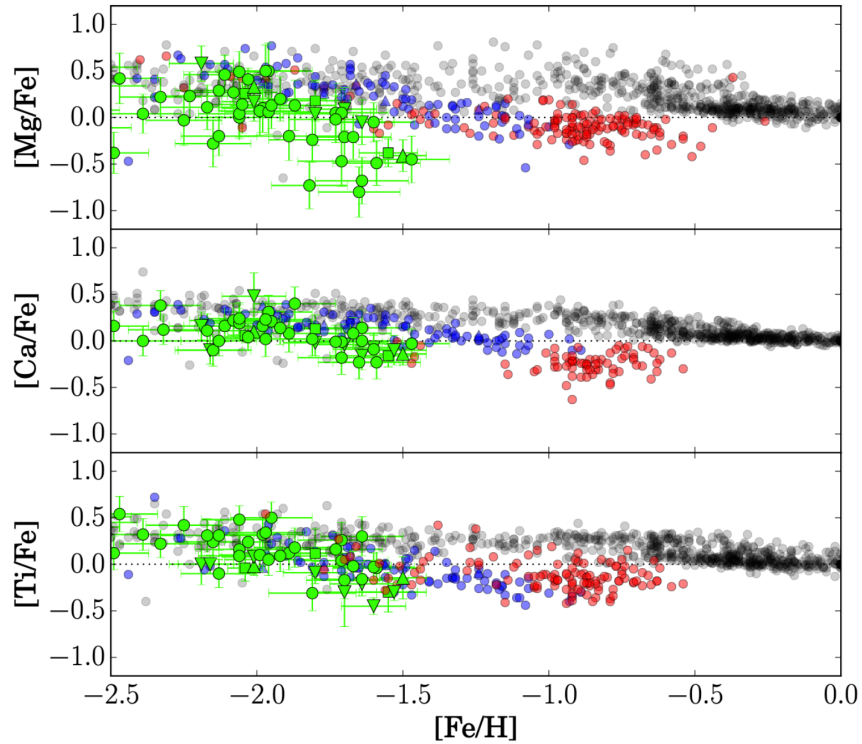


Figure 3.1 – Abundances of α -elements for the 3 dSphs observed by DART with FLAMES/GIRAFFE. Sextans is represented in green, Fornax in red, Sculptor in blue, compared to the MW halo in grey. Figure from Theiler et al. (2020).

The above presentation provides a brief overview of the diversity encountered among dwarf galaxies. This sample of three dSphs is important to study because it is very diverse on many properties : from the lower mass end of the classical dSphs with Sextans and Carina, to the most

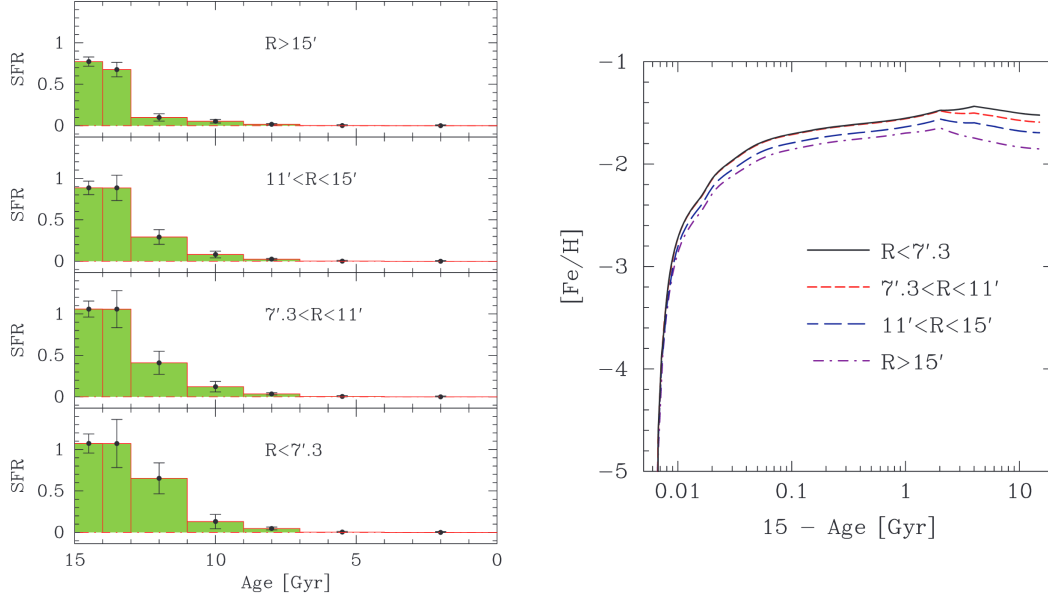


Figure 3.2 – Left : Star formation history computed in four different radii from the centre of Sextans. The most distant regions have the shortest SFH, while the more centred regions have longer SFH. Right : Metal enrichment history for the four regions in Sextans as a function of time. The figures are from [Lee et al. \(2009\)](#).

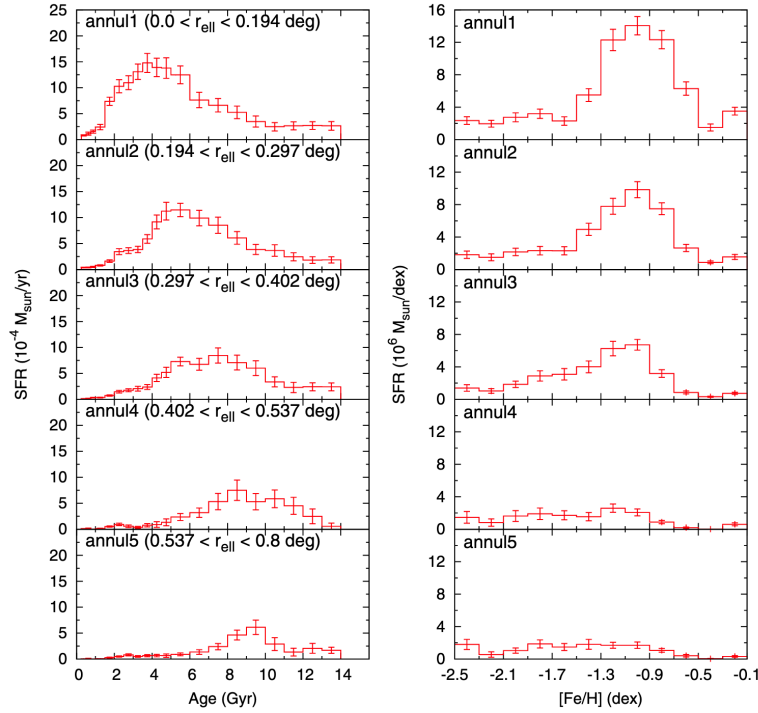


Figure 3.3 – Star formation history and metallicity distribution computed in five different radii from the centre of Fornax by [de Boer et al. \(2012\)](#).

3.3. Publication : Homogeneity in the early chemical evolution of the Sextans dwarf spheroidal galaxy

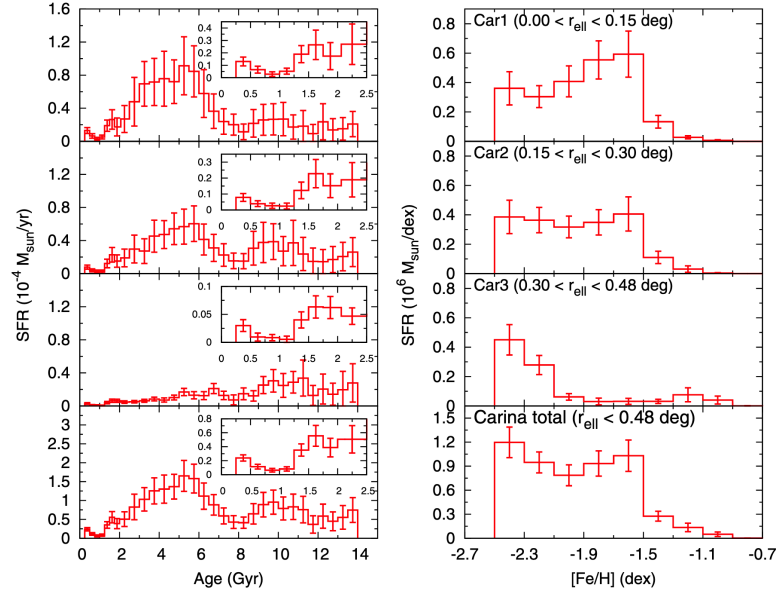


Figure 3.4 – Star formation history and metallicity distribution computed in four different radii from the centre of Carina by [de Boer et al. \(2014\)](#).

massive one (Fornax), from the very metal-poor Sextans to the more metal-rich Fornax, and finally from the very complex chemical evolution and SFH of Carina to the more homogeneous evolution of Sextans.

However, while the dSphs last stages of evolution start to be characterized thanks to the multi-fibre spectrograph observations ([Theler et al. 2020](#); [Hill et al. 2019](#); [Letarte et al. 2010](#); [Norris et al. 2017](#); [Venn et al. 2012](#)), the very early stage of their formation is key to link these systems with larger galaxies.

This is the framework of the first part of my thesis, providing new detailed high resolution spectroscopic analysis of EMP star candidates in the three Sextans, Fornax and Carina dSphs.

3.3 Publication : Homogeneity in the early chemical evolution of the Sextans dwarf spheroidal galaxy

This section presents my first work at high resolution on extremely metal-poor stars in the dwarf spheroidal galaxy Sextans. Sextans is one of the faintest classical dSphs, it is a very extended object (120 ± 20 arcmin, [Cicúéndez et al. \(2018\)](#)) with a very low surface brightness and thus was

Chapter 3. The low metallicity tail of 3 classical dwarfs spheroidal galaxies

discovered quite recently, in 1990 ([Irwin et al. 1990](#)). While Fornax is clearly seen on Image 3.5 and Carina is barely identified, Sextans would not be distinguishable at all from the foreground MW stars by eye.

Sextans is very little explored in its EMP regime : only 6 stars with $[\text{Fe}/\text{H}] < -2.5$ from [Aoki et al. \(2009\)](#) and 2 from [Tafelmeyer et al. \(2010\)](#) were previously known. The results of [Aoki et al. \(2009\)](#) with systematic low α abundances suggesting that Sextans-like dwarf galaxies can not be the building blocks of bigger galaxies when compared to MW halo stars, were in stark contradiction with the results of our 2 new EMP analysed, and the models presented in previous sections. Thus I decided to re-analyse this dataset in addition to our new sample.

The work presented below has been published in *Astronomy & Astrophysics*, Volume 644, id.A75, 14 pp. ([Lucchesi et al. 2020](#)) [NASA ADS link](#). I conducted the complete data processing, the stellar model optimisation and the chemical analysis of the stars presented in this paper.

3.3. Publication : Homogeneity in the early chemical evolution of the Sextans dwarf spheroidal galaxy



Figure 3.5 – Images of the Fornax dSph (on the top), and the Carina dSph (on the bottom). While Fornax is clearly identified on a picture, Carina at the low end mass of the classical dSphs is barely distinguishable. Credit : ESO.

Homogeneity in the early chemical evolution of the Sextans dwarf spheroidal galaxy[★]

R. Lucchesi^{1,2,★★}, C. Lardo², F. Primas¹, P. Jablonka^{2,3}, P. North², G. Battaglia^{4,5}, E. Starkenburg⁶, V. Hill⁷, M. Irwin⁸, P. Francois³, M. Shetrone⁹, E. Tolstoy¹⁰, and K. Venn¹¹

¹ European Southern Observatory, Karl-Schwarzschild-str. 2, 85748 Garching bei München, Germany

² Physics Institute, Laboratoire d'astrophysique, École Polytechnique Fédérale de Lausanne (EPFL), Observatoire, 1290 Versoix, Switzerland

³ GEPI, Observatoire de Paris, CNRS, Université de Paris Diderot, 92195 Meudon Cedex, France

⁴ Instituto de Astrofísica de Canarias (IAC), Calle Via Láctea, s/n, 38205, San Cristóbal de la Laguna, Tenerife, Spain

⁵ Departamento de Astrofísica, Universidad de La Laguna, 38206, San Cristóbal de la Laguna, Tenerife, Spain

⁶ Leibniz-Institut für Astrophysik Potsdam, An der Sternwarte 16, D-14482 Potsdam, Germany

⁷ Laboratoire Lagrange, Université de Nice Sophia-Antipolis, Observatoire de la Côte d'Azur, France

⁸ Institute of Astronomy, University of Cambridge, Madingley Road, Cambridge CB3 0HA, U.K.

⁹ McDonald Observatory, University of Texas at Austin, Fort David, TX, USA

¹⁰ Kapteyn Astronomical Institute, University of Groningen, Landleven 12, NL-9747AD Groningen, the Netherlands

¹¹ Department of Physics and Astronomy, University of Victoria, PO Box 3055, STN CSC, Victoria BC V8W 3P6, Canada

Received 20 January 2020; accepted 25 August 2020

ABSTRACT

We present the high-resolution spectroscopic analysis of two new extremely metal-poor star (EMPS) candidates in the dwarf spheroidal galaxy Sextans. These targets were preselected from medium-resolution spectra centered around the Ca II triplet in the near-infrared and were followed-up at higher resolution with VLT/UVES. We confirm their low metallicities with $[\text{Fe}/\text{H}] = -2.95$ and $[\text{Fe}/\text{H}] = -3.01$, which place them among the most metal-poor stars known in Sextans. The abundances of 18 elements, including C, Na, the α , Fe-peak, and neutron-capture elements, are determined. In particular, we present the first unambiguous detection of Zn in a classical dwarf at extremely low metallicity. Previous indications were made of a large scatter in the abundance ratios of the Sextans stellar population around $[\text{Fe}/\text{H}] \sim -3$ when compared to other galaxies, particularly with very low observed $[\alpha/\text{Fe}]$ ratios. We took the opportunity of reanalyzing the full sample of EMPS in Sextans and find a $[\alpha/\text{Fe}]$ Milky Way-like plateau and a ~ 0.2 dex dispersion at fixed metallicity.

Key words. stars: abundances – Local Group – galaxies: dwarf – galaxies: formation

1. Introduction

In the cosmological Λ cold dark matter paradigm (Λ CDM), the assembly of large structures in the Universe arose from the coalescence of small systems, and galaxy formation followed the cooling of the primordial gas in dark matter (DM) halos (Press & Schechter 1974; White & Rees 1978; Springel et al. 2006). Dwarf spheroidal galaxies (dSphs) are most probably among the best representatives of the protogalactic systems because they are the faintest and most DM-dominated galaxies known in the Universe. However, their exact significance and their role in galaxy formation remain to be clarified. In particular, the abundance patterns in dSph stars differ drastically from those of the field Milky Way (MW) halo population above $[\text{Fe}/\text{H}] \sim -2$ (Shetrone et al. 2001a; Venn et al. 2004a; Tolstoy et al. 2009; Letarte et al. 2010; Jablonka et al. 2015; Hill et al. 2019a; Theler et al. 2019). Nonetheless, dwarf galaxies offer the most metal-poor galactic environments that can be investigated. Their stellar populations therefore provide crucial insights into the star for-

mation conditions in the most pristine environments (e.g., Tolstoy et al. 2009; Frebel & Norris 2015).

Low-mass, long-lived extremely metal-poor (EMP, with $[\text{Fe}/\text{H}] \leq -3$) stars have retained the nucleosynthetic signatures of the first generation of stars in their atmospheres. By comparing the chemical patterns of these EMPS in galaxies of very different masses and star formation histories, from ultra-faint and classical dwarfs to the halo of the MW, we can therefore directly test whether the primordial chemical evolution was a universal process and understand the relation between dwarfs and the building blocks of the more massive systems. The proximity of a large number of MW satellites fortunately offers the unique opportunity of studying the relevant aspects of their evolution in great detail and on a star-by-star basis.

The Sextans dSph was discovered by Irwin et al. (1990). At a distance of ~ 90 kpc, it is one of the closest satellites of the MW (Mateo et al. 1995; Lee et al. 2003). It is very extended on the sky with a tidal radius of 120 ± 20 arcmin (Cicúéndez et al. 2018) and low surface brightness $\mu_{V,0} = 27.22 \pm 0.08$ mag.arcsec⁻² (Muñoz et al. 2018). It is a relatively low-mass but strongly dark-matter-dominated classical dSph, $M/L \gg 100$, with a dynamical mass of about $3 \times 10^8 M_\odot$ measured out to a radius of ~ 3 kpc, as seen in Fig. 6 of Breddels & Helmi (2013) (but see also Łokas (2009);

[★] Based on UVES observations collected at the ESO, proposal 093.D-0311.

^{★★} e-mail : romain.lucchesi@epfl.ch

Walker et al. (2010); Battaglia et al. (2011) for earlier measurements). The analysis of the color-magnitude diagram (CMD) of Sextans reveals a stellar population that is largely dominated by stars older than ~ 11 Gyr (Lee et al. 2009; Bettinelli et al. 2018), with evidence for radial metallicity and age gradients; the oldest stars forming the most spatially extended component (Lee et al. 2003; Battaglia et al. 2011; Okamoto et al. 2017; Cicu  ndez et al. 2018).

Very little is known about the metal-poor tail of the stellar population in Sextans. Only eight EMPS have so far been followed-up at high resolution (Aoki et al. 2009; Tafelmeyer et al. 2010; Honda et al. 2011). The analysis of Aoki et al. (2009) suggested the possible existence of a set of low, subsolar, $[\alpha/\text{Fe}]$ stars and an increased scatter at fixed metallicity compared to the MW or even Sculptor (Starkenburg et al. 2013; Jablonka et al. 2015), which today is the dSph with the largest number of studied EMPS. If confirmed, this has strong implications for the formation processes of Sextans. Cicu  ndez & Battaglia (2018) recently suggested that Sextans could have gone through an accretion or merger episode, which might explain the low $[\alpha/\text{Fe}]$ measurements of Aoki et al. (2009). The most pressing need nevertheless is to increase the number of EMPS with detailed chemical abundances.

The Dwarf Abundances and Radial velocity Team (DART), formed around the ESO Large Program 171.B-0588(A), has surveyed Sextans up to its tidal radius with the medium-resolution grism of FLAMES/GIRAFFE LR8 around the Ca II triplet (CaT). Starkenburg et al. (2010) provided the community with a metallicity calibration based on the CaT valid down to $[\text{Fe}/\text{H}] \sim -4$. This work enabled the identification of a set of new EMP candidates such as in Starkenburg et al. (2013) and Jablonka et al. (2015) and the two targets of this study.

This paper is the first of a series targeting EMP candidates at high resolution in Sextans, Fornax, and Carina to probe the first stages of the chemical enrichment processes occurring in the early Universe. The paper is structured as follows: § 2 presents the observational material and data reduction. The stellar parameters are determined and the elemental abundances are measured in § 3, along with their associated uncertainties. Comments and remarks on the abundances of specific elements are provided in § 4. Finally, we discuss our results and draw conclusions in § 5 and § 6.

2. Observations and data reduction

2.1. Target preselection, observations, and data reduction

The two EMP candidates of this work, S04–130 and S11–97, are red giant branch (RGB) stars that were selected from the CaT sample of Battaglia et al. (2011). The calibration of Starkenburg et al. (2013) led to low-metallicity estimates $[\text{Fe}/\text{H}]_{\text{CaT}} < -2.8$.

S04–130 and S11–97 were followed-up at high resolution with the UVES¹ spectrograph (Dekker et al. 2000) mounted at the ESO-VLT (program 093.D–0311(B)). We used dichroic1 mode with the gratings 390 blue arm CD 2 centered at 3900 Å and 580 red arm CD 3 centered at 5800 Å, together with a 1.2'' slit, leading to a nominal resolution $R \sim 34,000$. The total wavelength coverage is ~ 3200 – 6800 Å, and the effective usable spectral information starts from ~ 3800 Å. Each star has been observed for a total of five hours, split into six individual subexposures. The reduced data, including bias subtraction, flat fielding,

wavelength calibration, spectral extraction, and order merging, were taken from the ESO Science Archive Facility.

Table 1 presents some details of the observations (spectral coverage, and signal-to-noise ratios per spectroscopic pixel) along with the coordinates of stars, their estimated metallicities from the CaT calibration and measured heliocentric radial velocities (see § 2.2). Figure 1 shows the colour-magnitude diagram (CMD) of probable Sextans members from Battaglia et al. (2011). Our UVES targets are highlighted in red. For comparison purposes, we also display the two EMPS, Sex24–72 and Sex11–04, that were observed with UVES and originally presented in Tafelmeyer et al. (2010) and the six EMPS (S10–14, S11–13, S11–37, S12–28, S14–98, and S15–19) that were observed with the high-dispersion spectrograph installed on the 8.2m Subaru Telescope (Noguchi et al. 2002). They were discussed in Aoki et al. (2009). We refer to the original papers for additional details about the observations. We also show the spatial distribution of these EMPS.

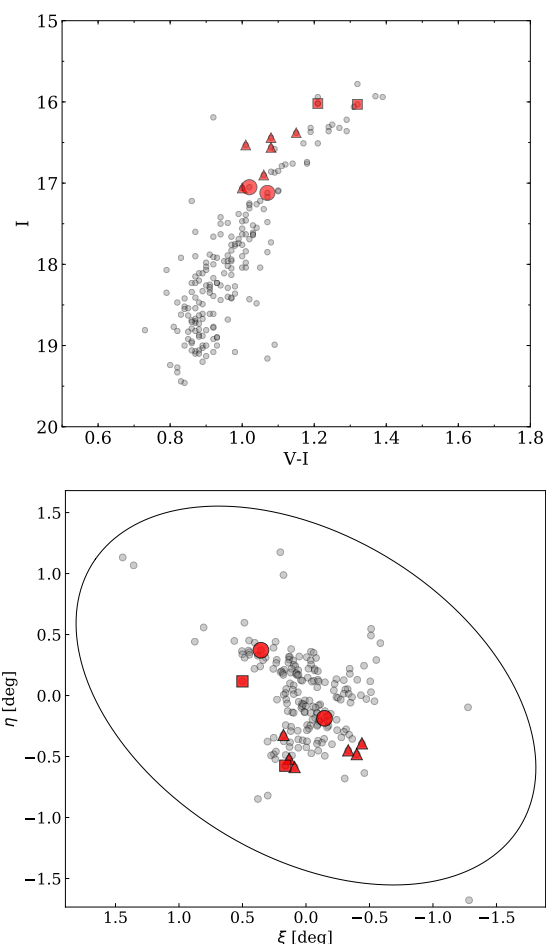


Fig. 1: *Top panel*: $V - I$, I CMD of Sextans. Gray circles are probable Sextans members based on their $[\text{Fe}/\text{H}]_{\text{CaT}}$ metallicities and radial velocities (Battaglia et al. 2011). The red symbols show the stars we discuss here. Large circles are the new targets of this work. The samples of Tafelmeyer et al. (2010) and Aoki et al. (2009) are shown with smaller squares and triangles, respectively. The *bottom panel* shows the spatial distribution of these stars. The ellipse indicates the tidal radius of Sextans.

¹ Ultraviolet and Visual Echelle Spectrograph

Table 1: Observation journal. The blue and red parts of the spectra acquired with the 580 red arm CD 3 are considered separately. The λ range refers to the spectral ranges used in the analysis.

ID	$\alpha(J2000)$ [h:m:s]	$\delta(J2000)$ [° :′ :″]	[Fe/H] _{CaT}	Setting [s]	λ range [Å]	S/N [pix]	$\langle V_{rad,helio} \rangle \pm \sigma$ [km s ⁻¹]
S04-130	10:14:28.02	-1:14:35.80	-2.89	Dic1-CD#2	3800–4520	15	215.29 ± 1.11
				Dic1-CD#3(Blue)	4780–5750	45	215.64 ± 0.82
				Dic1-CD#3(Red)	5830–6800	55	
S11-97	10:12:27.89	-1:48:05.20	-2.80	Dic1-CD#2	3800–4520	16	218.06 ± 1.15
				Dic1-CD#3(Blue)	4780–5750	52	218.50 ± 1.00
				Dic1-CD#3(Red)	5830–6800	59	

2.2. Radial velocity measurements and normalization

The heliocentric radial velocities (RVs) were measured with the IRAF² task *rvidlines* on each individual exposure. The final RV is the average of these individual values weighted by their uncertainties. This approach allows us to detect possible binary stars, at least those whose RV variations can be detected within about one year³. We did not find any evidence for binarity. After they were corrected for RV shifts, the individual exposures were combined into a single exposure using the IRAF task *scombine* with sigma clipping. As a final step, each spectrum was visually examined, and the few remaining cosmic rays were removed with the *splot* routine.

The average RV of each star (Table 1) coincides with the RV of Sextans ($226.0 \pm 0.6 \text{ km s}^{-1}$) within the velocity dispersion $\sigma = 8.4 \pm 0.4 \text{ km s}^{-1}$ measured by Battaglia et al. (2011). This confirms that our stars are highly probable members.

Spectra were normalized using DAOSPEC (Stetson & Pancino 2008) for each of the three wavelength ranges presented in Table 1. We used a 30 to 40 degree polynomial fit.

3. Chemical analysis

3.1. Line list and model atmospheres

Our line list combines those of Jablonka et al. (2015), Tafelmeyer et al. (2010), and Van der Swaelmen et al. (2013). Information on the spectral lines was taken from the VALD database (Piskunov et al. 1995; Ryabchikova et al. 1997; Kupka et al. 1999, 2000). The central wavelengths and oscillator strengths are given in Table 3. The adopted solar abundances in Table 4 are from Asplund et al. (2009).

We adopted the new MARCS 1D atmosphere models and selected the *Standard composition* class, that is, we included the classical α -enhancement of +0.4 dex at low metallicity. They were downloaded from the MARCS web site (Gustafsson et al. 2008), and interpolated using Thomas Masseron's *interpol_modeles* code, which is available on the same web site⁴. Inside a cube of eight reference models, this code performs a linear interpolation on three given parameters: T_{eff} , $\log g$, and [Fe/H].

² Image Reduction and Analysis Facility; Astronomical Source Code Library ascl:9911.002

³ Observations were performed between 22 April 2015 and 29 January 2016.

⁴ <http://marcs.astro.uu.se>

3.2. Photometric temperature and gravity

The atmospheric parameters (APs) were initially determined using photometric information. The first approximated determination of the stellar effective temperature was based on the V–I, V–J, V–H, and V–K color indices measured by Battaglia et al. (2011), and J and Ks photometry was taken from the VISTA commissioning data, which were also calibrated onto the 2MASS photometric system. We assumed $A_V = 3.24 \cdot E_{B-V}$ (Cardelli et al. 1989) and $E_{B-V} = 0.0477$ (Battaglia et al. 2011) for the reddening correction. The adopted photometric effective temperatures, T_{eff} , are listed in Table 2. They correspond to the simple average of the four color temperatures derived from V–I, V–J, V–H, and V–K with the calibration of Ramírez & Meléndez (2005).

Because only very few Fe II lines can be detected in the very low metallicity regime, we determined the stellar surface gravity ($\log g$) from their relation with T_{eff} :

$$\log g_{\star} = \log g_{\odot} + \log \frac{M_{\star}}{M_{\odot}} + 4 \times \log \frac{T_{\text{eff}\star}}{T_{\text{eff}\odot}} + 0.4 \times (M_{\text{bol}\star} - M_{\text{bol}\odot}) \quad (1)$$

assuming $\log g_{\odot} = 4.44$, $T_{\text{eff}\odot} = 5790 \text{ K}$, and $M_{\text{bol}\odot} = 4.75$ for the Sun. We adopted a stellar mass of $0.8 M_{\odot}$ and calculated the bolometric corrections using the Alonso et al. (1999) calibration and a distance of $d=90 \text{ kpc}$ (Karachentsev et al. 2004).

3.3. Final stellar parameters and abundance determination

We determined the stellar chemical abundances through the measurement of the equivalent widths (EWs) or the spectral synthesis of atomic transition lines, when necessary. The EWs were measured with DAOSPEC (Stetson & Pancino 2008). This code performs a Gaussian fit of each individual line and measures its corresponding EW. Although DAOSPEC fits saturated Gaussians to strong lines, it cannot fit the wider Lorentz-like wings of the profile of very strong lines, in particular beyond 200 mÅ . This is especially relevant at very high resolution (Kirby & Cohen 2012). For some of the strongest lines in our spectra, we therefore derived the abundances by spectral synthesis (see below).

The measured EWs are provided in Table 3. Values in bracket indicate that the corresponding abundances were derived by spectral synthesis. The abundance derivation from EWs and the spectral synthesis calculation were performed with the Turbospectrum code (Alvarez & Plez 1998; Plez 2012), which assumes local thermodynamic equilibrium (LTE), but treats continuum scattering in the source function. We used a plane-parallel transfer for the line computation; this is consistent with our previous work on EMP stars (Tafelmeyer et al. 2010; Jablonka et al. 2015).

The stellar atmospheric parameters were refined in an iterative manner. In order to constrain T_{eff} and the microturbulence velocities (v_t), we required no trend between the abundances derived from Fe I and excitation potential (χ_{exc}) or the predicted⁵ EWs (Magain 1984). Starting from the initial photometric parameters of Table 2, we adjusted T_{eff} and v_t by minimizing the slopes of the diagnostic plots allowing the slope to deviate from zero by no more than about twice the uncertainty on the slope. We did not force ionization equilibrium between Fe I and Fe II, taking into account that there will likely be non-LTE (NLTE) effects at these low metallicities (Mashonkina et al. 2017a; Ezzeddine et al. 2017). For each iteration the corresponding values of $\log g$ were computed from its relation with T_{eff} , assuming the updated values of T_{eff} , and adjusting the model metallicity to the mean iron abundance derived in the previous iteration.

We excluded from our analysis Fe I lines with $\chi_{\text{exc}} < 1.4$ eV in order to minimize the NLTE effect on the measured abundances (Jablonka et al. 2015). Additionally, we used only the 580 setting data to calculate $[\text{Fe}/\text{H}]$ and optimize the atmospheric parameters.

We derived the chemical abundances of the strong lines with measured $\text{EW} > 100$ mÅ by spectral synthesis. These abundances were obtained using our own code, which performs a χ^2 -minimization between the observed spectral features and a grid of synthetic spectra calculated on the fly with *Turbospectrum*. A line of a chemical element X is synthesized in a wavelength range of ~ 50 Å. It is optimized by varying its abundance in steps of 0.1 dex, from $[\text{X}/\text{Fe}] = -1.0$ dex to $[\text{X}/\text{Fe}] = +1.0$ dex. In the same way, the resolution of the synthetic spectra is optimized, starting from the theoretical instrumental resolution, by convolving the spectra in a wide range of Gaussian widths for each abundance step. A second optimization, with abundance steps of 0.01 dex, is then performed in a smaller range around the minimum χ^2 in order to refine the results. Similarly, the elements with a significant hyperfine structure (HFS) (Sc, Mn, Co, and Ba) have been determined by running *Turbospectrum* in its spectral synthesis mode in order to properly take into account blends and the HFS components in the abundance derivation, as in North et al. (2012), Prochaska & McWilliam (2000) for Sc and Mn, and from the Kurucz web site⁶ for Co and Ba.

The final (spectroscopic) parameters are given in Table 2. The typical uncertainties are ~ 100 K on T_{eff} , ~ 0.15 dex on $\log g$, assuming a $\pm 0.1 M_{\odot}$ error on M_{\odot} and a 0.2 mag error on M_{bol} , and about 0.15 km s⁻¹ on v_t .

The final abundances reported in Table 4 are the average abundances from Table 3 based on EWs or spectral synthesis, weighted by errors. For a few elements (V, Y, and Zr) we were only able to place upper limits on their abundances (see Table 4). They are based on visual inspection of the observed spectrum, on which synthetic spectra were overplotted with increasing abundances, until the χ^2 deviation became noticeable.

3.4. Error budget

1. Uncertainties due to the atmospheric parameters. To estimate the sensitivity of the derived abundances to the adopted atmospheric parameters, we repeated the abundance analysis and varied only one stellar atmospheric parameter at a time

by its corresponding uncertainty, keeping the others fixed and repeating the analysis. The estimated internal errors are ± 100 K in T_{eff} , ± 0.15 dex in $\log(g)$, and ± 0.15 km s⁻¹ in v_t . Table 5 lists the effects of these changes on the derived abundances for star S04–130. With comparable stellar parameters and S/N, the effects of changes in atmospheric parameters on abundances are expected to be the same for stars S11–97.

2. Uncertainties due to EWs or spectral fitting. The uncertainties on the individual EW measurements δ_{EWi} are provided by DAOSPEC (see Table 3) and computed according to the following formula (Stetson & Pancino 2008) :

$$\delta_{EWi} = \sqrt{\sum_p (\delta I_p)^2 \left(\frac{\partial EW}{\partial I_p} \right)^2 + \sum_p (\delta I_{C_p})^2 \left(\frac{\partial EW}{\partial I_{C_p}} \right)^2} \quad (2)$$

where I_p and δI_p are the intensity of the observed line profile at pixel p and its uncertainty, and I_{C_p} and δI_{C_p} are the intensity and uncertainty of the corresponding continuum. The uncertainties on the intensities are estimated from the scatter of the residuals that remain after subtraction of the fitted line (or lines, in the case of blends). The corresponding uncertainties σ_{EWi} on individual line abundances are propagated by *Turbospectrum*. This is a lower limit to the real EW error because systematic errors like the continuum placement are not accounted for. In order to account for additional sources of error, we quadratically added a 5% error to the EW uncertainty, so that no EW has an error smaller than 5%. This gives a typical uncertainty of $\sigma_{EW}(\text{Fe I}) = 0.08$ rather than 0.04 in Fe I abundance. For the abundances derived by spectral synthesis (e.g., strong lines, hyperfine structure, or carbon from the G band), the uncertainties were visually estimated by gradually changing the parameters of the synthesis until the deviation from the observed line became noticeable.

The final errors listed in Table 4 were computed following the recipes outlined in Hill et al. (2019b) and Jablonka et al. (2015). Typical abundance uncertainties for an element X due to the EW uncertainties (σ_{EWi} propagated from δ_{EWi}) are computed as

$$\sigma_{EW}(X) = \sqrt{\frac{N_X}{\sum_i 1/\sigma_{EWi}^2}} \quad (3)$$

where N_X represents the number of lines measured for element X .

The dispersion σ_X around the mean abundance of an element X measured from several lines is computed as

$$\sigma_X = \sqrt{\frac{\sum_i (\epsilon_i - \bar{\epsilon})^2}{N_X - 1}} \quad (4)$$

where ϵ stands for the logarithmic abundance.

The final error on the elemental abundances is defined as $\sigma_{\text{fin}} = \max(\sigma_{EW}(X), \sigma_X / \sqrt{N_X}, \sigma_{Fe} / \sqrt{N_X})$. As a consequence, no element X can have an estimated dispersion $\sigma_X < \sigma_{Fe}$; this is particularly important for species with very few lines.

⁵ The use of observed EWs would produce an increase of v_t by 0.1–0.2 km s⁻¹, which would be reflected in a decrease of the measured $[\text{Fe}/\text{H}]$ values by a few hundredths of a dex in a systematic way. A variation like this does not change the results in a significant way.

⁶ <http://kurucz.harvard.edu/line/line.html>

Table 2: Magnitudes, photometric, and spectroscopic parameters.

ID	V	I	J	H	K	Photometric Parameters					log(g) [cgs]	Final Parameters			[Fe/H]
						V − I	V − J	T _{eff} [K] V − H	V − K	mean		T _{eff} [K]	log(g) [cgs]	v _t [km s ^{−1}]	
S04–130	18.071	17.050	16.162	15.543	15.418	4624	4735	4555	4567	4620	1.13	4520	1.07	1.70	−2.94
S11–97	18.189	17.125	16.204	15.653	15.542	4543	4630	4549	4567	4572	1.15	4480	1.10	1.80	−3.01

4. Specific comments on the abundance determination

4.1. Carbon

The carbon abundance was determined from the intensity of the CH molecular band between 4323 Å and 4324 Å. Some of the carbon is locked in CO and CN molecules; as we are not able to measure the oxygen and nitrogen abundances, we assumed that $[O/Fe] = [Mg/Fe]$ and that $[N/Fe]$ has a solar value, following Tafelmeyer et al. (2010) and Starkenburg et al. (2013). Synthetic spectra were then compared to the observed spectra. As an example, Figure 2 shows the comparison between the observed spectrum of S04–130 and five synthetic spectra computed with increasing carbon abundances.

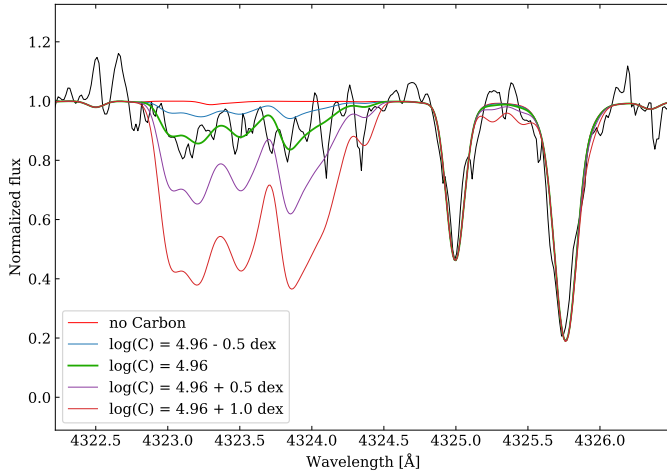


Fig. 2: From top to bottom, examples of synthetic spectra in the CH band are computed with increasing carbon abundances and are overplotted on the observed spectrum of S04–130 (black). The third green line shows our best representation of the data.

4.2. α elements

- *Magnesium*. The Mg abundance is based on five lines that are distributed from the violet to the yellow part of the spectrum. Four of them are rather strong, with $EW > 100$ mÅ and non-Gaussian line profiles. The abundances of these lines are not consistent with the weaker line. For this reason, we decided to derive the Mg abundance through spectral synthesis, after which all lines had consistent abundances. The EW-based abundances derived for the weaker line are consistent with those obtained using spectral synthesis. This confirms the validity of this method. One more Mg I line is present in our spectra, at 44351 Å, but it was discarded because it is strongly blended with Fe, CH, and Cr I lines.

- *Silicon*. Two Si lines are detected in our spectra, but they are in a noisy part of the spectrum and fall very close to the strong Ca II absorption bands. The continuum level is hard to determine in this region, and the derived abundances strongly depend on it. Therefore we did not derive any silicon abundance.
- *Titanium*. The Ti I abundances rely on 10–11 faint lines, all giving consistent abundance values. The Ti II abundances are based on 19–20 lines. They are slightly more scattered as many of them are rather strong. The mean abundances of Ti I and Ti II are different by $\Delta(Ti II - Ti I) = +0.26$ to $+0.29$ dex. This is explained by the fact that Ti II is less sensitive to NLTE effects than its neutral state. Thus, following Jablonka et al. (2015), for the purpose of our discussion we adopted the Ti II abundances as the most representative of the titanium content in our stars.

4.3. Iron-peak elements

- *Scandium*. The Sc abundance is based on seven lines. They are all derived by spectral synthesis taking into account their HFS components. The smallest line (25 mÅ) and the bluest line (44246.8 Å) both give slightly larger abundances, and the other four lines are more consistent.
- *Chromium*. Cr relies on seven to nine lines. Four are rather strong ($EW > 80$ mÅ), and the other five are weaker ($EW < 50$ mÅ). Strong and weaker lines give more consistent results when the abundances are determined through spectral synthesis. The 45208 Å line is blended with an Fe I line and therefore had to be analyzed through spectral synthesis.
- *Manganese*. All Mn lines (five) were synthesized taking into account their HFS components. They give consistent abundance results.
- *Cobalt*. Four lines are present in our spectra. They are all affected by hyperfine structure, and two of them (43894 Å and 43995 Å) are blended with Fe I lines. Therefore we derived all four line abundances by spectral synthesis.
- *Nickel*. The Ni abundance is estimated from one or two strong lines and several very faint ones. Spectral synthesis gives consistent abundances for all lines.
- *Zinc*. Only one line of zinc is present in our observed spectra, at 4810 Å. The detection is clear but the line is faint, therefore the zinc abundance was derived through spectral synthesis.

4.4. Neutron-capture elements

- *Strontium*. Two strong lines of strontium are detected in the blue part of our UVES spectra, but the abundances derived from their EWs are quite discrepant (0.2 dex and 0.8 dex in our two stars, respectively). The 4215.5 Å line of the star S11–97 is affected by the CN molecular band in this region. Spectral synthesis taking into account the carbon abundance

Table 3: Line parameters, observed EWs, and elemental abundances. EWs in brackets are given as indication only; the quoted abundances are derived through spectral synthesis for these lines.

El.	λ [Å]	χ_{ex} [eV]	log(g_f)	EW [mÅ] log(ϵ) S04–130	EW [mÅ] log(ϵ) S11–97
C(CH)	4323			4.96	4.87
Na I	5889.951	0.00	0.108	(198.9) \pm (16.3)	(189.1) \pm (11.9)
Na I	5895.924	0.00	-0.194	(162.3) \pm (9.9)	(179.2) \pm (11.9)
Mg I	3829.355	2.71	-0.227	- \pm -	(176.0) \pm (14.6)
Mg I	3832.304	2.71	0.125	(190.7) \pm (17.8)	- \pm -
Mg I	3838.294	2.72	-0.351	(214.5) \pm (16.1)	(221.2) \pm (18.0)
Mg I	5172.684	2.71	-0.450	(131.3) \pm (16.9)	(181.6) \pm (14.1)
Mg I	5183.604	2.72	-0.239	(146.8) \pm (17.2)	(153.9) \pm (15.2)
Mg I	5528.405	4.35	-0.498	(59.8) \pm (4.3)	(62.9) \pm (4.7)
Al I	3944.006	0.00	-0.623	(110.1) \pm (20.4)	- \pm -
Al I	3961.520	0.01	-0.323	(137.6) \pm (11.7)	(138.4) \pm (10.5)
Si I	3905.523	1.91	-1.041	(185.6)	(195.4)
Si I	4102.936	1.909	-3.140	(89.6)	(58.7)
Ca I	4283.011	1.89	-0.136	45.8 \pm 4.5	49.1 \pm 4.4
Ca I	4318.651	1.90	-0.139	41.7 \pm 5.0	- \pm -
Ca I	4434.957	1.89	-0.007	- \pm -	61.2 \pm 6.6
Ca I	4454.779	1.90	0.258	79.4 \pm 7.6	78.9 \pm 6.4
Ca I	5265.556	2.52	-0.113	- \pm -	24.9 \pm 2.7
Ca I	5349.465	2.71	-0.310	- \pm -	12.5 \pm 1.6
Ca I	5581.965	2.52	-0.555	11.1 \pm 1.4	- \pm -
Ca I	5588.749	2.53	0.358	37.1 \pm 3.2	40.5 \pm 3.2
Ca I	5857.451	2.93	0.240	- \pm -	19.9 \pm 2.1
Ca I	6102.723	1.88	-0.793	34.5 \pm 3.1	33.2 \pm 3.0
Ca I	6122.217	1.89	-0.316	57.3 \pm 4.7	59.7 \pm 4.5
Ca I	6162.173	1.90	-0.090	76.7 \pm 5.8	75.5 \pm 5.7
Ca I	6439.075	2.53	0.390	47.8 \pm 5.0	53.6 \pm 4.2
Sc II	4246.822	0.31	0.242	(128.0) \pm (11.5)	(129.0) \pm (8.8)
Sc II	4314.083	0.62	-0.096	(93.2) \pm (7.0)	(91.4) \pm (7.9)
Sc II	4400.389	0.61	-0.536	(73.8) \pm (6.3)	(67.6) \pm (5.9)
Sc II	4415.557	0.60	-0.668	(82.7) \pm (7.7)	(78.6) \pm (8.4)
Sc II	5031.021	1.36	-0.400	(31.5) \pm (3.4)	(28.1) \pm (6.2)
Sc II	5526.790	1.77	0.024	(28.8) \pm (3.3)	(28.2) \pm (3.1)
Sc II	5657.896	1.51	-0.603	(25.2) \pm (2.7)	(25.3) \pm (2.3)
Ti I	3989.758	0.02	-0.130	65.8 \pm 6.3	- \pm -
Ti I	3998.636	0.05	0.020	73.1 \pm 10.3	72.6 \pm 8.2
Ti I	4981.730	0.85	0.570	58.2 \pm 4.8	59.3 \pm 5.4
Ti I	4991.066	0.84	0.450	47.4 \pm 5.4	51.9 \pm 3.5
Ti I	4999.503	0.83	0.320	37.7 \pm 3.7	41.9 \pm 3.5
Ti I	5014.276	0.81	0.040	34.6 \pm 4.2	43.2 \pm 5.7
Ti I	5039.958	0.02	-1.080	26.7 \pm 2.6	26.7 \pm 3.4
Ti I	5064.653	0.05	-0.940	30.1 \pm 2.9	29.5 \pm 2.7
Ti I	5173.743	0.00	-1.060	29.7 \pm 2.9	31.9 \pm 3.2
Ti I	5192.969	0.02	-0.950	33.7 \pm 2.6	25.7 \pm 3.0
Ti I	5210.384	0.05	-0.820	37.5 \pm 3.2	38.1 \pm 3.0
Ti II	3913.461	1.12	-0.360	111.3 \pm 11.0	130.4 \pm 10.5
Ti II	4028.338	1.89	-0.920	51.8 \pm 5.3	- \pm -
Ti II	4290.215	1.16	-0.870	101.5 \pm 10.9	96.1 \pm 9.2
Ti II	4337.914	1.08	-0.960	- \pm -	88.6 \pm 9.9
Ti II	4394.059	1.22	-1.770	57.1 \pm 6.0	55.2 \pm 5.1
Ti II	4395.031	1.08	-0.540	119.8 \pm 11.3	120.5 \pm 9.0
Ti II	4395.839	1.24	-1.930	55.9 \pm 5.7	46.0 \pm 5.4
Ti II	4399.765	1.24	-1.200	89.2 \pm 8.7	89.0 \pm 8.7
Ti II	4417.713	1.16	-1.190	96.6 \pm 8.3	97.1 \pm 8.8
Ti II	4443.801	1.08	-0.710	103.7 \pm 8.1	112.6 \pm 7.4
Ti II	4444.554	1.12	-2.200	- \pm -	44.5 \pm 4.8
Ti II	4450.482	1.08	-1.520	82.1 \pm 7.5	80.9 \pm 8.8
Ti II	4464.449	1.16	-1.810	- \pm -	59.0 \pm 7.2
Ti II	4468.493	1.13	-0.630	95.2 \pm 7.3	- \pm -
Ti II	4501.270	1.12	-0.770	116.2 \pm 12.6	- \pm -
Ti II	4865.610	1.12	-2.700	- \pm -	25.9 \pm 3.8
Ti II	5129.156	1.89	-1.340	36.0 \pm 4.0	34.0 \pm 2.9
Ti II	5154.068	1.57	-1.750	31.4 \pm 2.6	35.5 \pm 3.3
Ti II	5185.902	1.89	-1.410	33.1 \pm 3.4	29.8 \pm 2.8
Ti II	5188.687	1.58	-1.050	77.5 \pm 7.0	73.7 \pm 6.0
Ti II	5226.539	1.57	-1.260	64.4 \pm 5.3	62.6 \pm 4.9
Ti II	5336.786	1.58	-1.600	48.0 \pm 3.9	42.1 \pm 3.8
Ti II	5381.021	1.57	-1.970	30.8 \pm 3.0	33.3 \pm 2.9
V II	3951.957	1.48	-0.730	(34.4) \pm (4.8)	- \pm -
Cr I	4254.352	0.00	-0.090	- \pm -	(119.5) \pm (8.9)
Cr I	4274.812	0.00	-0.220	- \pm -	(121.3) \pm (10.1)
Cr I	4289.730	0.00	-0.370	(96.8) \pm (8.0)	(113.9) \pm (9.9)
Cr I	5206.023	0.94	0.020	(82.8) \pm (5.7)	(80.9) \pm (5.5)
Cr I	5208.409	0.94	0.170	(64.9) \pm (26.3)	(106.1) \pm (11.3)
Cr I	5296.691	0.98	-1.360	- \pm -	(16.8) \pm (1.9)
Cr I	5298.271	0.98	-1.140	(29.6) \pm (2.8)	(27.3) \pm (2.4)
Cr I	5345.796	1.00	-0.896	(36.3) \pm (3.3)	(32.7) \pm (3.0)
Cr I	5348.314	1.00	-1.210	(22.3) \pm (2.1)	(21.1) \pm (2.5)
Cr I	5409.784	1.03	-0.670	(47.3) \pm (4.7)	- \pm -
Mn I	4030.750	0.00	-0.494	(142.7) \pm (12.1)	(127.8) \pm (11.9)
Mn I	4033.060	0.00	-0.644	(122.2) \pm (11.2)	(130.0) \pm (15.2)
Mn I	4034.480	0.00	-0.842	(132.2) \pm (9.9)	(94.8) \pm (10.8)

El.	λ [Å]	χ_{ex} [eV]	log(g_f)	EW [mÅ] log(ϵ) S04–130	EW [mÅ] log(ϵ) S11–97
Mn I	4041.350	2.11	0.277	(38.2) \pm (5.6)	(47.1) \pm (5.9)
Mn I	4823.520	2.32	0.121	(25.2) \pm (2.5)	(27.3) \pm (3.3)
Fe I	4859.741	2.88	-0.764	59.4 \pm 5.0	- \pm -
Fe I	4871.318	2.87	-0.363	73.3 \pm 5.5	74.8 \pm 6.4
Fe I	4872.138	2.88	-0.567	58.8 \pm 4.7	61.1 \pm 5.8
Fe I	4890.755	2.88	-0.394	78.2 \pm 6.1	75.4 \pm 5.6
Fe I	4891.492	2.85	-0.112	83.3 \pm 6.4	94.0 \pm 7.4
Fe I	4903.310	2.88	-0.926	52.6 \pm 4.3	43.6 \pm 3.5
Fe I	4918.994	2.87	-0.342	78.0 \pm 6.3	77.8 \pm 6.0
Fe I	4920.502	2.83	0.068	93.5 \pm 7.9	96.7 \pm 7.5
Fe I	4924.770	2.28	-2.241	- \pm -	28.4 \pm 3.0
Fe I	4938.814	2.88	-1.077	32.7 \pm 4.2	46.4 \pm 4.4
Fe I	4939.687	0.86	-3.340	- \pm -	76.0 \pm 6.2
Fe I	4994.129	0.92	-3.080	63.0 \pm 18.6	4.42*
Fe I	5006.119	2.83	-0.638	71.0 \pm 6.0	72.6 \pm 4.7
Fe I	5041.072	0.96	-3.087	53.3 \pm 19.7	4.30*
Fe I	5041.756	1.49	-2.203	82.1 \pm 7.0	89.3 \pm 6.5
Fe I	5049.820	2.28	-1.355	67.8 \pm 5.1	69.1 \pm 4.6
Fe I	5051.634	0.92	-2.795	107.4 \pm 8.6	5.03*
Fe I	5068.766	2.94	-1.042	- \pm -	37.3 \pm 3.7
Fe I	5079.223	2.20	-2.067	43.3 \pm 3.7	4.69
Fe I	5079.740	0.99	-3.220	76.0 \pm 6.1	4.89*
Fe I	5083.338	0.96	-2.958	88.7 \pm 6.9	4.84*
Fe I	5110.413	0.00	-3.760	116.9 \pm 7.7	4.91*
Fe I	5123.720	1.01	-3.068	81.7 \pm 5.8	4.87*
Fe I	5127.359	0.92	-3.307	78.6 \pm 5.2	4.92*
Fe I	5131.468	2.22	-2.515	21.1 \pm 1.7	4.70
Fe I	5141.739	2.42	-1.964	23.9 \pm 2.6	4.47
Fe I	5150.839	0.99	-3.003	75.2 \pm 6.1	4.64*
Fe I	5151.911	1.01	-3.322	63.1 \pm 4.9	4.76*
Fe I	5166.282	0.00	-4.195	97.1 \pm 7.6	4.93*
Fe I	5171.596	1.49	-1.793	- \pm -	108.0 \pm 7.2
Fe I	5191.455	3.04	-0.551	58.9 \pm 4.8	4.50
Fe I	5192.344	3.00	-0.421	- \pm -	62.7 \pm 5.4
Fe I	5194.941	1.56	-2.090	81.6 \pm 6.2	4.60
Fe I	5198.711	2.22	-2.135	37.1 \pm 3.5	4.66
Fe I	5202.336	2.18	-1.838	60.3 \pm 4.5	4.72
Fe I	5216.274	1.61	-2.150	84.6 \pm 5.8	4.78
Fe I	5217.389	3.21	-1.070	29.3 \pm 2.6	4.68
Fe I	5225.526	0.11	-4.789	54.2 \pm 4.7	4.88*
Fe I	5232.940	2.94	-0.058	- \pm -	93.5 \pm 7.0
Fe I	5254.956	0.11	-4.764	57.2 \pm 4.7	4.90*
Fe I	5266.555	3.00	-0.386	70.4 \pm 4.7	4.50
Fe I	5269.537	0.86	-1.321	168.6 \pm 13.4	4.60*
Fe I	5281.790	3.04	-0.834	45.6 \pm 3.5	4.53
Fe I	5302.300	3.28	-0.720	40.6 \pm 3.8	4.63
Fe I	5307.361	1.61	-2.987	- \pm -	36.5 \pm 3.1
Fe I	5324.179	3.21	-0.103	67.9 \pm 5.5	4.43
Fe I	5328.039	0.92	-1.466	157.6 \pm 12.2	4.60*
Fe I	5332.899	1.56	-2.777	51.7 \pm 4.5	4.70
Fe I	5367.466	4.41	0.443	20.4 \pm 2.2	4.42
Fe I	5369.961	4.37	0.536	31.5 \pm 3.3	4.54
Fe I	5371.489	0.96	-1.645	152.3 \pm 11.0	4.72*
Fe I	5383.369	4.31	0.645	37.2 \pm 2.6	4.47
Fe I	5393.167	3.24	-0.715	36.3 \pm 3.1	4.49
Fe I	5397.128	0.92	-1.993	137.9 \pm 9.3	4.72*
Fe I	5405.774	0.99	-1.844	143.0 \pm 10.3	4.77*
Fe I	5410.910	4.47	0.398	- \pm -	22.3 \pm 2.4
Fe I	5424.068	4.32	0.520	- \pm -	34.1 \pm 3.1
Fe I	5429.696	0.96	-1.879	149.9 \pm 10.7	4.88*
Fe I	5434.523	1.01	-2.122	129.9 \pm 9.3	4.81*
Fe I	5446.917	0.99	-1.914	140.1 \pm 10.2	4.77*
Fe I	5455.609	1.01	-2.091	132.9 \pm 11.7	4.83*
Fe I	5497.516	1.01	-2.849	96.5 \pm 6.9	4.86*
Fe I	5501.465	0.96	-3.047	93.4 \pm 6.9	4.93*
Fe I	5506.779	0.99	-2.797	110.7 \pm 7.2	5.06*
Fe I	5569.618	3.42	-0.486	41.6 \pm 3.2	4.56
Fe I	5572.842	3.40	-0.275	- \pm -	49.2 \pm 3.5
Fe I	5586.755	3.37	-0.120	63.5 \pm 5.1	4.53
Fe I	5615.644	3.33	0.050	- \pm -	70.6 \pm 5.5

Table 3: continued.

El.	λ [Å]	χ_{ex} [eV]	$\log(gf)$	EW [mÅ] S04–130	$\log\epsilon(X)$	EW [mÅ] S11–97	$\log\epsilon(X)$
Fe I	6430.845	2.18	−2.006	− ± −	−	57.4 ± 4.2	4.63
Fe I	6494.980	2.40	−1.273	82.4 ± 6.5	4.69	82.9 ± 5.5	4.60
Fe I	6592.913	2.73	−1.473	− ± −	−	37.1 ± 2.9	4.46
Fe I	6677.985	2.69	−1.418	52.0 ± 3.8	4.67	51.9 ± 3.9	4.60
Fe II	4923.921	2.89	−1.320	105.3 ± 8.4	4.84	77.4 ± 20.4	4.19
Fe II	5018.436	2.89	−1.220	112.8 ± 9.0	4.87	82.2 ± 18.1	4.17
Fe II	5197.567	3.23	−2.100	− ± −	−	32.9 ± 3.0	4.52
Fe II	5234.623	3.22	−2.230	42.2 ± 3.1	4.82	− ± −	−
Fe II	5275.997	3.20	−1.940	50.1 ± 4.8	4.65	54.6 ± 5.0	4.72
Fe II	5284.103	2.89	−2.990	24.3 ± 2.3	4.80	− ± −	−
Co I	3845.468	0.92	0.010	(71.7) ± (7.0)	2.12	(76.5) ± (8.0)	1.75
Co I	3894.077	1.05	0.100	(95.1) ± (10.0)	2.19	(105.7) ± (11.0)	1.74
Co I	3995.307	0.92	−0.220	(73.3) ± (7.9)	1.92	(80.2) ± (6.0)	1.80
Co I	4121.318	0.92	−0.320	(92.0) ± (8.2)	1.96	(76.7) ± (6.6)	1.82
Ni I	3858.297	0.42	−0.960	(116.3) ± (9.3)	3.44	− ± −	−
Ni I	5084.096	3.68	0.030	− ± −	−	(11.4) ± (2.1)	3.34
Ni I	5155.764	3.90	0.074	− ± −	−	(10.4) ± (1.5)	3.46
Ni I	5476.904	1.83	−0.780	(55.9) ± (18.2)	3.21	(76.2) ± (5.5)	3.13
Ni I	6643.630	1.68	−2.220	(20.7) ± (2.0)	3.33	− ± −	−
Ni I	6767.772	1.83	−2.140	(24.9) ± (2.6)	3.60	(19.1) ± (3.2)	3.54
Zn I	4810.528	4.08	−0.137	(29.1) ± (3.7)	2.25	(23.0) ± (2.9)	2.10
Sr II	4077.709	0.00	0.167	(144.5) ± (12.0)	0.17	(81.6) ± (15.4)	−0.60
Sr II	4215.519	0.00	−0.145	(122.0) ± (9.6)	−0.02	(132.1) ± (13.5)	−0.35
Y II	4883.682	1.08	0.070	(13.2) ± (2.0)	−1.20	(14.9) ± (2.4)	−1.33
Y II	5200.410	0.99	−0.570	− ± −	−	(12.0) ± (1.5)	−1.01
Y II	5205.722	1.03	−0.340	(11.7) ± (2.1)	−1.12	− ± −	−
Zr II	4208.980	0.71	−0.510	(24.2) ± (3.6)	−0.25	(30.1) ± (3.1)	−0.39
Ba II	4934.076	0.00	−0.150	(89.6) ± (7.4)	−1.59	(92.6) ± (8.4)	−1.62
Ba II	5853.668	0.60	−1.000	(13.3) ± (1.4)	−1.46	− ± −	−
Ba II	6141.713	0.70	−0.076	(42.1) ± (4.0)	−1.64	(44.8) ± (3.3)	−1.65
Ba II	6496.897	0.60	−0.377	(39.2) ± (3.3)	−1.53	(38.4) ± (3.4)	−1.57
Pr II	4143.112	0.37	0.609	− ± −	−	14.6 ± 4.3	−1.82
Nd II	4446.380	0.20	−0.350	15.1 ± 4.5	−1.12	− ± −	−

derived in the CH band led to an abundance that agrees better with the 4077.7 Å line.

- *Yttrium*. Two very faint lines (<15 mÅ) of yttrium were detected in our spectra, but we were only able to place upper limits on the Y abundance in our stars.
- *Barium*. Four lines of barium are present in our wavelength ranges. One is very faint ($\lambda 5853$ Å) and detected for only one star, and the other three lines are strong. Two of them are blended with weak iron lines ($\lambda 4934$ Å and $\lambda 6141$ Å). Therefore we proceeded by spectral synthesis, taking into account all blends and the Ba HFS components. Barium has five isotopes; different fractions of even-A and odd-A (A=atomic mass) nuclei ($^{134}\text{Ba} + ^{136}\text{Ba} + ^{138}\text{Ba}$) : ($^{135}\text{Ba} + ^{137}\text{Ba}$) were tested: the 82:18 solar fraction, and the r-process fractions of 54:46 and 28:72. The Ba $\lambda 4934$ Å resonance line is more sensitive than the three subordinate lines to the adopted fraction. The solar 82:18 fraction led to the best agreement between the resonance and the subordinate lines. We refer to Jablonka et al. (2015); Mashonkina et al. (2017b) for a more detailed investigation of the possible cause.

5. Discussion

5.1. Carbon

Figure 3 shows that none of our stars can be considered as carbon-enhanced based on the Aoki et al. (2007) criterion. Nonetheless, our stars are evolved enough to have converted C into N by the CNO cycle, as they are above $\log(L_\star/L_\odot) = 2.3$, that is, the limit above which a metal-poor $0.8 M_\odot$ star is thought to undergo additional mixing between the bottom of the stellar convective envelope and the outer layer of the advancing hydrogen shell (see Placco et al. 2014, and references therein for a discussion).

Placco et al. (2014) developed a procedure for correcting the measured carbon abundances based on stellar model evolution and depending on the $\log(g)$ of the stars. They showed that when these corrections were applied to their dataset, the fraction of carbon-rich stars $[\text{C}/\text{Fe}] > +0.7$ increased to 43% for $[\text{Fe}/\text{H}] < -3$. The corrections are interpolated⁷ at given $\log(g)$, $[\text{Fe}/\text{H}]$ and $[\text{C}/\text{Fe}]$. For the star S04–130, the corresponding correction is +0.73 dex, resulting in a ratio of $[\text{C}/\text{Fe}] = 0.20$ dex. For S11–97 the derived correction is +0.74 dex, resulting in $[\text{C}/\text{Fe}] = 0.19$ dex. This retains the two stars immediately below the limit of C-rich stars defined by Aoki et al. (2007) (Fig. 3, empty circles).

In the MW halo a significant fraction of metal-poor stars, that is, stars with $[\text{Fe}/\text{H}] \leq -2$, is enriched in carbon ($[\text{C}/\text{Fe}] > 0.7$ dex)⁸. The fraction of carbon-enriched metal-poor (CEMP) stars appears to be a function of decreasing metallicity (e.g., Beers & Christlieb 2005). This suggests that large amounts of carbon were synthesized in the early Universe when the oldest and most metal-poor stars formed.

Despite extensive observational searches, only a few carbon-rich stars have been known in dSphs until very recently, even at low metallicities. In Sextans, one CEMP star has been identified with $[\text{C}/\text{Fe}] = +1$ by Honda et al. (2011) (star S15–19 from Aoki et al. (2009)), and one moderately enhanced carbon star with $[\text{C}/\text{Fe}] = +0.4$ by Tafelmeyer et al. (2010). A CEMP star has been also discovered in Draco (Cohen & Huang 2009) and Sculptor (Skúladóttir et al. 2015; Salvadori et al. 2015). Finally, Kirby et al. (2015) studied a sample of 398 giants in Sculptor, Fornax, Ursa Minor, and Draco. They identified 11 very carbon-rich giants (eight were previously known) in three dSphs (Fornax, Ursa Minor, and Draco).

Because the MW halo is expected to be at least partially composed of disrupted dSphs accreted by the Galactic halo, it is important to carefully compare the carbon-enhanced fraction of the MW stellar halo with the values observed in dSphs. The recent study of Chiti et al. (2018) at low resolution ($R \sim 2000$) found that CEMP stars at metallicities below $[\text{Fe}/\text{H}] < -3.0$ constitute 36% of the observed stars in Sculptor. The measured fraction is comparable to the fraction of 30% observed by Yong et al. (2013) in the MW halo (Placco et al. 2014), suggesting that some stars that now populating the Galactic halo may have originated from accreted early analogs of dwarf galaxies. More and higher resolution studies are needed to confirm these fractions inside the dwarf galaxies. Moreover, the identification of carbon-rich stars and comparisons between galaxies may well be revised in light of 3D NLTE treatment at similar stellar evolutionary stage. Amarsi et al. (2019) have shown that for main-sequence stars, the rise in carbon overabundance with decreasing metallicity vanishes. However, most of our knowledge in dwarf galaxies comes from giant stars, therefore the effect of 3D NLTE on C still remains to be uncovered.

5.2. Sodium

Figure 4 presents the results of LTE calculations for $[\text{Na}/\text{Fe}]$ ratios as a function of metallicity in Sextans (this paper and Tafelmeyer et al. 2010), Sculptor (Jablonka et al. 2015), and Fornax (Tafelmeyer et al. 2010), compared to $[\text{Na}/\text{Fe}]$ abundances measured in MW halo stars. Similarly to the other dwarfs, Sextans follows the MW trend. Our stars lie on the upper envelope

⁷ <https://vplacco.pythonanywhere.com/>

⁸ Throughout this paper, we adopt the Aoki et al. (2007) criterion to define carbon-enhanced objects.

Table 4: Derived abundances for S04–130 and S11–97 and the Aoki 2009 stars along with their associated errors (see § 3.4).

	Fe I	Fe II	C	Na I	Mg I	Al I	Si I	Ca I	Sc II	Ti I	Ti II	V II	Cr I	Mn I	Co I	Ni I	Zn I	Sr II	Y II	Zr II	Ba II
$\log(\epsilon(X)_{\odot})$	7.50	7.50	8.43	6.24	7.60	6.45	7.51	6.34	3.15	4.95	4.95	3.93	5.64	5.43	4.99	6.22	4.56	2.87	2.21	2.58	2.18
S04-130																					
Nb lines*	42	5	1	2	5	2	–	9	7	11	19	1	7	5	4	4	1	2	2	1	4
$\log(\epsilon(X))$	4.56	4.80	4.96	3.80	5.11	2.96	–	3.58	0.37	2.04	2.30	<0.95	2.53	2.21	2.05	3.40	2.25	0.06	<–1.16	<–0.25	–1.56
[X/H]	–2.94	–2.70	–3.47	–2.44	–2.49	–3.49	–	–2.76	–0.37	–2.91	–2.65	<–2.98	–3.11	–3.22	–2.94	–2.82	–2.31	–2.80	<–3.37	<–2.83	–3.74
[X/Fe]	–	+0.24	–0.53	+0.50	+0.45	–0.55	–	+0.18	+0.16	+0.03	+0.29	<–0.04	–0.17	–0.28	–0.00	+0.11	+0.63	+0.13	<–0.43	<+0.11	–0.80
Error	0.11	0.11	0.15	0.11	0.11	0.11	–	0.14	0.15	0.11	0.15	–	0.11	0.11	0.13	0.17	0.11	0.11	–	–	0.11
S11-97																					
Nb lines*	44	4	1	2	5	1	–	11	7	10	20	–	9	5	4	4	1	2	2	1	3
$\log(\epsilon(X))$	4.49	4.54	4.87	3.79	5.08	3.05	–	3.59	0.37	1.97	2.26	–	2.52	2.07	1.78	3.37	2.10	–0.48	<–1.17	<–0.39	–1.61
[X/H]	–3.01	–2.96	–3.56	–2.45	–2.52	–3.40	–	–2.75	–2.78	–2.98	–2.69	–	–3.12	–3.36	–3.21	–2.85	–2.46	–3.34	<–3.38	<–2.97	–3.79
[X/Fe]	–	+0.05	–0.55	+0.56	+0.49	–0.39	–	+0.26	+0.23	+0.03	+0.32	–	–0.11	–0.35	–0.20	+0.16	+0.55	–0.34	<–0.37	<+0.04	–0.78
Error	0.11	0.27	0.16	0.11	0.11	0.11	–	0.11	0.13	0.11	0.13	–	0.16	0.11	0.11	0.18	0.11	0.18	–	–	0.11
S10-14																					
Nb lines*	30	4	–	–	1	–	–	1	–	–	2	–	2	–	–	–	–	–	–	–	1
$\log(\epsilon(X))$	4.49	4.63	–	–	4.88	–	–	3.55	–	–	2.12	–	2.20	–	–	–	–	–	–	–	–1.72
[X/H]	–3.01	–2.87	–	–	–2.72	–	–	–2.79	–	–	–2.83	–	–3.44	–	–	–	–	–	–	–	–3.90
[X/Fe]	–	+0.15	–	–	+0.29	–	–	+0.22	–	–	+0.19	–	–0.43	–	–	–	–	–	–	–	–0.89
Error	0.19	0.38	–	–	0.20	–	–	0.20	–	–	0.18	–	0.38	–	–	–	–	–	–	–	0.18
S11-13																					
Nb lines*	25	2	–	–	1	–	–	2	1	1	1	–	2	–	–	1	–	–	–	–	2
$\log(\epsilon(X))$	4.45	4.69	–	–	4.78	–	–	3.47	0.16	1.64	2.38	–	2.10	–	–	3.36	–	–	–	–	–1.65
[X/H]	–3.05	–2.81	–	–	–2.82	–	–	–2.87	–2.99	–3.31	–2.58	–	–3.53	–	–	–2.86	–	–	–	–	–3.83
[X/Fe]	–	+0.24	–	–	+0.23	–	–	+0.18	+0.06	–0.26	+0.48	–	–0.48	–	–	+0.19	–	–	–	–	–0.78
Error	0.20	0.20	–	–	0.20	–	–	0.20	0.20	0.20	0.20	–	0.20	–	–	0.20	–	–	–	–	0.20
S11-37																					
Nb lines*	26	3	–	–	1	–	–	2	1	1	2	–	2	–	–	1	–	–	–	–	2
$\log(\epsilon(X))$	4.52	4.70	–	–	4.94	–	–	3.51	0.31	1.76	2.17	–	2.21	–	–	3.30	–	–	–	–	–1.68
[X/H]	–2.98	–2.80	–	–	–2.66	–	–	–2.83	–2.84	–3.19	–2.78	–	–3.43	–	–	–2.92	–	–	–	–	–3.86
[X/Fe]	–	+0.18	–	–	+0.32	–	–	+0.15	+0.14	–0.21	+0.20	–	–0.45	–	–	+0.06	–	–	–	–	–0.87
Error	0.18	0.18	–	–	0.20	–	–	0.16	0.20	0.20	0.69	–	0.19	–	–	0.19	–	–	–	–	0.30
S12-28																					
Nb lines*	35	5	–	–	2	–	–	3	3	2	5	–	1	1	–	–	–	–	–	–	2
$\log(\epsilon(X))$	4.50	4.59	–	–	4.96	–	–	3.61	0.11	1.89	2.29	–	2.39	2.16	–	–	–	–	–	–	–1.06
[X/H]	–3.00	–2.91	–	–	–2.64	–	–	–2.73	–3.04	–3.06	–2.66	–	–3.25	–3.27	–	–	–	–	–	–	–3.24
[X/Fe]	–	+0.09	–	–	+0.36	–	–	+0.27	–0.04	–0.06	+0.34	–	–0.25	–0.27	–	–	–	–	–	–	–0.24
Error	0.18	0.19	–	–	0.16	–	–	0.16	0.19	0.17	0.17	–	0.20	0.22	–	–	–	–	–	–	0.17
S14-98																					
Nb lines*	17	1	–	–	1	–	–	3	1	1	4	–	2	–	–	–	–	–	–	–	2
$\log(\epsilon(X))$	4.58	5.07	–	–	4.96	–	–	3.89	0.21	2.57	2.53	–	2.38	–	–	–	–	–	–	–	–1.63
[X/H]	–2.92	–2.43	–	–	–2.64	–	–	–2.45	–2.94	–2.38	–2.42	–	–3.26	–	–	–	–	–	–	–	–3.81
[X/Fe]	–	+0.49	–	–	+0.29	–	–	+0.47	–0.01	+0.54	+0.50	–	–0.33	–	–	–	–	–	–	–	–0.89
Error	0.17	0.20	–	–	0.20	–	–	0.23	0.21	0.20	0.48	–	0.18	–	–	–	–	–	–	–	0.31
S15-19																					
Nb lines*	22	3	–	–	2	–	–	5	1	1	9	–	2	–	–	1	–	1	–	–	2
$\log(\epsilon(X))$	4.28	4.19	–	–	5.01	–	–	3.64	0.64	2.05	1.94	–	2.30	–	–	2.96	–	–1.27	–	–	–0.30
[X/H]	–3.22	–3.31	–	–	–2.59	–	–	–2.70	–2.51	–2.90	–3.01	–	–3.34	–	–	–3.26	–	–4.14	–	–	–2.48
[X/Fe]	–	–0.09	–	–	+0.63	–	–	+0.52	+0.71	+0.32	+0.21	–	–0.12	–	–	–0.04	–	–0.92	–	–	+0.74
Error	0.19	0.23	–	–	0.19	–	–	0.19	0.21	0.19	0.21	–	0.19	–	–	0.19	–	0.28	–	–	0.19

Notes. * Number of lines kept after a careful selection of the best fitted lines.

of the dispersion range. We did not consider the Na abundances measured by Aoki et al. (2009) because they were obtained from EW measurements of two strong Na D features at 5889 and 5895 Å with an EW that typically exceeds 100 mÅ (see § 5.3). However, the Na doublet at 5889 and 5895 Å is also strongly affected by NLTE. According to the NLTE calculation by Lind et al. (2011)⁹, the NLTE corrections for the two Na lines are both negative.

Mashonkina et al. (2017b) computed NLTE corrections for 59 very metal-poor stars in seven dSphs and the MW halo. At metallicity [Fe/H] = –3, the Na Δ [NLTE–LTE] range from –0.2 to –0.4 dex, which seems to agree with the Lind et al. (2011) com-

putations. These order-of-magnitude corrections for the NLTE are mentioned to provide an idea of where the stars might stand.

5.3. α elements

The plateau at $[\alpha/\text{Fe}] \sim +0.4$ dex seen in the MW metal-poor stellar population indicates that the ejecta from numerous massive stars contributed to the metallicity of the interstellar medium (ISM), as indicated by the low scatter around the mean $[\alpha/\text{Fe}]$ value at low metallicity. As pointed out by Audouze & Silk (1995), the chemical composition of the ejecta from a supernova (SN) depends on the mass of the progenitor, which means that the smaller the number of SNe that contributed to the ISM composition, the larger the abundance dispersion of the ISM. Even though this is further complicated by possible differences

⁹ <http://www.inspect-stars.com/>

Table 5: Changes in the mean abundances $\Delta[X/H]$ caused by a ± 100 K change in T_{eff} , a ± 0.15 dex change in $\log(g)$ and a ± 0.15 km s $^{-1}$ change on v_t for star S04-130.

X	$+\Delta T_{\text{eff}}$	$+\Delta \log(g)$	$\delta \log \epsilon(X)$		$-\Delta \log(g)$	$-\Delta v_t$
			$+\Delta v_t$	$-\Delta T_{\text{eff}}$		
Fe I	+0.11	-0.01	-0.03	-0.14	+0.00	+0.02
Fe II	+0.00	-0.05	-0.03	+0.01	-0.05	+0.02
Na I	+0.14	-0.01	-0.07	-0.12	+0.02	+0.06
Mg I	+0.07	-0.01	-0.03	-0.08	+0.02	+0.03
Al I	+0.17	-0.02	-0.09	-0.19	+0.02	+0.10
Ca I	+0.09	-0.01	-0.01	-0.10	+0.01	+0.03
Sc II	+0.05	+0.05	-0.02	-0.03	-0.05	+0.02
Ti I	+0.16	-0.01	-0.02	-0.17	+0.00	+0.01
Ti II	+0.03	+0.04	-0.03	-0.03	-0.05	+0.03
Cr I	+0.12	-0.01	-0.02	-0.17	+0.01	+0.02
Mn I	+0.13	-0.01	-0.04	-0.13	+0.01	+0.02
Co I	+0.19	+0.00	-0.11	-0.21	+0.00	+0.12
Ni I	+0.15	+0.00	-0.01	-0.16	+0.01	+0.02
Zn I	+0.03	+0.02	-0.02	-0.02	-0.03	+0.01
Sr II	+0.12	+0.02	-0.17	-0.12	-0.04	+0.12
Ba II	+0.07	+0.05	-0.02	-0.06	-0.05	+0.02

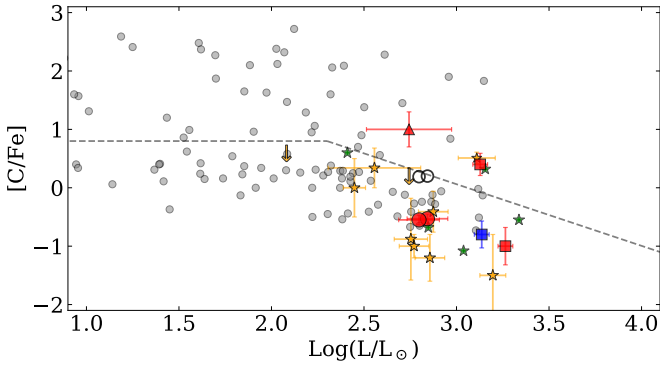


Fig. 3: $[C/Fe]$ as a function of $\log(L/L_{\text{sun}})$ for Galactic dwarf satellite and halo red giants with metallicities $[Fe/H] < -2.5$. The Sextans stars we analyzed are represented by large red circles. Red squares are Sextans stars from Tafelmeyer et al. (2010), the red triangle is the Sextans carbon-rich star from Honda et al. (2011). Gray dots denote the $[C/Fe]$ abundances of MW halo stars from Yong et al. (2013). RGB stars in Sculptor (Jablonka et al. 2015; Simon et al. 2015; Tafelmeyer et al. 2010), Fornax (Tafelmeyer et al. 2010), and Draco (Shetrone et al. 2013; Cohen & Huang 2009) are shown in orange, blue, and green, respectively. The dotted line is the Aoki et al. (2007) dividing line for carbon enhancement, which takes into account the depletion of carbon with evolution along the RGB.

in mixing efficiency, we therefore expect that the abundance dispersion increases with decreasing stellar mass of a galaxy. Thus the abundance dispersion would be minimal in the MW, and higher but still relatively low in dSph galaxies. At low metallicity ($[Fe/H] \lesssim -2.5$), most members of dSph galaxies follow the same plateau as the MW halo stars (see, e.g., Jablonka et al. (2015) for Sculptor). Nevertheless, even in the relatively massive Sculptor dSph galaxy (with a stellar mass of $2.3 \times 10^6 M_{\odot}$, McConnachie (2012)), about one to three stars in this metallicity range have $[\alpha/Fe] \leq 0.00$ (Figure 6). The question still remains whether lower mass classical dSphs, such as Sextans and Carina, have a higher dispersion at fixed metallicity. In the case of Carina this is expected because of its star formation history, which

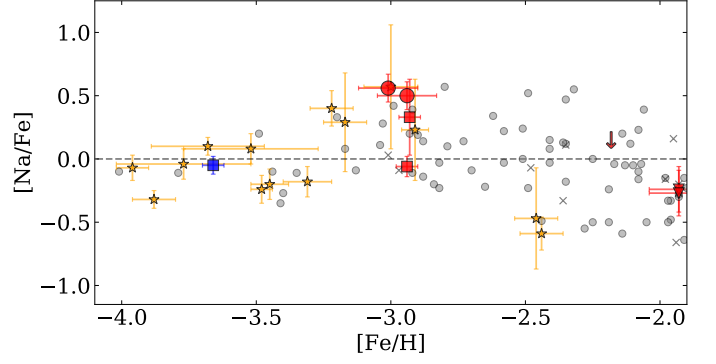


Fig. 4: Sodium-to-iron ratio as a function of $[Fe/H]$ are shown for metal-poor stars in Sextans, Sculptor, and MW halo stars. The symbols are the same as in Fig. 6. The stars studied in this paper are the large red symbols.

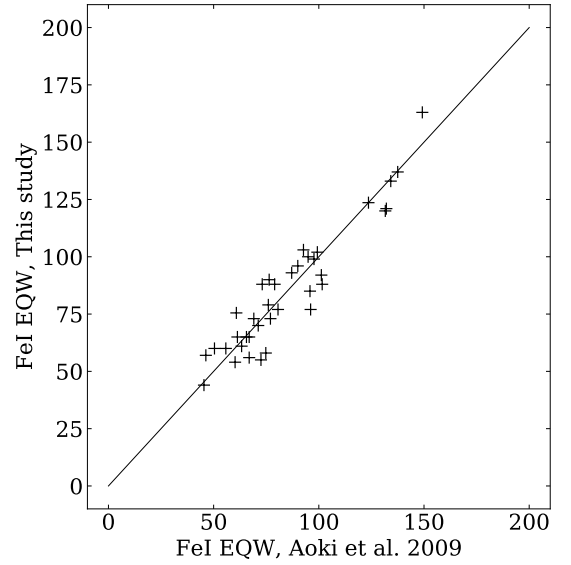


Fig. 5: Comparison for star S11-37 between Aoki et al. (2009) and our analysis on the measured Fe I EWs in common.

is characterized by at least three distinct bursts (Hurley-Keller et al. 1998; Santana et al. 2016) that so far have been interpreted as resulting from interactions with the MW (Fabrizio et al. 2011, 2016; Pasetto et al. 2011). In Sextans, the observed dispersion in $[\alpha/Fe]$, when data from Aoki et al. (2009) and Tafelmeyer et al. (2010) are considered, has been attributed to the effect that fewer SNe enriched the ISM from which the observed stars were born, and that pockets of ISM with various abundances coexist.

In the newly discovered EMPs observed with UVES, we measure an overabundance in $[\alpha/Fe] \sim +0.4$ dex (see Figure 6), which is comparable with the typical $[\alpha/Fe]$ value observed in the halo of the MW. This is in stark contrast with the result of Aoki et al. (2009), who obtained solar $[\alpha/Fe]$ ratios for the majority of their sample.

Because scatter can be artificially introduced when results from the different analyses are used, we applied the same method as we followed for the newly discovered EMPs to the literature sample. This allows for a fair and homogeneous comparison between the LTE abundances measured from Sextans stars and those observed in the Galactic halo.

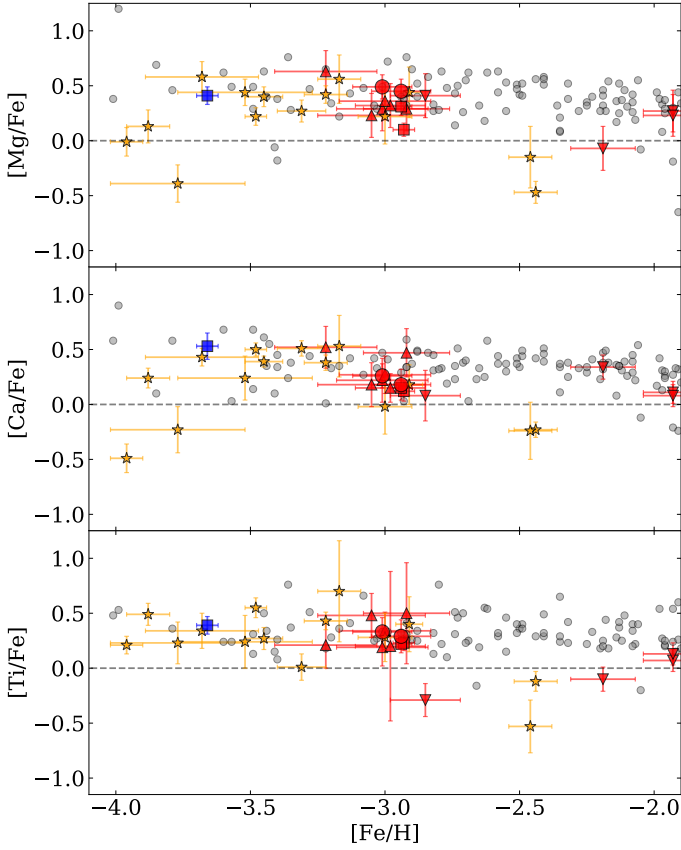


Fig. 6: Abundance ratios for the α elements Mg, Ca, and Ti (from top to bottom) as a function of $[\text{Fe}/\text{H}]$. Sextans stars are large red symbols. The new EMP stars studied in this paper are the red circles. The sample of Aoki et al. (2009) that we reanalyzed is shown as red triangles. Data from Shetrone et al. (2001b) are upside-down triangles. Gray dots are literature data for MW halo stars (Venn et al. 2004b; Cohen et al. 2013; Yong et al. 2013; Ishigaki et al. 2013). Orange and blue symbols refer to RGB stars observed in Sculptor (Jablonka et al. 2015; Tafelmeyer et al. 2010; Starkenburg et al. 2013; Simon et al. 2015) and Fornax (Tafelmeyer et al. 2010), respectively.

In order to investigate into this apparent discrepancy, we therefore started by comparing our measured EWs with those presented in Aoki et al. (2009). For this exercise, we considered the star S11–37, which has the lowest metallicity in the group characterized by the low α -element abundances. We retrieved the reduced spectra (eight exposures of 1800s for each, obtained in the blue and red arms of the Subaru High-Dispersion Spectrograph) from the JVO database¹⁰ and applied the same procedure as described in Sect. 2.2, with small adjustments to the HDS data. Briefly, the exposures were combined with IRAF, but the orders were extracted and fit individually with DAOSPEC in order to avoid any continuum modulation. Figure 5 shows that the EWs measured using our approach agree excellently well with those listed in Aoki et al. (2009). We therefore decided to use the Aoki et al. (2009) EWs to rederive the abundances as described in §3.

The star S15–19, with the lowest metallicity in the dataset of Aoki et al. (2009), has been re-observed and re-discussed by Honda et al. (2011) and has been confirmed to be a CEMP-s star.

¹⁰ <https://jvo.nao.ac.jp/portal/subaru/hds.do>

For the homogeneous reanalysis we used the new EWs measured by Honda et al. (2011).

The two analyses show some differences. First, Aoki et al. (2009) used the Kurucz (1993) atmosphere models while we use the MARCS 1D spherical models. Second, Aoki et al. (2009) determined the stellar effective temperatures by adopting the $V - K$ colour index (combined with a color-temperature calibration), while we derived our temperatures by minimizing the trend of Fe I abundances versus their excitation potential (χ_{exc}).

This different approach is reflected in the mean difference in the atmospheric parameters Δ (this study – Aoki et al.) of -65 K, -0.2 cgs, -0.7 km.s⁻¹ and -0.2 dex, in T_{eff} , $\log(g)$, v_t , and $[\text{Fe}/\text{H}]$, respectively.

Abundances of the α -elements echo this change in metallicity determination, but the largest difference between the two studies lies in the selection of lines that were used in the analysis. Specifically, Mg abundances in Aoki et al. (2009) are typically derived from three to four lines, including two very strong lines (at 5172 and 5183 Å) with EWs that exceed > 150 mÅ. Strong lines are not reliable when a Gaussian fitting routine is employed, and they give systematically lower Mg abundances than the Mg line at 5528 Å (with typical EW ~ 55 mÅ). They were therefore excluded from the analysis. As to whether $[\text{Fe}/\text{H}]$ or $[\text{Mg}/\text{H}]$ drives the change in $[\text{Mg}/\text{Fe}]$, we stress that retaining the strong Mg lines in a pure EW analysis (hence without proper synthesis) does affect the final result. This is clearly seen when we compare the $\log(\text{Mg})$ (absolute) abundances 1) when all lines are retained and 2) when the very strong lines are removed (see Table 6). Had we retained the very strong lines, the $[\text{Mg}/\text{Fe}]$ ratios would only have changed by 0.05 to 0.14 compared to Aoki et al. (2009).

Table 6: Comparison of the derived $\log(\text{Mg})$ abundances when all lines are retained, including the strong lines (SL), and when these strongest lines (noSL) are removed.

Star	$\log(\text{Mg})_{\text{SL}}$	$\log(\text{Mg})_{\text{noSL}}$	$\Delta(\log(\text{Mg}))$
S10–14	4.63	4.88	+0.25
S11–13	4.53	4.78	+0.25
S11–37	4.71	4.94	+0.23
S12–28	4.95	4.96	+0.01
S14–98	4.86	4.96	+0.10
S15–19	5.22	5.01	-0.21

Figure 6 shows the measured abundances of α -elements from our newly observed EMPs and the reanalysis of Aoki et al. (2009) stars. The two Sextans stars presented in the previous paper of this series (Tafelmeyer et al. 2010) are also shown.

Sextans stars have $[\text{Mg}/\text{Fe}]$ abundance ratios that nicely follow the trend of the Galactic halo. We do not confirm the presence of a low- α population as claimed in Aoki et al. (2009). The only exception is star S36 from Shetrone et al. (2001b) with $[\text{Mg}/\text{Fe}] = -0.07 \pm 0.20$, based on two strong lines fit by Gaussians on a spectrum with S/N=13 only. Stars with homogeneously derived abundances (e.g., large red symbols, triangles, and squares in Fig. 6) also appear to be enhanced in Ti II at the level observed in Mg and Ca with a normal ~ 0.2 dex dispersion.

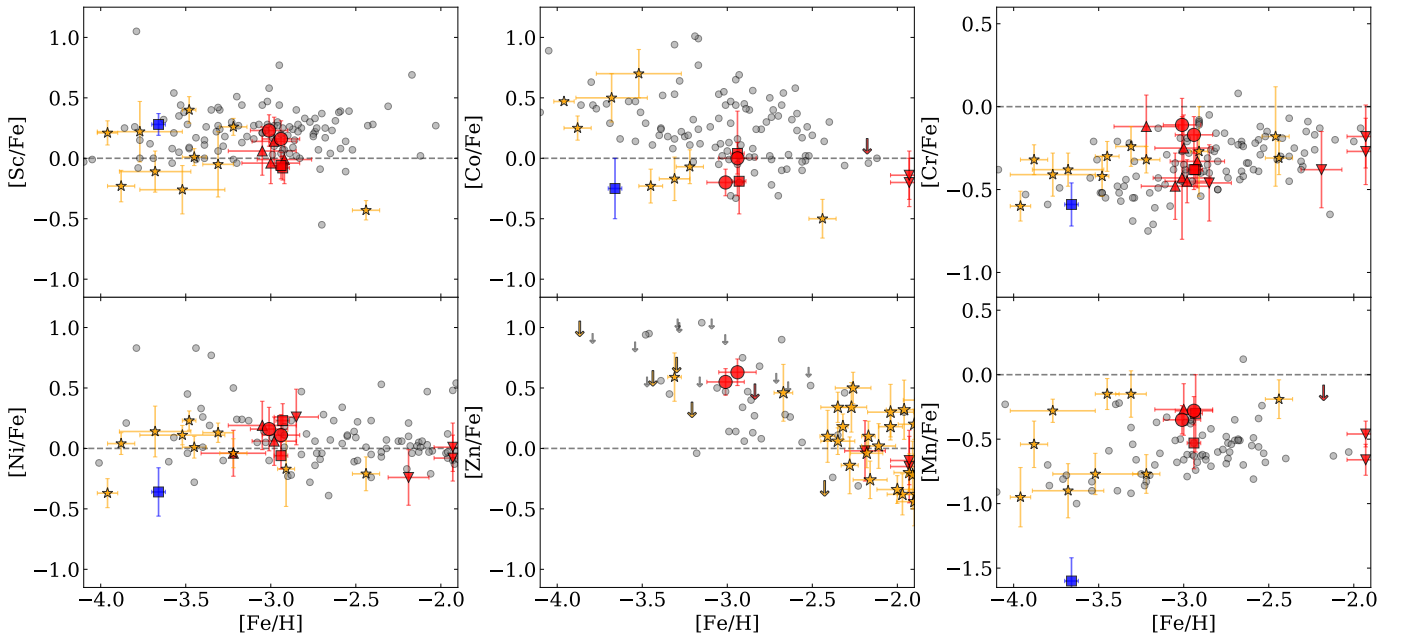


Fig. 7: From left to right, top to bottom: $[\text{Sc}/\text{Fe}]$, $[\text{Co}/\text{Fe}]$, $[\text{Cr}/\text{Fe}]$, $[\text{Ni}/\text{Fe}]$, $[\text{Zn}/\text{Fe}]$, and $[\text{Mn}/\text{Fe}]$ for metal-poor stars in Sextans, Sculptor, Fornax, and MW halo stars. The symbols are the same as in Fig. 6. The stars studied in this paper are the large red symbols.

5.4. Iron-peak elements

Figure 7 presents the abundance ratios of scandium, nickel, cobalt, zinc, chromium, and manganese as a function of metallicity. These elements are all produced by explosive nucleosynthesis.

The scandium abundances of our stars follow the MW halo trend very closely. The Sc production is dominated by SNeII (e.g., Woosley et al. 2002; Battistini & Bensby 2015), therefore the trend of $\text{Sc II}/\text{Fe}$ with iron nicely follows the run of the α -elements with metallicity.

Ni and Co can also be produced by SNeIa (e.g., Travaglio et al. 2005; Kirby et al. 2018). However, the contribution by SNeIa starts to dominate the chemical evolution of the galaxy at higher metallicities ($[\text{Fe}/\text{H}] \geq -2$; Theler et al. (2019)). The behavior of Ni/Fe in the low-metallicity range investigated here can therefore be attributed to Ni production by complete and incomplete Si burning.

Co and Zn are produced by the complete Si burning when the peak temperature of the shock material is above 5×10^9 K (Nomoto et al. 2013). The $[\text{Co}/\text{Fe}]$ ratios observed in our Sextans stars cover the lower tail of the distribution in the MW halo, similarly to the Fornax and three of the Sculptor EMPS. This might simply be an observational bias in our data sample because in dSphs we normally observe bright evolved RGB stars, which have lower temperatures and surface gravities than those in the MW halo. Additionally, these abundances should be corrected for the NLTE effect. These corrections depend on the stellar parameters as well (Bergemann et al. 2010; Kirby et al. 2018). It is interesting to note that the lowest $[\text{Co}/\text{Fe}]$ EMPS in Sculptor are also the coolest, in the same temperature range $\sim 4500\text{K}$ as in Sextans (Starkenburg et al. 2013; Jablonka et al. 2015). The Fornax EMPS is even cooler ($\sim 4300\text{K}$, Tafelmeyer et al. 2010). Unfortunately, no NLTE corrections for the range of atmospheric parameters of our stars are available, which would help shed light on the relative strength of the corrections.

The Zn abundances are measured from a weak line (with EW of 23 to 30 mÅ) at 4810 Å. However, because the (~ 50) S/N ratio

of the spectra around the Zn feature is relatively high, we were able to measure accurate Zn abundances. This is the first unambiguous measurement of Zn at low metallicity in a classical dwarf. Simon et al. (2015) reported on the detection of Zn in the EMP Scl07-49 in Sculptor. However, for the same star and the same spectrum, Tafelmeyer et al. (2010) have concluded only an upper limit. The measured Zn abundances perfectly follow the $[\text{Zn}/\text{Fe}]$ versus $[\text{Fe}/\text{H}]$ observed in the MW very metal-poor stars, with an enhancement up to ~ 0.7 dex. The production sites of Zn remain uncertain. The increasing enhancement at decreasing metallicity suggests that Zn was produced efficiently at the very early stages of the galaxy formation, likely in SNeII. The production through classical SNeII was shown to be insufficient to explain the observed $[\text{Zn}/\text{Fe}]$ (Hirai et al. 2018; Tsujimoto & Nishimura 2018), however.

In the incomplete Si-burning region, the after-decay products include chromium and manganese (Nomoto et al. 2013). Figure 7 shows that the $[\text{Cr}/\text{Fe}]$ and $[\text{Mn}/\text{Fe}]$ trends with $[\text{Fe}/\text{H}]$ in Sextans stars follow the Galactic trend well.

Bergemann & Cescutti (2010) have shown that in stars over the wide range of metallicities between $-3.2 \leq [\text{Fe}/\text{H}] \leq -0.5$, the $[\text{Cr}/\text{Fe}]$ ratio computed in NLTE is roughly solar, which is consistent with current views of the production of these iron peak elements in supernovae. This means that the apparent increase in $[\text{Cr}/\text{Fe}]$ ratios with metallicity in MW stars in Figure 7 is not real but rather due to the LTE approximation. NLTE corrections are not available for the range of stellar APs explored here. Nonetheless, NLTE corrections on Cr abundances are expected to be positive for bright giants (L. Mashonkina, *priv. comm.*).

5.5. Neutron-capture elements

The heavy elements (heavier than Zn) are synthesized through two main processes. The *s*-process operates by slow neutron capture on seed nuclei on a long timescale (i.e., the neutron capture is slower than the β decay of the affected nucleus). The stellar sources for *s*-process production are asymptotic giant

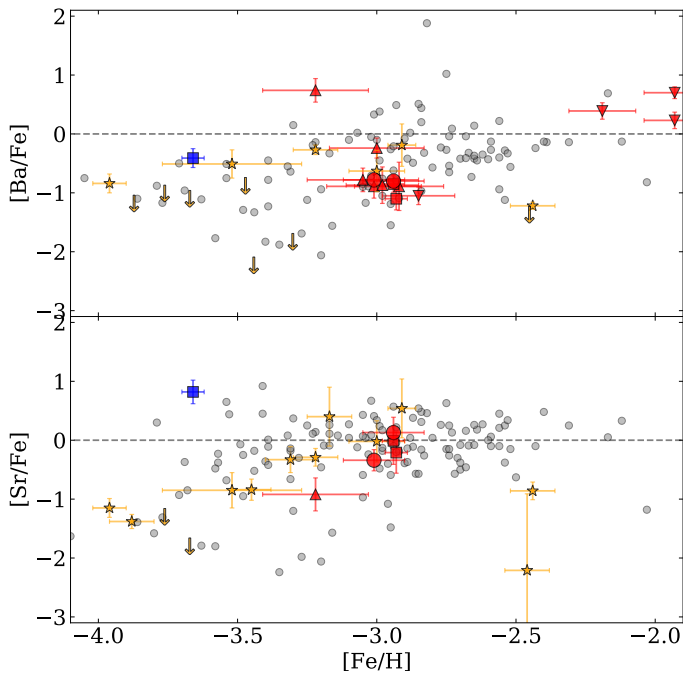


Fig. 8: Neutron-capture elements: Barium-to-iron ratio at the top and strontium-to-iron ratio at the bottom, as a function of $[\text{Fe}/\text{H}]$ in Sextans shown in red, compared to the MW halo stars in gray. The large circles represent the new sample in Sextans. Orange symbols refer to Sculptor.

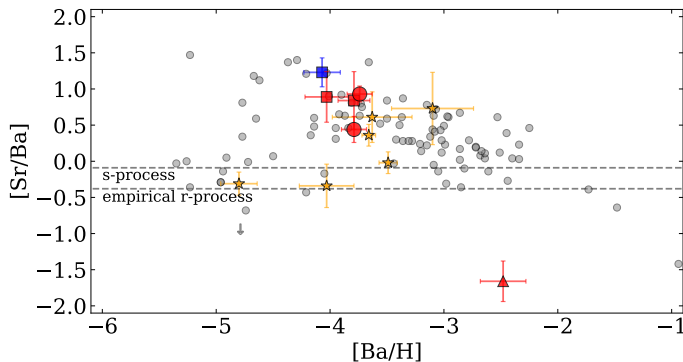


Fig. 9: Barium-to-strontium ratio as a function of $[\text{Ba}/\text{H}]$ in Sextans shown in red, compared to the MW halo stars presented in gray. Sculptor is shown in orange, and Fornax is in blue. References are the same as in Figure 6. The s-process and empirical r-process limits are shown with dashed lines (Mashonkina et al. 2017b).

branch (AGB) stars (e.g., Busso et al. 1999; Käppeler et al. 2011; Bisterzo et al. 2012). The *r*-process instead occurs on a very short timescale in violent events (e.g., Cameron 1957). High-entropy neutrino-driven winds of core-collapse supernovae (CC-SNe) have traditionally been considered the sites of *r*-process nucleosynthesis (e.g., Sneden et al. 2008). However, they have been ruled out as responsible for the origin of the main *r*-process elements by observations and simulations (Wanajo 2013; Macias & Ramirez-Ruiz 2018), and other exotic types of CC-SNe have been put forward (e.g., magnetorotational SNe; Nishimura et al. 2015). The recent LIGO/Virgo discovery of gravitational waves from the neutron star merger (NSM) GW170817 (Abbott et al.

2017) and the follow-up kilonova observations (e.g., Pian et al. (2017)) have shown that NSMs produce a copious amount of *r*-process material (e.g., Lattimer & Schramm 1974; Freiburghaus et al. 1999; Côté et al. 2017). This notion is also supported by the detection of *r*-process enrichment in the ultra-faint dwarf (UFD) Reticulum II (Ji et al. 2016; Roederer et al. 2016). However, the evidence that *r*-process is found also in low-mass systems where NSMs should be rare suggests that there might be different sites or conditions for the production of *r*-process elements (Travaglio et al. 2004; Jablonka et al. 2015; Mashonkina et al. 2017b; Hansen et al. 2018).

These two distinct processes produce generally different isotopes of a given heavy element, and different element ratios. Two neutron-capture elements can be measured in our stars: barium and strontium. At very low metallicity (i.e., $[\text{Fe}/\text{H}] \leq -2.5$), a significant enrichment by AGBs is not expected. In our EMP stars, we therefore expect a pure *r*-process origin for the neutron-capture elements.

Europium can be formed basically only through the *r*-process. However, Eu measurements in EMP stars are rare because Eu lines are very weak at low-metallicities. We were not able to detect clean Eu features in our spectra. Nonetheless, $[\text{Eu}/\text{Fe}]$ seems to correlate well with $[\text{Ba}/\text{Fe}]$ for metallicities $[\text{Fe}/\text{H}] \leq -2.5$ (e.g., Mashonkina et al. 2010; Spite & Spite 2014). At very low metallicity, even Ba has therefore been formed by the *r*-process.

Sr and Ba abundances are shown in Figure 8 as a function of metallicity. As found earlier, $[\text{Ba}/\text{Fe}]$ is generally below solar in the EMP stars, with a significant scatter (Travaglio et al. 2004; François et al. 2007). In the same plot, we also show abundances for stars observed at high resolution in the MW halo, Fornax, and Sculptor (see Fig. 6 for full references). In the MW halo sample a high dispersion in both $[\text{Sr}/\text{Fe}]$ and $[\text{Ba}/\text{Fe}]$ can be observed at metallicities lower than $[\text{Fe}/\text{H}] \leq -2.8$ and -2.5 for Sr and Ba; respectively (e.g., Andrievsky et al. 2009, 2010; Hansen et al. 2013; Mashonkina et al. 2017b). Above this metallicity, $[\text{Sr}/\text{Fe}]$ and $[\text{Ba}/\text{Fe}]$ steadily become solar, and their dispersion is largely diminished.

Figure 8 shows that except for S15-19, which is a carbon-rich star with evidence for s-process enrichment (Honda et al. 2011), all Sextans EMPS so far investigated at very high resolution have subsolar $[\text{Ba}/\text{Fe}]$ ratios at $[\text{Fe}/\text{H}] \sim -3$, to a level that is close to the level encountered at much lower metallicities for Fornax and Sculptor and in the UFDs (Simon 2019), hence tracing the initial trend between Fe and Ba, most likely arising from CCSNe. This concentration is most likely a coincidence because at higher metallicities, $[\text{Ba}/\text{Fe}]$ reaches the solar plateau. It is useful to appreciate the difference in Sr and Ba behaviors in general. For the same stars, $[\text{Sr}/\text{Fe}]$ is clumped around the solar value in a similar way as the MW halo population, suggesting similar enrichment processes for strontium.

Figure 9 shows the run of the $[\text{Sr}/\text{Ba}]$ ratio plotted against $[\text{Ba}/\text{H}]$. If Ba and Sr were formed by the same process, their ratio should not vary with $[\text{Ba}/\text{H}]$. All Sextans stars that so far have been observed at high resolution, except for the s-process star S15-19 (Honda et al. 2011), are perfectly located at the top of the decreasing branch of $[\text{Sr}/\text{Ba}]$ with $[\text{Ba}/\text{H}]$. This confirms that the source responsible for the production of lighter (Sr) neutron-capture elements is at work at earlier times than the processes that produce heavier (Ba) neutron-capture elements (e.g., François et al. 2007; Mashonkina et al. 2017b; Spite et al. 2018; Frebel 2018; Hansen et al. 2018).

6. Summary

We have presented the analysis of high-resolution spectra of two metal-poor stars in the dwarf spheroidal galaxy Sextans, including the abundance derivation of 18 chemical elements. In particular, we provide the first unambiguous measurement of Zn in a classical dSph in this metallicity range. These stars are confirmed as some of the most metal-poor stars known in Sextans. Literature spectra originally presented in Aoki et al. (2009) were reinvestigated in a homogeneous manner, and abundances for Fe I, Fe II, Mg, Ca, Sc II, Ti I, Ti II, Cr, and Ba II were rederived. This full sample significantly increases the number of stars in the low-metallicity range and gives new clues on the formation of Sextans. In particular, we demonstrated that the Sextans metal-poor population follows the MW halo-like plateau at $[\alpha/\text{Fe}] \sim 0.4$ with a normal scatter. This is different from previous results.

Most of the iron-peak elements are aligned with the MW halo distribution. Only cobalt is slightly depleted. We suggest on observational grounds that $[\text{Co}/\text{Fe}]$ might scale with the stellar effective temperature and that differential NLTE corrections would place the MW and dSph populations on the same scale.

The four Sextans (non-carbon rich) EMPS analyzed at high resolution have $[\text{Fe}/\text{H}] \sim -3$ and $[\text{Ba}/\text{Fe}] \sim -1$. This corresponds to the Ba floor seen at $[\text{Fe}/\text{H}]$ below -3.5 in the MW halo, in the UFDs, and in Sculptor. At this metallicity and this Ba enrichment, $[\text{Sr}/\text{Fe}]$ is already solar. This confirms that the source responsible for the production of the light neutron-capture elements precedes the production of the heavier ones. It also shows that this source is already efficient at the galaxy mass of Sextans.

Acknowledgements. The authors warmly thank Lyudmila Mashonkina for useful discussions on the NLTE corrections. The authors acknowledge the support and funding of the International Space Science Institute (ISSI) through the International Team "Pristine". CL acknowledges financial support from the Swiss National Science Foundation (Ambizione grant PZ00P2_168065). GB acknowledges financial support through the grant (AEI/FEDER, UE) AYA2017-89076-P, as well as by the Ministerio de Ciencia, Innovación y Universidades (MCIU), through the State Budget and by the Consejería de Economía, Industria, Comercio y Conocimiento of the Canary Islands Autonomous Community, through the Regional Budget.

References

- Abbott, B. P., Abbott, R., Abbott, T. D., et al. 2017, *Phys. Rev. Lett.*, 119, 161101
- Alonso, A., Arribas, S., & Martínez-Roger, C. 1999, *A&AS*, 140, 261
- Alvarez, R. & Plez, B. 1998, *A&A*, 330, 1109
- Amarsi, A. M., Nissen, P. E., Asplund, M., Lind, K., & Barklem, P. S. 2019, *A&A*, 622, L4
- Andrievsky, S. M., Spite, M., Korotin, S. A., et al. 2010, *A&A*, 509, A88
- Andrievsky, S. M., Spite, M., Korotin, S. A., et al. 2009, *A&A*, 494, 1083
- Aoki, W., Arimoto, N., Sadakane, K., et al. 2009, *A&A*, 502, 569
- Aoki, W., Beers, T. C., Christlieb, N., et al. 2007, *ApJ*, 655, 492
- Asplund, M., Grevesse, N., Sauval, A. J., & Scott, P. 2009, *ARA&A*, 47, 481
- Audouze, J. & Silk, J. 1995, *ApJ*, 451, L49
- Battaglia, G., Tolstoy, E., Helmi, A., et al. 2011, *VizieR Online Data Catalog*, 741
- Battistini, C. & Bensby, T. 2015, *A&A*, 577, A9
- Beers, T. C. & Christlieb, N. 2005, *ARA&A*, 43, 531
- Bergemann, M. & Cescutti, G. 2010, *A&A*, 522, A9
- Bergemann, M., Pickering, J. C., & Gehren, T. 2010, *MNRAS*, 401, 1334
- Bettinelli, M., Hidalgo, S. L., Cassisi, S., Aparicio, A., & Piotto, G. 2018, *MNRAS*, 476, 71
- Bisterzo, S., Gallino, R., Straniero, O., Cristallo, S., & Käppeler, F. 2012, *MNRAS*, 422, 849
- Breddels, M. A. & Helmi, A. 2013, *A&A*, 558, A35
- Busso, M., Gallino, R., & Wasserburg, G. J. 1999, *ARA&A*, 37, 239
- Cameron, A. G. W. 1957, *AJ*, 62, 9
- Cardelli, J. A., Clayton, G. C., & Mathis, J. S. 1989, *ApJ*, 345, 245
- Chiti, A., Simon, J. D., Frebel, A., et al. 2018, *ApJ*, 856, 142
- Cicúendez, L. & Battaglia, G. 2018, *MNRAS*, 480, 251
- Cicúendez, L., Battaglia, G., Irwin, M., et al. 2018, *A&A*, 609, A53
- Cohen, J. G., Christlieb, N., Thompson, I., et al. 2013, *ApJ*, 778, 56
- Cohen, J. G. & Huang, W. 2009, *ApJ*, 701, 1053
- Côté, B., Belczynski, K., Fryer, C. L., et al. 2017, *ApJ*, 836, 230
- Dekker, H., D'Odorico, S., Kaufer, A., Delabre, B., & Kotzlowski, H. 2000, in *Society of Photo-Optical Instrumentation Engineers (SPIE) Conference Series*, Vol. 4008, Proc. SPIE, ed. M. Iye & A. F. Moorwood, 534–545
- Ezzeddine, R., Frebel, A., & Plez, B. 2017, *ApJ*, 847, 142
- Fabrizio, M., Bono, G., Nonino, M., et al. 2016, *ApJ*, 830, 126
- Fabrizio, M., Nonino, M., Bono, G., et al. 2011, *PASP*, 123, 384
- François, P., Depagne, E., Hill, V., et al. 2007, *A&A*, 476, 935
- Frebel, A. 2018, *Annual Review of Nuclear and Particle Science*, 68, 237
- Frebel, A. & Norris, J. E. 2015, *ARA&A*, 53, 631
- Freiburghaus, C., Rosswog, S., & Thielemann, F. K. 1999, *ApJ*, 525, L121
- Gustafsson, B., Edvardsson, B., Eriksson, K., et al. 2008, *A&A*, 486, 951
- Hansen, C. J., Bergemann, M., Cescutti, G., et al. 2013, *A&A*, 551, A57
- Hansen, T. T., Holmbeck, E. M., Beers, T. C., et al. 2018, *ApJ*, 858, 92
- Hill, V., Skúladóttir, Á., Tolstoy, E., et al. 2019a, *A&A*, 626, A15
- Hill, V., Skúladóttir, Á., Tolstoy, E., et al. 2019b, *A&A*, 626, A15
- Hirai, Y., Saitoh, T. R., Ishimaru, Y., & Wanajo, S. 2018, *ApJ*, 855, 63
- Honda, S., Aoki, W., Arimoto, N., & Sadakane, K. 2011, *PASJ*, 63, 523
- Hurley-Keller, D., Mateo, M., & Nemec, J. 1998, *AJ*, 115, 1840
- Irwin, M. J., Bunclark, P. S., Bridgeland, M. T., & McMahon, R. G. 1990, *MNRAS*, 244, 16P
- Ishigaki, M. N., Aoki, W., & Chiba, M. 2013, *ApJ*, 771, 67
- Jablonka, P., North, P., Mashonkina, L., et al. 2015, *A&A*, 583, A67
- Ji, A. P., Frebel, A., Chiti, A., & Simon, J. D. 2016, *Nature*, 531, 610
- Käppeler, F., Gallino, R., Bisterzo, S., & Aoki, W. 2011, *Reviews of Modern Physics*, 83, 157
- Karachentseva, I. D., Karachentseva, V. E., Huchtmeier, W. K., & Makarov, D. I. 2004, *AJ*, 127, 2031
- Kirby, E. N. & Cohen, J. G. 2012, *AJ*, 144, 168
- Kirby, E. N., Guo, M., Zhang, A. J., et al. 2015, *ApJ*, 801, 125
- Kirby, E. N., Xie, J. L., Guo, R., Kovalev, M., & Bergemann, M. 2018, *ApJS*, 237, 18
- Kupka, F., Piskunov, N., Ryabchikova, T. A., Stempels, H. C., & Weiss, W. W. 1999, *A&AS*, 138, 119
- Kupka, F. G., Ryabchikova, T. A., Piskunov, N. E., Stempels, H. C., & Weiss, W. W. 2000, *Baltic Astronomy*, 9, 590
- Kurucz, R. L. 1993, in *Astronomical Society of the Pacific Conference Series*, Vol. 44, IAU Colloq. 138: Peculiar versus Normal Phenomena in A-type and Related Stars, ed. M. M. Dworetzky, F. Castelli, & R. Faraggiana, 87
- Lattimer, J. M. & Schramm, D. N. 1974, *ApJ*, 192, L145
- Lee, M. G., Park, H. S., Park, J.-H., et al. 2003, *AJ*, 126, 2840
- Lee, M. G., Yuk, I.-S., Park, H. S., Harris, J., & Zaritsky, D. 2009, *ApJ*, 703, 692
- Letarte, B., Hill, V., Tolstoy, E., et al. 2010, *A&A*, 523, A17
- Lind, K., Asplund, M., Barklem, P. S., & Belyaev, A. K. 2011, *A&A*, 528, A103
- Lokas, E. L. 2009, *MNRAS*, 394, L102
- Macias, P. & Ramirez-Ruiz, E. 2018, *ApJ*, 860, 89
- Magain, P. 1984, *A&A*, 134, 189
- Mashonkina, L., Christlieb, N., Barklem, P. S., et al. 2010, *A&A*, 516, A46
- Mashonkina, L., Jablonka, P., Pakhomov, Y., Sitnova, T., & North, P. 2017a, *A&A*, 604, A129
- Mashonkina, L., Jablonka, P., Sitnova, T., Pakhomov, Y., & North, P. 2017b, *A&A*, 608, A89
- Mateo, M., Fischer, P., & Krzeminski, W. 1995, *AJ*, 110, 2166
- McConnachie, A. W. 2012, *AJ*, 144, 4
- Muñoz, R. R., Côté, P., Santana, F. A., et al. 2018, *ApJ*, 860, 66
- Nishimura, N., Takiwaki, T., & Thielemann, F.-K. 2015, *ApJ*, 810, 109
- Noguchi, K., Aoki, W., Kawanomoto, S., et al. 2002, *PASJ*, 54, 855
- Nomoto, K., Kobayashi, C., & Tominaga, N. 2013, *Annual Review of Astronomy and Astrophysics*, 51, 457
- North, P., Cescutti, G., Jablonka, P., et al. 2012, *A&A*, 541, A45
- Okamoto, S., Arimoto, N., Tolstoy, E., et al. 2017, *MNRAS*, 467, 208
- Pasetto, S., Grebel, E. K., Berczik, P., Chiosi, C., & Spurzem, R. 2011, *A&A*, 525, A99
- Pian, E., D'Avanzo, P., Benetti, S., et al. 2017, *Nature*, 551, 67
- Piskunov, N. E., Kupka, F., Ryabchikova, T. A., Weiss, W. W., & Jeffery, C. S. 1995, *A&AS*, 112, 525
- Placco, V. M., Frebel, A., Beers, T. C., & Stancliffe, R. J. 2014, *ApJ*, 797, 21
- Plez, B. 2012, *Turbospectrum: Code for spectral synthesis*, Astrophysics Source Code Library
- Press, W. H. & Schechter, P. 1974, *ApJ*, 187, 425
- Prochaska, J. X. & McWilliam, A. 2000, *ApJ*, 537, L57
- Ramírez, I. & Meléndez, J. 2005, *ApJ*, 626, 465
- Roederer, I. U., Mateo, M., Bailey, John I., I., et al. 2016, *AJ*, 151, 82
- Ryabchikova, T. A., Piskunov, N. E., Kupka, F., & Weiss, W. W. 1997, *Baltic Astronomy*, 6, 244
- Salvadori, S., Skúladóttir, Á., & Tolstoy, E. 2015, *MNRAS*, 454, 1320
- Santana, F. A., Muñoz, R. R., de Boer, T. J. L., et al. 2016, *ApJ*, 829, 86
- Shetrone, M. D., Côté, P., & Sargent, W. L. W. 2001a, *ApJ*, 548, 592

- Shetrone, M. D., Côté, P., & Sargent, W. L. W. 2001b, *ApJ*, 548, 592
- Shetrone, M. D., Smith, G. H., Stanford, L. M., Siegel, M. H., & Bond, H. E. 2013, *AJ*, 145, 123
- Simon, J. D. 2019, *ARA&A*, 57, 375
- Simon, J. D., Jacobson, H. R., Frebel, A., et al. 2015, *ApJ*, 802, 93
- Skúladóttir, Á., Tolstoy, E., Salvadori, S., et al. 2015, *A&A*, 574, A129
- Snedden, C., Cowan, J. J., & Gallino, R. 2008, *ARA&A*, 46, 241
- Spite, F., Spite, M., Barbuy, B., et al. 2018, *A&A*, 611, A30
- Spite, M. & Spite, F. 2014, *Astronomische Nachrichten*, 335, 65
- Springel, V., Frenk, C. S., & White, S. D. M. 2006, *Nature*, 440, 1137
- Starkenburg, E., Hill, V., Tolstoy, E., et al. 2013, *A&A*, 549, A88
- Starkenburg, E., Hill, V., Tolstoy, E., et al. 2010, *A&A*, 513, A34
- Stetson, P. B. & Pancino, E. 2008, *PASP*, 120, 1332
- Tafelmeyer, M., Jablonka, P., Hill, V., et al. 2010, *A&A*, 524, A58
- Theler, R., Jablonka, P., Lardo, C., et al. 2019, arXiv e-prints, arXiv:1911.08627
- Tolstoy, E., Hill, V., & Tosi, M. 2009, *ARA&A*, 47, 371
- Travaglio, C., Gallino, R., Arnone, E., et al. 2004, *ApJ*, 601, 864
- Travaglio, C., Hillebrandt, W., & Reinecke, M. 2005, *A&A*, 443, 1007
- Tsujimoto, T. & Nishimura, N. 2018, *ApJ*, 863, L27
- Van der Swaelmen, M., Hill, V., Primas, F., & Cole, A. A. 2013, *A&A*, 560, A44
- Venn, K. A., Irwin, M., Shetrone, M. D., et al. 2004a, *AJ*, 128, 1177
- Venn, K. A., Irwin, M., Shetrone, M. D., et al. 2004b, *AJ*, 128, 1177
- Walker, M. G., McGaugh, S. S., Mateo, M., Olszewski, E. W., & Kuzio de Naray, R. 2010, *ApJ*, 717, L87
- Wanajo, S. 2013, *ApJ*, 770, L22
- White, S. D. M. & Rees, M. J. 1978, *MNRAS*, 183, 341
- Woosley, S. E., Heger, A., & Weaver, T. A. 2002, *Reviews of Modern Physics*, 74, 1015
- Yong, D., Norris, J. E., Bessell, M. S., et al. 2013, *ApJ*, 762, 26

3.4 Publication in preparation : Extremely metal-poor stars in the Fornax and Carina dwarf spheroidal galaxies

Even though the following work comes second in the sequence of this manuscript, in order to preserve homogeneity in the scientific questions, in practice this was the last project I conducted before the end of my thesis. The paper is still in preparation and close to its final form, it should be submitted to the journal *Astronomy & Astrophysics* in the coming weeks.

Two new EMP candidates were observed at high resolution with UVES in the Fornax dSph, and four new EMP candidates were observed at intermediate resolution with XSHOOTER in the Carina dSph. Both Fornax and Carina dSphs were very badly constrained in their EMP regime. Only three stars at $[\text{Fe}/\text{H}] < -2.5$ were studied at high resolution in Fornax, including a single EMP at $[\text{Fe}/\text{H}] = -3.4$ from [Tafelmeyer et al. \(2010\)](#). In Carina, four stars were known at $[\text{Fe}/\text{H}] < -2.5$ but none below $[\text{Fe}/\text{H}] = -3.0$. With this new sample I start to explore some metallicity domains and some chemical elements not covered yet.

I performed the complete data processing, and the chemical analysis of the stars presented.

Extremely metal-poor stars in the Fornax and Carina dwarf spheroidal galaxies

R. Lucchesi^{1,2}, P. Jablonka^{1,3}, C. Lardo^{1,4}, M. Irwin⁵, G. Battaglia⁶, A. Helmi⁷, V. Hill⁸, V. Mashonkina⁹, D. Minniti¹⁰, F. Primas², E. Starkenburg⁷, E. Tolstoy⁷, and K. Venn¹¹

¹ Physics Institute, Laboratoire d'astrophysique, École Polytechnique Fédérale de Lausanne (EPFL), Observatoire, 1290 Versoix, Switzerland

² European Southern Observatory, Karl-Schwarzschild-str. 2, 85748 Garching bei München, Germany

³ GEPI, Observatoire de Paris, Université PSL, CNRS, 5 Place Jules Janssen, 92190 Meudon, France

⁴ Dipartimento di Fisica e Astronomia, Università degli Studi di Bologna, Via Gobetti 93/2, I-40129 Bologna, Italy

⁵ Institute of Astronomy, University of Cambridge, Madingley Road, Cambridge CB3 0HA, UK

⁶ Instituto de Astrofísica de Canarias (IAC), Calle Via Láctea, s/n, 38205, San Cristóbal de la Laguna, Tenerife, Spain

⁷ Kapteyn Astronomical Institute, University of Groningen, Postbus 800, 9700 AV, Groningen, the Netherlands

⁸ Université Côte d'Azur, Observatoire de la Côte d'Azur, CNRS, Laboratoire Lagrange, Nice, France

⁹ Institute of Astronomy of the Russian Academy of Sciences, Pyatnitskaya st. 48, 119017, Moscow, Russia

¹⁰ Departamento de Ciencias Físicas, Facultad de Ciencias Exactas, Universidad Andrés Bello, Fernández Concha 700, Las Condes, Santiago, Chile

¹¹ Department of Physics and Astronomy, University of Victoria, PO Box 3055, STN CSC, Victoria, BC V8W 3P6, Canada

Received xx xxxx 2021; accepted xx xxxx 2021

ABSTRACT

We present our analysis of VLT/UVES and X-shooter observation of six very metal-poor stars, including four stars at $[\text{Fe}/\text{H}] \sim -3$ in the dwarf spheroidal galaxies (dSph) Fornax and Carina. So far this metallicity range in these two galaxies was either hardly or not yet investigated. The chemical abundances of 25 elements, based on 1D/LTE model atmospheres, are delivered. We report the discovery of a star in Fornax enriched with r-process elements at a metallicity of $[\text{Fe}/\text{H}] = -2.92$.

Key words. stars: abundances – Local Group – galaxies: dwarf – galaxies: formation

1. Introduction

We aim at understanding the characteristics of the first stars formed in the universe, from their imprints on low mass stars in dwarf spheroidal galaxies (dSph). The stellar abundance trends and dispersions of the most metal-poor stars reveal the nature of the now deceased first generations (e.g., mass, numbers), and the level of homogeneity of the primitive interstellar medium (ISM) (e.g., size/mass of star forming regions, nature and energetics of the explosion of supernovae). The proximity of the Local Group dSphs allows to derive chemical abundances in individual stars at comparable quality as in the Milky Way (MW). The confrontation of galaxies with very different evolutionary path brings crucial information on the universality of the star formation processes.

Carina, Sextans, Sculptor, and Fornax are the four Local Group dSphs, which have triggered so far the strongest observational efforts from the galactic archaeology community. They provided the first evidence for distinct star formation histories and chemical evolution from those of the Milky Way at $[\text{Fe}/\text{H}] > -2$ (Tolstoy et al. 2009). Carina, Sextans, Sculptor, and Fornax form a sequence of mass from the lowest to the highest mass limits of the classical dSphs. They followed very different evolution: The bulk of the Sextans and Sculptor stars was formed within the first 4-6 Gyrs (Lee et al. 2009; de Boer et al. 2011). In contrast, Carina is famous by its star-forming episodes well separated by long quiescent periods (de Boer et al. 2014).

With a stellar mass 4 times larger than Sculptor, Fornax has a population dominated by intermediate age stars (de Boer et al. 2012) and six globular clusters (GC) (Hodge 1961; Pace et al. 2021). The diversity of these four dSphs allows us to probe the relation between the very early stages of star formation and the subsequent evolutionary paths.

While we now broadly understand their latest stages of evolution, we essentially ignore everything from their early times. So far, Sculptor and Sextans are the classical dSphs with the largest number of metal poor stars observed at sufficiently high spectral resolution to derive accurate chemical abundances. To date there are 10 extremely metal-poor stars (EMPS, $[\text{Fe}/\text{H}] \leq -3$) have been found and analysed in Sculptor (out of 12 $[\text{Fe}/\text{H}] < -2.5$ stars) (Tafelmeyer et al. 2010; Frebel et al. 2010; Starkenburg et al. 2013; Jablonka et al. 2015; Simon et al. 2015) and only 4 in Sextans (out of 14 stars at $[\text{Fe}/\text{H}] < -2.5$) (Shetrone et al. 2001; Aoki et al. 2009; Starkenburg et al. 2013; Lucchesi et al. 2020; Theler et al. 2020), Fornax has only one known EMP chemically characterized (with 2 stars at $[\text{Fe}/\text{H}] < -2.5$) (Tafelmeyer et al. 2010; Lemasle et al. 2014) and Carina has none so far (out of 4 stars at $[\text{Fe}/\text{H}] < -2.5$) (Venn et al. 2012; Susmitha et al. 2017; Norris et al. 2017).

These pioneering efforts have nevertheless already led to a number of important results among which: *i*) While the level of a plateau at $[\alpha/\text{Fe}] \sim 0.4$ suggests a well sampled classical IMF in the early days of Sculptor, similarly to the halo of the MW, two stars have been found at sub-solar value, possibly reflect-

ing a lack of enrichment by the ejecta of the most massive core collapse supernovae (SNeII). These type of low- α stars do exist in the MW halo but are statistically less frequent. *ii*) While below $[\text{Fe}/\text{H}] \sim -3.5$ essentially all galaxies, seem to have similar very low strontium, above this metallicity, the ultra-faint dwarfs, with a few exception (ReticulumII & TucanaII Ji et al. 2016; Roederer et al. 2016; Marshall et al. 2019), stay at this low level, whereas a more massive galaxy such as Sculptor and Sextans eventually reaches the solar value observed in the MW (Jablonka et al. 2015; Mashonkina et al. 2017b; Lucchesi et al. 2020; Ji et al. 2019). The nucleosynthetic site of the neutron capture elements is still largely debated in the literature. By investigating a different galaxy mass range, these comparisons provide very crucial constraints, and support a double origin of the neutron capture elements, by massive stars that generate the abundance floor (e.g., Winteler et al. 2012) and rare events, such as neutron star mergers (e.g., Wanajo et al. 2014).

This work contributes to the study of the chemical patterns of the most metal-deficient stars in dwarf galaxies, this time focusing on Fornax and Carina.

The paper is structured as follows: Section 2 describes the selection of the sample, the observations, and the data reduction. Section 3 presents the determination of the stellar atmospheric parameters and the calculation of the elemental chemical abundances and their uncertainties. Section 3. Section 4 discusses our results in depth. They are summarized in Sec. 5.

2. Observations and data reduction

2.1. Target preselection, observations, and data reduction

The EMP candidates of this work are red giant branch (RGB) stars (Fig. 1). Their selection was based on the estimate of their metallicity ($[\text{Fe}/\text{H}]_{\text{CaT}} < -2.5$) via the calcium triplet. Starkenburg et al. (2010) delivered a CaII triplet (CaT) calibration down to $[\text{Fe}/\text{H}] = -4$, which was applied to the samples of Battaglia et al. (2011) for Fornax and Koch et al. (2006) for Carina.

The two EMPS candidates in Fornax, fnx-06_109 and fnx0579x-1, were sufficiently bright to enable follow-up at high resolution with the UVES spectrograph (Dekker et al. 2000) mounted at the ESO-VLT (program 0100.D-0820(A)). We used the dichroic1 with the CCD#2 centered at 3900 Å and the CCD#3 centered at 5800 Å. Setting the slit width at 1.2'' led to a nominal resolution of $R \sim 34,000$. The total wavelength coverage is $\sim 3200\text{--}6800$ Å, and the effective usable spectral information starts from ~ 3800 Å. Each star has been observed for a total of five hours, split into six individual sub-exposures.

The four EMPS candidates in Carina, LG04c_0008, Car1_t200, Car1_t174, and Car1_t194 were observed (program 094.D-0853(B)) with X-shooter (Vernet et al. 2011). The UVB slit was open to 0.8×11 arcsec² while the VIS slit was open to 0.9×11 arcsec², which led to a nominal resolution of $R \sim 6,200$ and $R \sim 7,400$ respectively. The total exposure time, in STARE mode, was 2.5 hours for LG04c_0008 and 3 hours for the other stars divided in 3 and 4 OBs of ~ 3000 s, respectively. The usable wavelength range spans the range 3040–6800 Å.

In all cases, the reduced data, including bias subtraction, flat fielding, wavelength calibration, spectral extraction, and order merging, were taken from the ESO Science Archive Facility.

Table 1 provides the coordinates of our targets, the signal-to-noise ratios (SN), and the radial velocities as measured in each wavelength interval. Table 2 lists the optical and near-infrared magnitudes of our sample. Figure 2 indicates the spatial location

of our targets relative to the position of other spectroscopic studies in Carina and Fornax, which serves as comparison samples in subsequent figures.

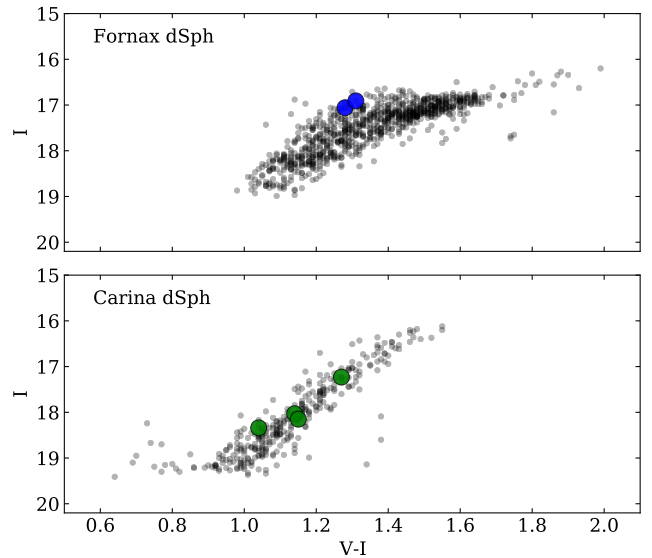


Fig. 1: $V-I$, I CMD in the region of the red giant branch of Fornax (top panel) and Carina (bottom panel). The blue and green symbols show respectively the Fornax and Carina stars. Gray circles are probable Fornax and Carina members based on their radial velocities (Koch et al. 2006; Battaglia et al. 2011; Starkenburg et al. 2010).

2.2. Radial velocity measurements and normalization

The stellar heliocentric radial velocities (RVs) were measured with the IRAF¹ task *rvidlines* on each individual exposure. The final RV is the average of these individual values weighted by their uncertainties. This approach allows us to detect possible binary stars, at least those whose RV variations can be detected within about one year. We did not find any evidence for binarity. After they were corrected for RV shifts, the individual exposures were combined into a single spectrum using the IRAF task *scombine* with sigma clipping. As a final step, each spectrum was visually examined, and the few remaining cosmic rays were removed with the *splot* routine.

The mean RV of each star (Table 1) coincides with the RV of Fornax ($54.1 \pm 0.5 \text{ km s}^{-1}$) within the velocity dispersion $\sigma = 13.7 \pm 0.4 \text{ km s}^{-1}$ measured by Battaglia et al. (2006), and the RV of Carina ($224.4 \pm 5.95 \text{ km s}^{-1}$) measured by Lemasle et al. (2012). This confirms that our stars are galaxy members. Spectra were further normalized using DAOSPEC (Stetson & Pancino 2008) for each of the wavelength ranges presented in Table 1. We used a 30 to 40 degree polynomial fit.

3. Stellar model determination and chemical analysis

3.1. Line list and model atmospheres

Our line list combines those of Jablonka et al. (2015), Tafelmeyer et al. (2010), and Van der Swaelmen et al. (2013).

¹ Image Reduction and Analysis Facility; Astronomical Source Code Library ascl:9911.002

Table 1: Observation journal. The λ range refers to the spectral ranges used in the analysis.

ID	$\alpha(J2000)$ [h:mn:s]	$\delta(J2000)$ [° :':"]	Setting	λ range Å	<S/N> [/pix]	$V_{rad,helio} \pm \sigma$ [km s ⁻¹]
UVES						
fnx-06_019	02:37:00.91	-34:10:43.10	Dic1-CCD#2	3800-4515	12	53.78 ± 1.90
			Dic1-CCD#3(Blue)	4790-5760	30	54.43 ± 1.06
			Dic1-CCD#3(Red)	5840-6805	45	53.98 ± 1.61
fnx0579x-1	02:40:47.79	-34:26:46.50	Dic1-CCD#2	3800-4520	12	49.43 ± 2.60
			Dic1-CCD#3(Blue)	4790-5760	30	49.62 ± 1.17
			Dic1-CCD#3(Red)	5840-6805	43	49.17 ± 1.28
X-shooter						
car1_t174	06:41:58.72	-51:06:40.30	UBV	3040-5550	38	205.37 ± 19.90
			VIS	5550-6800	24	209.26 ± 9.33
car1_t194	06:41:42.87	-51:05:30.10	UBV	3040-5550	33	202.50 ± 13.87
			VIS	5550-6800	30	207.11 ± 14.51
car1_t200	06:41:49.67	-51:01:31.30	UBV	3040-5550	34	214.69 ± 21.46
			VIS	5550-6800	25	208.40 ± 20.19
LG04c_0008	06:40:49.14	-51:00:33.00	UBV	3040-5550	37	219.13 ± 16.35
			VIS	5550-6800	40	221.05 ± 16.32

Information on the spectral lines was taken from the VALD database (Piskunov et al. 1995; Ryabchikova et al. 1997; Kupka et al. 1999, 2000). The corresponding central wavelengths and oscillator strengths are given in Table A.1.

We adopted the new MARCS 1D atmosphere models and selected the *Standard composition* class, that is, we included the classical α -enhancement of +0.4 dex at low metallicity. They were downloaded from the MARCS web site (Gustafsson et al. 2008), and interpolated using Thomas Masseron’s *interpol_modeler* code, which is available on the same web site². Inside a cube of eight reference models, this code performs a linear interpolation on three given parameters : T_{eff} , $\log g$, and $[\text{Fe}/\text{H}]$.

Table 2: Optical and near-IR photometry. V , I from ESO 2.2m WFI. J , H , K_s from ESO VISTA

ID	V	I	J	H	K_s
fnx_06_109	18.336	17.062	16.005	15.455	15.310
fnx0579x-1	18.220	16.910	16.090	15.532	15.393
car1_t174	19.170	18.030	17.112	16.612	16.531
car1_t194	19.300	18.150	17.203	16.689	16.584
car1_t200	19.380	18.340	17.463	16.938	16.780
LG04c_0008	18.500	17.230	16.282	15.798	15.666

3.2. Photometric temperature and gravity

The atmospheric parameters (APs) were initially determined using photometric information as in Table 2. The first approximated determination of the stellar effective temperature was based on the $V-I$, $V-J$, $V-H$, and $V-K$ color indices mea-

² <http://marcs.astro.uu.se>

sured by Battaglia et al. (2011), and J and K_s photometry was taken from the VISTA commissioning data, which were also calibrated onto the 2MASS photometric system. We assumed $A_V = 3.24 \cdot E_{B-V}$ (Cardelli et al. 1989) and $E_{B-V} = 0.03$ for Fornax (Letarte et al. 2010) and $E_{B-V} = 0.061$ for Carina (de Boer et al. 2014) for the reddening correction. The adopted photometric effective temperatures, T_{eff} , are listed in Table 3. They correspond to the simple average of the four color temperatures derived from $V-I$, $V-J$, $V-H$, and $V-K$ with the calibration of Ramírez & Meléndez (2005).

Because only very few Fe II lines can be detected in our X-shooter spectra, the determination of surface gravities from the ionisation balance of Fe I vs. Fe II was not possible. Non-local thermodynamic equilibrium (NLTE) effects also play a role at extremely low metallicity and impact the abundances of Fe I, with $\Delta(\text{Fe II}-\text{Fe I})$ up to +0.20 dex at $[\text{Fe}/\text{H}] = -3$, thus surface gravities were determined from their relation with T_{eff} :

$$\log g_{\star} = \log g_{\odot} + \log \frac{M_{\star}}{M_{\odot}} + 4 \times \log \frac{T_{\text{eff}\star}}{T_{\text{eff}\odot}} + 0.4 \times (M_{\text{bol}\star} - M_{\text{bol}\odot}) \quad (1)$$

assuming $\log g_{\odot} = 4.44$, $T_{\text{eff}\odot} = 5790$ K, and $M_{\text{bol}\odot} = 4.75$ for the Sun. We adopted a stellar mass of $0.8 M_{\odot}$ and calculated the bolometric corrections using the Alonso et al. (1999) calibration, with a distance of $d=138$ kpc (Battaglia et al. 2006) for Fornax and $d=106$ kpc (de Boer et al. 2014) for Carina.

3.3. Final stellar parameters and abundance determination

We determined the stellar chemical abundances through the measurement of the equivalent widths (EWs) or the spectral synthesis of atomic transition lines, when necessary. The EWs were measured with DAOSPEC (Stetson & Pancino 2008). This code performs a Gaussian fit of each individual line and measures its

Table 3: CaT metallicity estimates, photometric and final spectroscopic parameters.

ID	Photometric Parameters							Final Parameters			
	$V - I$	$V - J$	T_{eff} [K] $V - H$	$V - K_s$	mean	$\log(g)$	$[\text{Fe}/\text{H}]_{\text{CaT}}$	T_{eff} [K]	$\log(g)$ [cgs]	v_t km s ⁻¹	$[\text{Fe}/\text{H}]$
fnx_06_109	4379	4257	4248	4362	4311	0.70	-2.54	4280	0.68	1.80	-2.92
fnx0579x-1	4338	4422	4386	4427	4393	0.71	-2.55	4255	0.62	1.70	-2.73
car1_t174	4711	4678	4592	4646	4657	1.42	-3.41	4650	1.42	1.90	-3.01
car1_t194	4619	4533	4519	4544	4554	1.42	-2.68	4550	1.43	1.71	-2.58
car1_t200	4862	4813	4690	4663	4757	1.56	-3.26	4750	1.56	1.69	-2.95
LG04c_0008	4518	4504	4466	4507	4499	1.07	-3.29	4520	1.08	1.78	-3.05

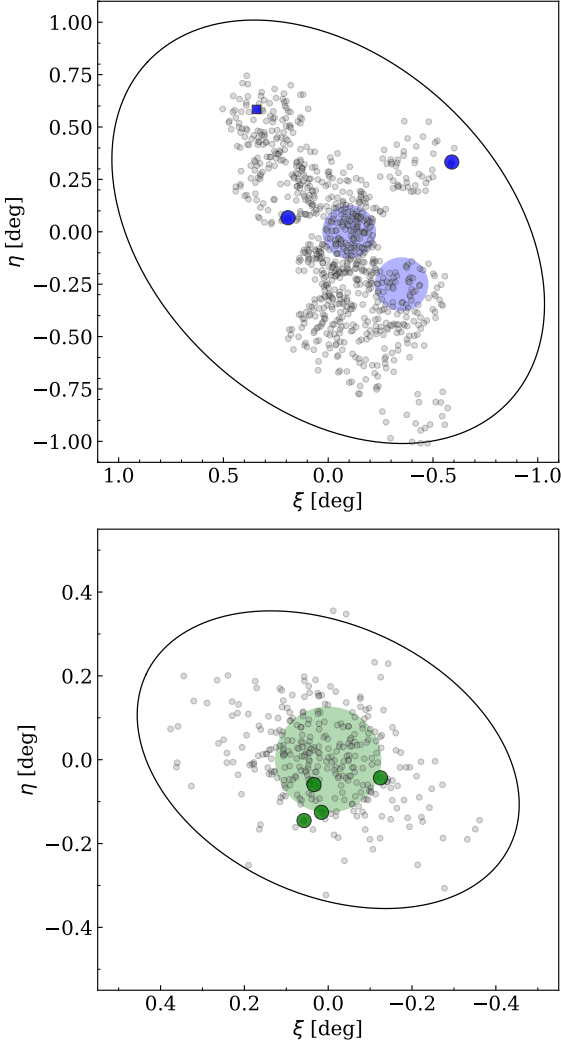


Fig. 2: Top panel : Spatial distribution of Fornax stars. Symbols are same as in Fig 1, the large shaded blue circles correspond to the VLT/FLAMES observations of Letarte et al. (2010) (center of Fornax) and Lemasle et al. (2014) (off-center). Bottom panel : Spatial distribution of Carina stars. The large shaded green circle corresponds to the VLT/FLAMES observations of Lemasle et al. (2012). The ellipses indicates the tidal radius of Fornax and Carina respectively.

corresponding EW. Although DAOSPEC fits saturated Gaussians to strong lines, it cannot fit the wider Lorentz-like wings of the

profile of very strong lines, in particular beyond 120 mÅ at very high resolution (Kirby & Cohen 2012). For some of the strongest lines in our spectra, we therefore derived the abundances by spectral synthesis (see below).

The measured EWs are provided in Table A.1. Values in bracket indicate that the corresponding abundances were derived by spectral synthesis. The abundance derivation from EWs and the spectral synthesis calculation were performed with the Turbospectrum code (Alvarez & Plez 1998; Plez 2012), which assumes local thermodynamic equilibrium (LTE), but treats continuum scattering in the source function. We used a plane-parallel transfer for the line computation; this is consistent with our previous work on EMP stars (Tafelmeyer et al. 2010; Jablonka et al. 2015; Lucchesi et al. 2020).

In order to derive the final T_{eff} and the microturbulence velocities (v_t), we checked or required no trend between the abundances derived from Fe I and excitation potential (χ_{exc}) or the predicted³ EWs (Magain 1984). We excluded from this part of the analysis Fe I lines with $\chi_{\text{exc}} < 1.4$ eV in order to minimize the NLTE effect on the measured abundances.

Starting from the initial photometric parameters of Table 3, we adjusted T_{eff} and v_t by minimizing the slopes of the diagnostic plots, within its 2σ uncertainty. We did not force ionization equilibrium between Fe I and Fe II, taking into account that there will likely be NLTE effects at these low metallicities (Mashonkina et al. 2017a; Ezzeddine et al. 2017). For each iteration the corresponding values of $\log g$ were computed from its relation with T_{eff} (Eq. 1), assuming the updated values of T_{eff} , and adjusting the model metallicity to the mean iron abundance derived in the previous iteration. The final values of T_{eff} are less than 30K away from the initial photometric estimates, at the exception of fnx0579x-1 which is 138K cooler than the mean photometric temperature.

We derived the chemical abundances of the strong lines with measured EW > 100 mÅ by spectral synthesis. These abundances were obtained using our own code, which performs a χ^2 -minimization between the observed spectral features and a grid of synthetic spectra calculated on the fly with Turbospectrum. A line of a chemical element X is synthesized in a wavelength range of ~50 Å. It is optimized by varying its abundance in steps of 0.1 dex, from $[X/\text{Fe}] = -2.0$ dex to $[X/\text{Fe}] = +2.0$ dex. In the same way, the resolution of the synthetic spectra is optimized when needed. Starting from the nominal instrumental resolution, synthetic spectra can be convolved in a wide range of Gaussian widths for each abundance step. A second optimiza-

³ The use of observed EWs would produce an increase of v_t by 0.1–0.2 km s⁻¹, which would be reflected in a decrease of the measured $[\text{Fe}/\text{H}]$ values by a few hundredths of a dex in a systematic way. A variation like this does not change the results in a significant way.

tion, with abundance steps of 0.01 dex, is then performed in a smaller range around the minimum χ^2 in order to refine the results. Similarly, the elements with a significant hyperfine structure (HFS) (Sc, Mn, Co, and Ba) have been determined by running *Turbospectrum* in its spectral synthesis mode in order to properly take into account blends and the HFS components in the abundance derivation, as in [North et al. \(2012\)](#), [Prochaska & McWilliam \(2000\)](#) for Sc and Mn, and from the Kurucz web site⁴ for Co and Ba.

The final abundances are listed in Table 4. The solar abundances are taken from [Asplund et al. \(2009\)](#).

3.4. Error budget

The uncertainties on the abundances were derived considering the uncertainties on the atmospheric parameters and on the EWs.

1. *Uncertainties due to the atmospheric parameters.* To estimate the sensitivity of the derived abundances to the adopted atmospheric parameters, we repeated the abundance analysis and varied only one stellar atmospheric parameter at a time by its corresponding uncertainty, keeping the others fixed and repeating the analysis. The estimated internal errors are ± 100 K in T_{eff} , ± 0.15 dex in $\log(g)$, and ± 0.15 km s⁻¹ in v_t . Because the atmospheric parameters of our sample stars are very close to each other, we estimated the typical errors linked to UVES and X-shooter, taking the example of one star.

As to UVES, Tab. 5 lists the effects of these changes on the derived abundances for fnx_06_019. With comparable stellar parameters and S/N, the effects of changes in atmospheric parameters on abundances are expected to be the same for stars fnx0579x-1.

2. *Uncertainties due to EWs or spectral fitting.* The uncertainties on the individual EW measurements δ_{EWi} are provided by DAOSPEC (see Table A.1) and computed according to the following formula ([Stetson & Pancino 2008](#)) :

$$\delta_{EWi} = \sqrt{\sum_p (\delta I_p)^2 \left(\frac{\partial EW}{\partial I_p} \right)^2 + \sum_p (\delta I_{C_p})^2 \left(\frac{\partial EW}{\partial I_{C_p}} \right)^2} \quad (2)$$

where I_p and δI_p are the intensity of the observed line profile at pixel p and its uncertainty, and I_{C_p} and δI_{C_p} are the intensity and uncertainty of the corresponding continuum. The uncertainties on the intensities are estimated from the scatter of the residuals that remain after subtraction of the fitted line (or lines, in the case of blends). The corresponding uncertainties σ_{EWi} on individual line abundances are propagated by *Turbospectrum*. This is a lower limit to the real EW error because systematic errors like the continuum placement are not accounted for.

In order to account for additional sources of error, we quadratically added a 5% error to the EW uncertainty, so that no EW has an error smaller than 5%. For the abundances derived by spectral synthesis (e.g., strong lines, hyperfine structure, or carbon from the G band), the uncertainties were visually estimated by gradually changing the parameters of the synthesis until the deviation from the observed line became noticeable.

The abundance uncertainty for an element X due to the individual EW uncertainties (σ_{EWi} propagated from δ_{EWi}) are computed as :

$$\sigma_{EW}(X) = \sqrt{\frac{N_X}{\sum_i 1/\sigma_{EWi}^2}} \quad (3)$$

where N_X represents the number of lines measured for element X.

The dispersion σ_X around the mean abundance of an element X measured from several lines is computed as :

$$\sigma_X = \sqrt{\frac{\sum_i (\epsilon_i - \bar{\epsilon})^2}{N_X - 1}} \quad (4)$$

where ϵ stands for the logarithmic abundance.

The final error on the elemental abundances is defined as $\sigma_{fin} = \max(\sigma_{EW}(X), \sigma_X / \sqrt{N_X}, \sigma_{Fe} / \sqrt{N_X})$. As a consequence, no element X can have an estimated dispersion $\sigma_X < \sigma_{Fe}$; this is particularly important for species with very few lines.

3.5. Specific comments on the abundance determination

3.5.1. Carbon

Carbon abundances were determined by spectral synthesis in the region of the CH molecular band. The carbon abundances of the UVES Fornax sample were determined in the deeper and unblended 4222 Å – 4225 Å region, while carbon was determined in a larger range of the CH molecular band between 4270 Å – 4330 Å for the X-shooter sample in Carina.

3.5.2. α elements

- *Magnesium.* The UVES Mg I abundances are based on 3 lines. Two of them are rather strong (5172.684 and 5183.604 Å), with EW > 100 mÅ and have non-Gaussian line profiles. The abundances of these lines are not consistent with the weaker 5528.405 Å line. For this reason, we decided to derive the Mg I abundance through spectral synthesis, after which all lines had consistent abundances. Three additional Mg I lines (4167.271 4351.906 and 5711.088 Å) are detected in our spectra, but were discarded because they are too affected by the noise, strongly blended and too weak, respectively. Mg I abundances of the X-shooter sample are obtained through spectral synthesis in two 20 Å windows, centered on the 5172.684 Å line taking into account the blends at the X-shooter resolution, and centered on the 5183.604 Å line.
- *Titanium.* The Ti I abundances rely on 10–11 lines, all giving consistent abundance values from their EW. The Ti II abundances are based on 8–14 lines. They are slightly more scattered as many of them are rather strong. The mean abundances of Ti I and Ti II are different by $\Delta(\text{Ti II} - \text{Ti I}) = +0.50$. This is explained by the fact that Ti II is less sensitive to NLTE effects than its neutral state. Thus, following [Jablonka et al. \(2015\)](#), for the purpose of our discussion we adopted the Ti II abundances as the most representative of the titanium content in our stars.

3.5.3. Iron-peak elements

- *Chromium.* Cr I relies on 4 to 5 lines in the red part of the UVES spectra, all of them give consistent results from

⁴ <http://kurucz.harvard.edu/linelists.html>

Table 4: Derived abundances for the Fornax stars observed with UVES, and the Carina stars observed with XSHOOTER along with their associated errors (see § 3).

	Fe I	Fe II	C	O I	Na I	Mg I	Al I	Si I	Ca I	Sc II	Ti I	Ti II	Cr I	Mn I	Co I	Ni I	Cu I	Zn I	Sr II	Y II	Zr II	Ba II	La II	Pr II	Nd II	Eu II	Dy II	
$\log \epsilon(X_{\odot})$	7.50	7.50	8.43	8.69	6.24	7.60	6.45	7.51	6.34	3.15	4.95	4.95	5.64	5.43	4.99	6.22	4.19	4.56	2.87	2.21	2.58	2.18	1.10	0.72	1.42	0.52	1.10	
fmx-06_019																												
Nb lines*	67	2	1	1	2	3	1	1	6	6	11	14	4	3	1	3	1	1	1	5	1	4	4	4	1	3	2	3
$\log \epsilon(X)$	4.58	4.67	5.05	6.67	3.54	5.23	3.56	5.62	3.82	0.40	2.01	2.51	2.39	2.09	2.12	3.34	<0.41	1.93	0.74	-0.86	-0.12	-0.43	-1.28	-1.14	-0.89	-1.60	-0.74	
[X/H]	-2.92	-2.83	-3.38	-2.02	-2.70	-2.37	-2.89	-1.89	-2.52	-2.75	-2.94	-2.44	-3.25	-3.34	-2.87	-2.88	<-3.78	-2.63	-2.13	-3.07	-2.70	-2.61	-2.38	-1.86	-2.31	-2.12	-1.84	
[X/Fe]	-0.00	+0.09	-0.46	+0.90	+0.22	+0.55	+0.03	+1.03	+0.40	+0.17	-0.02	+0.48	-0.33	-0.42	+0.05	+0.04	<-0.86	+0.29	+0.79	-0.15	+0.22	+0.31	+0.54	+1.06	+0.61	+0.79	+1.08	
Error	0.10	0.10	0.12	0.12	0.10	0.11	0.12	0.12	0.10	0.10	0.10	0.12	0.10	0.10	0.16	0.10	-	0.12	0.12	0.10	0.12	0.10	0.10	0.16	0.10	0.10	0.10	
fmx0579x-1																												
Nb lines*	76	4	1	1	2	4	-	1	11	5	10	8	5	3	1	4	1	-	1	2	-	4	-	-	-	-	-	
$\log \epsilon(X)$	4.77	4.97	5.46	6.99	3.50	5.24	-	4.76	3.91	0.64	2.01	2.53	2.62	2.24	2.07	3.39	0.82	-	-0.52	-1.03	-	-1.21	-	-	-	-	-	
[X/H]	-2.73	-2.53	-2.97	-1.70	-2.74	-2.36	-	-2.75	-2.43	-2.51	-2.94	-2.42	-3.02	-3.19	-2.92	-2.83	-3.37	-	-3.39	-3.24	-	-3.39	-	-	-	-	-	
[X/Fe]	+0.00	+0.20	-0.24	+1.03	-0.00	+0.37	-	-0.02	+0.30	+0.22	-0.21	+0.31	-0.29	-0.46	-0.19	-0.10	-0.64	-	-0.66	-0.52	-	-0.66	-	-	-	-	-	
Error	0.10	0.13	0.12	0.12	0.10	0.10	-	0.12	0.10	0.10	0.13	0.13	0.10	0.10	0.12	0.10	0.12	-	0.12	0.15	-	0.10	-	-	-	-	-	
car1_t174																												
Nb lines*	10	2	1	-	1	2	-	-	1	-	-	1	1	1	-	-	-	-	-	-	-	2	-	-	-	-	-	
$\log \epsilon(X)$	4.51	4.64	4.59	-	3.80	4.98	-	-	3.64	-	-	2.08	2.07	1.55	-	-	-	-	-	-	-	-1.99	-	-	-	-	-	
[X/H]	-2.99	-2.86	-3.84	-	-2.44	-2.63	-	-	-2.70	-	-	-2.87	-3.57	-3.88	-	-	-	-	-	-	-	-4.17	-	-	-	-	-	
[X/Fe]	-0.00	+0.14	-0.85	-	+0.55	+0.37	-	+0.29	-	-	+0.12	-0.58	-0.89	-	-	-	-	-	-	-	-	-1.18	-	-	-	-	-	
Error	0.13	0.13	0.17	-	0.17	0.13	-	-	0.17	-	-	0.17	0.17	0.17	-	-	-	-	-	-	-	0.26	-	-	-	-	-	
car1_r194																												
Nb lines*	24	2	1	-	2	2	-	-	2	-	3	3	1	-	-	1	-	-	1	-	-	2	-	-	-	-	-	
$\log \epsilon(X)$	4.92	5.10	4.90	-	4.12	5.26	-	-	4.10	-	2.63	2.62	2.85	-	-	3.61	-	-	0.33	-	-	0.03	-	-	-	-	-	
[X/H]	-2.58	-2.40	-3.53	-	-2.12	-2.34	-	-	-2.24	-	-2.32	-2.33	-2.79	-	-	-2.61	-	-	-2.54	-	-	-2.15	-	-	-	-	-	
[X/Fe]	-0.00	+0.18	-0.95	-	+0.47	+0.24	-	+0.34	-	+0.26	+0.25	-0.21	-	-	-	-0.03	-	-	+0.04	-	-	+0.43	-	-	-	-	-	
Error	0.10	0.16	0.16	-	0.11	0.11	-	-	0.27	-	0.10	0.18	0.16	-	-	0.16	-	-	0.16	-	-	0.11	-	-	-	-	-	
car1_r200																												
Nb lines*	12	-	1	-	2	2	-	-	-	-	-	2	1	1	-	-	-	-	1	-	-	2	-	-	-	-	-	
$\log \epsilon(X)$	4.60	-	5.06	-	4.43	5.08	-	-	-	-	-	2.49	2.41	2.16	-	-	-	-	-0.53	-	-	-0.60	-	-	-	-	-	
[X/H]	-2.90	-	-3.37	-	-1.80	-2.52	-	-	-	-	-2.46	-3.23	-2.79	-	-	-3.40	-	-	-3.40	-	-	-2.78	-	-	-	-	-	
[X/Fe]	+0.00	-	-0.47	-	+1.10	+0.38	-	-	-	-	+0.44	-0.33	-0.37	-	-	-	-	-	-0.50	-	-	+0.12	-	-	-	-	-	
Error	0.21	-	0.21	-	0.21	0.21	-	-	-	-	-	0.49	0.21	0.21	-	-	-	-	0.21	-	-	0.27	-	-	-	-	-	
LG04c_0008																												
Nb lines*	35	6	1	-	2	2	-	-	1	-	-	2	1	1	2	1	-	-	1	-	-	2	-	-	-	-	-	
$\log \epsilon(X)$	4.47	4.53	4.22	-	3.89	4.91	-	-	3.55	-	2.25	1.83	1.90	1.78	1.78	3.17	-	-	-1.06	-	-	-2.02	-	-	-	-	-	
[X/H]	-3.03	-2.97	-4.21	-	-2.35	-2.69	-	-	-2.79	-	-2.70	-3.81	-3.53	-3.21	-3.05	-3.93	-	-	-3.93	-	-	-4.20	-	-	-	-	-	
[X/Fe]	-0.00	+0.06	-1.18	-	+0.68	+0.34	-	+0.24	-	-	+0.33	-0.78	-0.50	-0.18	-0.02	-0.02	-	-	-0.90	-	-	-1.17	-	-	-	-	-	
Error	0.17	0.21	0.17	-	0.17	0.17	-	-	0.17	-	0.23	0.17	0.17	0.17	0.17	0.17	-	-	0.17	-	-	0.22	-	-	-	-	-	

Notes. * Number of lines kept after a careful selection of the best fitted or synthesized lines.

Table 5: Changes in the mean abundances $\Delta[X/H]$ caused by a ± 100 K change in T_{eff} , a ± 0.15 dex change in $\log(g)$ and a ± 0.15 km s $^{-1}$ change on v_t for star fnx-06_019.

El.	$\delta \log \epsilon(X)$					
	$+\Delta T_{\text{eff}}$	$-\Delta T_{\text{eff}}$	$+\Delta \log g$	$-\Delta \log g$	$+\Delta v_t$	$-\Delta v_t$
	fnx-06_019 (4280 0.68 1.8 -2.92)					
Fe I	+0.14	-0.15	+0.00	+0.00	-0.03	+0.03
Fe II	-0.02	+0.04	+0.05	-0.05	+0.02	+0.02
C I	+0.13	-0.08	+0.00	+0.01	+0.00	+0.00
O I	+0.06	-0.03	+0.06	-0.05	+0.01	+0.01
Mg I	+0.09	-0.10	-0.02	+0.02	+0.04	+0.04
Ca I	+0.11	-0.13	-0.02	+0.01	-0.03	+0.02
Sc II	+0.03	-0.01	+0.05	-0.05	+0.03	+0.03
Ti I	+0.27	-0.26	+0.02	-0.03	+0.03	+0.03
Ti II	+0.02	+0.00	+0.05	-0.04	+0.05	+0.05
Cr I	+0.20	-0.20	+0.00	+0.00	-0.02	+0.02
Co I	+0.22	-0.18	+0.01	-0.02	-0.13	+0.15
Ni I	+0.18	-0.16	+0.01	+0.00	+0.03	+0.03
Sr II	+0.00	+0.00	+0.00	+0.00	+0.00	+0.00
Y II	+0.05	-0.02	+0.05	-0.05	+0.02	+0.02
Ba II	+0.06	-0.04	+0.06	-0.05	-0.05	+0.07

their EW. Five extra lines are detected (4254.352 4274.812 4289.73 5206.023 and 5208.409 Å) but they are stronger (>110 mÅ) or more affected by the noise, so they were rejected. In the X-shooter spectra only the strongest $\lambda 5206.023$ and 5208.409 Å lines were accessible, Cr I abundances were obtained from a single spectral synthesis in a 20 Å wavelength range covering the two lines and taking into account the blends at this resolution.

- *Manganese*. Mn I abundance relies on the three 4030.75 Å 4033.06 Å and 4034.48 Å lines, there were synthesized taking into account their HFS components and give consistent abundance results. Mn 4041.35 Å and 4823.52 Å are weak (~ 30 mÅ) and too much affected by the noise and were discarded. In the case of X-shooter spectra, a single spectral synthesis have been done in a 20 Å window centered on the Mn triplet.

3.5.4. Neutron-capture elements

- *Strontium*. Sr II
- *Barium*. Ba II

Additional neutron-capture elements were measurable in the spectrum of the star fnx_06_019 in Fornax (Fig B.1) :

- *Lanthanum*. The La II abundance was determined from the $\lambda 4920.98$ Å line which is the most red La II line and the less affected by the noise. The detection was confirmed by computing synthetic spectra for the 4077.34, 4086.71, and 4123.23 Å lines using the abundance derived from the 4920.98 Å line.
- *Neodymium*. The Nd II abundance was determined from the 2 clean and unblended 4825.48 and 5319.81 Å lines, and further confirmed with the 4109.45 and 4061.08 Å lines.
- *Dysprosium*. The abundance is measured from the 4103.31 Å line by spectral synthesis, the 3944.68 Å line is too affected by the noise and a continuum level uncertainty, while the 4449.7 Å line is strongly blended

4. Results

4.1. Carbon

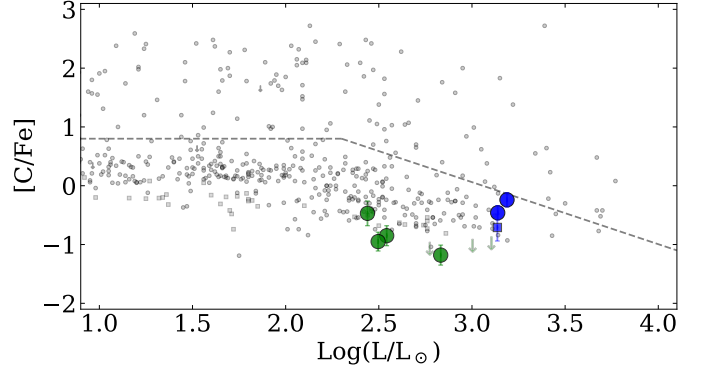


Fig. 3: $[C/Fe]$ as a function of $\log(L/L_{\odot})$ for the Fornax (blue) and Carina (green) members analyzed in this work. Gray stands for the MW halo stars from Placco et al. (2014); Gratton et al. (2000). The blue square is the Fornax member from Tafelmeyer et al. (2010). The green upper limits are from the Carina sample of Venn et al. (2012). The dotted line show trace the criterion of Aoki et al. (2007a) to define carbon enhanced stars, which takes into account the depletion of carbon along the RGB.

4.2. α elements

4.3. light elements: sodium

4.4. Iron-peak elements

Figure 6 presents the variation of Sc, Co, Cr, Ni, Mn and Zn with iron in Carina and Fornax, and the comparison with the Milky Way halo and disc population. Sc could only be determined in the two Fornax stars of our sample. The production of Sc is dominated by SNeII (Woosley et al. 2002; Battistini & Bensby 2015) and therefore, as expected, $[Sc/Fe]$ is at the same level as the α -elements seen in Fig. 4.

Nickel can be produced in core-collapse, as well as in thermonuclear supernovae (e.g., Jerkstrand 2018). Letarte et al. (2010) had noticed a subsolar mean value of the Fornax population at $[Fe/H] > -1.2$ and (Lemasle et al. 2014) pushed back the metallicity origin of the trend at > -1.5 . Looking closely at the results of Norris et al. (2017), Carina also seems to have a decline of $[Ni/Fe]$ beyond $[Fe/H] = -1.5$. While it is not yet possible to strictly identify when this subsolar trend appears, it clearly corresponds to a stage of the galaxy chemical evolution when the ejecta of SNeIa dominate the composition of the interstellar medium. This is also seen in Sextans. Theler et al. (2020) found subsolar $[Ni/Fe]$ starting at $[Fe/H] = -2$, concomitantly with the $[\alpha/Fe]$ knee. The star formation history of Fornax and even more so Carina being more extended than that of Sextans, it is likely that their $[Ni/Fe]$ ratios will decrease at higher metallicity. Before SNeIa dominate, our sample definitely set the level of $[Fe/H]$ at solar value for both Carina and Fornax, implying that the global production of nickel follows that of iron in core-collapse supernovae.

For both Fornax and Carina Co, Cr, Mn and Zn closely follow the Milky Way trends at $[Fe/H] < -2.5$ as derived from 1D LTE methods. NLTE calculations for the neutral species of these three elements conclude to an overionization, leading to weak-

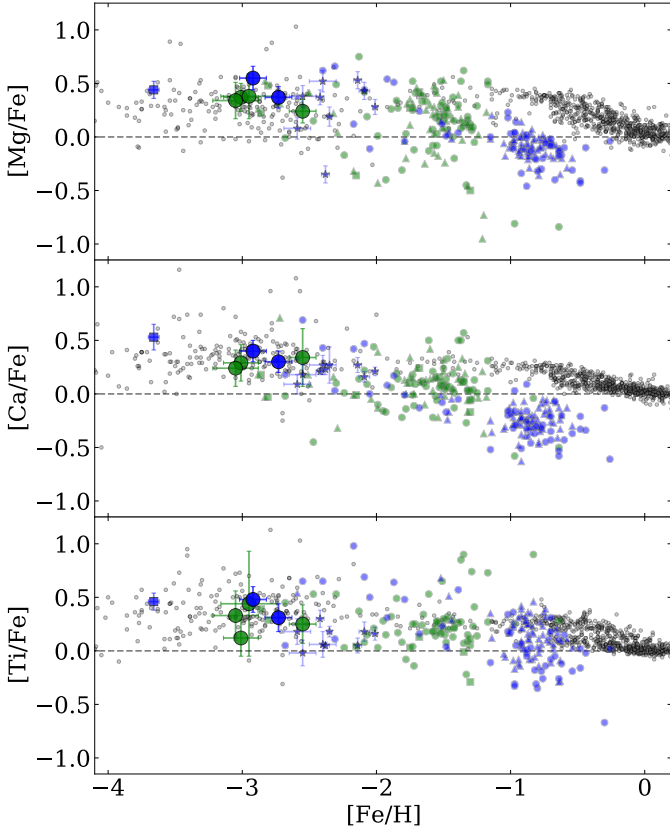


Fig. 4: Abundance ratios for the α elements Mg, Ca, and Ti (from top to bottom) as a function of $[\text{Fe}/\text{H}]$. Fornax members are in blue : large circles are the two stars analyzed in this paper, small circles are from [Lemasle et al. \(2014\)](#), small triangles are from [Letarte et al. \(2010\)](#), small star symbols are members of Fornax globular clusters 1,2 and 3 from [Letarte et al. \(2006\)](#). The EMP at $[\text{Fe}/\text{H}] = -3.66$ is from [Tafelmeyer et al. \(2010\)](#). Carina members are in green : large circles are the four stars analyzed in this paper, small circles are from [Norris et al. \(2017\)](#), small triangles are from [Lemasle et al. \(2012\)](#), small squares are from [Venn et al. \(2012\)](#). Gray dots are literature data for MW stars ([Bensby et al. 2014](#); [Yong et al. 2013](#))

ened lines and positive NLTE abundance corrections ([Bergemann & Gehren 2008](#); [Bergemann et al. 2010](#)). In contrast, the NLTE corrections of Zn ([Takeda et al. 2005](#)) are small in metal-poor regime and not fully suppressing the rise of $[\text{Zn}/\text{Fe}]$ with decreasing metallicity. Fnx-06019 for which we could measure Zn falls on the MW halo trend at $[\text{Zn}/\text{Fe}] = +0.29$ at the level of the $[\alpha/\text{Fe}]$ plateau. This was also observed in two Sextans EMPS ([Lucchesi et al. 2020](#)) and in Sculptor ([Skúladóttir et al. 2017](#)), highlighting the role of core collapse supernovae in the production of zinc in the early stage of galaxy evolution.

4.5. Neutron-capture elements

Definition of r-II : $[\text{Eu}/\text{Fe}] > +1$; $[\text{Ba}/\text{Eu}] < 0$; r-I : $+0.3 \leq [\text{Eu}/\text{Fe}] < +1.0$, $[\text{Ba}/\text{Eu}] < 0$ [Hansen et al. \(2018\)](#)

From the survey carried out by [Barklem et al. \(2005\)](#), (2005), the expected frequencies of r-II and r-I stars in the halo system are $\sim 3\%$ and $\sim 15\%$, respectively. The first determination of the actinide Th abundance for a red giant star, UMi 19/COS

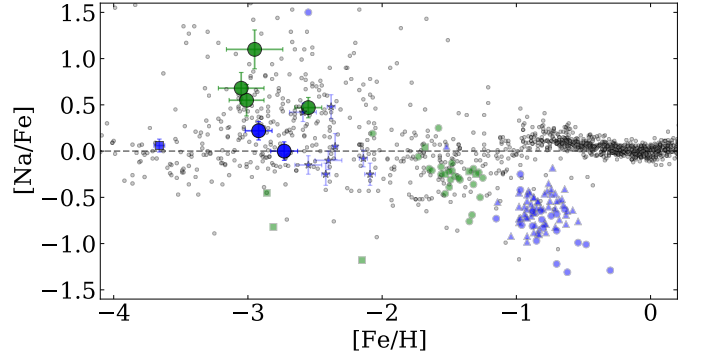


Fig. 5: Sodium-to-iron ratio as a function of $[\text{Fe}/\text{H}]$ are shown for stars in Fornax, Carina, and MW. The symbols are the same as in Fig. 4.

82 ($[\text{Fe}/\text{H}] \sim -1.4$; $[\text{Eu}/\text{Fe}] = 1.49$) , in the Ursa Minor dwarf galaxy ([Shetrone et al. 2001](#); [Aoki et al. 2007b](#))

Five more r-I stars in Ursa Minor between $[\text{Fe}/\text{H}] = -2.43$ and -1.76

Two stars (Draco 3150 & 21456, $[\text{Fe}/\text{H}] = -1.84$ and -2.39) in Draco ([Cohen & Huang 2009](#))

In Fornax, three r-II stars [Reichert et al. \(2021\)](#) The Fornax late (~ 4 Gyr ago) burst of star formation agrees well with the age of the r-process enhanced stars. According to [Lemasle et al. \(2014\)](#), Fnx-mem0556 has an age of 4.36 ± 0.86 Gyr and Fnx-mem0595 an age of 5.75 ± 1.78 Gyr. ([Letarte et al. 2010](#)): about 10 r-I stars but at $[\text{Fe}/\text{H}] > -1.5$

In UFDs: Tucana III ([Hansen et al. 2017](#)) *DES J235532.66 – 593114.9* $[\text{Fe}/\text{H}] = -2.25$, shows a mild enhancement in neutron-capture elements associated with the r-process and can be classified as an r-I star. *DES J235532* is the first r-I star to be discovered in an ultra-faint satellite, and Tuc III is the second extremely low-luminosity system found to contain r- process enriched material, after Reticulum II.

The r-I stars discovered in dwarf galaxies so far seem to cover the more metal-rich end of the metallicity distribution of halo r-I stars

See also ([Reichert et al. 2020](#)) [Wanajo et al. \(2021\)](#) [Jeon et al. \(2021\)](#)

5. Summary

- This follow-up of EMP candidates in the Fornax and Carina dSphs has made it possible to populate the yet uncovered $-3.1 \leq [\text{Fe}/\text{H}] \leq -2.5$ metallicity range in Fornax and to identify the first EMPS in Carina.
- It is now clear that regardless of the subsequent evolution of the local classical dwarf galaxies, which harbor very different star formation histories, the first generations of stars took place in very similar way in these systems. Almost all chemical elements follow the same trend with (low) metallicity, and match the known relations for our Galaxy.
- At the exception of the neutron-capture elements, the abundance ratios reveal an homogeneous interstellar medium very early in the evolution of the galaxies.
- We report the discovery of a Eu-rich, r-I star in Fornax (fnx-06_019, $[\text{Eu}/\text{Ba}] = 0.48$). It shows an outstanding enrichment in La II, Nd II and Dy II. This is first such case at this low metallicity ($[\text{Fe}/\text{H}] = -2.92$) in a classical dwarf galaxy, So far the majority of the halo stars had indeed been found

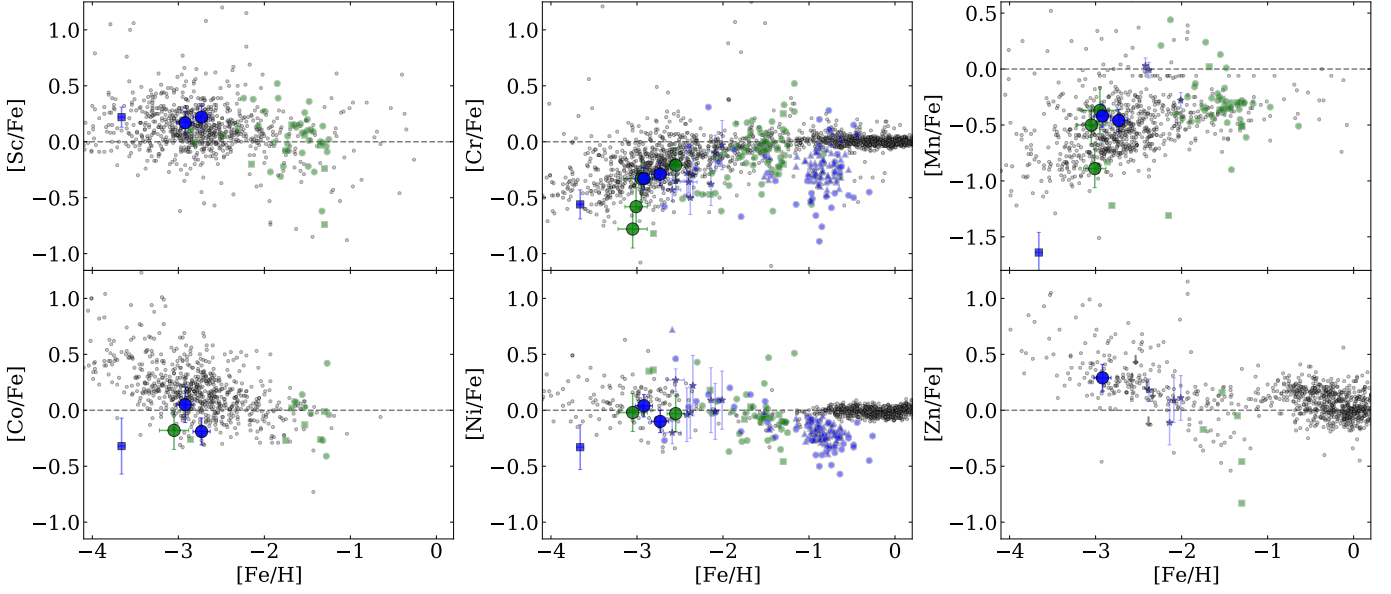


Fig. 6: From left to right, top to bottom: $[\text{Sc}/\text{Fe}]$, $[\text{Cr}/\text{Fe}]$, $[\text{Mn}/\text{Fe}]$, $[\text{Co}/\text{Fe}]$, $[\text{Ni}/\text{Fe}]$, and $[\text{Zn}/\text{Fe}]$ for metal-poor stars in Fornax, Carina, and MW. The symbols are the same as in Fig. 4. The stars studied in this paper are the large circles. MW data are from Venn et al. (2004); Frebel et al. (2010); Bensby et al. (2014).

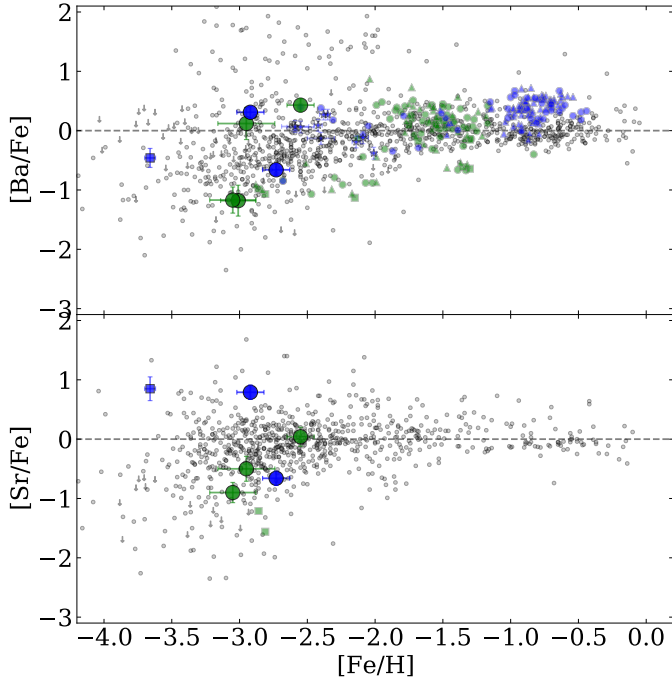


Fig. 7: Neutron-capture elements: Barium-to-iron ratio at the top and strontium-to-iron ratio at the bottom, as a function of $[\text{Fe}/\text{H}]$ in Fornax (blue) and Carina (green), compared to MW stars in gray from Roederer (2013). The symbols are the same as in Fig. 4, large circles represent the new sample analyzed here.

more metal-poor than the r-I stars identified in dwarf galaxies.

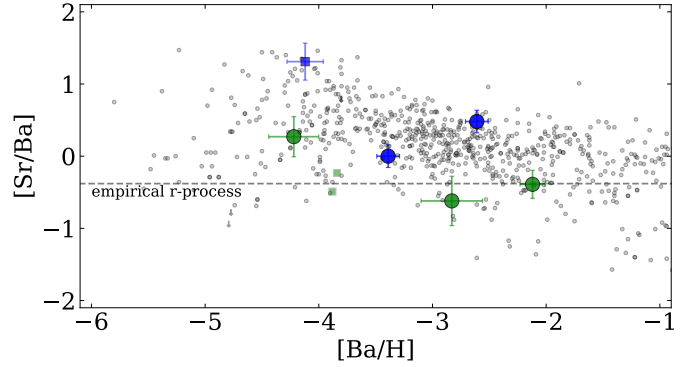


Fig. 8: Barium-to-strontium ratio as a function of $[\text{Ba}/\text{H}]$. References are the same as in Figure 7. The empirical r-process limit is shown with dashed line (Mashonkina et al. 2017b).

References

- Alonso, A., Arribas, S., & Martínez-Roger, C. 1999, *A&AS*, 140, 261
- Alvarez, R. & Plez, B. 1998, *A&A*, 330, 1109
- Aoki, W., Arimoto, N., Sadakane, K., et al. 2009, *A&A*, 502, 569
- Aoki, W., Beers, T. C., Christlieb, N., et al. 2007a, *ApJ*, 655, 492
- Aoki, W., Honda, S., Sadakane, K., & Arimoto, N. 2007b, *PASJ*, 59, L15
- Asplund, M., Grevesse, N., Sauval, A. J., & Scott, P. 2009, *ARA&A*, 47, 481
- Barklem, P. S., Christlieb, N., Beers, T. C., et al. 2005, *A&A*, 439, 129
- Battaglia, G., Tolstoy, E., Helmi, A., et al. 2011, *VizieR Online Data Catalog*, 741
- Battaglia, G., Tolstoy, E., Helmi, A., et al. 2006, *A&A*, 459, 423
- Battistini, C. & Bensby, T. 2015, *A&A*, 577, A9
- Bensby, T., Feltzing, S., & Oey, M. S. 2014, *A&A*, 562, A71
- Bergemann, M. & Gehren, T. 2008, *A&A*, 492, 823
- Bergemann, M., Pickering, J. C., & Gehren, T. 2010, *MNRAS*, 401, 1334
- Cardelli, J. A., Clayton, G. C., & Mathis, J. S. 1989, *ApJ*, 345, 245
- Cohen, J. G. & Huang, W. 2009, *ApJ*, 701, 1053
- de Boer, T. J. L., Tolstoy, E., Hill, V., et al. 2012, *A&A*, 544, A73
- de Boer, T. J. L., Tolstoy, E., Lemasle, B., et al. 2014, *A&A*, 572, A10
- de Boer, T. J. L., Tolstoy, E., Saha, A., et al. 2011, *A&A*, 528, A119
- Dekker, H., D'Odorico, S., Kaufer, A., Delabre, B., & Kotzlowski, H. 2000, in *Society of Photo-Optical Instrumentation Engineers (SPIE) Conference Series*, Vol. 4008, Proc. SPIE, ed. M. Iye & A. F. Moorwood, 534–545

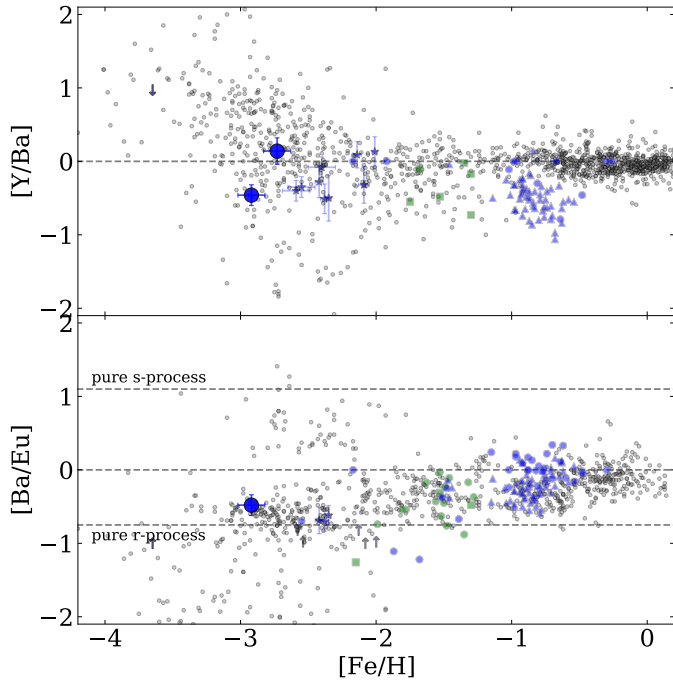


Fig. 9: Yttrium-to-Barium ratio (top) and barium-to-europium ratio (bottom) as a function of $[\text{Fe}/\text{H}]$. The symbols are the same as in Fig. 4. MW stars are from Yong et al. (2013); Venn et al. (2004); Frebel et al. (2010).

Plez, B. 2012, Turbospectrum: Code for spectral synthesis, Astrophysics Source Code Library
 Prochaska, J. X. & McWilliam, A. 2000, *ApJ*, 537, L57
 Ramírez, I. & Meléndez, J. 2005, *ApJ*, 626, 465
 Reichert, M., Hansen, C. J., & Arcones, A. 2021, *ApJ*, 912, 157
 Reichert, M., Hansen, C. J., Hanke, M., et al. 2020, *A&A*, 641, A127
 Roederer, I. U. 2013, *AJ*, 145, 26
 Roederer, I. U., Mateo, M., Bailey, John I., I., et al. 2016, *AJ*, 151, 82
 Ryabchikova, T. A., Piskunov, N. E., Kupka, F., & Weiss, W. W. 1997, *Baltic Astronomy*, 6, 244
 Shetrone, M. D., Côté, P., & Sargent, W. L. W. 2001, *ApJ*, 548, 592
 Simon, J. D., Jacobson, H. R., Frebel, A., et al. 2015, *ApJ*, 802, 93
 Skúladóttir, Á., Tolstoy, E., Salvadori, S., Hill, V., & Pettini, M. 2017, *A&A*, 606, A71
 Starkenburg, E., Hill, V., Tolstoy, E., et al. 2013, *A&A*, 549, A88
 Starkenburg, E., Hill, V., Tolstoy, E., et al. 2010, *A&A*, 513, A34
 Stetson, P. B. & Pancino, E. 2008, *PASP*, 120, 1332
 Susmitha, A., Koch, A., & Sivarani, T. 2017, *A&A*, 606, A112
 Tafelmeyer, M., Jablonka, P., Hill, V., et al. 2010, *A&A*, 524, A58
 Takeda, Y., Hashimoto, O., Taguchi, H., et al. 2005, *PASJ*, 57, 751
 Theler, R., Jablonka, P., Lucchesi, R., et al. 2020, *A&A*, 642, A176
 Tolstoy, E., Hill, V., & Tosi, M. 2009, *ARA&A*, 47, 371
 Van der Swaelmen, M., Hill, V., Primas, F., & Cole, A. A. 2013, *A&A*, 560, A44
 Venn, K. A., Irwin, M., Shetrone, M. D., et al. 2004, *AJ*, 128, 1177
 Venn, K. A., Shetrone, M. D., Irwin, M. J., et al. 2012, *ApJ*, 751, 102
 Vernet, J., Dekker, H., D'Odorico, S., et al. 2011, *A&A*, 536, A105
 Wanajo, S., Hirai, Y., & Prantzos, N. 2021, arXiv e-prints, arXiv:2106.03707
 Wanajo, S., Sekiguchi, Y., Nishimura, N., et al. 2014, *ApJ*, 789, L39
 Winteler, C., Käppeli, R., Perego, A., et al. 2012, *ApJ*, 750, L22
 Woosley, S. E., Heger, A., & Weaver, T. A. 2002, *Reviews of Modern Physics*, 74, 1015
 Yong, D., Norris, J. E., Bessell, M. S., et al. 2013, *ApJ*, 762, 26

Ezzeddine, R., Frebel, A., & Plez, B. 2017, *ApJ*, 847, 142
 Frebel, A., Kirby, E. N., & Simon, J. D. 2010, *Nature*, 464, 72
 Gratton, R. G., Sneden, C., Carretta, E., & Bragaglia, A. 2000, *A&A*, 354, 169
 Gustafsson, B., Edvardsson, B., Eriksson, K., et al. 2008, *A&A*, 486, 951
 Hansen, T. T., Holmbeck, E. M., Beers, T. C., et al. 2018, *ApJ*, 858, 92
 Hansen, T. T., Simon, J. D., Marshall, J. L., et al. 2017, *The Astrophysical Journal*, 838, 44
 Hodge, P. W. 1961, *AJ*, 66, 83
 Jablonka, P., North, P., Mashonkina, L., et al. 2015, *A&A*, 583, A67
 Jeon, M., Besla, G., & Bromm, V. 2021, *MNRAS*[arXiv:2106.13383]
 Jerkstrand, A. 2018, in American Institute of Physics Conference Series, Vol. 1947, 14th International Symposium on Origin of Matter and Evolution of Galaxies (OMEG 2017), 020013
 Ji, A. P., Frebel, A., Chiti, A., & Simon, J. D. 2016, *Nature*, 531, 610
 Ji, A. P., Simon, J. D., Frebel, A., Venn, K. A., & Hansen, T. T. 2019, *ApJ*, 870, 83
 Kirby, E. N. & Cohen, J. G. 2012, *AJ*, 144, 168
 Koch, A., Grebel, E. K., Wyse, R. F. G., et al. 2006, *AJ*, 131, 895
 Kupka, F., Piskunov, N., Ryabchikova, T. A., Stempels, H. C., & Weiss, W. W. 1999, *A&AS*, 138, 119
 Kupka, F. G., Ryabchikova, T. A., Piskunov, N. E., Stempels, H. C., & Weiss, W. W. 2000, *Baltic Astronomy*, 9, 590
 Lee, M. G., Yuk, I.-S., Park, H. S., Harris, J., & Zaritsky, D. 2009, *ApJ*, 703, 692
 Lemasle, B., de Boer, T. J. L., Hill, V., et al. 2014, *A&A*, 572, A88
 Lemasle, B., Hill, V., Tolstoy, E., et al. 2012, *A&A*, 538, A100
 Letarte, B., Hill, V., Jablonka, P., et al. 2006, *A&A*, 453, 547
 Letarte, B., Hill, V., Tolstoy, E., et al. 2010, *A&A*, 523, A17
 Lucchesi, R., Lardo, C., Primas, F., et al. 2020, *A&A*, 644, A75
 Magain, P. 1984, *A&A*, 134, 189
 Marshall, J. L., Hansen, T., Simon, J. D., et al. 2019, *ApJ*, 882, 177
 Mashonkina, L., Jablonka, P., Pakhomov, Y., Sitnova, T., & North, P. 2017a, *A&A*, 604, A129
 Mashonkina, L., Jablonka, P., Sitnova, T., Pakhomov, Y., & North, P. 2017b, *A&A*, 608, A89
 Norris, J. E., Yong, D., Venn, K. A., et al. 2017, *ApJS*, 230, 28
 North, P., Cescutti, G., Jablonka, P., et al. 2012, *A&A*, 541, A45
 Pace, A. B., Walker, M. G., Koposov, S. E., et al. 2021, arXiv.org [2105.00064v1]
 Piskunov, N. E., Kupka, F., Ryabchikova, T. A., Weiss, W. W., & Jeffery, C. S. 1995, *A&AS*, 112, 525
 Placco, V. M., Frebel, A., Beers, T. C., & Stancliffe, R. J. 2014, *ApJ*, 797, 21

Appendix A: Additional tables

Table A.1: Lines measured in the Fornax UVES spectra. Line parameters, observed EWs, and elemental abundances are provided. EWs in brackets are given as indication only; the quoted abundances are derived through spectral synthesis for these lines.

El.	λ [Å]	χ_{ex} [eV]	$\log(gf)$	EW [mÅ] fnx_06–19	$\log\epsilon(X)$	EW [mÅ] fnx0579x–1	$\log\epsilon(X)$
Al I	3961.52	0.01	–0.323	(162.4)	3.56	–	–
Ba II	4934.076	0.0	–0.150	(192.8)	–0.39	(93.2)	–1.35
Ba II	5853.668	0.6	–1.000	(70.4)	–0.65	(35.9)	–1.17
Ba II	6141.713	0.7	–0.076	(126.8)	–0.45	(83.9)	–1.23
Ba II	6496.897	0.6	–0.377	(136.7)	–0.22	(81.5)	–1.10
C I	4325.0	–	–	–	5.05	–	5.46
Ca I	5581.965	2.52	–0.555	–	–	25.2 ± 3.6	3.86
Ca I	5588.749	2.53	0.358	–	–	67.7 ± 6.1	3.73
Ca I	5590.114	2.52	–0.571	–	–	31.9 ± 3.8	4.02
Ca I	5601.277	2.53	–0.523	–	–	27.8 ± 4.3	3.89
Ca I	5857.451	2.93	0.240	33.6 ± 4.2	3.80	41.0 ± 5.0	3.90
Ca I	6102.723	1.88	–0.793	55.4 ± 5.6	3.78	71.1 ± 6.3	3.97
Ca I	6122.217	1.89	–0.316	88.3 ± 7.4	3.81	98.8 ± 9.1	3.93
Ca I	6162.173	1.9	–0.090	105.6 ± 7.5	3.87	–	–
Ca I	6169.042	2.52	–0.797	–	–	20.6 ± 3.9	3.95
Ca I	6169.563	2.53	–0.478	27.4 ± 3.6	3.84	31.4 ± 3.4	3.87
Ca I	6439.075	2.53	0.390	79.3 ± 8.4	3.82	88.5 ± 7.6	3.93
Ca I	6717.681	2.71	–0.524	–	–	21.6 ± 4.4	3.91
Co I	4121.318	0.92	–0.320	105.6 ± 6.3	2.12	(130.5)	2.07
Cr I	5296.691	0.98	–1.360	36.9 ± 4.7	2.51	48.9 ± 5.6	2.62
Cr I	5298.271	0.98	–1.140	–	–	63.6 ± 6.3	2.63
Cr I	5345.796	1.0	–0.896	56.2 ± 6.0	2.39	72.5 ± 5.4	2.55
Cr I	5348.314	1.0	–1.210	34.4 ± 4.8	2.34	59.6 ± 4.5	2.66
Cr I	5409.784	1.03	–0.670	64.2 ± 5.7	2.31	90.3 ± 8.4	2.64
Cu I	5105.537	1.39	–1.542	–	< 0.41	(20.7)	0.82
Dy II	3944.68	0.0	0.000	–	–0.74	–	–
Dy II	4103.31	0.0	0.000	–	–0.74	–	–
Dy II	4449.7	0.0	0.000	–	–0.74	–	–
Eu II	4129.708	0.0	0.220	(84.6)	–1.56	–	–
Eu II	4205.042	0.0	0.210	(143.7)	–1.65	–	–
Fe I	4859.741	2.88	–0.764	73.9 ± 6.3	4.50	79.6 ± 7.8	4.58
Fe I	4871.318	2.87	–0.363	100.4 ± 9.8	4.60	–	–
Fe I	4872.138	2.88	–0.567	87.0 ± 8.3	4.56	106.4 ± 9.9	4.93
Fe I	4890.755	2.88	–0.394	101.7 ± 8.3	4.66	104.8 ± 9.7	4.71
Fe I	4891.492	2.85	–0.112	104.7 ± 11.2	4.41	–	–
Fe I	4903.31	2.88	–0.926	78.8 ± 8.4	4.75	85.1 ± 8.8	4.85
Fe I	4924.77	2.28	–2.241	53.1 ± 6.1	4.77	67.3 ± 8.2	4.97
Fe I	4938.814	2.88	–1.077	58.4 ± 7.7	4.51	73.9 ± 8.5	4.76
Fe I	4966.088	3.33	–0.871	45.0 ± 5.5	4.68	58.5 ± 8.2	4.89
Fe I	5001.863	3.88	0.010	41.9 ± 4.7	4.47	49.7 ± 5.2	4.58
Fe I	5006.119	2.83	–0.638	90.2 ± 10.5	4.59	–	–
Fe I	5014.942	3.94	–0.303	38.9 ± 4.5	4.80	35.8 ± 7.0	4.71
Fe I	5044.211	2.85	–2.038	–	–	32.1 ± 5.9	4.90
Fe I	5049.82	2.28	–1.355	93.8 ± 9.4	4.59	101.9 ± 11.0	4.72
Fe I	5068.766	2.94	–1.042	46.3 ± 4.7	4.33	73.7 ± 7.9	4.78
Fe I	5074.748	4.22	–0.200	–	–	24.7 ± 3.5	4.72
Fe I	5079.223	2.2	–2.067	73.5 ± 6.5	4.81	86.1 ± 7.8	5.00
Fe I	5131.468	2.22	–2.515	37.2 ± 4.7	4.67	50.7 ± 5.0	4.84
Fe I	5141.739	2.42	–1.964	38.3 ± 4.8	4.41	48.1 ± 4.7	4.52
Fe I	5145.094	2.2	–2.876	–	–	20.7 ± 3.9	4.57
Fe I	5162.272	4.18	0.020	30.4 ± 4.0	4.60	40.9 ± 4.5	4.78
Fe I	5191.455	3.04	–0.551	78.1 ± 8.0	4.52	89.6 ± 8.5	4.71
Fe I	5192.344	3.0	–0.421	86.1 ± 7.9	4.48	102.5 ± 9.0	4.77
Fe I	5198.711	2.22	–2.135	57.4 ± 6.1	4.62	70.3 ± 5.8	4.78
Fe I	5202.336	2.18	–1.838	83.4 ± 6.7	4.70	–	–
Fe I	5215.18	3.27	–0.871	44.0 ± 4.1	4.54	–	–
Fe I	5216.274	1.61	–2.150	99.9 ± 11.6	4.50	–	–
Fe I	5217.389	3.21	–1.070	33.4 ± 4.8	4.47	56.4 ± 5.4	4.84
Fe I	5242.491	3.63	–0.967	–	–	27.8 ± 6.1	4.77
Fe I	5266.555	3.0	–0.386	–	–	101.9 ± 10.5	4.70
Fe I	5281.79	3.04	–0.834	50.8 ± 8.7	4.31	69.0 ± 7.0	4.58
Fe I	5283.621	3.24	–0.432	69.2 ± 8.0	4.50	87.4 ± 9.4	4.81
Fe I	5302.3	3.28	–0.720	45.9 ± 5.4	4.44	60.3 ± 7.3	4.65
Fe I	5307.361	1.61	–2.987	65.1 ± 5.9	4.72	77.3 ± 6.1	4.86
Fe I	5322.041	2.28	–2.803	20.3 ± 3.9	4.65	26.1 ± 4.4	4.72
Fe I	5324.179	3.21	–0.103	87.6 ± 7.2	4.46	97.5 ± 9.5	4.62
Fe I	5332.899	1.56	–2.777	78.8 ± 8.9	4.66	92.5 ± 7.4	4.84
Fe I	5339.929	3.27	–0.647	53.0 ± 5.9	4.46	70.4 ± 7.8	4.73
Fe I	5364.871	4.45	0.228	–	–	32.1 ± 3.3	4.73
Fe I	5365.399	3.57	–1.020	–	–	21.9 ± 4.5	4.59
Fe I	5367.466	4.41	0.443	–	–	41.8 ± 6.1	4.67

El.	λ [Å]	χ_{ex} [eV]	$\log(gf)$	EW [mÅ] fnx_06–19	$\log\epsilon(X)$	EW [mÅ] fnx0579x–1	$\log\epsilon(X)$
Fe I	5369.961	4.37	0.536	37.6 ± 5.0	4.46	43.9 ± 4.3	4.55
Fe I	5383.369	4.31	0.645	41.3 ± 4.0	4.35	58.3 ± 7.8	4.63
Fe I	5393.167	3.24	–0.715	51.1 ± 5.3	4.46	67.1 ± 5.8	4.69
Fe I	5410.91	4.47	0.398	27.2 ± 4.2	4.52	33.8 ± 3.9	4.63
Fe I	5415.199	4.39	0.642	45.1 ± 5.3	4.51	54.2 ± 5.6	4.65
Fe I	5424.068	4.32	0.520	45.1 ± 5.1	4.55	56.0 ± 6.7	4.72
Fe I	5445.042	4.39	–0.020	20.0 ± 2.7	4.64	30.3 ± 3.2	4.86
Fe I	5569.618	3.42	–0.486	52.9 ± 4.8	4.47	–	–
Fe I	5572.842	3.4	–0.275	68.0 ± 7.0	4.49	80.7 ± 7.6	4.68
Fe I	5586.755	3.37	–0.120	80.4 ± 6.9	4.51	96.9 ± 9.5	4.78
Fe I	5615.644	3.33	0.050	101.2 ± 8.8	4.65	106.0 ± 8.9	4.72
Fe I	5701.544	2.56	–2.216	29.0 ± 3.9	4.61	49.3 ± 4.7	4.91
Fe I	6065.482	2.61	–1.530	67.9 ± 5.9	4.60	84.5 ± 7.6	4.81
Fe I	6136.615	2.45	–1.400	89.7 ± 7.9	4.58	–	–
Fe I	6137.691	2.59	–1.403	72.3 ± 7.0	4.50	95.5 ± 8.6	4.82
Fe I	6151.617	2.18	–3.299	–	–	20.7 ± 3.5	4.87
Fe I	6173.334	2.22	–2.880	21.8 ± 2.1	4.62	32.1 ± 4.0	4.76
Fe I	6191.558	2.43	–1.417	84.1 ± 6.8	4.47	98.8 ± 9.0	4.66
Fe I	6200.312	2.61	–2.437	–	–	26.7 ± 3.7	4.74
Fe I	6213.429	2.22	–2.482	43.5 ± 5.2	4.62	56.0 ± 5.6	4.75
Fe I	6219.28	2.2	–2.433	52.0 ± 4.9	4.67	70.2 ± 6.5	4.88
Fe I	6230.722	2.56	–1.281	98.2 ± 7.6	4.73	–	–
Fe I	6240.646	2.22	–3.233	–	–	25.3 ± 3.9	4.97
Fe I	6246.318	3.6	–0.733	31.3 ± 3.7	4.53	46.2 ± 5.3	4.75
Fe I	6252.555	2.4	–1.687	77.1 ± 6.2	4.58	91.0 ± 9.3	4.75
Fe I	6265.132	2.18	–2.550	43.1 ± 4.7	4.62	62.3 ± 5.5	4.84
Fe I	6297.792	2.22	–2.740	–	–	49.4 ± 8.6	4.90
Fe I	6301.5	3.65	–0.718	–	–	59.5 ± 7.4	5.01
Fe I	6302.494	3.69	–0.973	–	–	22.1 ± 2.2	4.63
Fe I	6322.685	2.59	–2.426	26.7 ± 3.3	4.76	37.8 ± 4.9	4.90
Fe I	6335.33	2.2	–2.177	66.0 ± 6.7	4.61	83.0 ± 7.0	4.80
Fe I	6344.148	2.43	–2.923	–	–	23.0 ± 3.2	4.89
Fe I	6355.028	2.85	–2.350	–	–	22.1 ± 3.7	4.86
Fe I	6393.601	2.43	–1.432	84.5 ± 6.2	4.46	100.0 ± 9.5	4.65
Fe I	6400.0	3.6	–0.290	53.7 ± 10.8	4.46	73.6 ± 13.8	4.73
Fe I	6408.018	3.69	–1.018	–	–	28.1 ± 3.7	4.80
Fe I	6411.648	3.65	–0.595	32.7 ± 3.6	4.47	48.8 ± 6.1	4.71
Fe I	6421.35	2.28	–2.027	75.6 ± 6.8	4.70	95.9 ± 7.5	4.96
Fe I	6430.845	2.18	–2.006	90.5 ± 6.7	4.75	104.1 ± 7.7	4.90
Fe I	6592.913	2.73	–1.473	62.2 ± 5.2	4.56	79.9 ± 7.0	4.77
Fe I	6593.87	2.43	–2.422	33.1 ± 3.7	4.64	45.3 ± 4.2	4.78
Fe I	6609.11	2.56	–2.692	–	–	23.4 ± 2.4	4.82
Fe I	6677.985	2.69	–1.418	80.3 ± 6.5	4.71	104.0 ± 9.9	5.03
Fe I	6750.151	2.42	–2.621	28.6 ± 3.7	4.73	44.4 ± 5.1	4.94
Fe II	5197.567	3.23	–2.100	45.5 ± 4.9	4.68	53.5 ± 7.8	4.88
Fe II	5234.623	3.22	–2.230	–	–	54.6 ± 7.8	5.02
Fe II	5284.103	2.89	–2.990	23.3 ± 4.0	4.66	31.0 ± 5.6	4.86
Fe II	6516.077	2.89	–3.320	–	–	28.5 ± 4.4	5.06
La II	4920.98	0.13	–0.580	(37.6)	–1.28	–	–
La II	3995.75	0.0	0.000	–	–1.28	–	–
La II	4077.34	0.0	0.000	–	–1.28	–	–
La II	4123.23	0.0	0.000	–	–1.28	–	–
Mg I	5172.684	2.71	–0.450	(235.1)	5.17	(134.2)	5.17
Mg I	5183.604	2.72	–0.239	(180.3)	5.27	(163.9)	5.20
Mg I	5528.405	4.35	–0.498	90.4 ± 9.3	5.26	(55.9)	5.25
Mn I	4030.75	0.0	–0.494	(162.2)	2.06	–	–
Mn I	4033.06	0.0	–0.644	(171.8)	2.10	(191.7)	2.27
Mn I	4034.48	0.0	–0.842	(125.0)	2.10	(103.0)	2.27
Mn I	4823.52	2.32	0.121	–	–	45.3 ± 5.9	2.17
Na I	5889.951	0.0	0.108	(208.8)	3.52	(207.0)	3.48
Na I	5895.924	0.0	–0.194	(186.0)	3.57	(186.3)	3.53
Nd II	4825.48	0.18	–0.420	(41.4)	–0.89	–	–
Nd II	5319.81	0.55	–0.140	(28.4)	–0.89	–	–
Nd II	4061.08	0.0	0.000	–	–0.89	–	–
Ni I	5081.11	3.85	0.300	–	–	20.9 ± 4.2	3.39
Ni I	5476.904	1.83	–0.780	101.0 ± 7.6	3.20	107.0 ± 10.1	3.29
Ni I	6643.63	1.68	–2.220	40.2 ± 5.0	3.29	48.7 ± 5.7	3.36
Ni I	6767.772	1.83	–2.140	39.8 ± 3.8	3.40	44.2 ± 4.4	3.41
O I	6300.304	0.0	–9.750	(31.0)	6.67	(31.0)	6.99
Pr II	4222.934	0.05	0.271	60.6 ± 7.3	–1.14	–	–
Sc II	4246.822	0.31	0.242	–	–	(167.7)	0.73
Sc II	4400.389	0.61	–0.536	(94.5)	0.46	–	–
Sc II	4415.557	0.6	–0.668	(88.4)	0.35	(104.4)	0.90
Sc II	5031.021	1.36	–0.400	(49.6)	0.30	(51.4)	0.35
Sc II	5526.79	1.77	0.024	(49.4)	0.39	(58.6)	0.57
Sc II	5657.896	1.51	–0.603	(42.9)	0.51	(51.7)	0.67
Sc II	6604.601	1.36	–1.309	(17.4)	0.40	–	–
Si I	4102.936	1.91	–3.140	(122.7)	5.62	(78.8)	4.76
Sm II	4424.34	0.49	0.140	42.5 ± 6.8	–1.12	–	–
Sr II	4215.519	0.0	–0.145	(170.7)	0.74	(126.4)	–0.52

Table A.2: continued.

El.	λ [Å]	χ_{ex} [eV]	$\log(gf)$	EW [mÅ] fnx_06–19	$\log\epsilon(X)$	EW [mÅ] fnx0579x–1	$\log\epsilon(X)$
Ti I	3989.758	0.02	−0.130	109.3 ± 7.1	2.34	–	–
Ti I	4840.874	0.9	−0.430	–	–	30.4 ± 4.7	2.09
Ti I	4981.73	0.85	0.570	85.8 ± 8.2	2.01	93.8 ± 9.1	2.06
Ti I	4991.066	0.84	0.450	82.1 ± 9.6	2.05	80.0 ± 10.1	1.92
Ti I	4999.503	0.83	0.320	68.9 ± 7.6	1.95	72.0 ± 7.9	1.90
Ti I	5014.276	0.81	0.040	83.0 ± 8.2	2.44	97.8 ± 10.5	2.59
Ti I	5016.161	0.85	−0.480	25.3 ± 3.9	2.04	–	–
Ti I	5039.958	0.02	−1.080	54.5 ± 4.8	1.94	64.6 ± 7.0	1.95
Ti I	5064.653	0.05	−0.940	61.5 ± 6.5	1.94	79.9 ± 8.2	2.07
Ti I	5173.743	0.0	−1.060	64.8 ± 5.9	2.01	69.9 ± 8.1	1.94
Ti I	5192.969	0.02	−0.950	71.3 ± 6.3	2.02	79.0 ± 10.0	1.99
Ti I	5210.384	0.05	−0.820	67.8 ± 6.5	1.88	72.7 ± 11.4	1.81
Ti II	4028.338	1.89	−0.920	73.6 ± 7.6	2.61	–	–
Ti II	4394.059	1.22	−1.770	94.7 ± 6.3	2.90	–	–
Ti II	4395.839	1.24	−1.930	78.1 ± 5.3	2.73	–	–
Ti II	4399.765	1.24	−1.200	90.8 ± 5.5	2.27	–	–
Ti II	4418.331	1.24	−1.990	66.9 ± 7.1	2.53	–	–
Ti II	4450.482	1.08	−1.520	108.5 ± 7.1	2.77	–	–
Ti II	4798.531	1.08	−2.660	43.6 ± 7.3	2.49	–	–
Ti II	5129.156	1.89	−1.340	53.4 ± 6.3	2.39	64.4 ± 7.2	2.63
Ti II	5154.068	1.57	−1.750	61.5 ± 7.0	2.50	62.2 ± 6.3	2.55
Ti II	5185.902	1.89	−1.410	49.2 ± 4.4	2.38	54.7 ± 6.1	2.51
Ti II	5188.687	1.58	−1.050	108.1 ± 11.5	2.71	109.4 ± 12.8	2.81
Ti II	5226.539	1.57	−1.260	94.0 ± 7.9	2.61	93.6 ± 8.2	2.66
Ti II	5336.786	1.58	−1.600	–	–	63.7 ± 10.6	2.42
Ti II	5381.021	1.57	−1.970	53.2 ± 6.2	2.55	45.1 ± 6.5	2.43
Ti II	5418.768	1.58	−2.130	34.5 ± 5.2	2.40	39.8 ± 4.5	2.52
Y II	4883.682	1.08	0.070	(36.5)	−0.92	(23.1)	−1.18
Y II	4900.119	1.03	−0.090	(38.0)	−0.78	–	–
Y II	5087.419	1.08	−0.170	(26.2)	−0.92	(27.0)	−0.89
Y II	5200.41	0.99	−0.570	(18.0)	−0.86	–	–
Y II	5205.722	1.03	−0.340	(31.0)	−0.80	–	–
Zn I	4810.528	4.08	−0.137	(24.4)	1.93	–	< 1.91
Zr II	4161.2	0.71	−0.590	(42.9)	−0.12	–	–

Table A.3: Lines measured in the Carina XSHOOTER spectra. Line parameters, observed EWs, and elemental abundances are provided. EWs in brackets are given as indication only; the quoted abundances are derived through spectral synthesis for these lines.

El.	λ [Å]	χ_{ex} [eV]	$\log(gf)$	EW [mÅ] car1_t174	$\log\epsilon(X)$	EW [mÅ] car1_t194	$\log\epsilon(X)$	EW [mÅ] car1_t200	$\log\epsilon(X)$	EW [mÅ] LG04c_0008	$\log\epsilon(X)$
Ba II	4554.029	0.0	0.170	(79.2)	-1.73	(165.8)	0.14	(139.2)	-0.32	(84.7)	-1.80
Ba II	4934.076	0.0	-0.150	(38.4)	-2.25	(164.7)	-0.08	(115.0)	-0.87	(51.9)	-2.23
C I	4300.0	—	—	—	4.59	—	4.90	—	5.06	—	4.22
Ca I	4226.728	0.0	0.244	239.1 ± 13.6	3.64	—	—	—	—	—	—
Ca I	6122.217	1.89	-0.316	—	—	78.9 ± 15.2	3.96	—	—	—	—
Ca I	6439.075	2.53	0.390	—	—	92.4 ± 16.5	4.30	—	—	48.1 ± 8.5	3.55
Co I	4118.773	1.05	-0.490	—	—	—	—	—	—	(102.1)	1.81
Co I	4121.318	0.92	-0.320	—	—	—	—	—	—	(107.7)	1.75
Cr I	5206	0.94	0.020	—	2.07	—	2.85	—	2.41	—	1.83
Fe I	4202.029	1.49	-0.708	—	—	—	—	120.2 ± 11.6	4.70	—	—
Fe I	4337.045	1.56	-1.695	—	—	—	—	—	—	96.8 ± 7.5	4.74
Fe I	4352.735	2.22	-1.287	—	—	—	—	—	—	66.7 ± 11.5	4.49
Fe I	4430.614	2.22	-1.659	—	—	—	—	—	—	47.0 ± 13.3	4.44
Fe I	4442.339	2.2	-1.255	—	—	—	—	—	—	84.2 ± 13.1	4.76
Fe I	4459.117	2.18	-1.279	—	—	—	—	—	—	76.8 ± 15.2	4.59
Fe I	4602.941	1.49	-2.209	—	—	—	—	—	—	72.2 ± 9.7	4.52
Fe I	4733.591	1.49	-2.988	—	—	—	—	—	—	40.0 ± 7.7	4.67
Fe I	4871.318	2.87	-0.363	—	—	—	—	75.0 ± 13.2	4.69	78.6 ± 11.9	4.50
Fe I	4872.138	2.88	-0.567	—	—	—	—	—	—	55.3 ± 11.8	4.28
Fe I	4890.755	2.88	-0.394	—	—	93.2 ± 7.1	4.83	69.3 ± 9.6	4.61	—	—
Fe I	4891.492	2.85	-0.112	—	—	110.0 ± 7.4	4.85	75.7 ± 8.9	4.43	94.4 ± 18.8	4.56
Fe I	4903.31	2.88	-0.926	—	—	68.3 ± 7.4	4.87	—	—	51.2 ± 8.2	4.56
Fe I	4918.994	2.87	-0.342	—	—	114.4 ± 3.6	5.17	70.4 ± 11.0	4.57	—	—
Fe I	4920.502	2.83	0.068	—	—	—	—	—	—	98.1 ± 10.9	4.43
Fe I	4938.814	2.88	-1.077	—	—	—	—	39.0 ± 6.2	4.71	—	—
Fe I	5006.119	2.83	-0.638	—	—	—	—	51.0 ± 12.6	4.44	71.3 ± 14.8	4.57
Fe I	5049.82	2.28	-1.355	55.2 ± 5.9	4.41	96.9 ± 7.6	5.10	—	—	62.7 ± 17.9	4.42
Fe I	5110.413	0.0	-3.760	—	—	—	—	81.4 ± 11.1	4.73	—	—
Fe I	5171.596	1.49	-1.793	—	—	—	—	—	—	98.6 ± 12.8	4.53
Fe I	5191.455	3.04	-0.551	62.5 ± 8.6	4.64	—	—	—	—	—	—
Fe I	5192.344	3.0	-0.421	65.2 ± 13.9	4.51	—	—	—	—	61.3 ± 9.9	4.35
Fe I	5194.941	1.56	-2.090	71.3 ± 11.8	4.52	—	—	75.4 ± 13.4	4.83	70.1 ± 15.1	4.35
Fe I	5202.336	2.18	-1.838	—	—	89.2 ± 5.0	5.26	—	—	54.3 ± 9.9	4.60
Fe I	5216.274	1.61	-2.150	—	—	80.9 ± 5.4	4.68	—	—	55.6 ± 8.2	4.21
Fe I	5217.389	3.21	-1.070	—	—	40.2 ± 7.2	4.88	—	—	—	—
Fe I	5232.94	2.94	-0.058	—	—	103.2 ± 6.1	4.70	—	—	—	—
Fe I	5266.555	3.0	-0.386	—	—	86.3 ± 4.2	4.76	56.0 ± 10.3	4.45	—	—
Fe I	5281.79	3.04	-0.834	—	—	68.8 ± 6.7	4.93	—	—	37.3 ± 8.1	4.37
Fe I	5283.621	3.24	-0.432	—	—	71.4 ± 4.6	4.83	—	—	44.2 ± 9.2	4.35
Fe I	5302.3	3.28	-0.720	—	—	49.6 ± 4.2	4.78	—	—	—	—
Fe I	5324.179	3.21	-0.103	53.5 ± 9.6	4.24	—	—	59.3 ± 11.8	4.48	61.8 ± 5.9	4.29
Fe I	5332.899	1.56	-2.777	—	—	67.5 ± 4.8	4.97	—	—	35.6 ± 7.0	4.41
Fe I	5339.929	3.27	-0.647	—	—	54.6 ± 3.9	4.77	—	—	—	—
Fe I	5369.961	4.37	0.536	—	—	43.9 ± 5.2	4.76	—	—	—	—
Fe I	5371.489	0.96	-1.645	126.3 ± 4.7	4.41	—	—	114.8 ± 10.5	4.54	—	—
Fe I	5383.369	4.31	0.645	—	—	68.4 ± 6.9	5.02	—	—	—	—
Fe I	5393.167	3.24	-0.715	—	—	48.4 ± 6.7	4.69	—	—	—	—
Fe I	5410.91	4.47	0.398	—	—	50.6 ± 4.1	5.14	—	—	—	—
Fe I	5415.199	4.39	0.642	—	—	65.6 ± 9.3	5.06	—	—	—	—
Fe I	5424.068	4.32	0.520	—	—	59.2 ± 4.4	4.99	—	—	38.0 ± 6.5	4.61
Fe I	5434.523	1.01	-2.122	112.7 ± 7.0	4.66	—	—	—	—	—	—
Fe I	6065.482	2.61	-1.530	—	—	69.0 ± 12.6	5.01	—	—	34.3 ± 10.1	4.41
Fe I	6136.615	2.45	-1.400	42.7 ± 7.9	4.37	—	—	—	—	69.5 ± 6.4	4.68
Fe I	6137.691	2.59	-1.403	—	—	—	—	—	—	57.1 ± 8.4	4.64
Fe I	6191.558	2.43	-1.417	—	—	—	—	—	—	62.7 ± 12.3	4.55
Fe I	6230.722	2.56	-1.281	51.7 ± 6.8	4.52	—	—	—	—	58.2 ± 10.4	4.50
Fe I	6252.555	2.4	-1.687	—	—	76.9 ± 15.0	5.02	—	—	42.8 ± 10.2	4.45
Fe I	6393.601	2.43	-1.432	—	—	—	—	—	—	50.1 ± 11.5	4.34
Fe I	6400.0	3.6	-0.290	—	—	—	—	—	—	31.5 ± 3.9	4.34
Fe I	6421.35	2.28	-2.027	—	—	63.7 ± 10.7	4.96	—	—	—	—
Fe I	6430.845	2.18	-2.006	—	—	—	—	—	—	48.0 ± 12.7	4.55
Fe I	6494.98	2.4	-1.273	—	—	—	—	—	—	62.3 ± 11.2	4.33
Fe I	6677.985	2.69	-1.418	—	—	—	—	—	—	41.5 ± 8.0	4.49
Fe II	4522.627	2.84	-2.030	—	—	—	—	—	—	45.2 ± 12.2	4.26
Fe II	4583.829	2.81	-1.860	—	—	—	—	—	—	78.6 ± 13.3	4.72
Fe II	4923.921	2.89	-1.320	(88.1)	4.53	109.4 ± 6.7	5.06	—	—	97.7 ± 6.9	4.62
Fe II	5018.436	2.89	-1.220	(104.9)	4.76	—	—	—	—	108.2 ± 13.6	4.72
Fe II	5197.567	3.23	-2.100	—	—	—	—	—	—	56.6 ± 17.0	4.96
Fe II	5234.623	3.22	-2.230	—	—	52.6 ± 10.1	5.17	—	—	—	—
Fe II	5275.997	3.2	-1.940	—	—	—	—	—	—	32.2 ± 8.1	4.30
Mg I	5172.684	2.71	-0.450	(162.6)	4.88	(209.5)	5.36	(132.0)	4.92	(151.8)	4.80
Mg I	5183.604	2.72	-0.239	(173.6)	5.07	(158.6)	5.16	(181.3)	5.25	(174.3)	5.02
Mn I	4030	0.0	-0.494	—	1.55	—	—	—	2.16	—	1.90
Na I	5889.951	0.0	0.108	(132.4)	3.80	(226.7)	4.16	(224.7)	4.52	(193.5)	3.78
Na I	5895.924	0.0	-0.194	—	—	(174.9)	4.09	(169.7)	4.35	(183.4)	4.00
Ni I	5476.904	1.83	-0.780	—	—	96.9 ± 7.5	3.61	—	—	74.8 ± 7.4	3.17
Sr II	4077.709	0.0	0.167	—	—	(240.9)	0.33	(124.7)	-0.53	(143.1)	-1.06
Ti I	4681.909	0.05	-1.030	—	—	(60.1)	2.68	—	—	—	—
Ti I	4999.503	0.83	0.320	—	—	(74.1)	2.64	—	—	—	—
Ti I	5064.653	0.05	-0.940	—	—	(75.5)	2.57	—	—	—	—
Ti II	4468.493	1.13	-0.630	—	—	143.9 ± 14.2	3.05	110.1 ± 22.7	2.52	122.8 ± 11.3	2.45
Ti II	4563.757	1.22	-0.690	96.3 ± 8.0	2.08	119.1 ± 13.3	2.71	102.3 ± 19.7	2.46	100.0 ± 9.4	2.08
Ti II	5336.786	1.58	-1.600	—	—	54.0 ± 3.3	2.59	—	—	—	—

Appendix B: Measured lines of r-process elements

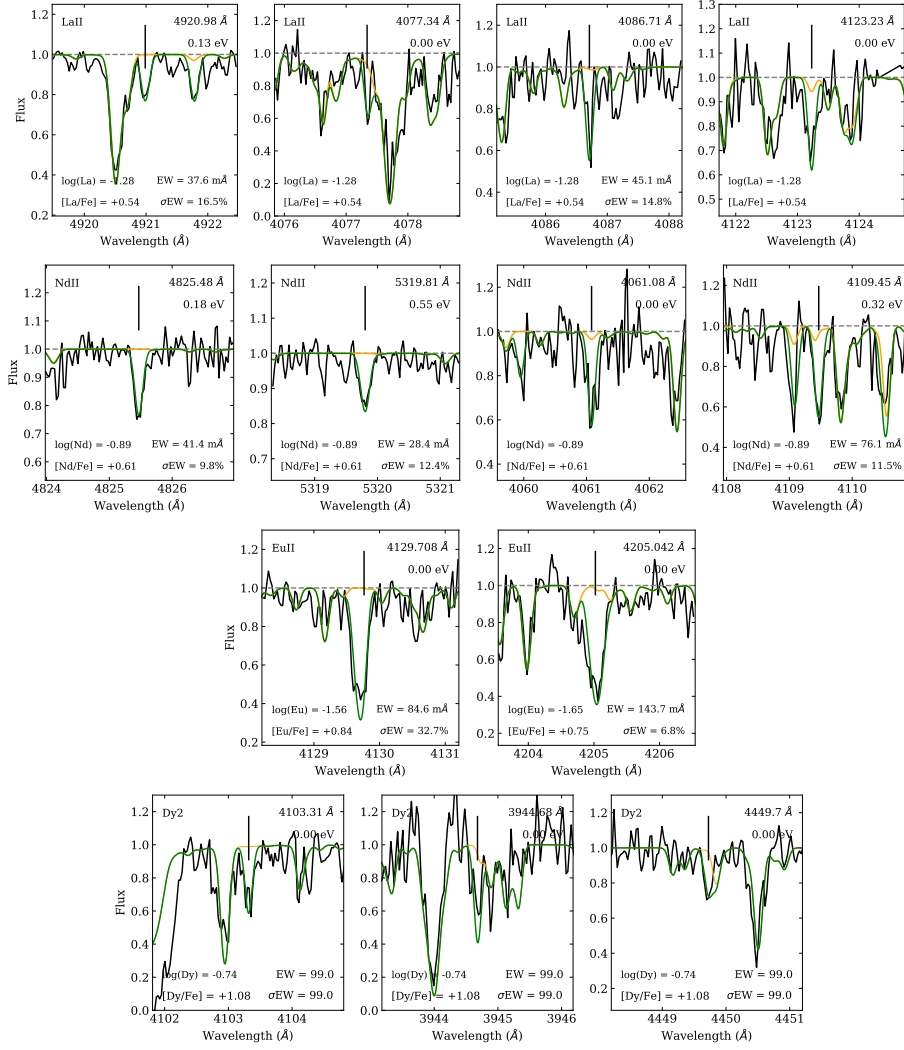


Fig. B.1: Individual lines of heavy ($Z>56$) neutron-capture elements measured in the r-process fnx_06_019 star. From top to bottom La II, Nd II, Eu II, Dy II. The best synthetic spectrum is in green, in orange the synthetic spectrum is computed without the element of interest, allowing the identification of blends.

4 A Milky Way chemical evolution view from the *Pristine* survey

4.1 The *Pristine* survey : overview and its photometric calibration

This section presents my work on a sample of MW disk and halo stars done in the context of the *Pristine* survey.

As we saw in previous chapters, the search for the most metal-poor stars is not an easy task. According to [Robin et al. \(2003\)](#), only 1/2000 stars blindly observed is expected to be an EMP in the magnitude range of $14 < V < 18$. Thus we can expect that doing blind spectroscopy on large sample of stars is not the most optimized way to find the most metal-poor stars. Since doing spectroscopy on individual stars is highly time consuming for the telescopes, the need of large photometric surveys with a quick and efficient way to estimate metallicities was critical to detect these very rare objects.

One of the most notable survey dedicated to the hunt of metal-poor stars is the SkyMapper Survey ([Keller et al. 2007](#); [Wolf et al. 2018](#)) which covered more than $17,000 \text{ deg}^2$ in six photometric bands, including a filter centred on the metallicity sensitive region of the calcium II doublet H&K lines. It led to the discovery of hundreds of EMP stars, and particularly to the most iron-poor stars known to this day ([Keller et al. 2014](#)), the Keller star, with an upper limit for the iron content fixed to $[\text{Fe}/\text{H}] < -7.1$. The Keller star is the most iron-poor star known, however the star is highly enhanced in carbon, thus the star identified by [Caffau et al. \(2011\)](#) with a metallicity of $[\text{Fe}/\text{H}] = -5$ and no carbon enhancement is actually the most metal-poor star.

SkyMapper and previous surveys showed the efficiency and the usefulness of such photometric surveys to find the oldest stars of the MW. However, they were all based on the southern sky, and the need of a similar survey in the northern hemisphere was clear. Thus, the *Pristine* survey ([Starkenburg et al. 2017](#)) was initiated by Dr. Else Starkenburg (Leibniz-Institut für Astrophysik Potsdam) and Dr. Nicolas Martin (Observatoire Astronomique de Strasbourg), with the aim to efficiently increase, and characterize, the number of known metal-poor stars. The survey started in 2015 at the Canadian French Hawaii Telescope (CFHT). It uses the main instrument MegaCam combined with a unique narrow-band filter centred in the region of the metallicity-sensitive calcium II doublet (CaH&K) lines, between 3900 and 4000 Å (see Figure 4.2).

The region observed by *Pristine*, presented in Figure 4.1, already covers more than 6,000 deg². It was chosen to overlap with the SDSS observations, including different regions and structures of the MW, its halo and beyond. Extensive work has been done by the team to observe the most promising metal-poor candidates with medium resolution spectroscopy. Between 2016 March and 2019 February, 1008 stars have been observed from the Isaac Newton Telescope (INT), the William Herschel Telescope (WHT) and the New Technology Telescope (NTT) within ~ 2500 deg² of the total footprint. It allowed the discovery of 707 new very metal-poor stars and 95 new EMPs, giving a success rate of 56% and 23% in discovering stars with $[\text{Fe}/\text{H}] < -2.5$ and $[\text{Fe}/\text{H}] = -3.0$ respectively (Aguado et al. 2019). *Pristine* also discovered one of the most metal-poor stars known, the UMP *Pristine*_221.8781+9.7844 with a metallicity as low as $[\text{Fe}/\text{H}] = -4.66 \pm 0.13$ and not enhanced in carbon (Starkenburg et al. 2018). The survey is also covering 22 dwarf-galaxies and dwarf-galaxies candidates located in the northern hemisphere. Three of the most observed dwarfs have been characterized in their nature, radial velocity dispersion and metallicity dispersion (see e.g. Longeard et al. (2018, 2021)). The predominantly metal-rich bulge and inner galactic disk of the MW was also explored in its metal-poor regime by *Pristine* (Arentsen et al. 2020b,a), showing the inner kinematics and radial velocity dispersion in function of metallicity for the first time.

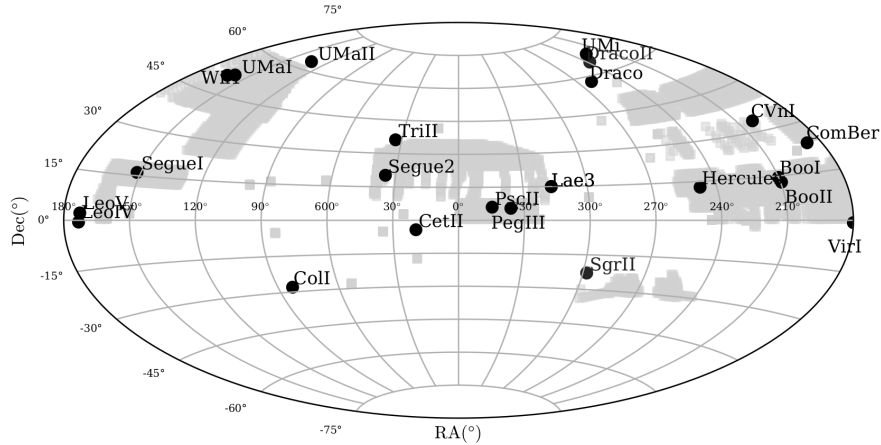


Figure 4.1 – The total *Pristine* footprint, 22 dwarf-galaxies or dwarf-galaxies candidates from the northern hemisphere and covered by the survey are also shown.

The selection of metal-poor candidates is based on a photometric calibration developed by Starkenburg et al. (2017), using the stars that are in common with the Sloan Extension for Galactic Understanding and Exploration survey (SEGUE, Yanny et al. (2009)). The SEGUE spectroscopic survey observed more than 200,000 MW stars blindly at moderate-resolution ($R \sim 1800$), providing an extremely large sample of spectroscopic metallicities. To ensure that the SEGUE metallicities ($[\text{Fe}/\text{H}]_{\text{SEGUE}}$) are robust, a very strict selection is done. Stars with too high uncertainties, or too low SNR are rejected. The final sample contains 7,000 stars in common between *Pristine* and SEGUE for which reliable spectroscopic metallicities are available.

4.1. The *Pristine* survey : overview and its photometric calibration

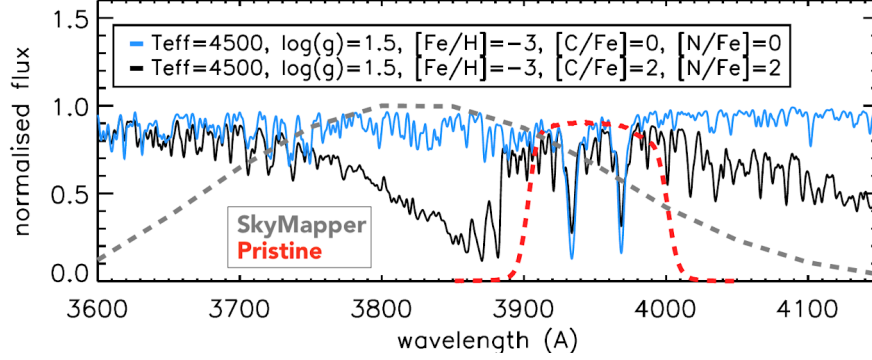


Figure 4.2 – The spectral region covered by the *Pristine* Ca H&K filter (in red), compared to the wider sensitive band of the SkyMapper survey. Two synthetic spectra are shown with different carbon enhancements. (Starkenburg et al. 2017).

Figure 4.3 shows the flux sensitivity on the metallicity in the Ca II H&K region for 3 sets of parameters and different metallicities. For a given set of parameters, the information on the metallicity is "encoded" in the flux measured in this region. This flux is converted into "*Pristine* magnitudes" noted "CaHK". Thanks to the SDSS broadband photometry, we can obtain a temperature proxy from the $(g-i)$ colour. This leads to the *Pristine* colour-colour diagram shown in Figure 4.4, with the "metallicity information" in function of the "temperature information". The colour-coded sample by the spectroscopic $[\text{Fe}/\text{H}]_{\text{SEGUE}}$ is revealing a specific distribution depending on the metallicity. The solar $[\text{Fe}/\text{H}]$ in red is located at the bottom of the distribution, and the EMP stars in blue at the top of the distribution. Thus, with the CaHK and $(g-i)_0$ photometric parameters only, a metallicity estimate can be inferred from this diagram.

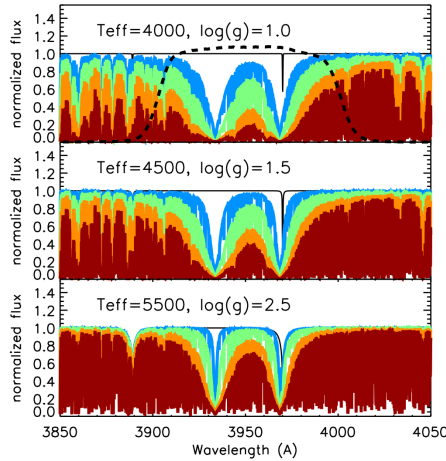


Figure 4.3 – Synthetic spectra in the Ca II H&K region for 3 set of fixed T_{eff} , $\log(g)$ and 4 different metallicities : $[\text{Fe}/\text{H}] = 0$ in red, $[\text{Fe}/\text{H}] = -1.0$ in orange, $[\text{Fe}/\text{H}] = -2.0$ in green, $[\text{Fe}/\text{H}] = -3.0$ in blue.

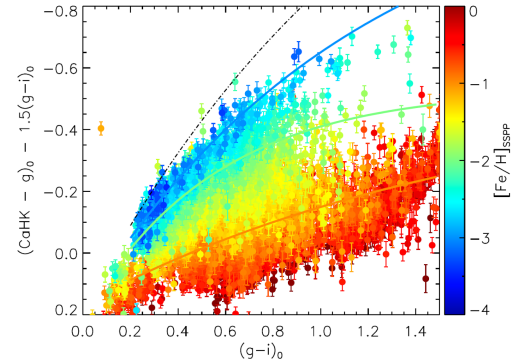


Figure 4.4 – The *Pristine* colour-colour diagram. The photometric CaHK metallicity information is plotted in function of the SDSS $(g-i)_0$ colour. The points are colour-coded with the SEGUE spectroscopic metallicities.

4.2 Publication : The *Pristine* survey – XV. A CFHT ESPaDOnS view on the Milky Way halo and disc populations

In the work presented below, I performed an homogeneous spectroscopic chemical analysis of the largest sample of metal-poor candidates observed at high resolution ($R = 40,000$) by *Pristine*. The observations were conducted with the Echelle SpectroPolarimetric Device for the Observation of Stars (ESPaDOnS) at the CFHT. The stars were selected on their probability to be metal-poor inside the first $1,000 \text{ deg}^2$ region covered by *Pristine*. After a spectroscopic optimization of the stellar parameters, nearly half of the sample (56 stars out of 132) were confirmed to be metal-poor ($[\text{Fe}/\text{H}] < -2$). While *Pristine* is mainly aimed to find the most metal-poor stars of our galaxy, I decided to proceed to the chemical and dynamical analysis of the complete dataset, covering a wide range of metallicities and parameters, from the EMP regime $[\text{Fe}/\text{H}] \sim -3$ to the super-solar $[\text{Fe}/\text{H}] \sim +0.25$ one, and from the higher end of the RGB, to the Main Sequence (MS) and turn-off stars.

As seen in Figure 2, a pipeline has been developed in order to improve the quality of the reduced ESPaDOnS spectra. Some extra details on the different steps are included in Appendix A.

I first focused on the α -elements, giving a first global *Pristine* view on the chemical composition of the Milky Way. I then derived carbon abundances, and showed that despite the narrower band of the *Pristine* Ca H&K filter compared to the SkyMapper filter, which should be less sensitive to the carbon content of the star (as seen in Figure 4.2) that none of our MP RGB stars are carbon-enhanced. This is an important bias against the carbon-rich stars that will require more exploration on its origin. According to Placco et al. (2014), the fraction of carbon-enhanced metal-poor (CEMP) stars is increasing with decreasing metallicity, with 43% CEMP stars at $[\text{Fe}/\text{H}] \leq -3.0$ and up to 81% CEMP stars at $[\text{Fe}/\text{H}] \leq -4.0$. CEMP stars are thus important objects. Their characterisation and frequency is critical to understand the early epochs of the galaxy formation, any possible bias in the selection process should be identified and solved.

Finally, I derived two neutron-capture elements, and focused on some stars that show peculiar n-capture enhancements and could be considered for further investigations on their origins.

I conducted the complete data reduction, the stellar model determination and the chemical analysis of this sample. The dynamical analysis and the orbits computation (Part 5 ORBITS) were conducted by our *Pristine* collaborator Federico Sestito, as in Sestito et al. (2019, 2020); Venn et al. (2020).

The work presented below was published in the peer-reviewed journal Monthly Notices of the Royal Astronomical Society (MNRAS), volume 511, 1004, (Lucchesi et al. 2022) [NASA ADS link](#).



The Pristine survey – XV. A CFHT ESPaDOnS view on the Milky Way halo and disc populations

R. Lucchesi^{1,2,★}, C. Lardo^{1,3}, P. Jablonka^{1,4}, F. Sestito⁵, L. Mashonkina⁶, A. Arentsen⁷,
W. Suter¹, K. Venn⁵, N. Martin^{7,8}, E. Starkenburg⁹, D. Aguado¹⁰, V. Hill¹¹, G. Kordopatis¹¹,
J. F. Navarro⁵, J. I. González Hernández^{12,13}, K. Malhan¹⁴ and Z. Yuan⁷

¹Institut de Physique, Laboratoire d'astrophysique, École Polytechnique Fédérale de Lausanne (EPFL), Observatoire, CH-1290 Versoix, Switzerland

²European Southern Observatory, Karl-Schwarzschild-str 2, D-85748 Garching bei München, Germany

³Dipartimento di Fisica e Astronomia, Università degli Studi di Bologna, Via Gobetti 93/2, I-40129 Bologna, Italy

⁴GEPI, Observatoire de Paris, Université PSL, CNRS, 5 Place Jules Janssen, F-92190 Meudon, France

⁵Department of Physics and Astronomy, University of Victoria, PO Box 3055, STN CSC, Victoria, BC V8W 3P6, Canada

⁶Institute of Astronomy of the Russian Academy of Sciences, Pyatnitskaya st. 48, 119017 Moscow, Russia

⁷Université de Strasbourg, CNRS, Observatoire astronomique de Strasbourg, UMR 7550, F-67000 Strasbourg, France

⁸Max-Planck-Institut für Astronomie, Königstuhl 17, D-69117 Heidelberg, Germany

⁹Kapteyn Astronomical Institute, University of Groningen, Postbus 800, NL-9700 AV Groningen, the Netherlands

¹⁰Institute of Astronomy, University of Cambridge, Madingley Road, Cambridge CB3 0HA, UK

¹¹Université Côte d'Azur, Observatoire de la Côte d'Azur, CNRS, Laboratoire Lagrange, F-06300 Nice, France

¹²Instituto de Astrofísica de Canarias, Vía Lactea, E-38205 La Laguna, Tenerife, Spain

¹³Departamento de Astrofísica, Universidad de La Laguna, E-38206 La Laguna, Tenerife, Spain

¹⁴The Oskar Klein Centre for Cosmoparticle Physics, Department of Physics, Stockholm University, AlbaNova, SE-10691 Stockholm, Sweden

Accepted 2021 December 17. Received 2021 December 8; in original form 2021 June 24

ABSTRACT

We present a one-dimensional, local thermodynamic equilibrium homogeneous analysis of 132 stars observed at high resolution with ESPaDOnS. This represents the largest sample observed at high resolution ($R \sim 40\,000$) from the *Pristine* survey. This sample is based on the first version of the *Pristine* catalogue and covers the full range of metallicities from $[\text{Fe}/\text{H}] \sim -3$ to $\sim +0.25$, with nearly half of our sample (58 stars) composed of very metal-poor (VMP) stars ($[\text{Fe}/\text{H}] \leq -2$). This wide range of metallicities provides the opportunity of a new detailed study of the Milky Way stellar population. Because it includes both dwarf and giant stars, it also enables the analysis of any potential bias induced by the *Pristine* selection process. Based on *Gaia* EDR3, the orbital analysis of this *Pristine*-ESPaDOnS sample shows that it is composed of 65 halo stars and 67 disc stars. After a general assessment of the sample chemical properties with the α -elements Mg and Ca, we focus on the abundance of carbon and the neutron capture elements Ba and Sr. While most of our VMP subsample is carbon normal, we also find that 14 stars out of the 38 stars with $[\text{Fe}/\text{H}] \leq -2$ and measured carbon abundances turn out to be carbon-enhanced metal-poor (CEMP) stars. We show that these CEMP stars are nearly exclusively (i.e. 12 stars out of 14) in the regime of low luminosity, unevolved, dwarf stars, which we interpret as the consequence of bias of the *Pristine* filter against C-rich giants. Among the VMP stars, we identify two CEMP stars with no enhancement in neutron-capture process elements and another one enriched in s-process element. Finally, one VMP star is found with a very low $[\text{Sr}/\text{Fe}]$ abundance ratio for its metallicity, as expected if it had been accreted from an ultra-faint dwarf galaxy.

Key words: stars: abundances – galaxies: dwarf – galaxies: formation – Local Group.

1 INTRODUCTION

The most metal-poor stars in the Galaxy and its close satellites are witnesses of the early stages of star formation in the Universe (e.g. Pagel 1997; Bromm & Larson 2004; Heger & Woosley 2010; Frebel & Norris 2015, and references therein). Their formation follows the explosions of a few population III (Pop III) supernovae only. Hence, their elemental abundances reflect the physical conditions and the nucleosynthesis of the primordial chemical evolution (e.g. Beers, Pre-

ston & Sheiman 1992; Cayrel et al. 2004; Beers & Christlieb 2005; Keller et al. 2007; Christlieb et al. 2008; Caffau et al. 2013; Yong et al. 2013; Roederer et al. 2014; Jacobson et al. 2015; Frebel 2018).

The detection of very metal-poor (VMP; $[\text{Fe}/\text{H}] \leq -2.0$), extremely metal-poor (EMP; $[\text{Fe}/\text{H}] \leq -3.0$), and ultra metal-poor (UMP; $[\text{Fe}/\text{H}] \leq -4.0$) stars is a challenging task that requires surveying large volumes of the sky.¹ Indeed, many observational efforts have been devoted to the search and identification of such key stellar

¹In a high Galactic latitude field towards the anticentre direction only $\sim 1/2000$ stars in the magnitude range between $14 < V < 18$ are expected to have metallicity less than $[\text{Fe}/\text{H}] \leq -3$; (Youakim et al. 2017).

* E-mail: romain.lucchesi@epfl.ch (RL)

population – e.g. the HK objective-prism survey (Beers et al. 1992); the RAdial Velocity Experiment survey (Steinmetz et al. 2006); the Hamburg/ESO objective-prism survey (Christlieb et al. 2008); the Sloan Extension for Galactic Understanding and Exploration Survey (Yanny et al. 2009); the LAMOST Experiment for Galactic Understanding and Exploration (Deng et al. 2012); the Apache Point Observatory Galactic Evolution Experiment (Majewski, APOGEE Team & APOGEE-2 Team 2016); and the SkyMapper Southern Sky Survey (Keller et al. 2007).

Along these lines, *Pristine* is a photometric survey designed to efficiently pre-select VMP star candidates (Starkenburg et al. 2017; Youakim et al. 2017; Aguado et al. 2019). It takes advantage of a narrow-band filter centred on the Ca H&K spectral lines and of the large field of view of MegaCam at the Canada–France–Hawaii Telescope (CFHT). Briefly, the *Pristine* selection method combines information from the metallicity-sensitive Ca H&K filter with broad-band photometry from large-field, multiband photometric surveys; e.g. the Sloan Digital Survey (SDSS; York et al. 2000; Eisenstein et al. 2011; Blanton et al. 2017) and *Gaia* DR2 (Gaia Collaboration 2016, 2018).

Spectroscopic follow-up of EMP star candidates is ongoing. These observations are conducted both at medium and high spectroscopic resolution (Caffau et al. 2017; Youakim et al. 2017; Starkenburg et al. 2018; Aguado et al. 2019; Bonifacio et al. 2019; Caffau et al. 2020; Venn et al. 2020; Kieley et al. 2021). The detailed chemical analysis of individual stars allows us to address three main threads of open issues related to stellar evolution and galaxy formation: (i) the nature and properties of the first stars, (ii) how and when the different components of the structure of the Milky Way (MW) assemble, and, finally, (iii) in the hierarchical galaxy formation paradigm, the mass and the degree of chemical evolution of the dwarf galaxy building blocks.

The existence of α -poor stars ($[(\text{Mg}+\text{Ca})/\text{Fe}] \leq 0$) in some of the *Pristine* subsample was reported by Caffau et al. (2020) in their ESO/FORS2 medium-resolution spectroscopic follow-up. These stars were found in a metallicity regime that is more metal-poor ($[\text{Fe}/\text{H}] < -1.2$) than the sample of Nissen & Schuster (2010), which is interpreted as the result of quiescent star formation forming the MW thin disc (Khoperskov et al. 2021). Such metal deficient and α -poor stars were also identified in other studies (e.g. Ivans et al. 2003; Cohen et al. 2013). Their origin is still unclear and could be heterogeneous, such as a formation from pockets of interstellar medium enhanced in Type Ia supernovae (SNeIa) products, biased initial mass function (IMF) sampling, or accretion of merging dwarf systems (Sakari et al. 2019; Xing et al. 2019). The present *Pristine* sample is large enough to shed some light on the fraction of α -poor stars in the MW halo.

Carbon-enhanced metal-poor (CEMP; i.e. stars having $[\text{C}/\text{Fe}] \geq 1.0$ according to the definition given in Beers & Christlieb 2005) represent an increased fraction of the halo component of the MW with decreasing metallicity (see Frebel & Norris 2015, for a complete discussion). For three metallicity bins in the range between $-4.5 < [\text{Fe}/\text{H}] < -3.0$, Yong et al. (2013) found that the fraction of CEMP stars was increasing from 0.22 to 0.32, and 0.33 with decreasing metallicity, up to 1.00 for $[\text{Fe}/\text{H}] < -4.5$. Higher fractions were derived by Placco et al. (2014) when correcting for internal mixing effects depleting surface carbon abundance with stellar evolution – e.g. they derive a fraction of 0.43, 0.60, 0.70, and 1.00, respectively, for the same metallicity bins defined in Yong et al. (2013). The exact origin of this increase in CEMP stars towards lower metallicities has yet to be unveiled, however, this result suggest that significant amounts of carbon were produced in the early Universe. This produc-

tion could be a necessary condition for the transition from massive pop III to low-mass stars (Bromm & Loeb 2003). However, the discoveries of SDSS J102915+172927 at $[\text{Fe}/\text{H}] = -4.73$ (Caffau et al. 2011) and *Pristine* 221.8781+9.7844 at -4.66 (Starkenburg et al. 2018), two stars with a significant low enrichment of carbon, nitrogen, and oxygen suggest that there must have been more than one formation channel of low-mass stars in the early Universe. Unexpectedly *Pristine* has found two contradictory results on this matter. While Aguado et al. (2019) reported a normal fraction of CEMP stars, Caffau et al. (2020) found a fraction of CEMP stars much lower than those provided by Placco et al. (2014), thereby suggesting some sensitivity of the *Pristine* filter to carbon abundance. This issue can be addressed in this study.

In the following, we present the analysis of the 132 bright ($V < 15.5$) metal-poor candidates from the original 1000 deg² of the *Pristine* survey, calibrated using the original SDSS gri photometry and observed at the CFHT with the high-resolution spectrograph ESPaDOnS. Out of this full sample, Venn et al. (2020) presented the detailed abundances of 10 elements (Na, Mg, Ca, Sc, Ti, Cr, Fe, Ni, Y, and Ba) for the 28 VMP stars identified at the time, as well as the analysis of their orbital properties. Because the full sample comes from the first stages of the *Pristine* calibration, the confirmation of very metal-deficient stars does not reach a success rate as high as in the later stages. Nevertheless, near half of the present sample (58 stars) is composed of VMP stars ($[\text{Fe}/\text{H}] \leq -2$). The more metal-rich stars offer us the opportunity of a new and detailed study of the MW halo stellar population.

This paper is organized as follows: in Section 2, we first discuss observations and data reduction. The abundance analysis is presented in Section 3 and the discussion of the abundances of C, Mg, Ca, Sr, and Ba takes place in Section 4. In Section Section 5, we look into the orbits of our sample stars. Finally, Section 6 summarizes our results and conclusions.

2 OBSERVATIONAL MATERIAL

2.1 Source catalogue and sample selection

The targets were selected from the *Pristine* diagnostics originally presented in Starkenburg et al. (2017). Stars were selected upon their probability to be VMP, in the bright ($V \lesssim 15.5$) regime of the original ~ 1000 deg² footprint of *Pristine*.

The final sample consists in 132 stars and includes the following:

- (i) 112 stars which were introduced in Venn et al. (2020). $[\text{Fe}/\text{H}]$ was spectroscopically derived only for a subset of those (86) using the equivalent widths (EWs) of six selected iron lines (four Fe I lines and two Fe II lines). In the following, we adopt the same nomenclature as Venn et al. (2020) and refer to this metallicity estimate as the quick six (Q6) one. Only stars with metallicity estimate $[\text{Fe}/\text{H}] \leq -2.5$ were then retained for further spectroscopic chemical analysis (28 stars).
- (ii) 20 new stars from the CFHT ESPaDOnS programs 16BF10, 17AF09, and 17BF18.

Fig. 1 shows the distribution of the full sample in the dereddened g_0 SDSS magnitude, with $E(B - V)$ values taken from the galactic reddening maps of Schlegel, Finkbeiner & Davis (1998). Stellar magnitudes range from $g_0 = 13.6$ to 15.3 with a peak around $g_0 = 14.7$. Table 1 provides the coordinates, dereddened g_0 and i_0 SDSS magnitudes along with the corresponding $E(B - V)$ values, and dereddened *Pristine* CaH&K magnitudes for all stars analysed in this study.

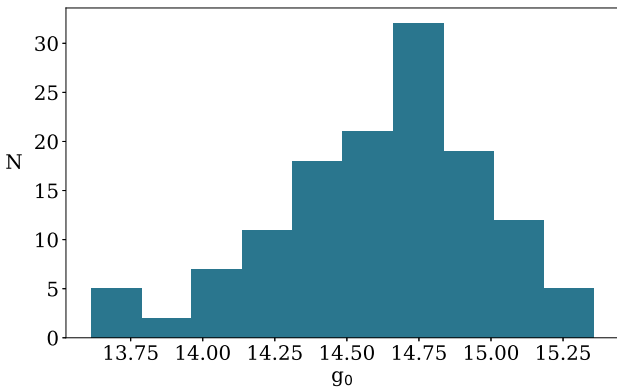


Figure 1. Histogram of the SDSS dereddened g magnitudes (g_0) of the 132 stars analysed in this work.

The full data set is analysed in a homogeneous way. The data reduction has been improved compared to Venn et al. (2020); all stellar atmospheric parameters are now spectroscopically derived and we provide detailed chemical abundances for C, Mg, Ca, Fe, Sr, and Ba.

2.2 Observations and data reduction

The observations were performed during the periods 2016A and 2018B with the high-resolution spectrograph ESPaDOnS at the CFHT (Donati et al. 2006). To enable a good sky subtraction, ESPaDOnS was used in the ‘star + sky’ mode, providing a high-resolution ($R = 68\,000$) spectrum from 4000 to 10 000 Å. Exposure times range from ~ 12 min for the brightest targets to ~ 120 min for the faintest ones.

The data reduction was performed with the dedicated pipeline LIBRE-ESPRIT.² This includes bias subtraction, flat fielding, wavelength calibration, and spectral extraction. ESPaDOnS records 40 orders and each of them is curved. LIBRE-ESPRIT proceeds in two steps. First, the pipeline performs a geometrical analysis from a sequence of calibration exposures. The position and shape of each order is derived from a mean flat-field image. The details of the wavelength-to-pixel relationship along and across each spectral order is measured from a thorium lamp exposure. Second, LIBRE-ESPRIT performs an optimal extraction of each object spectrum, using the geometrical information found in the previous step. It computes the intensity spectra with error bars, and applies corrections to compensate for Earth’s motion.

The Echelle orders were merged using a procedure developed by the authors of this paper. In short, the script isolates the different echelle orders to remove, in the overlapping wavelength regions, the part with the lowest signal-to-noise ratio (SNR). The orders are then combined again with a sigma clipping routine.

Spectra with multiple exposures were corrected for radial velocity (RV) shifts before combination. RVs were measured with the DAOSPEC package (Stetson & Pancino 2008) using the 4DAO wrapper (Mucciarelli 2013). The spectra were then degraded to $R = 40\,000$ to increase the SNR and allow for the automatic EW measurement under the assumption that the line profile has a Gaussian shape. The final RV corrected and combined spectra are normalized using

DAOSPEC in three wavelength ranges (4000–4800, 4800–5800, and 5800–6800 Å), using a 40–60 order polynomial. The final RV measurements and their associated errors, along with the number of exposures for each stars, are presented in Table 1.

Fig. 2 illustrates how the quality of the reduced spectra is improved by this procedure. It shows a portion of the original ESPaDOnS spectrum of the star Pr_236.1077+10.5311 and its spectrum after our optimal merging procedure, degraded to a resolution of $R = 40\,000$.

3 ATMOSPHERIC PARAMETERS AND CHEMICAL ABUNDANCES

The chemical abundances of iron, carbon, the α -Mg and Ca, and neutron (n)-capture (Sr and Ba) elements are calculated in 1D local thermodynamic equilibrium (LTE) with TURBOSPECTRUM (Plez 2012) combined with MARCS model atmospheres.³

The EWs of unblended spectral lines with Gaussian shape together with their associated uncertainties were measured with DAOSPEC (Stetson & Pancino 2008) that was launched iteratively with the code 4DAO (Mucciarelli 2013).

A χ^2 minimization between the observed and synthetic spectra was applied for the strong and blended lines, and for the elements presenting hyper fine splitting (HFS) of their energy levels such as barium and carbon. The latter was estimated from the CH molecular feature at 4300 Å. All synthetic spectra were convoluted to the instrumental resolution, then rebinned at the same pixel step as the observed spectra.

The abundance analysis is carried out with our own code. It enables the interpolation of the stellar atmosphere models, allows the derivations of the atmospheric parameters and chemical abundances from EW measurements, as well as enables a spectral synthesis χ^2 minimization for a set of chosen lines and elements. Spectral synthesis is typically done over small wavelength ranges, centred on the line of interest. The abundance of an element X is varied between $-2.0 \leq [X/Fe] \leq +2.0$ dex in steps of 0.1 dex, and refined in a second iteration with smaller steps.

The linelist used in the calculations is the same as in Lucchesi et al. (2020). It combines the list from Jablonka et al. (2015), Tafelmeyer et al. (2010), and Van der Swaelmen et al. (2013). The data for the selected atomic and molecular transitions are taken from the VALD data base (Piskunov et al. 1995; Ryabchikova et al. 1997; Kupka et al. 2000). The solar abundances are taken from Asplund et al. (2009).

3.1 Atmospheric parameters and metallicities

The stellar atmospheric parameters, i.e. effective temperature (T_{eff}), surface gravity ($\log g$), micro-turbulence velocity (v_t), and metallicity ($[Fe/H]$), were adjusted spectroscopically using the classical EW method. Only Fe lines with $EW \geq 25$ mÅ were considered, in order to exclude the weak and noisy ones. Lines with $EW \geq 110$ mÅ were also excluded from the EW analysis, in order to avoid the flat part of the curve of growth that is less sensitive to the abundance. These lines are highly sensitive to the microturbulent velocity and the velocity fields. Moreover the Gaussian approximation of the line profile starts to fail. Lines with excitation potential $\chi_{\text{ex}} > 1.4$ eV were also rejected in order to minimize non-local thermodynamic equilibrium (NLTE) effects. Finally, the Fe I lines at wavelength shorter than $\lambda \leq 4500$ Å

²https://www.cfht.hawaii.edu/Instruments/Spectroscopy/Espadons/Espadons_esprit.html

³<https://marcs.astro.uu.se/>

Table 1. Right ascension, declination, dereddened SDDS g and i magnitudes, averaged radial velocities, uncertainties on radial velocities, spectroscopic T_{eff} , $\log g$ micro-turbulence velocities and metallicities for the 132 stars analysed. Stars marked with * were rejected by the new *Pristine* photometric selection. Stars marked with † are three fast rotators and discarded from the analysis.

Star	RA (deg)	Dec. (deg)	g_0	i_0	CaHK $_0$	$E(B - V)$	RV (km s $^{-1}$)	σ_{RV}	T_{eff} (K)	$\log g$ (cgs)	v_t (km s $^{-1}$)	[Fe/H] (dex)
Pr_134.3232+17.6970	134.3232	17.6970	14.671	14.310	15.002	0.033	+115.27 (5)	1.78	6350	4.40	1.12	− 2.63
Pr_180.0090+3.7165	182.5090	03.7165	13.613	13.040	14.227	0.018	− 17.30 (1)	1.32	5200	4.40	1.12	− 0.18*
Pr_180.2206+9.5683	180.2206	09.5683	15.186	14.370	15.890	0.020	+22.12 (6)	0.46	5050	1.86	1.55	− 2.96
Pr_180.3790+0.9470	180.3790	00.9470	14.353	13.776	14.987	0.019	− 57.47 (1)	0.90	5684	3.70	1.05	− 0.74
Pr_180.7918+3.4084	180.7918	03.4084	13.748	12.456	14.884	0.027	+21.20 (1)	0.81	4800	3.70	1.26	− 0.08*
Pr_180.9118+11.3258	180.9118	11.3258	14.244	13.630	14.855	0.026	+33.98 (1)	0.95	5800	3.80	1.15	− 0.49*
Pr_181.2243+7.4160	181.2243	07.4160	15.057	14.694	15.450	0.014	− 146.70 (2)	0.77	6455	3.81	1.24	− 2.92
Pr_181.3119+11.6850	181.3119	11.6850	14.270	13.488	15.006	0.032	+1.49 (2)	0.02	5300	4.60	1.08	− 1.84*
Pr_181.3473+11.6698	181.3473	11.6698	14.414	13.722	15.006	0.032	+11.90 (2)	0.02	5900	4.45	1.11	− 0.49
Pr_181.3708+11.7636	181.3708	11.7636	14.443	13.689	15.119	0.033	+79.06 (1)	3.03	5494	3.18	1.36	− 1.48†
Pr_181.4395+1.6294	181.4395	01.6294	14.969	14.052	15.795	0.021	+206.58 (1)	2.00	4935	1.80	1.80	− 2.50
Pr_181.6954+13.8076	181.6954	13.8076	14.714	14.055	15.384	0.030	+78.01 (1)	1.06	5608	3.60	1.05	− 0.80
Pr_182.1670+3.4771	182.1670	03.4771	14.209	13.107	14.967	0.020	− 19.09 (1)	0.64	5350	4.45	1.11	− 0.35*
Pr_182.5364+0.9431	182.5364	00.9431	15.053	14.645	15.476	0.029	+222.71 (2)	0.34	6270	3.75	1.25	− 1.74
Pr_182.8521+14.1594	182.8521	14.1594	14.409	13.462	15.333	0.045	+78.56 (1)	1.35	4959	1.75	1.60	− 1.79
Pr_183.6850+4.8619	183.6850	04.8619	15.038	14.718	15.374	0.017	+41.00 (2)	0.30	6491	4.44	1.11	− 3.16
Pr_185.4112+7.4778	185.4112	07.4778	14.847	14.412	15.234	0.020	+175.18 (2)	0.40	6304	4.53	1.09	− 1.85*
Pr_187.8517+13.4560	187.8517	13.4560	13.914	13.382	14.269	0.025	+1.99 (1)	0.43	5700	4.10	1.18	− 0.45*
Pr_187.9786+8.7294	187.9786	08.7294	15.190	14.532	15.775	0.018	− 54.11 (2)	0.06	5618	3.66	1.27	− 0.50
Pr_188.1264+8.7740	188.1264	08.7740	14.528	13.780	15.228	0.017	− 48.83 (1)	1.11	5600	3.60	1.00	− 1.05
Pr_189.9449+11.5535	189.9449	11.5535	14.427	14.033	14.812	0.037	+30.35 (1)	6.00	6491	3.83	1.23	− 2.57
Pr_190.2669+11.1092	190.2669	11.1092	14.076	13.854	14.759	0.027	− 15.71 (1)	1.18	5800	4.20	1.16	− 0.34*
Pr_190.5813+12.8577	190.5813	12.8577	14.327	13.632	14.779	0.030	+4.42 (1)	0.70	5800	4.20	1.16	− 0.20*
Pr_190.6313+8.5138	190.6313	08.5138	15.114	14.511	16.060	0.021	− 64.16 (2)	0.02	5500	3.80	1.24	− 0.24
Pr_192.2121+15.9263	192.2121	15.9263	14.843	13.809	15.837	0.025	− 4.56 (1)	0.76	5600	4.30	1.14	+0.25
Pr_192.4285+15.9119	192.4285	15.9119	14.238	13.795	15.031	0.026	− 62.24 (1)	0.62	5450	4.65	1.07	− 0.49*
Pr_192.8540+15.8199	192.8540	15.8199	14.277	13.748	14.763	0.023	+0.98 (1)	0.39	5700	4.05	1.19	− 0.20*
Pr_192.9068+6.8314	192.9068	06.8314	13.766	13.017	14.490	0.034	+15.64 (1)	1.52	5800	4.25	1.15	− 0.35
Pr_193.1159+8.0557	193.1159	08.0557	14.660	14.224	15.129	0.026	+42.13 (1)	4.43	6100	4.55	1.09	− 1.85
Pr_193.1501+15.7966	193.1501	15.7966	13.757	13.536	14.373	0.025	+9.57 (1)	0.93	5800	4.00	1.20	− 0.31*
Pr_193.5542+11.5036	193.5542	11.5036	14.460	13.681	15.087	0.032	+16.20 (1)	0.66	5679	4.15	1.17	− 0.30
Pr_193.8390+11.4150	193.8390	11.4150	15.072	13.983	16.070	0.030	+2.53 (2)	0.07	4650	1.22	1.76	− 2.91
Pr_196.3755+8.5138	196.3755	08.5138	14.914	14.051	15.656	0.029	− 72.24 (1)	3.59	5012	1.73	1.65	− 2.77
Pr_196.4126+14.3177	196.4126	14.3177	14.884	14.003	15.634	0.029	− 49.36 (2)	0.00	5702	4.55	1.09	− 0.44
Pr_196.5323+8.7716	196.5323	08.7716	14.157	13.874	14.491	0.031	− 100.40 (2)	1.59	6483	4.55	1.09	− 2.55
Pr_196.5453+12.1211	196.5453	12.1211	14.745	14.468	15.090	0.028	+54.47 (2)	0.24	5950	3.40	1.32	− 2.51
Pr_196.6013+15.6768	196.6013	15.6768	14.624	14.001	15.438	0.027	− 103.91 (2)	0.17	5600	4.60	1.08	− 0.69
Pr_197.5045+15.6970	197.5045	15.6970	13.980	13.807	14.490	0.022	− 59.46 (1)	0.98	5920	4.05	1.19	− 0.80*
Pr_197.9861+12.3578	197.9861	12.3578	15.074	14.626	15.647	0.028	+114.83 (2)	0.35	6050	3.80	1.24	− 1.22
Pr_198.5288+12.1493	198.5288	12.1493	14.232	14.111	14.840	0.024	− 26.75 (1)	1.23	6120	4.25	1.15	− 0.59*
Pr_198.5495+11.4125	198.5495	11.4125	14.357	13.988	14.772	0.022	+74.45 (1)	5.31	6494	4.35	1.13	− 2.20
Pr_199.9269+8.3816	199.9269	08.3816	14.100	13.423	15.092	0.022	+3.17 (1)	0.54	5300	4.55	1.09	− 0.15*
Pr_200.0999+13.7229	200.0999	13.7229	15.282	14.223	16.288	0.024	+189.83 (4)	0.56	4750	1.24	1.75	− 2.48
Pr_200.5298+8.9768	200.5298	08.9768	15.358	14.664	16.306	0.027	+96.79 (2)	0.14	5363	3.45	1.20	− 1.02
Pr_200.7620+9.4376	200.7620	09.4376	14.695	14.096	15.680	0.023	+33.26 (1)	0.68	5650	4.35	1.13	− 0.15
Pr_201.1159+15.4382	201.1159	15.4382	14.548	13.859	15.586	0.021	− 5.77 (1)	0.70	5589	4.40	1.12	− 0.19
Pr_202.3435+13.2291	202.3435	13.2291	14.398	13.840	14.795	0.021	+100.81 (2)	0.20	5950	2.80	1.50	− 0.75
Pr_203.2831+13.6326	203.2831	13.6326	15.116	14.249	15.833	0.024	− 139.55 (1)	3.42	5008	1.95	1.45	− 2.70
Pr_204.9008+10.5513	204.9008	10.5513	14.894	14.617	15.171	0.031	− 246.62 (1)	6.02	6718	4.22	1.16	− 2.66
Pr_205.1342+13.8234	205.1342	13.8234	14.803	14.188	15.402	0.022	+126.90 (1)	3.05	5462	2.90	1.42	− 2.12
Pr_205.8132+15.3832	205.8132	15.3832	14.678	14.371	15.076	0.032	+121.42 (1)	5.22	6718	4.23	1.15	− 2.13
Pr_206.3487+9.3099	206.3487	09.3099	14.365	14.027	14.726	0.026	+157.19 (1)	4.17	6522	3.94	1.21	− 1.80
Pr_207.9961+1.1795	207.9961	01.1795	14.306	13.493	14.823	0.030	+36.17 (1)	0.51	5450	4.40	1.12	− 0.49*
Pr_208.0799+4.4267	208.0799	04.4267	14.686	14.132	15.151	0.026	− 129.96 (1)	5.27	5572	2.97	1.41	− 2.77
Pr_209.2123+1.5275	209.2123	01.5275	14.562	14.030	15.100	0.035	+13.53 (1)	2.67	5540	3.30	1.15	− 1.90
Pr_209.7189+10.8613	209.7189	10.8613	14.642	14.250	15.069	0.024	− 136.51 (2)	0.33	6358	4.40	1.12	− 1.98*
Pr_209.9364+15.9251	209.9364	15.9251	14.903	14.611	15.281	0.021	− 91.43 (2)	0.37	6664	3.96	1.21	− 2.25
Pr_210.0175+14.6289	210.0175	14.6289	14.789	14.079	15.464	0.018	− 74.32 (2)	0.67	5150	2.37	1.53	− 2.67
Pr_210.0316+14.0027	210.0322	14.0036	14.590	14.019	15.247	0.016	+22.68 (2)	0.03	5400	3.55	1.29	− 0.98*
Pr_210.7513+12.7744	210.7513	12.7744	14.881	13.714	16.127	0.028	+40.58 (1)	1.65	4652	1.35	1.60	− 2.12
Pr_210.8633+8.1798	210.8633	08.1798	14.675	14.067	15.237	0.024	− 12.33 (3)	0.79	5542	3.31	1.34	− 1.95
Pr_211.2766+10.3280	211.2766	10.3280	14.825	14.393	15.348	0.022	+44.59 (1)	1.79	5740	3.75	1.25	− 1.39*

Table 1 – *continued*

Star	RA (deg)	Dec. (deg)	g_0	i_0	CaHK ₀	$E(B - V)$	RV (km s ⁻¹)	σ_{RV}	T_{eff} (K)	log g (cgs)	v_t (km s ⁻¹)	[Fe/H] (dex)
Pr_211.7184+15.5516	211.7184	15.5516	14.885	13.876	15.899	0.017	-111.27 (2)	0.19	4750	1.31	1.74	-2.42
Pr_212.5834+10.5365	212.5834	10.5365	14.553	14.082	15.036	0.023	-125.50 (1)	3.96	6222	4.55	1.09	-1.79
Pr_213.2814+14.8983	213.2814	14.8983	14.643	14.283	15.006	0.019	-11.28 (1)	5.46	6002	3.55	1.29	-1.95 [†]
Pr_213.7878+8.4232	213.7878	08.4232	14.989	14.254	15.573	0.030	-106.36 (1)	3.40	5289	2.45	1.51	-2.45*
Pr_214.5557+7.4670	214.5557	07.4670	14.713	14.350	15.106	0.029	+47.24 (1)	5.51	6482	4.10	1.18	-2.14
Pr_215.6129+15.0163	215.6129	15.0163	14.419	13.688	15.164	0.023	-120.21 (1)	0.81	5180	2.62	1.40	-1.92
Pr_215.6783+7.6929	215.6783	07.6929	14.530	13.849	15.019	0.028	+9.50 (1)	0.54	5527	4.00	1.20	-0.35*
Pr_216.1245+10.2135	216.1245	10.2135	14.683	13.999	15.341	0.027	+106.05 (1)	3.65	5412	2.88	1.30	-2.21
Pr_217.3862+15.1651	217.3862	15.1651	14.675	14.349	15.125	0.025	-161.83 (1)	4.11	5700	3.30	1.34	-1.97
Pr_217.5786+14.0379	217.5786	14.0379	14.765	13.867	15.489	0.029	-17.17 (3)	0.40	4968	1.64	1.67	-2.66
Pr_217.6444+15.9634	217.6444	15.9634	14.897	14.562	15.277	0.031	-19.95 (2)	0.85	6550	4.17	1.17	-1.82
Pr_218.4256+7.5213	218.4256	07.5213	14.661	13.992	15.322	0.024	+11.45 (2)	0.15	5500	3.80	1.24	-0.60*
Pr_218.4622+10.3683	218.4622	10.3683	14.998	14.595	15.363	0.023	-125.40 (2)	1.22	5923	3.50	1.30	-2.40
Pr_218.4977+15.7251	218.4977	15.7251	14.022	13.144	15.178	0.023	-32.61 (2)	0.00	5150	4.40	1.12	-0.16*
Pr_223.5283+11.1353	223.5283	11.1353	14.612	13.537	15.772	0.033	+123.90 (1)	1.31	4540	1.05	1.50	-2.30
Pr_227.2895+1.3378	227.2895	01.3378	13.917	13.304	14.570	0.051	+4.91 (1)	0.49	5750	4.30	1.14	-0.35*
Pr_228.4607+8.3553	228.4607	08.3553	14.894	14.587	15.252	0.030	+8.08 (2)	0.01	6525	4.32	1.14	-2.20
Pr_228.6558+9.0914	228.6558	09.0914	14.832	14.530	15.166	0.032	-147.32 (2)	0.02	6695	4.26	1.15	-2.26*
Pr_228.8159+0.2222	228.8159	00.2222	14.751	14.366	15.129	0.052	+5.61 (2)	0.12	6520	4.36	1.13	-2.02
Pr_229.0409+10.3020	229.0409	10.3020	14.728	13.727	15.790	0.038	-8.15 (2)	0.21	5400	4.55	1.09	-0.10
Pr_229.1219+0.9089	229.1219	00.9089	14.747	14.403	15.118	0.048	-223.25 (2)	0.64	6385	3.70	1.26	-2.25
Pr_229.8911+0.1106	229.8911	00.1106	14.430	13.577	15.016	0.064	-2.05 (1)	0.47	5600	4.00	1.20	+0.10*
Pr_230.4663+6.5252	230.4663	06.5252	14.521	13.737	15.098	0.040	-26.63 (1)	1.09	5348	3.45	1.31	-1.15*
Pr_231.0318+6.4867	231.0318	06.4867	14.626	13.893	15.183	0.041	+21.45 (1)	0.63	5468	3.90	1.22	-0.35*
Pr_232.6956+8.3392	232.6956	08.3392	15.076	14.462	15.661	0.044	-37.84 (2)	0.20	5641	3.40	1.32	-2.22
Pr_232.8039+6.1178	232.8039	06.1178	15.016	14.268	15.867	0.052	-212.58 (1)	3.92	5280	2.30	1.54	-2.26*
Pr_233.5730+6.4702	233.5730	06.4702	14.774	13.869	15.545	0.044	-80.66 (1)	4.16	4991	1.90	1.62	-2.74
Pr_233.9312+9.5596	233.9312	09.5596	14.970	14.368	15.557	0.037	-99.38 (2)	0.29	5505	3.50	1.20	-2.20
Pr_234.4403+13.3742	234.4403	13.3742	14.817	13.506	15.815	0.046	-66.48 (2)	0.05	5600	4.51	0.90	-0.40*
Pr_235.1448+8.7464	235.1448	08.7464	14.649	14.151	15.086	0.042	-156.26 (1)	4.79	6167	3.64	1.27	-2.54
Pr_235.7578+9.0000	235.7578	09.0000	14.937	14.601	15.330	0.042	-58.70 (2)	0.37	6654	4.20	1.16	-1.81
Pr_235.9710+9.1864	235.9710	09.1864	14.631	14.257	15.069	0.042	-32.49 (1)	3.69	6300	3.70	1.26	-1.83*
Pr_236.1077+10.5311	236.1077	10.5311	14.808	13.753	15.809	0.048	-41.51 (1)	1.79	4650	1.47	1.71	-2.55
Pr_236.4855+10.6903	236.4855	10.6903	14.575	14.005	14.933	0.052	-36.42 (1)	0.93	5850	3.70	1.26	-0.27*
Pr_236.7138+9.6084	236.7138	09.6084	14.529	13.466	15.271	0.045	+54.25 (1)	0.92	5450	3.45	1.31	-0.85*
Pr_237.8246+10.1427	237.8246	10.1427	15.216	14.501	15.776	0.046	-165.90 (2)	1.08	5405	2.80	1.44	-3.23
Pr_237.8353+10.5902	237.8353	10.5902	14.734	13.964	15.370	0.056	-237.67 (2)	0.31	5250	2.70	1.46	-2.32*
Pr_237.9609+15.4023	237.9609	15.4023	14.543	14.215	14.916	0.046	-267.22 (2)	0.66	6557	4.09	1.18	-1.90
Pr_238.7217+6.1945	238.7217	06.1945	14.770	14.462	15.103	0.039	-195.14 (2)	0.23	6551	4.20	1.16	-2.06
Pr_240.0348+13.8279	240.0348	13.8279	14.785	13.835	15.721	0.052	+3.55 (1)	1.80	4760	1.52	1.70	-2.30
Pr_240.4216+9.6761	240.4216	09.6761	14.944	14.164	15.528	0.040	+37.59 (3)	0.23	5204	2.60	1.47	-2.98
Pr_241.1186+9.4156	241.1186	09.4156	14.532	14.070	14.999	0.044	-51.47 (1)	4.89	6299	3.95	1.21	-1.92
Pr_241.7900+14.0920	241.7900	14.0920	14.680	14.351	15.078	0.038	-127.80 (2)	0.91	6485	3.90	1.22	-2.51
Pr_242.3556+7.9425	242.3556	07.9425	14.851	14.461	15.249	0.046	-181.11 (2)	1.00	6326	3.90	1.22	-1.95
Pr_243.8390+6.9966	243.8390	06.9966	14.748	14.242	15.192	0.063	-17.94 (3)	0.32	5878	3.52	1.30	-1.95
Pr_244.4872+16.8936	244.4872	16.8936	14.379	13.953	14.701	0.043	-192.08 (2)	0.46	6214	3.90	1.22	-2.10
Pr_245.1096+8.8947	245.1096	08.8947	14.463	13.739	15.033	0.064	-30.90 (1)	0.59	5567	4.45	1.11	-0.35*
Pr_245.4387+8.9954	245.4387	08.9954	14.780	14.354	15.199	0.055	-82.89 (2)	0.60	6464	4.10	1.18	-1.67
Pr_245.5747+6.8844	245.5747	06.8844	15.041	14.323	15.579	0.062	-188.96 (4)	0.79	5424	2.95	1.40	-3.17
Pr_245.8364+13.8778	245.8364	13.8778	14.012	13.264	14.641	0.045	-176.99 (1)	4.42	5150	2.28	1.40	-3.06
Pr_246.8588+12.3193	246.8588	12.3193	14.763	13.932	15.500	0.056	-86.02 (2)	0.05	5070	2.21	1.50	-2.25
Pr_248.4394+7.9230	248.4394	07.9230	14.340	13.892	14.767	0.081	-15.66 (3)	0.85	6350	4.40	1.12	-1.72
Pr_248.4959+15.0776	248.4959	15.0776	14.717	13.830	15.454	0.062	-74.03 (2)	0.25	5069	1.86	1.63	-2.63
Pr_248.5263+8.9342	248.5263	08.9342	15.089	14.279	15.829	0.069	-109.73 (2)	0.63	5300	2.45	1.51	-2.07
Pr_250.6971+8.3743	250.6971	08.3743	14.615	13.696	20.337	0.085	-4.08 (1)	3.84	5020	1.80	1.64	-2.66
Pr_250.8797+12.1101	250.8797	12.1101	14.261	13.069	15.327	0.053	+4.67 (1)	0.52	5600	4.40	1.12	+0.05*
Pr_251.4082+12.3657	251.4082	12.3657	15.062	14.076	15.785	0.056	-4.43 (2)	0.03	4919	1.54	1.69	-3.22
Pr_252.1648+15.0648	252.1648	15.0648	14.621	13.615	15.518	0.068	-157.06 (1)	2.24	4770	1.35	1.50	-2.43
Pr_252.4208+12.6477	252.4208	12.6477	14.486	13.739	15.172	0.053	+35.27 (2)	0.05	5500	3.60	1.28	-1.30*
Pr_252.4917+15.2984	252.4917	15.2984	14.349	13.443	15.056	0.070	+62.65 (1)	0.93	5900	3.70	1.26	-0.60*
Pr_252.6179+16.0546	252.6179	16.0546	14.178	13.208	15.057	0.074	-113.39 (2)	0.04	4810	1.60	1.68	-2.52
Pr_253.8582+15.7240	253.8582	15.7240	14.973	14.037	15.720	0.088	-98.39 (3)	0.44	5077	2.25	1.50	-2.58
Pr_254.0662+14.2694	254.0662	14.2694	13.658	13.079	14.172	0.071	-29.70 (1)	0.46	5500	3.80	1.24	-0.56*
Pr_254.3844+12.9653	254.3844	12.9653	14.969	13.978	15.743	0.059	-386.12 (2)	0.47	5300	2.80	1.44	-2.45 [†]

Table 1 – continued

Star	RA (deg)	Dec. (deg)	g_0	i_0	CaHK ₀	$E(B - V)$	RV (km s ⁻¹)	σ_{RV}	T_{eff} (K)	log g (cgs)	v_t (km s ⁻¹)	[Fe/H] (dex)
Pr_254.5215+15.4969	254.5215	15.4969	14.045	13.246	14.807	0.096	+25.01 (1)	0.52	5640	4.30	1.14	-0.09
Pr_254.5478+10.9129	254.5478	10.9129	14.447	13.687	15.096	0.077	+94.21 (1)	2.72	5460	3.35	1.33	-2.15
Pr_254.7768+13.8208	254.7768	13.8208	14.018	13.239	14.479	0.077	-16.41 (1)	0.51	5600	4.05	1.19	-0.35*
Pr_255.2679+14.9714	255.2679	14.9714	14.332	13.867	14.700	0.083	+27.92 (1)	5.11	6479	3.88	1.22	-2.09
Pr_255.5564+10.8613	255.5564	10.8613	14.782	14.125	15.306	0.075	-372.85 (2)	0.43	5495	2.86	1.43	-2.55
Pr_255.8043+10.8443	255.8043	10.8443	14.246	13.859	14.629	0.082	-266.01 (2)	1.12	5600	3.20	1.36	-3.00*

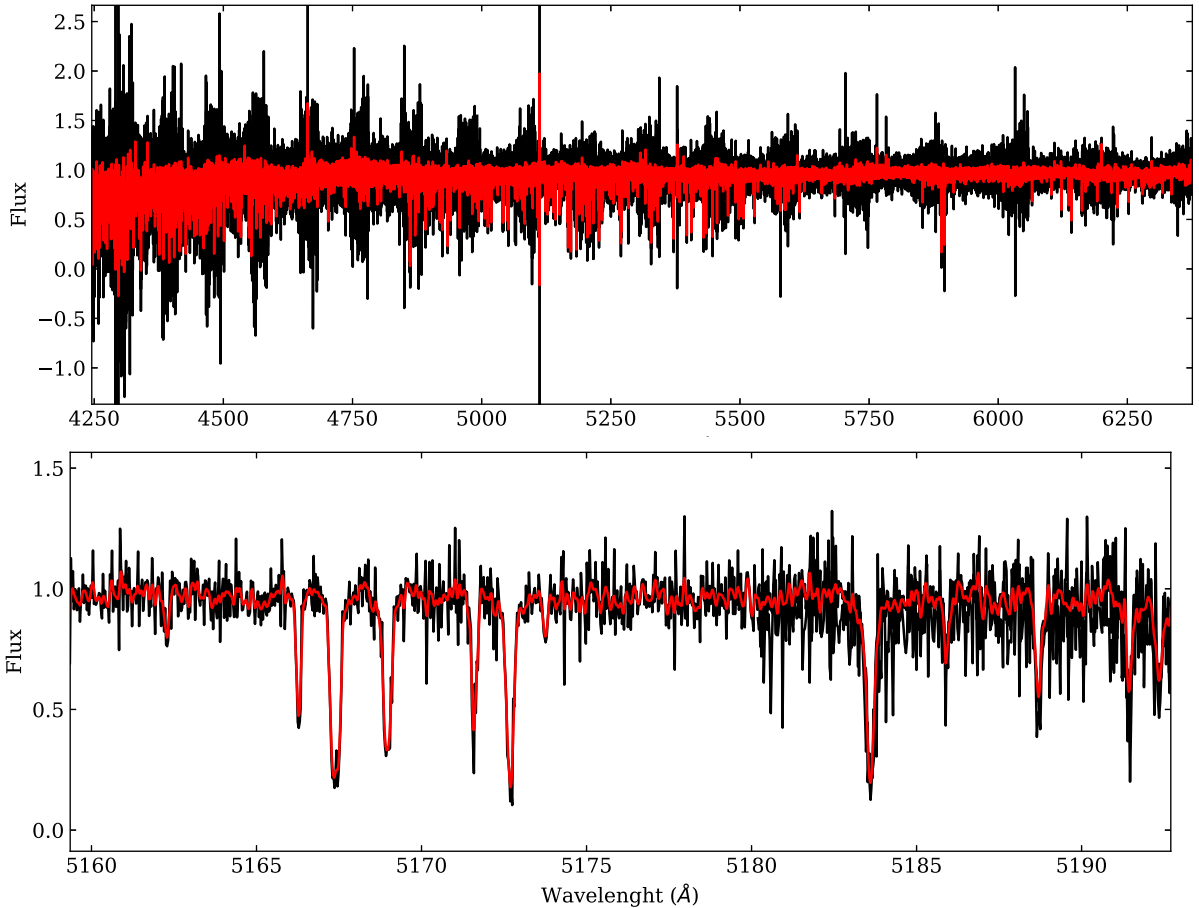


Figure 2. The top panel shows the spectrum of Pr_236.1077+10.5311 in the wavelength range between 4250 and 6300 Å. The bottom panel shows the spectrum of the same star over a limited wavelength range around the magnesium triplet spectral features. The raw ESPaDOnS spectrum from the LIBRE-ESPRIT pipeline is plotted in black. The red line shows the spectrum degraded to a resolution of $R = 40\,000$ and with optimal order merging applied to data (see text).

were excluded as the consequence of the low SNR at the blue end of the spectra.

The stellar atmospheric parameters have been optimized iteratively as follows:

(i) The effective temperatures were derived by minimizing the slopes between iron abundance and excitation potential, allowing the slope to deviate from zero by less than about twice the uncertainty on the slope;

(ii) The surface gravities were obtained from ionization equilibrium between Fe II and Fe I. However, since NLTE impacts the abundances derived from the Fe I lines at low metallicities (e.g. Mashonkina et al. 2017), we tolerated a difference in abundance $\Delta(\text{Fe II} - \text{Fe I}) = +0.15$ dex for stars with $[\text{Fe/H}] \leq -2.5$.

(iii) The initial microturbulent velocities were obtained from the empirical relation $\log g: v_t = 2.0 - 0.2 \cdot \log g$ as in Theiler et al. (2020). Convergence to the final value was reached by minimizing the slope between the neutral iron lines and their EWs.

(iv) The model’s metallicity was adjusted to the derived Fe I abundance after each iteration until they agreed within ± 0.05 dex.

Fig. 3 presents the distribution of our sample in the T_{eff} versus $\log g$ diagram. Stars are colour coded according to their metallicity. We consider two sets of isochrones both taken at 13 Gyr and at metallicities $[\text{Fe/H}] = -3, -2, -1$, and 0. The Yonsei–Yale (YY) stellar isochrones (Demarque et al. 2004) (solid lines) assumes an enhancement in α -elements of $[\alpha/\text{Fe}] = +0.3$ at $[\text{Fe/H}] < -1$. The MESA/MIST isochrones are currently only available for solar-scaled

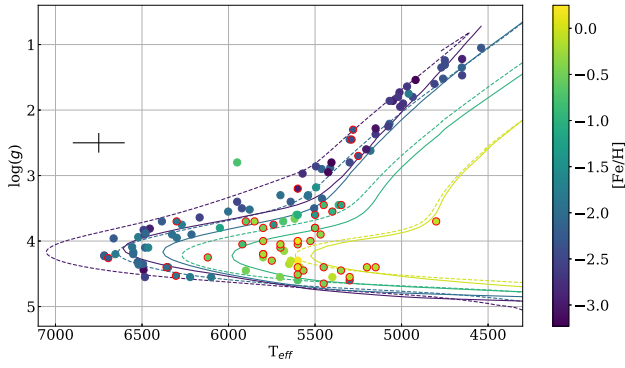


Figure 3. T_{eff} versus $\log g$ diagram. Stars are colour coded according to their metallicities. The YY stellar isochrones (solid lines) are shown for the age of 13 Gyr and metallicities $[\text{Fe}/\text{H}] = [-3, -2, -1, 0]$ from left to right, respectively, with α -enhancement $[\alpha/\text{Fe}] = +0.3$ at $[\text{Fe}/\text{H}] < -1$. The MIST/MESA isochrones (dashed lines) with same parameters are also shown, at constant $[\alpha/\text{Fe}] = 0$. Stars denoted with an open red circle have been rejected from the later versions of the *Pristine* catalogues (see text). The black cross indicates the typical uncertainty of 150 K on T_{eff} and 0.15 dex on $\log g$.

abundances (e.g. Choi et al. 2016; Dotter 2016). The YY isochrones seem to better fit our spectroscopic results. Indeed, the TO region of the MIST isochrones is significantly warmer (~ 500 K) than the corresponding YY isochrone at $[\text{Fe}/\text{H}] = -3$ and none of our sample stars reach this extremely hot temperature. At higher metallicities, the difference between the two sets of models decreases, reaching differences in temperature smaller than $\Delta T_{\text{eff}} < 100$ K at $[\text{Fe}/\text{H}] = 0$, well within the errors of the spectroscopic T_{eff} . As to red giant branch (RGB) stars, the largest difference between the two sets of isochrones is again observed at low metallicities (e.g. $\Delta(T_{\text{eff}})_{\text{MIST-YY}} = -100$ K and $\Delta(\log g)_{\text{MIST-YY}} = +0.2$ and at $[\text{Fe}/\text{H}] = -3$). However, their difference stays well within the typical spectroscopic uncertainties (150 K in T_{eff} and 0.15 in $\log g$). Thus, both sets of isochrones represent a good fit to data in this region of stellar evolution.

Table 1 lists the final stellar atmospheric parameters adopted in the rest of our analysis. Our sample includes both unevolved and evolved stars with effective temperatures and surface gravities in the interval $T_{\text{eff}} = 4540\text{--}6720$ K and $\log g = 1.05\text{--}4.65$. It covers a wide range in metallicity, from $[\text{Fe}/\text{H}] = -3.2$ to $+0.25$. As also seen in Fig. 3, all the RGB stars selected by *Pristine* are confirmed VMP stars.

One star stands out from the rest of the sample, Pr_202.3435+13.2291 at $T_{\text{eff}} = 5950$ K, $\log g = 2.80$, and $[\text{Fe}/\text{H}] = -0.75$. It is most likely a horizontal branch (HB) star. It was removed from further chemical analysis.

Three stars have very broad lines, one originates from the new sample and two from the Q6 sample. They are fast rotators (identified with the \dagger symbol in Table 1) and their spectroscopic metallicity is poorly constrained. As a consequence, they were also removed from further chemical analysis. Abundances are provided for a total of 128 stars in Table 2.

3.2 Specific comments on individual abundances

The abundance of carbon was derived by spectral synthesis of the CH absorption at 4300 Å, assuming $[\text{O}/\text{Fe}] = [\text{Mg}/\text{Fe}]$ and $[\text{N}/\text{Fe}] = 0$ to take into account that some of C can be locked into the CO and CN molecules. While the χ^2 minimization was performed in the 4309–4315 Å window, the continuum was estimated from a wider 60 Å region around the molecular band. The resulting C abundance

was finally checked against the 4323 Å absorption band and only concordant band strengths were considered as robust measurements. Fig. 4 provides three examples of our synthesis, corresponding to actual measurements for a cool giant star and a hot dwarf star, and finally the case of an upper limit for a hot star.

The abundance of magnesium was obtained from 2 to 5 Mg I lines at 4571.096 Å, 4702.991 Å, 5172.684 Å, 5183.604 Å, and 5711.088 Å. Spectral synthesis was performed on the strong Mg I lines at 5172.684 Å and 5183.604 Å with EWs larger than 110 mÅ. Fig. 5 illustrates the case of Pr_211.7184+15.5516, for which both strong and weaker lines are available. The results from the four Mg lines are consistent, with a mean $[\text{Mg}/\text{Fe}] = +0.39$ and a standard deviation of $\sigma = 0.05$.

The abundance of Ca I was obtained from 2 to 20 lines, with EWs between 25 and 100 mÅ. All lines were carefully inspected to retain only the best-fitting ones. This was usually the case in the red part of the spectrum between 5300 and 6700 Å that has a higher SNR.

The abundance of strontium was determined from the single Sr II 4215.519 Å line, since both Sr II 4161.792 Å and 4077.709 Å are too weak and noisy to be measured. Strontium abundances were derived primarily from EW analysis. Additionally, spectral synthesis was performed in case of weak and noisy features. A careful comparison was carried out between results from different methods in order to keep only lines with a good fit or a clear χ^2 convergence.

Barium was measured from 1 to 4 Ba II lines at 4934.076, 5853.668, 6141.713, and 6496.897 Å by spectral synthesis to take into account the HFS of the lines and some small blends with iron lines. The HFS data in the line list are from Prochaska & McWilliam (2000) and Arlandini et al. (1999).

3.3 Uncertainties

(i) Uncertainties due to the atmospheric parameters.

To estimate the sensitivity of the abundances to the adopted atmospheric parameters, we chose three stars representative of three regions in the T_{eff} versus $\log g$ diagram (Fig. 3). We repeated the abundance analysis and varied only one stellar atmospheric parameter at a time by its corresponding uncertainty, keeping the others fixed. The estimated internal errors are ± 150 K in T_{eff} , ± 0.15 dex in $\log g$, and ± 0.15 km s $^{-1}$ in v_t for cool stars ($T_{\text{eff}} < 6000$ K), and ± 200 K in T_{eff} , ± 0.20 dex in $\log g$, and ± 0.20 km s $^{-1}$ in v_t for the warmest stars of the sample ($T_{\text{eff}} > 6000$ K). These errors are presented in Table 3.

(ii) Uncertainties due to EWs measurement. The uncertainties on the individual EW measurements δ_{EW_i} are provided by DAOSPEC and computed according to the following formula (Stetson & Pancino 2008):

$$\delta_{EW_i} = \sqrt{\sum_p (\delta I_p)^2 \left(\frac{\partial EW}{\partial I_p} \right)^2 + \sum_p (\delta I_{C_p})^2 \left(\frac{\partial EW}{\partial I_{C_p}} \right)^2}, \quad (1)$$

where I_p and δI_p are the intensity of the observed line profile at pixel p and its uncertainty, and I_{C_p} and δI_{C_p} are the intensity and uncertainty of the corresponding continuum. The uncertainties on the intensities are estimated from the scatter of the residuals that remain after subtraction of the fitted line. The corresponding uncertainties σ_{EW_i} on individual line abundances are propagated by TURBOSPECTRUM.

The final errors listed in Table 2 were computed following the recipes outlined in Jablonka et al. (2015), Hill et al. (2019), and Lucchesi et al. (2020).

Table 2. Elemental abundances of the 129 stars kept for the chemical analysis. The number of lines used is indicated in parentheses for each element and each star. The quoted errors correspond to the uncertainties resulting from the EW analysis or spectral fitting (see text).

Star	[Fe/H]	log(Fe I) $\pm \sigma$ (N)	log(Fe II) $\pm \sigma$ (N)	[C/Fe] $\pm \sigma$	[Mg/Fe] $\pm \sigma$ (N)	[Ca/Fe] $\pm \sigma$ (N)	[Sr/Fe] $\pm \sigma$ (N)	[Ba/Fe] $\pm \sigma$ (N)
134.3232	-2.63	4.87 \pm 0.04 (17)	4.63 \pm 0.09 (3)	+1.17 \pm 0.24	+0.19 \pm 0.08 (2)	-	+0.03 \pm 0.12 (1)	-
180.0090	-0.18	7.32 \pm 0.01 (47)	7.30 \pm 0.04 (10)	-0.47 \pm 0.19	+0.17 \pm 0.12 (1)	+0.14 \pm 0.08 (2)	-	-0.05 \pm 0.09 (4)
180.2206	-2.96	4.54 \pm 0.02 (34)	4.58 \pm 0.04 (7)	+0.86 \pm 0.22	+0.40 \pm 0.09 (2)	+0.25 \pm 0.09 (2)	<-2.05 (1)	-1.26 \pm 0.12 (1)
180.3790	-0.74	6.76 \pm 0.02 (95)	6.78 \pm 0.02 (16)	+0.02 \pm 0.20	+0.22 \pm 0.04 (4)	+0.16 \pm 0.02 (15)	-0.19 \pm 0.08 (1)	+0.05 \pm 0.06 (4)
180.7918	-0.08	7.42 \pm 0.03 (32)	7.40 \pm 0.04 (15)	-0.08 \pm 0.20	+0.18 \pm 0.12 (1)	-0.05 \pm 0.07 (3)	-	+0.18 \pm 0.09 (3)
180.9118	-0.49	7.01 \pm 0.03 (100)	7.04 \pm 0.03 (20)	-0.30 \pm 0.25	+0.14 \pm 0.06 (3)	+0.11 \pm 0.04 (11)	+0.20 \pm 0.10 (1)	+0.13 \pm 0.06 (4)
181.2243	-2.92	4.58 \pm 0.14 (3)	4.37 \pm 0.14 (3)	<+2.07	+0.71 \pm 0.17 (2)	<+1.00 (4)	-	+0.71 \pm 0.24 (1)
181.3119	-1.84	5.66 \pm 0.01 (80)	5.67 \pm 0.04 (7)	-0.07 \pm 0.21	+0.34 \pm 0.07 (1)	+0.38 \pm 0.02 (15)	-0.19 \pm 0.07 (1)	-0.08 \pm 0.05 (3)
181.3473	-0.49	7.01 \pm 0.01 (94)	7.03 \pm 0.02 (18)	+0.25 \pm 0.21	+0.11 \pm 0.08 (1)	+0.07 \pm 0.02 (18)	-0.06 \pm 0.08 (1)	+0.08 \pm 0.05 (3)
181.4395	-2.50	5.00 \pm 0.02 (70)	5.04 \pm 0.06 (10)	<-0.12	+0.58 \pm 0.07 (4)	+0.35 \pm 0.04 (7)	-0.09 \pm 0.16 (1)	-0.79 \pm 0.06 (3)
181.6954	-0.80	6.70 \pm 0.03 (102)	6.75 \pm 0.04 (11)	-0.03 \pm 0.20	+0.25 \pm 0.07 (2)	+0.29 \pm 0.03 (14)	-	+0.03 \pm 0.05 (4)
182.1670	-0.35	7.15 \pm 0.01 (58)	7.20 \pm 0.03 (17)	+0.11 \pm 0.20	+0.15 \pm 0.08 (1)	+0.15 \pm 0.03 (9)	+0.24 \pm 0.08 (1)	+0.17 \pm 0.07 (3)
182.5364	-1.74	5.76 \pm 0.03 (53)	5.78 \pm 0.04 (10)	<+1.06	+0.24 \pm 0.08 (4)	+0.12 \pm 0.06 (3)	+0.81 \pm 0.10 (1)	+0.07 \pm 0.07 (2)
182.8521	-1.79	5.71 \pm 0.02 (88)	5.81 \pm 0.03 (13)	-0.35 \pm 0.20	+0.26 \pm 0.06 (4)	+0.20 \pm 0.03 (14)	+0.37 \pm 0.11 (1)	+0.26 \pm 0.07 (3)
183.6850	-3.16	4.34 \pm 0.05 (2)	-	<+2.30	+0.01 \pm 0.05 (2)	-	-	-
185.4112	-1.85	5.65 \pm 0.02 (39)	5.71 \pm 0.04 (4)	+0.85 \pm 0.22	+0.16 \pm 0.06 (2)	+0.42 \pm 0.03 (9)	+0.24 \pm 0.09 (1)	+0.05 \pm 0.12 (2)
187.8517	-0.45	7.05 \pm 0.01 (100)	7.13 \pm 0.01 (22)	-0.08 \pm 0.20	+0.05 \pm 0.07 (1)	+0.14 \pm 0.02 (13)	-0.19 \pm 0.07 (1)	+0.03 \pm 0.05 (3)
187.9786	-0.50	7.00 \pm 0.01 (73)	6.99 \pm 0.03 (15)	-0.02 \pm 0.20	+0.30 \pm 0.07 (2)	+0.13 \pm 0.03 (16)	-	+0.02 \pm 0.05 (4)
188.1264	-1.05	6.45 \pm 0.02 (112)	6.50 \pm 0.04 (15)	+0.24 \pm 0.20	+0.18 \pm 0.14 (1)	+0.21 \pm 0.04 (10)	-0.25 \pm 0.14 (1)	-0.46 \pm 0.10 (2)
189.9449	-2.57	4.93 \pm 0.05 (8)	4.87 \pm 0.10 (4)	<+1.44	+0.20 \pm 0.14 (1)	+0.46 \pm 0.09 (3)	-	<-0.03 (1)
190.2669	-0.34	7.16 \pm 0.03 (88)	7.21 \pm 0.03 (23)	+0.09 \pm 0.20	+0.26 \pm 0.10 (1)	+0.08 \pm 0.04 (10)	-	+0.28 \pm 0.06 (3)
190.5813	-0.20	7.30 \pm 0.01 (79)	7.31 \pm 0.02 (20)	+0.41 \pm 0.20	-0.10 \pm 0.06 (3)	+0.12 \pm 0.03 (13)	+0.09 \pm 0.09 (1)	-0.02 \pm 0.05 (4)
190.6313	-0.24	7.26 \pm 0.02 (67)	7.30 \pm 0.03 (20)	+0.15 \pm 0.19	+0.16 \pm 0.08 (1)	+0.06 \pm 0.03 (12)	-	-0.01 \pm 0.05 (3)
192.2121	+0.25	7.75 \pm 0.02 (44)	7.71 \pm 0.03 (17)	-0.02 \pm 0.18	-0.31 \pm 0.05 (2)	-0.00 \pm 0.03 (6)	-0.80 \pm 0.07 (1)	+0.11 \pm 0.09 (3)
192.4285	-0.49	7.01 \pm 0.01 (65)	7.11 \pm 0.03 (15)	+0.32 \pm 0.19	+0.09 \pm 0.07 (1)	+0.07 \pm 0.03 (11)	-	+1.06 \pm 0.05 (3)
192.8540	-0.20	7.30 \pm 0.01 (82)	7.31 \pm 0.01 (22)	+0.10 \pm 0.20	-0.01 \pm 0.04 (3)	+0.15 \pm 0.03 (6)	-0.23 \pm 0.07 (1)	+0.12 \pm 0.05 (4)
192.9068	-0.35	7.15 \pm 0.02 (78)	7.17 \pm 0.02 (18)	+0.12 \pm 0.20	-0.01 \pm 0.05 (3)	+0.13 \pm 0.04 (7)	+0.17 \pm 0.09 (1)	-0.03 \pm 0.07 (4)
193.1159	-1.85	5.65 \pm 0.03 (52)	5.60 \pm 0.05 (7)	+0.82 \pm 0.22	+0.37 \pm 0.07 (3)	+0.27 \pm 0.07 (4)	+0.35 \pm 0.12 (1)	-0.02 \pm 0.12 (1)
193.1501	-0.31	7.19 \pm 0.01 (91)	7.34 \pm 0.03 (20)	-0.03 \pm 0.20	-0.08 \pm 0.07 (2)	+0.10 \pm 0.03 (13)	-	+0.15 \pm 0.05 (4)
193.5542	-0.30	7.20 \pm 0.01 (72)	7.19 \pm 0.02 (18)	-0.04 \pm 0.20	+0.03 \pm 0.05 (2)	+0.20 \pm 0.02 (10)	+0.31 \pm 0.07 (1)	+0.12 \pm 0.05 (4)
193.8390	-2.91	4.59 \pm 0.01 (64)	4.64 \pm 0.04 (10)	+0.00 \pm 0.25	+0.49 \pm 0.06 (3)	+0.25 \pm 0.04 (4)	+0.40 \pm 0.10 (1)	<-2.00 (1)
196.3755	-2.77	4.73 \pm 0.02 (47)	4.74 \pm 0.04 (4)	+0.60 \pm 0.24	+0.35 \pm 0.04 (3)	+0.36 \pm 0.04 (3)	-	-0.63 \pm 0.05 (3)
196.4126	-0.44	7.06 \pm 0.01 (81)	7.01 \pm 0.02 (18)	+0.26 \pm 0.20	+0.24 \pm 0.05 (3)	+0.21 \pm 0.03 (11)	-0.15 \pm 0.09 (1)	-0.25 \pm 0.08 (3)
196.5323	-2.55	4.95 \pm 0.04 (24)	4.74 \pm 0.14 (3)	-	+0.03 \pm 0.10 (3)	+0.27 \pm 0.17 (1)	+0.50 \pm 0.17 (1)	<-0.04 (1)
196.5453	-2.51	4.99 \pm 0.03 (18)	5.08 \pm 0.06 (6)	<+0.84	+0.43 \pm 0.10 (2)	+0.45 \pm 0.06 (5)	+0.41 \pm 0.14 (1)	<-0.45 (1)
196.6013	-0.69	6.81 \pm 0.01 (76)	6.85 \pm 0.03 (10)	+0.16 \pm 0.20	+0.34 \pm 0.09 (1)	+0.12 \pm 0.03 (8)	-0.04 \pm 0.09 (1)	+0.06 \pm 0.07 (2)
197.5045	-0.80	6.70 \pm 0.02 (105)	6.67 \pm 0.03 (17)	+0.37 \pm 0.21	+0.11 \pm 0.07 (2)	+0.22 \pm 0.03 (15)	+0.07 \pm 0.09 (1)	+0.06 \pm 0.06 (4)
197.9861	-1.22	6.28 \pm 0.03 (72)	6.30 \pm 0.07 (14)	<+0.67	+0.42 \pm 0.14 (1)	+0.45 \pm 0.06 (7)	-	-
198.5288	-0.59	6.91 \pm 0.02 (91)	6.88 \pm 0.03 (19)	+0.29 \pm 0.23	+0.12 \pm 0.05 (3)	+0.00 \pm 0.03 (12)	-0.55 \pm 0.08 (1)	+0.31 \pm 0.05 (3)
198.5495	-2.20	5.30 \pm 0.03 (33)	5.23 \pm 0.04 (6)	<+1.12	+0.36 \pm 0.09 (2)	<+0.24 (4)	+1.06 \pm 0.07 (2)	<-0.35 (1)
199.9269	-0.15	7.35 \pm 0.01 (56)	7.47 \pm 0.02 (19)	+0.11 \pm 0.19	-0.01 \pm 0.07 (1)	+0.12 \pm 0.03 (7)	-	+0.14 \pm 0.05 (3)
200.0999	-2.48	5.02 \pm 0.04 (57)	5.27 \pm 0.07 (8)	<+0.39	+0.26 \pm 0.14 (1)	+0.32 \pm 0.09 (3)	-	+0.42 \pm 0.14 (1)
200.5298	-1.02	6.48 \pm 0.03 (98)	6.49 \pm 0.03 (12)	-0.05 \pm 0.19	+0.42 \pm 0.08 (2)	+0.38 \pm 0.04 (11)	-	+0.69 \pm 0.07 (3)
200.7620	-0.15	7.35 \pm 0.02 (63)	7.31 \pm 0.03 (15)	+0.14 \pm 0.20	-0.04 \pm 0.10 (1)	+0.13 \pm 0.04 (8)	-	+0.12 \pm 0.10 (4)
201.1159	-0.19	7.31 \pm 0.02 (63)	7.19 \pm 0.02 (18)	-0.01 \pm 0.20	+0.06 \pm 0.09 (1)	+0.10 \pm 0.03 (11)	-0.02 \pm 0.09 (1)	-0.04 \pm 0.05 (4)
203.2831	-2.70	4.80 \pm 0.03 (54)	4.79 \pm 0.04 (9)	+0.35 \pm 0.23	+0.20 \pm 0.08 (4)	+0.28 \pm 0.04 (7)	-	-0.65 \pm 0.07 (3)
204.9008	-2.66	4.84 \pm 0.12 (4)	4.83 \pm 0.17 (2)	<+2.25	+0.32 \pm 0.14 (3)	-	<-0.49 (1)	-
205.1342	-2.12	5.38 \pm 0.03 (66)	5.56 \pm 0.05 (6)	-0.01 \pm 0.25	+0.17 \pm 0.07 (4)	+0.30 \pm 0.05 (5)	+0.85 \pm 0.12 (1)	+1.30 \pm 0.10 (3)
205.8132	-2.13	5.37 \pm 0.04 (19)	5.39 \pm 0.07 (6)	<+1.43	+0.43 \pm 0.11 (2)	-	+1.03 \pm 0.15 (1)	<+0.13 (1)
206.3487	-1.80	5.70 \pm 0.02 (31)	5.79 \pm 0.04 (9)	<+1.17	-	+0.43 \pm 0.04 (10)	-0.11 \pm 0.10 (1)	-0.38 \pm 0.08 (1)
207.9961	-0.49	7.01 \pm 0.01 (71)	7.09 \pm 0.02 (17)	-0.03 \pm 0.19	+0.27 \pm 0.08 (1)	+0.22 \pm 0.03 (10)	-0.22 \pm 0.08 (1)	-0.10 \pm 0.05 (4)
208.0799	-2.77	4.73 \pm 0.03 (29)	4.80 \pm 0.05 (6)	<+0.59	+0.26 \pm 0.07 (2)	<+0.39 (5)	-	<-0.10 (1)
209.2123	-1.90	5.60 \pm 0.03 (71)	5.56 \pm 0.04 (9)	+0.29 \pm 0.25	+0.30 \pm 0.04 (5)	+0.39 \pm 0.04 (8)	+0.69 \pm 0.10 (1)	-0.36 \pm 0.06 (3)
209.7189	-1.98	5.52 \pm 0.03 (22)	5.56 \pm 0.06 (5)	<+0.72	+0.06 \pm 0.10 (2)	+0.20 \pm 0.07 (4)	+0.88 \pm 0.14 (1)	<-0.18 (3)
209.9364	-2.25	5.25 \pm 0.03 (20)	5.27 \pm 0.07 (6)	+2.18 \pm 0.23	+0.22 \pm 0.07 (3)	+0.37 \pm 0.09 (2)	+0.62 \pm 0.12 (1)	<+0.91 (2)
210.0175	-2.67	4.83 \pm 0.01 (46)	4.95 \pm 0.04 (6)	+0.54 \pm 0.22	+0.35 \pm 0.04 (4)	+0.32 \pm 0.03 (7)	+0.21 \pm 0.09 (1)	+0.79 \pm 0.05 (4)
210.0316	-0.98	6.52 \pm 0.01 (93)	6.46 \pm 0.01 (16)	-0.08 \pm 0.19	+0.38 \pm 0.04 (2)	+0.39 \pm 0.02 (12)	+0.04 \pm 0.07 (1)	-0.20 \pm 0.05 (4)
210.7513	-2.12	5.38 \pm 0.02 (83)	5.42 \pm 0.04 (11)	-0.30 \pm 0.22	+0.42 \pm 0.04 (4)	+0.35 \pm 0.03 (12)	-1.10 \pm 0.09 (1)	+0.49 \pm 0.05 (4)
210.8633	-1.95	5.55 \pm 0.03 (66)	5.57 \pm 0.04 (7)	<+0.16	+0.20 \pm 0.12 (1)	+0.07 \pm 0.06 (4)	+0.46 \pm 0.12 (1)	+0.63 \pm 0.12 (1)
211.2766	-1.39	6.11 \pm 0.02 (88)	6.06 \pm 0.03 (11)	+0.08 \pm 0.23	+0.64 \pm 0.04 (5)	+0.27 \pm 0.03 (14)	+0.67 \pm 0.10 (1)	+1.12 \pm 0.05 (4)
211.7184	-2.42	5.08 \pm 0.02 (79)	5.13 \pm 0.04 (11)	-0.18 \pm 0.23	+0.42 \pm 0.04 (4)	+0.29 \pm 0.04 (7)	-0.58 \pm 0.17 (1)	-0.31 \pm 0.05 (4)
212.5834	-1.79	5.71 \pm 0.03 (47)	5.65 \pm 0.07 (2)	<+0.59	+0.06 \pm 0.07 (2)	+0.24 \pm 0.04 (8)	+0.22 \pm 0.10 (1)	+0.02 \pm 0.10 (1)
213.7878	-2.45	5.05 \pm 0.03 (54)	5.04 \pm 0.04 (9)	+0.73 \pm 0.23	+0.71 \pm 0.06 (4)	+0.38 \pm 0.04 (6)	+0.43 \pm 0.10 (1)	-0.69 \pm 0.10 (3)
214.5557	-2.14	5.36 \pm 0.04 (15)	5.31 \pm 0.07 (3)	+2.02 \pm 0.30	+0.46 \pm 0.07 (2)	-	-	+1.90 \pm 0.07 (4)

Table 2 – *continued*

Star	[Fe/H]	log(Fe I) $\pm \sigma$ (N)	log(Fe II) $\pm \sigma$ (N)	[C/Fe] $\pm \sigma$	[Mg/Fe] $\pm \sigma$ (N)	[Ca/Fe] $\pm \sigma$ (N)	[Sr/Fe] $\pm \sigma$ (N)	[Ba/Fe] $\pm \sigma$ (N)
215.6129	−1.92	5.58 \pm 0.01 (86)	5.58 \pm 0.03 (11)	+0.15 \pm 0.21	+0.33 \pm 0.04 (4)	+0.34 \pm 0.02 (20)	+0.57 \pm 0.09 (1)	−0.05 \pm 0.05 (4)
215.6783	−0.35	7.15 \pm 0.02 (74)	7.22 \pm 0.02 (19)	−0.01 \pm 0.20	+0.16 \pm 0.07 (2)	+0.10 \pm 0.03 (11)	−0.42 \pm 0.09 (1)	+0.08 \pm 0.05 (3)
216.1245	−2.21	5.29 \pm 0.03 (64)	5.24 \pm 0.04 (9)	+0.82 \pm 0.23	+0.28 \pm 0.07 (2)	+0.34 \pm 0.07 (2)	–	+0.04 \pm 0.06 (3)
217.3862	−1.97	5.53 \pm 0.03 (65)	5.58 \pm 0.04 (9)	+0.51 \pm 0.23	+0.41 \pm 0.05 (4)	+0.41 \pm 0.03 (11)	+0.19 \pm 0.10 (1)	−0.51 \pm 0.06 (3)
217.5786	−2.66	4.84 \pm 0.01 (57)	4.99 \pm 0.04 (9)	+0.02 \pm 0.25	+0.47 \pm 0.06 (3)	+0.38 \pm 0.04 (4)	+1.50 \pm 0.09 (1)	+0.35 \pm 0.06 (3)
217.6444	−1.82	5.68 \pm 0.03 (24)	–	<+1.27	+0.20 \pm 0.08 (3)	–	–	+0.63 \pm 0.07 (1)
218.4256	−0.60	6.90 \pm 0.01 (91)	6.91 \pm 0.03 (17)	+0.02 \pm 0.19	+0.25 \pm 0.07 (2)	+0.41 \pm 0.03 (11)	−0.01 \pm 0.17 (2)	+0.01 \pm 0.06 (3)
218.4622	−2.40	5.10 \pm 0.03 (24)	5.15 \pm 0.09 (9)	<+0.80	–	+0.39 \pm 0.14 (2)	+1.00 \pm 0.12 (1)	–
218.4977	−0.16	7.34 \pm 0.01 (50)	7.35 \pm 0.03 (18)	+0.12 \pm 0.19	−0.02 \pm 0.07 (1)	+0.05 \pm 0.03 (7)	−0.38 \pm 0.07 (1)	−0.02 \pm 0.09 (3)
223.5283	−2.30	5.20 \pm 0.01 (89)	5.32 \pm 0.03 (10)	−0.39 \pm 0.21	+0.58 \pm 0.04 (4)	+0.44 \pm 0.03 (10)	+0.74 \pm 0.09 (1)	−0.14 \pm 0.05 (4)
227.2895	−0.35	7.15 \pm 0.02 (92)	7.15 \pm 0.02 (23)	+0.13 \pm 0.23	+0.20 \pm 0.10 (2)	+0.29 \pm 0.03 (11)	−0.04 \pm 0.09 (1)	+0.21 \pm 0.05 (3)
228.4607	−2.20	5.30 \pm 0.04 (17)	5.15 \pm 0.09 (3)	<+1.30	+0.13 \pm 0.09 (3)	–	+0.34 \pm 0.14 (1)	<−0.52 (1)
228.6558	−2.26	5.24 \pm 0.03 (17)	5.18 \pm 0.06 (4)	+1.84 \pm 0.25	+0.42 \pm 0.12 (1)	+0.28 \pm 0.07 (3)	−0.21 \pm 0.12 (1)	–
228.8159	−2.02	5.48 \pm 0.02 (36)	5.55 \pm 0.05 (4)	+1.39 \pm 0.25	+0.18 \pm 0.04 (4)	+0.37 \pm 0.04 (5)	+1.07 \pm 0.10 (1)	<−0.29 (1)
229.0409	−0.10	7.40 \pm 0.03 (50)	7.47 \pm 0.04 (15)	−0.05 \pm 0.22	+0.04 \pm 0.07 (2)	–	−0.54 \pm 0.10 (1)	+0.29 \pm 0.06 (3)
229.1219	−2.25	5.25 \pm 0.03 (19)	5.26 \pm 0.06 (6)	+1.74 \pm 0.25	+0.16 \pm 0.12 (1)	+0.22 \pm 0.07 (3)	+0.92 \pm 0.12 (1)	–
229.8911	+0.10	7.60 \pm 0.02 (62)	7.59 \pm 0.03 (20)	+0.11 \pm 0.22	+0.04 \pm 0.09 (1)	+0.03 \pm 0.03 (10)	–	−0.01 \pm 0.05 (3)
230.4663	−1.15	6.35 \pm 0.02 (102)	6.35 \pm 0.04 (13)	+0.13 \pm 0.23	+0.49 \pm 0.06 (4)	+0.38 \pm 0.03 (12)	+0.45 \pm 0.10 (1)	+0.13 \pm 0.06 (3)
231.0318	−0.35	7.15 \pm 0.02 (69)	7.19 \pm 0.03 (22)	−0.16 \pm 0.19	+0.10 \pm 0.06 (2)	+0.17 \pm 0.03 (8)	−0.39 \pm 0.09 (1)	−0.06 \pm 0.08 (3)
232.6956	−2.22	5.28 \pm 0.03 (63)	5.25 \pm 0.04 (8)	+0.65 \pm 0.23	+0.22 \pm 0.06 (3)	+0.26 \pm 0.10 (6)	−0.11 \pm 0.13 (1)	+0.15 \pm 0.07 (2)
232.8039	−2.26	5.24 \pm 0.03 (54)	5.21 \pm 0.04 (7)	+0.56 \pm 0.22	–	+0.15 \pm 0.06 (6)	+0.15 \pm 0.10 (1)	−1.17 \pm 0.07 (2)
233.5730	−2.74	4.76 \pm 0.02 (53)	4.76 \pm 0.04 (7)	+0.74 \pm 0.25	+0.39 \pm 0.06 (2)	+0.26 \pm 0.04 (5)	+0.31 \pm 0.09 (1)	−0.48 \pm 0.06 (2)
233.9312	−2.20	5.30 \pm 0.02 (50)	5.22 \pm 0.03 (7)	+0.53 \pm 0.22	+0.33 \pm 0.04 (3)	+0.37 \pm 0.03 (5)	–	−0.23 \pm 0.06 (3)
234.4403	−0.40	7.10 \pm 0.02 (72)	7.09 \pm 0.04 (10)	+0.25 \pm 0.22	+0.33 \pm 0.10 (2)	+0.32 \pm 0.04 (9)	–	+0.10 \pm 0.06 (4)
235.1448	−2.54	4.96 \pm 0.04 (22)	4.72 \pm 0.05 (4)	<+1.29	+0.55 \pm 0.07 (2)	+0.24 \pm 0.07 (4)	+0.72 \pm 0.10 (1)	+0.01 \pm 0.10 (1)
235.7578	−1.81	5.69 \pm 0.03 (21)	5.74 \pm 0.04 (6)	+1.38 \pm 0.25	+0.12 \pm 0.07 (4)	+0.32 \pm 0.03 (8)	+0.99 \pm 0.09 (1)	<−0.42 (2)
235.9710	−1.83	5.67 \pm 0.03 (40)	5.67 \pm 0.03 (9)	+1.06 \pm 0.23	+0.35 \pm 0.05 (4)	+0.33 \pm 0.04 (6)	+0.56 \pm 0.10 (1)	−0.09 \pm 0.07 (2)
236.1077	−2.55	4.95 \pm 0.01 (77)	4.95 \pm 0.04 (9)	−0.22 \pm 0.23	+0.42 \pm 0.04 (4)	+0.27 \pm 0.03 (7)	−0.07 \pm 0.10 (1)	+0.09 \pm 0.05 (3)
236.4855	−0.27	7.23 \pm 0.01 (84)	7.27 \pm 0.02 (18)	−0.07 \pm 0.22	−0.08 \pm 0.05 (3)	+0.07 \pm 0.03 (12)	+0.39 \pm 0.09 (1)	+0.09 \pm 0.07 (3)
236.7138	−0.85	6.65 \pm 0.02 (92)	6.70 \pm 0.03 (19)	−0.18 \pm 0.20	+0.34 \pm 0.06 (2)	+0.32 \pm 0.02 (14)	–	−0.10 \pm 0.10 (3)
237.8246	−3.23	4.27 \pm 0.04 (16)	4.16 \pm 0.07 (3)	<+0.58	+0.66 \pm 0.07 (3)	+0.34 \pm 0.07 (3)	+0.05 \pm 0.13 (1)	+0.37 \pm 0.07 (3)
237.8353	−2.32	5.18 \pm 0.02 (58)	5.18 \pm 0.04 (8)	+0.35 \pm 0.23	+0.35 \pm 0.05 (2)	+0.30 \pm 0.03 (10)	−0.09 \pm 0.12 (1)	−0.07 \pm 0.05 (3)
237.9609	−1.90	5.60 \pm 0.03 (46)	5.59 \pm 0.07 (8)	<+0.76	+0.26 \pm 0.07 (3)	+0.26 \pm 0.07 (3)	+0.28 \pm 0.13 (1)	−0.08 \pm 0.13 (1)
238.7217	−2.06	5.44 \pm 0.03 (19)	5.15 \pm 0.09 (5)	<+0.59	−0.21 \pm 0.07 (2)	+0.01 \pm 0.10 (1)	–	<−0.32 (1)
240.0348	−2.30	5.20 \pm 0.02 (85)	5.27 \pm 0.03 (12)	+0.12 \pm 0.22	+0.43 \pm 0.04 (5)	+0.39 \pm 0.03 (6)	+0.46 \pm 0.07 (1)	−0.12 \pm 0.05 (4)
240.4216	−2.98	4.52 \pm 0.02 (27)	4.53 \pm 0.05 (5)	+0.74 \pm 0.25	+0.27 \pm 0.06 (3)	+0.30 \pm 0.04 (4)	+0.77 \pm 0.08 (1)	+0.84 \pm 0.07 (4)
241.1186	−1.92	5.58 \pm 0.03 (32)	5.59 \pm 0.06 (5)	<+1.14	+0.13 \pm 0.12 (1)	+0.24 \pm 0.08 (2)	+0.16 \pm 0.12 (1)	−0.48 \pm 0.12 (1)
241.7900	−2.51	4.99 \pm 0.04 (15)	4.65 \pm 0.20 (3)	<+2.38	+0.30 \pm 0.12 (2)	+0.33 \pm 0.07 (6)	+0.12 \pm 0.18 (1)	<+0.13 (1)
242.3556	−1.95	5.55 \pm 0.03 (22)	5.43 \pm 0.07 (5)	<+1.13	+0.01 \pm 0.15 (1)	<+0.17 (4)	−0.08 \pm 0.15 (1)	<−0.82 (2)
243.8390	−1.95	5.55 \pm 0.03 (52)	5.49 \pm 0.06 (10)	<+0.15	+0.43 \pm 0.09 (3)	+0.39 \pm 0.04 (5)	+0.72 \pm 0.09 (1)	+0.39 \pm 0.09 (1)
244.4872	−2.10	5.40 \pm 0.07 (10)	5.34 \pm 0.10 (5)	+0.83 \pm 0.30	–	–	–	<+0.03 (2)
245.1096	−0.35	7.15 \pm 0.01 (69)	7.14 \pm 0.03 (15)	−0.02 \pm 0.20	+0.06 \pm 0.06 (2)	+0.16 \pm 0.03 (10)	+0.21 \pm 0.07 (1)	−0.06 \pm 0.05 (4)
245.4387	−1.67	5.83 \pm 0.03 (44)	5.74 \pm 0.04 (9)	<+0.94	+0.08 \pm 0.12 (3)	+0.26 \pm 0.03 (9)	+1.05 \pm 0.07 (1)	−0.32 \pm 0.07 (2)
245.5747	−3.17	4.33 \pm 0.03 (10)	4.17 \pm 0.07 (2)	+1.26 \pm 0.25	+0.45 \pm 0.06 (2)	–	−0.11 \pm 0.07 (1)	–
245.8364	−3.06	4.44 \pm 0.02 (26)	4.49 \pm 0.06 (3)	+0.63 \pm 0.23	+0.58 \pm 0.05 (4)	+0.44 \pm 0.05 (4)	+0.38 \pm 0.10 (1)	−0.50 \pm 0.07 (2)
246.8588	−2.25	5.25 \pm 0.02 (78)	5.27 \pm 0.04 (10)	−0.18 \pm 0.23	+0.44 \pm 0.06 (3)	+0.42 \pm 0.04 (6)	+0.13 \pm 0.10 (1)	−0.03 \pm 0.05 (4)
248.4394	−1.72	5.78 \pm 0.01 (51)	5.75 \pm 0.04 (8)	+0.61 \pm 0.22	+0.23 \pm 0.11 (3)	+0.35 \pm 0.03 (7)	+0.53 \pm 0.06 (1)	+0.11 \pm 0.05 (3)
248.4959	−2.63	4.87 \pm 0.02 (58)	4.88 \pm 0.06 (6)	+0.02 \pm 0.25	+0.33 \pm 0.05 (3)	+0.30 \pm 0.03 (7)	−0.31 \pm 0.09 (1)	−0.31 \pm 0.05 (3)
248.5263	−2.07	5.43 \pm 0.03 (49)	5.36 \pm 0.04 (4)	+0.25 \pm 0.30	+0.47 \pm 0.05 (3)	+0.30 \pm 0.04 (4)	+0.24 \pm 0.09 (1)	<−0.09 (4)
250.6971	−2.66	4.84 \pm 0.03 (58)	4.99 \pm 0.04 (8)	<−0.01	+0.36 \pm 0.09 (3)	+0.23 \pm 0.06 (2)	+0.84 \pm 0.09 (1)	−0.25 \pm 0.05 (3)
250.8797	+0.05	7.55 \pm 0.01 (65)	7.55 \pm 0.02 (18)	−0.06 \pm 0.20	−0.08 \pm 0.06 (2)	+0.05 \pm 0.03 (8)	−0.19 \pm 0.09 (1)	−0.09 \pm 0.05 (3)
251.4082	−3.22	4.28 \pm 0.02 (31)	4.20 \pm 0.05 (4)	+0.58 \pm 0.25	+0.14 \pm 0.07 (2)	+0.10 \pm 0.10 (1)	<+1.20 (1)	−0.68 \pm 0.06 (3)
252.1648	−2.43	5.07 \pm 0.01 (69)	5.18 \pm 0.05 (3)	−0.06 \pm 0.23	+0.31 \pm 0.04 (4)	+0.29 \pm 0.04 (7)	−0.73 \pm 0.09 (1)	−0.72 \pm 0.05 (4)
252.4208	−1.30	6.20 \pm 0.01 (96)	6.24 \pm 0.03 (16)	+0.02 \pm 0.22	+0.56 \pm 0.06 (4)	+0.35 \pm 0.03 (13)	+0.03 \pm 0.09 (1)	+0.05 \pm 0.05 (4)
252.4917	−0.60	6.90 \pm 0.01 (86)	6.99 \pm 0.02 (14)	−0.07 \pm 0.24	+0.22 \pm 0.04 (4)	+0.10 \pm 0.02 (14)	+0.17 \pm 0.07 (1)	−0.20 \pm 0.05 (4)
252.6179	−2.52	4.98 \pm 0.01 (72)	5.07 \pm 0.03 (8)	+0.34 \pm 0.22	+0.57 \pm 0.04 (4)	+0.47 \pm 0.03 (9)	+0.69 \pm 0.07 (1)	−0.09 \pm 0.05 (4)
253.8582	−2.58	4.92 \pm 0.03 (44)	4.94 \pm 0.04 (5)	<+0.55	+0.47 \pm 0.06 (3)	+0.17 \pm 0.04 (5)	<−1.16 (1)	−0.31 \pm 0.06 (3)
254.0662	−0.56	6.94 \pm 0.02 (92)	7.01 \pm 0.02 (21)	+0.03 \pm 0.19	+0.28 \pm 0.04 (4)	+0.27 \pm 0.02 (13)	−0.02 \pm 0.07 (1)	+0.02 \pm 0.05 (4)
254.5215	−0.09	7.41 \pm 0.01 (66)	7.41 \pm 0.01 (19)	+0.07 \pm 0.18	−0.07 \pm 0.05 (2)	+0.09 \pm 0.02 (10)	−0.36 \pm 0.07 (1)	+0.12 \pm 0.06 (4)
254.5478	−2.15	5.35 \pm 0.02 (64)	5.33 \pm 0.04 (9)	+0.22 \pm 0.21	+0.23 \pm 0.04 (4)	+0.26 \pm 0.04 (6)	+0.12 \pm 0.09 (1)	+0.23 \pm 0.05 (4)
254.7768	−0.35	7.15 \pm 0.01 (75)	7.12 \pm 0.01 (20)	+0.14 \pm 0.20	+0.07 \pm 0.05 (2)	+0.18 \pm 0.02 (11)	−0.09 \pm 0.07 (1)	−0.13 \pm 0.05 (3)
255.2679	−2.09	5.41 \pm 0.03 (33)	5.34 \pm 0.07 (7)	<+1.42	+0.11 \pm 0.08 (3)	+0.17 \pm 0.08 (3)	–	<−0.49 (1)
255.5564	−2.55	4.95 \pm 0.03 (33)	5.12 \pm 0.06 (4)	+0.56 \pm 0.25	+0.61 \pm 0.07 (1)	–	+0.50 \pm 0.07 (1)	+0.59 \pm 0.06 (2)
255.8043	−2.99	4.51 \pm 0.05 (9)	4.58 \pm 0.09 (3)	+1.23 \pm 0.30	+0.63 \pm 0.09 (3)	+0.74 \pm 0.09 (3)	−0.54 \pm 0.14 (1)	<−0.45 (2)

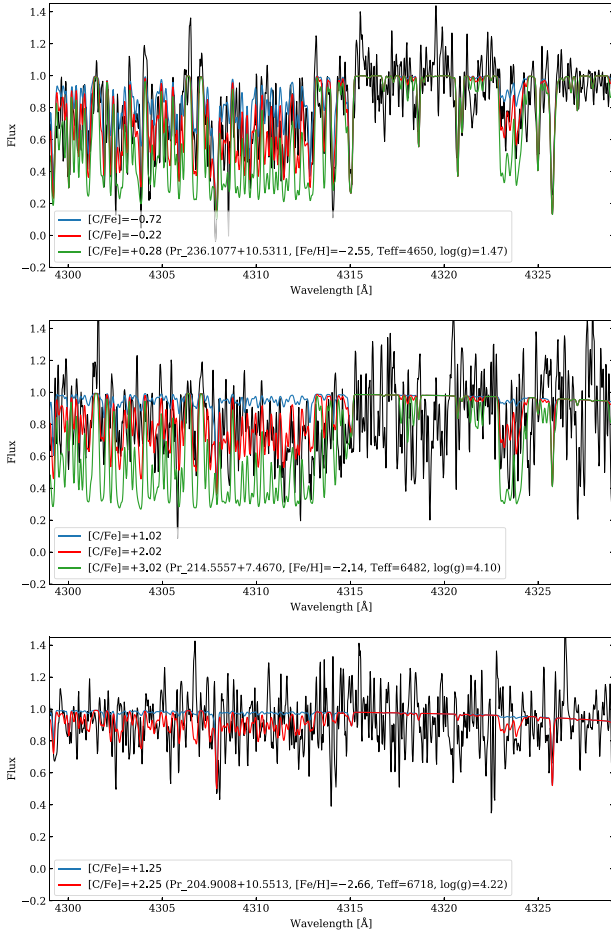


Figure 4. Examples of observed and synthetic spectra in the region of the CH molecular absorption band. *Top panel:* The cool (4650 K) RGB star Pr.236.1077+10.5311 is presented. The red line shows the best synthetic spectrum at $[C/Fe] = -0.22$. The blue and green lines correspond to the synthetic spectrum when the carbon abundance is decreased and increased by 0.5 dex ($[C/Fe] = -0.72$ and $+0.28$), respectively. The difference is clearly seen, especially in the $\lambda 4323$ Å region, illustrating that the determination of the carbon abundance is robust in cool giants. *Middle panel:* The warm (~ 6500 K) TO star Pr.214.5557+7.4670 is presented. At these very high T_{eff} , the CH feature is very weak, only high carbon-enhancement can be measured. The red line represents the best synthetic spectrum with $[C/Fe] = +2.02$, the blue and green colour shows how the CH feature change when the C abundance is decreased and increased by 1.0 dex ($[C/Fe] = +1.02$ and $+3.02$), respectively. *Bottom panel:* The warm (~ 6700 K) TO star Pr.204.9008+10.5513 is presented. The carbon upper limit is represented by the red synthetic spectrum with $[C/Fe] = +2.25$. The blue line corresponds to the synthetic spectrum when the carbon abundance is decreased by 1.0 dex ($[C/Fe] = +1.25$). Both synthetic spectra are at the level of the noise, illustrating that only upper limits at a high $[C/Fe]$ level can be placed for the warmest and most metal-poor stars of the sample.

The dispersion σ_X around the weighted mean abundance of an element X measured from several lines is computed as

$$\sigma_X = \sqrt{\frac{\sum_i (\epsilon_i - \bar{\epsilon})^2}{N_X - 1}}, \quad (2)$$

where N_X represents the number of lines measured for element X, and ϵ stands for the logarithmic abundance.

The final error on the elemental abundances is defined as

$$\sigma_{fin} = \max \left(\frac{\sigma_X}{\sqrt{N_X}}, \frac{\sigma_{Fe}}{\sqrt{N_X}} \right). \quad (3)$$

As a consequence, no element X can have an estimated dispersion $\sigma_X < \sigma_{Fe}$; this is particularly important for species with very few lines.

4 RESULTS

In the following, we compare results from our spectroscopic analysis to literature and discuss the derived elemental abundances in the broader context of evolution of low-mass stars and Galactic chemical evolution.

4.1 Comparison with previous work

To verify the reliability of the derived chemical abundances, we compare our abundance estimates to literature values.

We show in Fig. 6 a comparison between our spectroscopic metallicities and the results derived by Venn et al. (2020) for the stars in common (see Section 2.1). The two investigations agree very well for the 28 stars with $[Fe/H] \leq -2.5$ for which Venn et al. (2020) provided full spectroscopic analysis (star symbols in Fig. 6). For these stars, we compute an average difference in metallicity as small as $\Delta[Fe/H]_{(\text{Venn et al.-this work})} = -0.06$ dex ($\sigma = 0.15$ dex). Differences in the adopted atmospheric parameters are also small –e.g. $\Delta T_{\text{eff}}(\text{Venn et al.-this work}) = 20$ K ($\sigma = 40$ K) and $\Delta \log g(\text{Venn et al.-this work}) = -0.09$ dex ($\sigma = 0.17$ dex).

For the stars with previous Q6 analysis only (circles in Fig. 6), the agreement is good ($\Delta[Fe/H]_{(\text{Venn et al.-this work})} = -0.15$ dex), however, we also note a significant dispersion ($\sigma = 0.5$ dex) towards the metal-rich tail of the $[Fe/H]$ distribution. In this case, part of the observed differences likely results from the adoption of different atmospheric parameters in the two studies. In this work, we derive parameters using the information encoded in the spectra (see Section 3). In contrast, Venn et al. (2020) adopt the ‘Bayesian inference method’ (Sestito et al. 2019) that makes combined use of SDSS and *Gaia* DR2 photometry, and adopts a priori photometric metallicities from *Pristine* to select the appropriate MESA/MIST isochrone with solar-scaled composition (Paxton et al. 2011; Dotter 2016) to infer parameters. Hence, the assumption of an incorrect metallicity affects the derivation of atmospheric parameters and the estimation of the final $[Fe/H]$. This is particularly true for stars in the metal-rich regime ($[Fe/H] \geq -1.5$) in Fig. 6. For stars with $[Fe/H] \geq -1.5$, we compute an average difference of $\Delta T_{\text{eff}}(\text{Venn et al.-this work}) = 175$ K ($\sigma = 300$ K), and $\Delta \log g(\text{Venn et al.-this work}) = -0.20$ dex ($\sigma = 0.60$ dex) that is significantly larger than the one derived for stars with $[Fe/H] \leq -1.5$; e.g. $\Delta T_{\text{eff}}(\text{Venn et al.-this work}) = 120$ K ($\sigma = 200$ K), and $\Delta \log g(\text{Venn et al.-this work}) = 0.05$ dex ($\sigma = 0.25$ dex).

As Venn et al. (2020) adopted the *Pristine* photometric metallicity estimates a priori, metal-rich stars turn out to be not well calibrated (e.g. T_{eff} and $[Fe/H]$ are degenerate; see section 4.3 in Venn et al. 2020). However, we note that the spectra presented in Venn et al. (2020) were collected between 2016 and 2018 and the *Pristine* metallicity calibrations have improved over the course of these spectroscopic follow-up observations (see discussion in Venn et al. 2020).

Different line list, codes, and minimizing procedures can also play a role. A careful investigation of the observed discrepancy is not the main goal of this study.

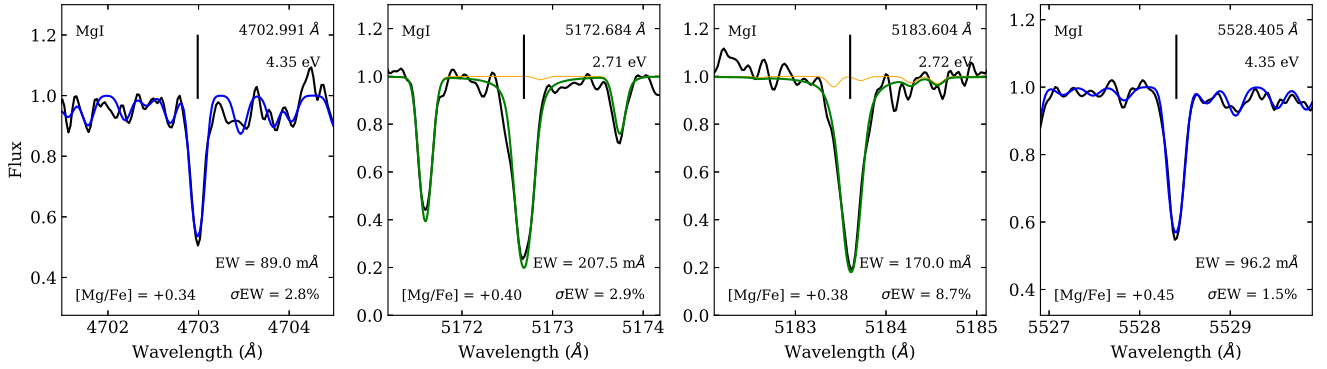


Figure 5. Comparison for star Pr.211.7184+15.5516 of the derived abundances from the four Mg lines available in the spectrum. Abundances from Mg 4702.991 Å and 5528.405 Å were obtained through their EWs (blue colour), abundances of the stronger Mg 5172.684 Å and 5183.604 Å lines were obtained by spectral synthesis (green colour). EW measurements of the latest two are given as indication only and not used for the abundance determination. Abundances are obtained by spectral synthesis, they are very consistent, and they well agree with the EW results with a standard deviation of $\sigma = 0.05$ dex. Orange lines are synthetic spectra without Mg, allowing the identification of blends.

Table 3. Changes in the mean abundances $\delta \log \epsilon(X)$ caused by a change of ± 150 K on T_{eff} , ± 0.15 on $\log g$, and ± 0.15 on v_t for cool stars (< 6000 K) and ± 200 K on T_{eff} , ± 0.20 on $\log g$, and ± 0.20 on v_t for warm stars (> 6000 K), corresponding to the typical uncertainties on the stellar parameters. We provide T_{eff} , $\log g$, v_t and $[\text{Fe}/\text{H}]$ for each of the three representative stars.

El.	$+\Delta T_{\text{eff}}$	$-\Delta T_{\text{eff}}$	$+\Delta \log g$	$-\Delta \log g$	$+\Delta v_t$	$-\Delta v_t$
Pr.203-2831+13-6326 (5008 1.95 1.45 – 2.7)						
Fe I	+0.12	–0.15	+0.00	+0.01	–0.02	+0.03
Fe II	+0.01	–0.01	+0.04	–0.06	–0.03	+0.03
C I	+0.35	–0.38	–0.05	+0.05	+0.00	+0.01
Mg I	+0.09	–0.08	+0.00	+0.01	+0.00	+0.01
Ca I	+0.10	–0.12	–0.01	+0.00	–0.02	+0.02
Sr II	+0.21	–0.24	–0.03	+0.03	+0.00	+0.00
Ba II	+0.11	–0.11	+0.05	–0.05	–0.02	+0.02
Pr.196-6013+15-6768 (5600 4.6 1.08 – 0.69)						
Fe I	+0.06	–0.10	–0.02	+0.01	–0.02	+0.02
Fe II	–0.04	+0.05	+0.05	–0.06	–0.04	+0.04
C I	+0.20	–0.21	–0.03	+0.02	–0.02	+0.02
Mg I	+0.09	–0.09	–0.04	+0.03	–0.01	+0.01
Ca I	+0.10	–0.11	–0.04	+0.03	–0.03	+0.02
Sr II	+0.16	–0.22	–0.05	+0.01	–0.05	+0.01
Ba II	+0.07	–0.07	+0.03	–0.03	–0.04	+0.05
Pr.206-3487+9-3099 (6522 3.94 1.21 – 1.8)						
Fe I	+0.15	–0.14	–0.02	+0.02	–0.04	+0.06
Fe II	+0.03	–0.03	+0.10	–0.10	–0.10	+0.10
C I	+0.29	–0.28	–0.08	+0.09	+0.00	+0.00
Mg I	+0.13	–0.12	–0.05	+0.04	+0.0	+0.02
Ca I	+0.12	–0.10	–0.03	+0.02	–0.05	+0.03
Sr II	+0.15	–0.14	+0.09	–0.07	–0.17	+0.19
Ba II	+0.14	–0.15	+0.07	–0.09	–0.05	+0.04

4.2 Newly detected very metal-poor stars

We identify 31 new VMP stars in total that were whether missed by the quick analysis in Venn et al. (2020), or are presented in this work for the first time (see Section 2.1).

Among the sample of 20 stars presented in this study for the first time, eight VMP stars (including five stars with $[\text{Fe}/\text{H}] < -2.5$ and one EMP star at $[\text{Fe}/\text{H}] = -3$, Pr.255.8043+10.8443) have been identified. Interestingly, two of these VMP stars were removed from the more recent versions of the *Pristine* catalogue.

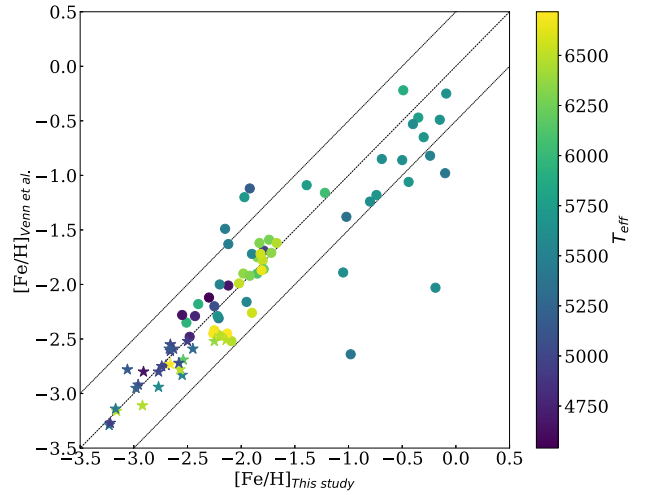


Figure 6. Comparison with the metallicities of Venn et al. (2020) for the 86 stars in common. Colours code the stellar effective temperature. Circles represent the stars whose metallicities were previously only based on the Q6 method of Venn et al. (2020). Star symbols identify stars for which Venn et al. (2020) provided full chemical characterization. For convenience, the one-to-one line and the ± 0.5 dex lines are also shown.

Among the 57 stars from Venn et al. (2020) with a Q6 estimation only, no star previously marked at $[\text{Fe}/\text{H}] < -2.5$ was missed by the quick analysis. However, an additional set of 19 stars are now identified as VMP, with $[\text{Fe}/\text{H}] < -2.0$. From those three have $[\text{Fe}/\text{H}] \sim -2.5$.

Among the 26 stars from Venn et al. (2020) that were rejected by the *Pristine* photometric selection before any analysis, 4 turn out to be actually VMP with $-2.5 < [\text{Fe}/\text{H}] < -2.0$.

The six VMP stars ($[\text{Fe}/\text{H}] \leq -2$) that were erroneously rejected from the more recent version *Pristine* catalogue, are highlighted in red in Fig. 3. Because we are working at the bright end of the catalogue, these stars have saturated flags in one of the *ugri* magnitudes of SDSS. Since *Pristine* aims at maximizing the rejection of contaminants, the later versions of the catalogue conservatively rejects any star that could *potentially* be affected by saturation. In some cases, the *g* and *i* magnitudes that are mainly used to infer the *Pristine* metallicities may in fact not be affected and the inferred

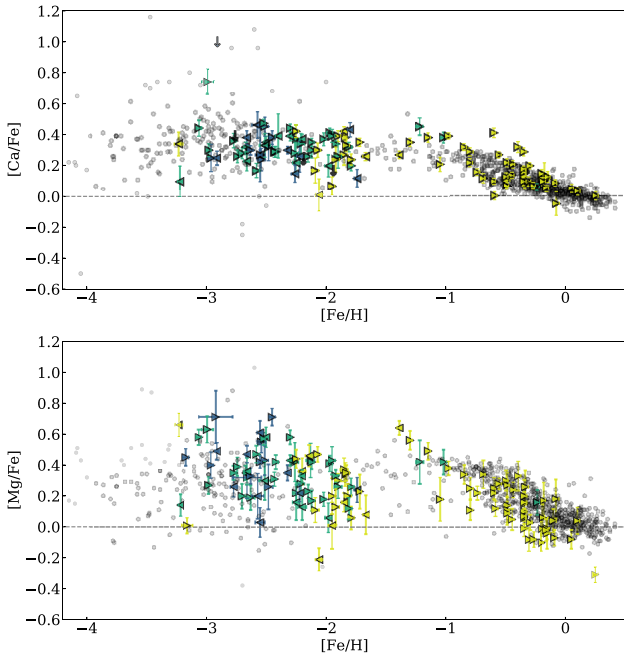


Figure 7. α -elements: Calcium (top panel) and magnesium (bottom panel) abundances and upper limits are plotted against metallicity for the full sample. Left and right arrows stand for stars with prograde and retrograde motions, respectively. Yellow, green, and dark blue identify stars in the MW disc, inner halo, outer halo, respectively (see Section 5). Comparison galactic stars (in grey) are from Yong et al. (2013) and Bensby, Feltzing & Oey (2014).

metallicity can be accurate, as shown with some of the rejected stars studied here that we determine to be VMP.

4.3 Abundances for the α -elements: Mg and Ca

In order to gauge the general composition of our sample, Fig. 7 presents the trend of the α -elements, calcium and magnesium, with $[\text{Fe}/\text{H}]$. While Mg is produced in hydrostatic H and He nuclear burning in massive core-collapse SNe progenitors, Ca originates mainly from the pre-SN explosion, and can also be produced later by SNeIa (Woosley & Weaver 1986).

Our sample follows closely the MW halo distribution in Ca and Mg (e.g. Yong et al. 2013). The large majority of the stars in the metal-poor regime ($[\text{Fe}/\text{H}] < -1$) are enhanced in α -elements. There is a well-defined plateau at $[\text{Ca}/\text{Fe}] = +0.3$ dex with a small dispersion of $\sigma \sim 0.1$ dex. We do not find any sub-solar $[\text{Ca}/\text{Fe}]$ stars in our sample as it had been the case for Caffau et al. (2020). Metal-poor stars are also enhanced in Mg, with a larger dispersion ($\sigma \sim 0.3$ dex) though, arising from the larger uncertainties induced by the smaller number of lines for Mg than for Ca.

Two stars have $[\text{Mg}/\text{Fe}]$ significantly lower than the rest of our sample at similar $[\text{Fe}/\text{H}]$. Pr_192.2121+7.4778 at $[\text{Fe}/\text{H}] = +0.25$ ($T_{\text{eff}} = 5600\text{K}$, $\log g = 4.3$) and Pr_238.7217+6.1945 at $[\text{Fe}/\text{H}] = -2.06$ ($T_{\text{eff}} = 6551$, $\log g = 4.2$). The calcium abundance places Pr_238.7217+6.1945 at the low edge of the distribution, at solar $[\text{Ca}/\text{Fe}]$, as well. Considering that it is among the hottest stars of our sample, very few lines are accessible to the analysis. It looks also depleted in Mg with respect to stars with the same metallicity. However, its $[\text{Mg}/\text{Fe}]$ abundance ratio is compatible with the main body of the ESPaDOnS sample when errors due to atmospheric parameters (see Table 3) are taken into account.

Pr_192.2121+7.4778 is the most metal-rich star of our sample. At this metallicity, with $[\text{Mg}/\text{Fe}] = -0.31 \pm 0.05$, it could resemble the Mg-poor MW field stars with globular cluster chemical patterns that Fernández-Trincado et al. (2017) have analysed. However Pr_192.2121+7.4778 is not particularly enriched in Al. Further specific investigation for this star shows that it is not particularly abundant in SNe type Ia products such as Cr or Co either. Moreover $[\text{Si}/\text{Fe}] \sim 0$, just as $[\text{Ca}/\text{Fe}]$, typical of the MW disc stars. Mackereth et al. (2019) have shown from the analysis of APOGEE DR14 the correspondence between the lowest $[\text{Mg}/\text{Fe}]$ and lowest eccentricity even in the MW disc. At this stage, one can only say that, with $e = 0.175$ this star is indeed in the low quartile of the e -distribution in our sample.

Pr_251.4082+12.3657 at $[\text{Fe}/\text{H}] = -3.22$ has relatively low α ratios, $[\text{Ca}/\text{Fe}] = +0.1$ and $[\text{Mg}/\text{Fe}] = +0.14$, but we do not confirm the sub-solar $[\text{Mg}/\text{Fe}]$ value found by Venn et al. (2020). However, this star is one of the most metal-poor one of the sample and the single Ca line measurable is weak (< 20 mÅ), making its abundance difficult to ascertain.

At the other end of the abundance ratio distribution, Pr_255.8043+10.8443, at $[\text{Fe}/\text{H}] = -3$, the EMP from the new sample, is very enriched in both Ca and Mg, at $+0.63$ and $+0.74$, respectively, however, with no other outstanding chemical feature. In particular, only an upper limit to its C abundance could be estimated. As found by Venn et al. (2020), Pr_181.2243+07.4160 has high $[\text{Mg}/\text{Fe}] = +0.7$ dex and high calcium abundance, however, this is a warm TO star (6450 K) with small Ca features, hence only an upper limit can be placed.

4.4 Carbon abundances and internal mixing

Our sample allows for the investigation of the carbon abundance of MW stars over a wide range of metallicities and to simultaneously explore the impact of internal mixing.

Indeed, during the evolution on the RGB, carbon is converted into nitrogen due to the CN cycle, then mixed to the surface of the star. This mechanism occurs when low-mass stars ($\leq 2.5 M_{\odot}$) evolve off the main sequence (MS). Their outer convective envelope starts to move inward, dredging up material that has been processed through the CN-cycle in the inner regions (First Dredge-up, Iben 1964). In a more advanced stage of evolution along the RGB, these stars experience an additional mixing episode just after the RGB bump, when the molecular weight barrier (the μ -barrier) left by the convective envelope at the point of deepest inward progress is canceled out by the outward expansion of the H-burning shell. This extra-mixing episode (Sweigart & Mengel 1979; Charbonnel 1995; Angelou et al. 2012) produces a decline in the surface abundance of carbon ($[\text{C}/\text{Fe}]$) and $^{12}\text{C}/^{13}\text{C}$ (Briley et al. 1990; Gratton et al. 2000; Martell, Smith & Briley 2008; Gerber, Briley & Smith 2019) and lithium (Lind et al. 2009), and an increase in the nitrogen abundance (Gratton et al. 2000).

The degree of carbon depletion is a function of both metallicity and the initial stellar carbon and nitrogen abundances. This is already discussed extensively in the literature (Spite et al. 2005, 2006; Aoki et al. 2007; Placco et al. 2014; Shetrone et al. 2019). Along this line, Fig. 8 presents the $[\text{C}/\text{Fe}]$ abundance ratio of our sample stars as a function of their luminosity in three different metallicity bins. The different evolutionary phases, MS and turn-off (TO) stars, lower RGB and upper RGB stars, are identified following the Gratton et al. (2000) classification. In unevolved stars ($\log L/L_{\odot} < 0.8$), the average C abundance in stars with $[\text{Fe}/\text{H}] > -1.5$ is $[\text{C}/\text{Fe}] = 0.05 \pm 0.16$ (48 stars). The C abundance appears to increase at first

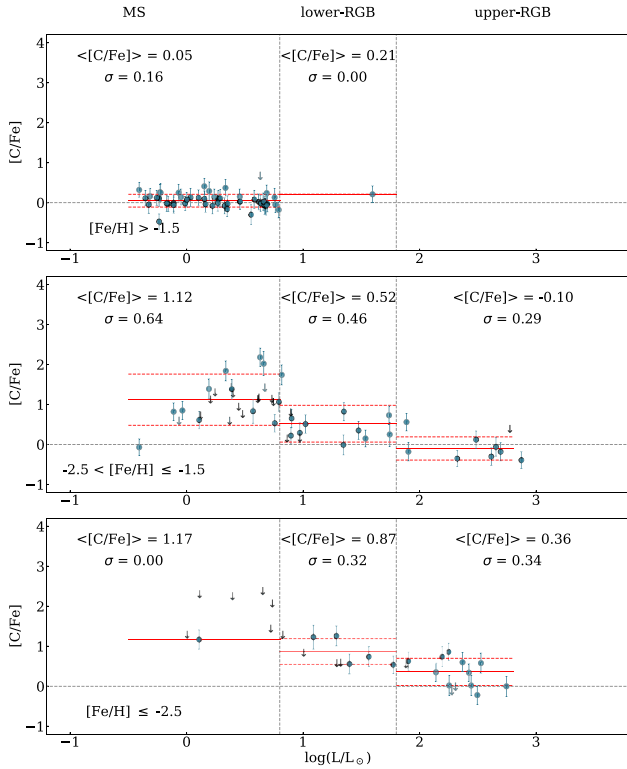


Figure 8. Run of the abundance ratios of $[C/Fe]$ with luminosity for stars with different metallicities (from top to bottom: $[Fe/H] > -1.5$; $-2.5 < [Fe/H] \leq -1.5$, and $[Fe/H] \leq -2.5$). The dotted vertical lines separate different evolutionary phases – MS and TO stars; lower RGB and upper RGB stars – following the Gratton et al. (2000) classification. The red lines represent the mean carbon abundances along with their standard deviation in the various different evolutionary stages (solid and dashed lines; respectively).

dredge up with a value of $[C/Fe] = 0.21$, however, this apparent increase is only based on a single stars on the lower RGB and thus not significant. In the lower metallicity bins, the carbon depletion is more severe. At the first dredge up, C abundances decrease from $[C/Fe] = +1.12$ to $[C/Fe] = +0.52$ for the stars in the metallicity range $-2.5 < [Fe/H] \leq -1.5$, and from $[C/Fe] = +1.17$ to $[C/Fe] = +0.87$ for the lowest metallicity bin $[Fe/H] \leq -2.5$.

4.5 Frequency of C-enhanced stars

As discussed by Norris & Yong (2019), the 3D-NLTE treatment of Fe I and CH-based carbon abundances could change our view of the genuine fraction of CEMP stars in the future. Until these calculations are fully accessible, 1D-LTE studies, such as this one, are important.

CEMP stars are commonly separated into two broad categories, according to their chemical composition: carbon enriched stars that display an overabundance of heavy elements formed in slow (s), intermediate (i), or rapid (r) neutron capture processes (CEMP-s, CEMP-i, CEMP-r, and CEMP-r/s); and CEMP-no, stars that display no such excess of neutron-capture elements (Spite et al. 2013). The observed chemical pattern of CEMP-s and CEMP-r/s stars is thought to be the result of mass transfer in a binary system (e.g. Masseron et al. 2010 but see also Hansen et al. 2016).

Our sample encompasses 38 stars with $[Fe/H] \leq -2.0$ and measured C abundance (Table 2). 14 of them have $[C/Fe] \geq 0.7$ (criterion for CEMP stars of Aoki et al. 2007) and 8 of them have $[C/Fe] \geq 1$ (criterion for CEMP stars of Beers & Christlieb 2005).

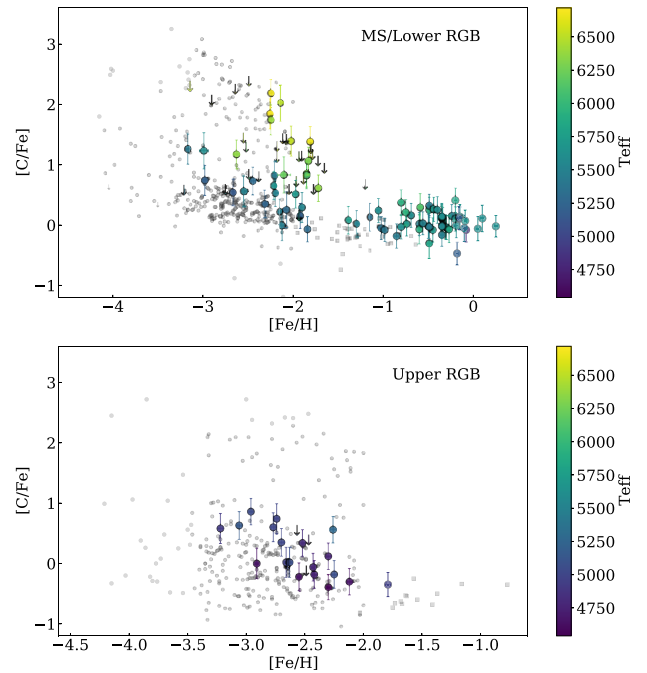


Figure 9. Top panel: $[C/Fe]$ abundance ratios are plotted against stellar metallicities $[Fe/H]$ for unevolved stars (e.g. stars with $\log(L/L_\odot) < 1.8$) and colour coded by T_{eff} . Bottom panel: $[C/Fe]$ abundance ratios are plotted against stellar metallicities $[Fe/H]$ for evolved stars (e.g. stars with $\log(L/L_\odot) > 1.8$). Upper limits for carbon are plotted as downward arrows. The evolutionary phases are based on the work of Gratton et al. (2000). Grey circles are MW halo stars from Placco et al. (2014), whereas grey squares are from Gratton et al. (2000).

This translates into a frequency of CEMP stars of 37 per cent and 21 per cent for the two criteria, respectively. This is consistent with the results of Aguado et al. (2019) that found 41 per cent and 23 per cent, respectively, of CEMP stars in the large medium-resolution survey of *Pristine*. However, we note the number of CEMP stars in Aguado et al. (2019) is likely overestimated due to systematic biases in their derived $\log g$ values and a strong dependence of $[C/Fe]$ on $\log g$ in their analysis. This issue will be further discussed in Arentsen et al. (in preparation).

Fig. 9 presents the carbon abundances of our ESPaDOnS sample stars depending on their evolutionary stage. The top panel shows the run of $[C/Fe]$ abundance ratios for unevolved stars in the sample ($\log(L/L_\odot) < 1.8$; Gratton et al. 2000), while the bottom panel displays the same trend for the evolved stars ($\log(L/L_\odot) \geq 1.8$) we have analysed.

As summarized in Table 4, the dwarf sub-sample of Placco et al. (2014) has a fraction of 35 per cent and 29 per cent of carbon-rich stars depending on the criterion adopted ($[C/Fe] > +0.7$ versus $[C/Fe] > +1.0$), while our sub-sample of VMP dwarfs is composed of 60 per cent and 40 per cent of C-rich stars considering the same criteria. However, we note that large uncertainties are associated with the derived CEMP fractions (e.g. of the order of ~ 15 per cent) because of the small size of the observed sample. Also, for warm stars, carbon abundances could be measured only for object with a relatively high level of C overabundance. Both factors must be taken into account when the fractions in Table 4 are compared to literature and larger (an un-biased) samples of EMP stars are required.

The trend with temperature in the dwarf sub-sample is clearly seen in Fig. 9 – the C-rich stars having the highest T_{eff} (> 5800 K). This

Table 4. Fraction of CEMP stars in our sample of stars compared to the work of Placco et al. (2014), we consider only the stars with carbon measurements (not the upper limits), and compare the results with the criterion $[C/Fe] > +0.7$ of Aoki et al. (2007), and $[C/Fe] > +1.0$ of Beers & Christlieb (2005)

Study	VMP dwarfs	$[C/Fe] \geq +0.7$	Fraction	$[C/Fe] \geq +1.0$	Fraction
Placco 2014	348 (56 per cent)	123	35 per cent	101	29 per cent
This work	20 (52.5 per cent)	12	60 per cent	8	40 per cent
	VMP giants	$[C/Fe] \geq +0.7$	Fraction	$[C/Fe] \geq +1.0$	Fraction
Placco 2014	268 (44 per cent)	60	22.4 per cent	48	18 per cent
This work	18 (47.5 per cent)	2	11 per cent	0	0 per cent

correlation is very much driven by the fact that at the low SNR (7–25) in the blue part of the spectra, normal carbon abundances were out of reach for the hot stars. Only the very strong absorption bands of the CEMP stars were measurable (see Fig. 4). In that case, we were facing observational limits rather than a bias in the *Pristine* selection.

The comparison between the upper and lower panels of Fig. 9 illustrates the clear dichotomy between the giants and the dwarfs in our sample. We almost totally lack C-rich giant stars, with only two stars with $[C/Fe] > +0.7$ (and none with $[C/Fe] > +1.0$) among our 18 VMP giants, i.e. 11 per cent compared to 22 per cent in the sample of Placco et al. (2014). However, given the small sample size, the errors associated with such fraction is as large as the estimated fraction itself (of the order of ± 10 per cent). Thus we cannot draw firm conclusions on the CEMP fraction for evolved giants from such a comparison.

Placco et al. (2014) developed a procedure to compute corrections for the evolutionary depletion of carbon. The corrections tend to increase the C abundances and they depend on the surface gravity, the metallicity of the star, and the observed carbon abundance. The corrections reach up to $+0.70$ dex at $[Fe/H] = -3$, $\log g = 1.0$. They would increase the number of giants that can be considered as C-rich in our sample, however, Fig. 9 and Table 4 compare non-corrected abundances only, thus the low CEMP fractions in our subsample of VMP giant is real and probably results from a bias in the *Pristine* photometric selection process of the VMP candidates. This selection appears to favour the warm C-rich TO stars but to be biased against the cooler evolved CEMP stars. Most probably this is also the reason for the very low fraction of C-enhanced stars in Caffau et al. (2020), in which nearly all VMP stars are cool giants. The origin of this *Pristine* selection bias will be further discussed in a forthcoming study (Arentsen et al., in preparation).

4.6 Abundances for the heavy-elements Sr and Ba

Heavy elements (e.g. elements with atomic number greater than 30; $Z > Z_{Zn}$) are produced through the slow (s) and rapid (r) neutron-capture processes. The main sources of s-process elements are asymptotic giant branch stars (Busso, Gallino & Wasserburg 1999; Bisterzo et al. 2012), while r-process occurs instead in different types of core-collapse SNe (Hillebrandt, Takahashi & Kodama 1976; Woosley et al. 1994; Wanajo et al. 2001; Nishimura et al. 2006; Kratz, Farouqi & Möller 2014) and neutron star merger (Lattimer & Schramm 1974; Freiburghaus, Rosswog & Thielemann 1999; Rosswog et al. 2000; Wanajo 2013; Thielemann et al. 2017).

The wavelength range of the ESPaDOnS spectra includes the spectral features of two neutron-capture elements, Sr and Ba. Because europium is mostly produced by the r-process, $[Ba/Eu]$ ratios are commonly used to identify the origin of the heavy elements. Unfortunately, no Eu lines were measurable in our spectra.

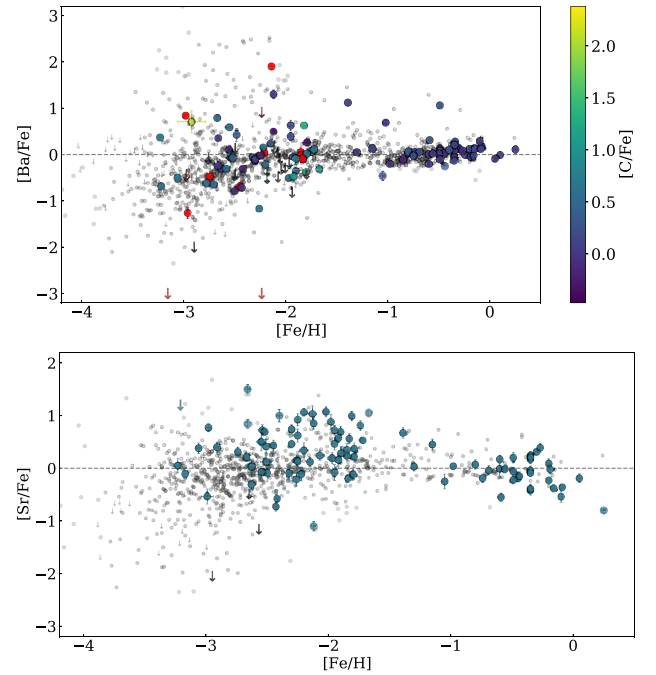


Figure 10. Neutron-capture elements: Barium-to-iron ratio as a function of metallicity at the top, and strontium-to-iron ratio at the bottom. Pointing down arrows are upper limits. Grey dots are galactic comparison stars compiled by Roederer (2013). The $[Ba/Fe]$ ratios are colour coded by their carbon content, red points are carbon-rich stars defined by the criterion of Aoki et al. (2007).

Fig. 10 presents the $[Ba/Fe]$ and $[Sr/Fe]$ measurements of the ESPaDOnS data set compared to MW halo population (Roederer 2013). Barium is generally sub-solar at $[Fe/H] < -2$ with nevertheless a large scatter with some stars highly enhanced or depleted in barium. Above $[Fe/H] \sim -2$, $[Ba/Fe]$ converges to the solar value and the scatter is almost completely removed at $[Fe/H] > -1$.

The comparison between the C and Ba abundances allows one to identify CEMP-no and CEMP-s stars (Beers & Christlieb 2005). In the absence of Eu, we base our classification on the work of Matsuno et al. (2017), $[Ba/Fe] > 1$ for CEMP-s, adding $[Sr/Ba]$ when possible following Hansen et al. (2019) ($[Ba/Fe] > 0$, $[Sr/Ba] < -1.5$ for CEMP-r, $-1.5 < [Sr/Ba] < -0.5$ for CEMP-r/s, and $-0.5 < [Sr/Ba] < 0.75$ for CEMP-s). While it would not be sufficient to discriminate between CEMP-s and CEMP-r/s (Goswami, Singh Rathour & Goswami 2021), it is probably good enough to distinguish between CEMP-r and the other categories.

We colour code in red in Fig. 10 the stars that are carbon enhanced ($[C/Fe] > +0.7$). The arrows indicate the CEMP stars for which

only upper limits in Ba could be derived; most of these stars are hot ($T_{\text{eff}} > 6200$ K).

A few stars stand out from our sample: Pr.245.5747+6.8844 ($[\text{Fe}/\text{H}] = -3.17$) is a CEMP-no star ($[\text{C}/\text{Fe}] = +1.26$) without any detectable barium line, while at $T_{\text{eff}} = 5424$ K it could be measurable, and its strontium abundance is normal ($[\text{Sr}/\text{Fe}] = -0.1$). It is identified in Fig. 10 by its upper limit arbitrarily put at $[\text{Ba}/\text{Fe}] = -3$. Again, following the classification of Hansen et al. (2019), Pr.180.2206+9.5683 is another possible CEMP-no star ($[\text{Fe}/\text{H}] = -2.96$, $[\text{C}/\text{Fe}] = +0.86$) with both low Ba and Sr ($[\text{Ba}/\text{Fe}] = -1.26$, $[\text{Sr}/\text{Fe}] < -2.05$). Barium was not detectable in two other CEMP stars (Pr.134.3232+17.6970, and Pr.228.6558+9.0914) with $[\text{Fe}/\text{H}] < -2.0$. They are all carbon-rich but they are TO stars with effective temperatures ≥ 6350 K. At these temperatures the barium spectral features are very weak and require a much higher SNR.

We confirm the finding of Venn et al. (2020) that Pr.214.5557+7.4670 ($[\text{Fe}/\text{H}] = -2.14$) is enriched in Ba. This is most probably a CEMP-s candidate with $[\text{Ba}/\text{Fe}] = +1.90$ and $[\text{C}/\text{Fe}] = +2.22$ (fig. 7 of Matsuno et al. 2017). Unfortunately, its strontium lines are buried in the noise, and the Y lines very much so as well.

The bottom panel of Fig. 10 presents $[\text{Sr}/\text{Fe}]$ as a function of $[\text{Fe}/\text{H}]$. Although our sample is relatively devoid of low abundance ratios, it matches the distribution of the MW stars known so far. One star, Pr.210.7513+12.7744 at $[\text{Fe}/\text{H}] = -2.12$, stands out of the general distribution with a significantly lower strontium content level $[\text{Sr}/\text{Fe}] = -1.10$ for its metallicity, while its Ba content is normal ($[\text{Ba}/\text{Fe}] = +0.49$). This depletion in Sr has essentially been observed in (most of) the ultra-faint dwarfs (UFDs) and is so far understood as the evidence for the second channel of Sr production to be missing in these faint systems, possibly by undersampling of the initial mass function (e.g. Tafelmeyer et al. 2010; Jablonka et al. 2015; Mashonkina et al. 2017; Ji et al. 2019; Sitnova et al. 2021). Interestingly the kinematic analysis of the orbit of Pr.210.7513+12.7744 confirms that it is a halo member, with an orbit almost perpendicular to the plane of the MW (see Section 5), with an apocentre of $R_{\text{apo}} = 10.7^{+1.8}_{-1.3}$ kpc.

5 ORBITS

Thanks to *Gaia* EDR3 (Gaia Collaboration 2016, 2021), we can now measure the distances and the orbital parameters of our sample with increased accuracy. The first step for determining the kinematic properties of our stars is to measure their distances. Since it is ill advised to invert the parallax (Bailer-Jones 2015), we infer the distances using a Bayesian inference method. The posterior probability on the distance is composed by two factors, a Gaussian likelihood on the parallax and a prior on the stellar density distribution as in equation (8) from Sestito et al. (2019). We choose a method that does not depend on theoretical isochrones, thereby differing from previous *Pristine* papers (e.g. Sestito et al. 2020; Venn et al. 2020). For the zero-point on the *Gaia* EDR3 parallax, we use the PYTHON code GAIADR3_ZEROPOINT⁴ as described in Lindegren et al. (2021). Then, we use GALPY package (Bovy 2015) to determine the orbital parameters. For this analysis, we modify their `MWPotential14` assuming a more massive halo of $M = 1.2 \times 10^{12} M_{\odot}$ compatible with the value from Bland-Hawthorn & Gerhard (2016), as fully described in Sestito et al. (2019, and references therein). We run the orbital inference also for the 112 stars from Venn et al. (2020),

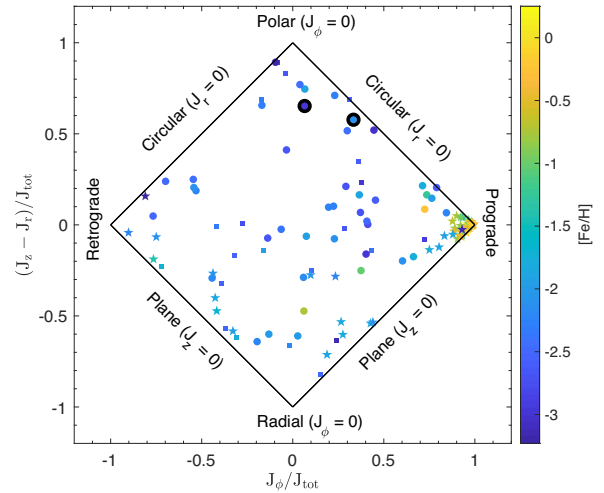


Figure 11. Action plot of the stellar sample colour coded by metallicity. The x-axis is the azimuthal component of the action vector, proxy for rotation. The vertical axis is the difference between the vertical and the radial component of the action vector. Both the axis are normalized by $J_{\text{tot}} = J_r + J_z + |J_\phi|$. Squares denote outer halo stars ($R_{\text{apo}} \geq 15$ kpc and $Z_{\text{max}} > 3.5$ kpc), circles marked the inner halo stars ($R_{\text{apo}} < 15$ kpc and $Z_{\text{max}} > 3.5$ kpc), while the star symbol denotes the stars confined to the MW plane ($Z_{\text{max}} \leq 3.5$ kpc). The two bigger markers with edge colour in black represent Pr.210.7513+12.7744 and Pr.255.8043+10.8443.

since *Gaia* EDR3 provides a better measurement of the astrometric solution than *Gaia* DR2 (Gaia Collaboration 2018), and therefore on the distance and the orbits.

Fig. 11 shows the azimuthal component of the action vector versus the difference between the vertical and the radial components of the action, both axis normalized by the sum of the action components. In this space, stars with different kinematics occupy different portions of this diagram. We divide the total sample of 132 stars into three groups: outer halo ($R_{\text{apo}} \geq 15$ kpc and $Z_{\text{max}} > 3.5$ kpc), inner halo ($R_{\text{apo}} < 15$ kpc and $Z_{\text{max}} > 3.5$ kpc), and confined to the disc ($Z_{\text{max}} \leq 3.5$ kpc). The limits on the apocentre distance R_{apo} and the maximum height Z_{max} from the MW plane are arbitrarily chosen and follow Sestito et al. (2019, 2020). The chemical distribution of these populations is illustrated in Fig. 7.

This *Pristine*-ESPaDOs sample is composed of 65 halo stars. The 22 outer halo stars have $[\text{Fe}/\text{H}] \leq -1.75$. The 43 inner halo stars share the same metallicity distribution at the exception of 4 stars, 3 prograde, and 1 $J_\phi = 0$, at $[\text{Fe}/\text{H}] > -1.5$ that overlay on the region covered by the MW disc stars. These four stars have a Z_{max} between 3.9 and 7 kpc and the apocentre is between 8 and 9.6 kpc. Two of them have a high eccentricity, 0.77 and 0.9. Their maximum height place them clearly above the plane. They might be born in the disc and then heated up afterwards. In total 67 stars, mostly prograde, are confined in the MW disc. This planar subsample contains 10 high eccentricity stars in the range $-2.25 \leq [\text{Fe}/\text{H}] \leq -1.56$, 7 of which are prograde, and 4 retrograde. There are also two EMP stars on a disc orbit, one is prograde and the other is retrograde. Finally, all but one planar stars at $[\text{Fe}/\text{H}] \geq -1.5$ are prograde. A full analysis of this sample, in particular regarding the possible association with known stellar structures, is beyond the scope of this paper. However, we focus on two objects, Pr.210.7513+12.7744 and Pr.255.8043+10.8443, whose chemistry stands out from the rest of the sample. The former has a low content of Sr, while the latter is a new EMP star. Both the stars are located in the top region of the action plot in Fig. 11 (see the

⁴<https://gitlab.com/icc-ub/public/gaiadr3.zeropoint>

larger markers), and they display a prograde polar orbit. This region has been shown to be occupied by the recently discovered LMS-1 stream (Yuan et al. 2020; Malhan et al. 2021), a 60 deg long structure wrapping around the inner region of the MW. The proper motion and position on the sky of Pr.255.8043+10.8443 do not match the ones of LMS-1 (see fig. 4 of Malhan et al. 2021), hence we can exclude a possible association with this stream. As to Pr.210.7513+12.7744, we find differences in RV ($RV \sim 40 \text{ km s}^{-1}$) and right ascension (~ 8 deg) between this star and the best-fitting orbit of LMS-1 (see fig. 4 of Malhan et al. 2021). The comparison of the orbital parameters of Pr.210.7513+12.7744 with the ones of the simulated stars in this stream indicates that an association with the leading trail can be excluded. However, this star might belong to the older wraps of LMS-1, which display a much larger dispersion on their orbital parameters than the leading trail. Would Pr.210.7513+12.7744 be confirmed as a member in the future, it would undoubtedly open new insight into the star formation history of the parent galaxy of LMS-1.

6 SUMMARY AND CONCLUSIONS

We have presented the homogeneous 1D, LTE analysis of 132 stars observed at high resolution with ESPaDOnS, so far the largest sample at high resolution ($R \sim 40\,000$) from the *Pristine* survey. This study expands on the earlier work of Venn et al. (2020), in which only 28 VMP stars were fully chemically characterized. Because this sample is based on the first version of the *Pristine* catalogue, the success rate of identification of genuine EMP stars is not as high as in the later versions. As a consequence, the range of metallicity of our sample extends much beyond -2 , reaching $[\text{Fe}/\text{H}] = +0.25$. Nevertheless, near half of our sample (58 stars) is composed of VMP stars ($[\text{Fe}/\text{H}] \leq -2$). The more metal-rich stars offer us the opportunity of a new and detailed study of the MW halo stellar population. Because it encompasses both dwarf and giant stars, it also enables the analysis of any potential biases induced by the *Pristine* selection process.

Based on *Gaia* EDR3, the orbital analysis of this *Pristine*-ESPaDOnS sample showed that it is composed of 65 halo stars and 67 disc stars. After a general assessment of the sample chemical properties with the α -elements Mg and Ca, we focused on the abundance of carbon and the neutron capture elements, Ba and Sr. Our results can be summarized as follows.

(i) We presented a chemical analysis of 31 newly identified VMP stars, out of which 23 were already presented in Venn et al. (2020) but they were not identified as VMP stars in their Q6 analysis. Eight VMP stars (including five stars with $[\text{Fe}/\text{H}] < -2.5$ and one EMP star at $[\text{Fe}/\text{H}] = -3$) were identified in the subset of 20 stars analysed in this study for the first time.

(ii) Comparing the earliest and latest version of the *Pristine* catalogues, it appears that some VMP stars (six) are missed because their SDSS magnitudes, at the bright end of the selection, are saturated or polluted by instrumental failure. The latest *Pristine* catalogues conservatively reject these objects, even if the *Pristine* metallicity estimate is in fact correct.

(iii) We provide carbon abundances for 97 stars and upper limits for the rest of the sample. From the 38 stars with $[\text{Fe}/\text{H}] \leq -2.0$ and carbon measurements, 14 are CEMP stars following the criterion of Aoki et al. (2007), which sets the C-enrichment threshold at $[\text{C}/\text{Fe}] = +0.7$. This results in a global frequency of CEMP stars at 37 per cent, which is consistent with other studies.

(iv) However, we almost completely miss the C-rich stars in VMP giants, with only 11 per cent of CEMP stars compared to 22 per cent in the sample of Placco et al. (2014). This is a clear sign for *Pristine*

selection bias against carbon-rich giants, which will be analysed in a future work.

(v) Looking at the abundances in Ba, a few VMP stars stand out: Pr.245.5747+6.8844 at $[\text{Fe}/\text{H}] = -3.17$ is a CEMP-no star. Pr.180.2206+9.5683 at $[\text{Fe}/\text{H}] = -2.96$ is another CEMP-no candidate. Pr.214.5557+7.4670 ($[\text{Fe}/\text{H}] = -2.14$) is most probably a CEMP-s star.

(vi) While most our sample is a good match to the known Sr content of the MW population, one star, Pr.210.7513+12.7744 at $[\text{Fe}/\text{H}] = -2.12$ has a particularly low $[\text{Sr}/\text{Fe}] = -1.10$ for its metallicity. This is typical of the abundance ratios found in most of the UFDs, making it a possible fossil of accretion in the MW halo. The orbit of Pr.210.7513+12.7744 is perpendicular to the MW plane. Its kinematical parameters are not far from those of the older wraps of LMS-1 stream.

This work clearly shows the enormous potential of the *Pristine* survey and its spectroscopic follow-ups at low and high resolution. Many open issues in modern astrophysics and cosmology can be tackled thanks to the accurate chemical tagging of the EMPs identified by the *Pristine* photometry and studied with spectroscopy, especially when abundances are combined with the information provided by *Gaia*. For example, large samples of stars with a chemo-dynamical characterization, like the one presented in this paper, can be used to check for possible associations with streams in the halo (e.g. Venn et al. 2020; Kienly et al. 2021). Along the same lines, it would be of interest to obtain high-resolution observations covering larger wavelength ranges (and spectral features of a wider variety of elements) for the two stars that chemo-dynamically stand out from the others (e.g. Pr.210.7513+12.7744 and Pr.255.8043+10.8443; see Section 5) to investigate for possible associations with known structures/accretion events.

Finally, upcoming spectroscopic surveys with high multiplex capabilities – e.g. WAVE (Dalton et al. 2012), 4MOST (de Jong et al. 2019) – will provide us with even larger and more representative samples of metal deficient stars to investigate in fine details the first stages of chemical enrichment of the Galaxy.

ACKNOWLEDGEMENTS

We warmly thank Ian Roederer who very kindly sent us his compilation of Sr and Ba measurements in Milky Way halo stars. This work is based on observations obtained with ESPaDOnS as well as MegaPrime/MegaCam, a joint project of CFHT and CEA/DAPNIA, at the Canada–France–Hawaii Telescope (CFHT) which is operated by the National Research Council (NRC) of Canada, the Institut National des Science de l’Univers of the Centre National de la Recherche Scientifique (CNRS) of France, and the University of Hawaii. The observations at the CFHT were performed with care and respect from the summit of Maunakea which is a significant cultural and historic site. NFM gratefully acknowledge support from the French National Research Agency (ANR) funded project ‘Pristine’ (ANR-18-CE31-0017) along with funding from INSU/CNRS through the Programme National Galaxies et Cosmologie and through the CNRS grant PICS07708 and from the European Research Council (ERC) under the European Unions Horizon 2020 research and innovation programme (grant agreement No. 834148). The authors thank the International Space Science Institute, Berne, Switzerland for providing financial support and meeting facilities to the international team ‘Pristine’. CL acknowledges funding from Ministero dell’Università e della Ricerca through the Programme ‘Rita Levi Montalcini’ (grant PGR18YRML1). ES acknowledges funding through VIDI grant

‘Pushing Galactic Archaeology to its limits’ (with project number VI.Vidi.193.093) which is funded by the Dutch Research Council (NWO). KAV is grateful for funding through the National Science and Engineering Research Council Discovery Grants program. This work has made use of data from the European Space Agency (ESA) mission *Gaia* (<https://www.cosmos.esa.int/gaia>), processed by the *Gaia* Data Processing and Analysis Consortium (DPAC, <https://www.cosmos.esa.int/web/gaia/dpac/consortium>). Funding for the DPAC has been provided by national institutions, in particular the institutions participating in the *Gaia* Multilateral Agreement.

DATA AVAILABILITY

The data underlying this article will be shared on reasonable request to the corresponding author.

REFERENCES

- Aguado D. S. et al., 2019, *MNRAS*, 490, 2241
- Angelou G. C., Stancliffe R. J., Church R. P., Lattanzio J. C., Smith G. H., 2012, *ApJ*, 749, 128
- Aoki W., Beers T. C., Christlieb N., Norris J. E., Ryan S. G., Tsangarides S., 2007, *ApJ*, 655, 492
- Arlandini C., Käppeler F., Wisshak K., Gallino R., Lugaro M., Busso M., Straniero O., 1999, *ApJ*, 525, 886
- Asplund M., Grevesse N., Sauval A. J., Scott P., 2009, *ARA&A*, 47, 481
- Bailer-Jones C. A. L., 2015, *PASP*, 127, 994
- Beers T. C., Christlieb N., 2005, *ARA&A*, 43, 531
- Beers T. C., Preston G. W., Shtetman S. A., 1992, *AJ*, 103, 1987
- Bensby T., Feltzing S., Oey M. S., 2014, *A&A*, 562, A71
- Bisterzo S., Gallino R., Straniero O., Cristallo S., Käppeler F., 2012, *MNRAS*, 422, 849
- Bland-Hawthorn J., Gerhard O., 2016, *ARA&A*, 54, 529
- Blanton M. R. et al., 2017, *AJ*, 154, 28
- Bonifacio P. et al., 2019, *MNRAS*, 487, 3797
- Bovy J., 2015, *ApJS*, 216, 29
- Briley M. M., Bell R. A., Hoban S., Dickens R. J., 1990, *ApJ*, 359, 307
- Bromm V., Larson R. B., 2004, *ARA&A*, 42, 79
- Bromm V., Loeb A., 2003, *Nature*, 425, 812
- Busso M., Gallino R., Wasserburg G. J., 1999, *ARA&A*, 37, 239
- Caffau E. et al., 2011, *Nature*, 477, 67
- Caffau E. et al., 2013, *A&A*, 560, A71
- Caffau E. et al., 2017, *Astron. Nachr.*, 338, 686
- Caffau E. et al., 2020, *MNRAS*, 493, 4677
- Cayrel R. et al., 2004, *A&A*, 416, 1117
- Charbonnel C., 1995, *ApJ*, 453, L41
- Choi J., Dotter A., Conroy C., Cantiello M., Paxton B., Johnson B. D., 2016, *ApJ*, 823, 102
- Christlieb N., Schörrck T., Frebel A., Beers T. C., Wisotzki L., Reimers D., 2008, *A&A*, 484, 721
- Cohen J. G., Christlieb N., Thompson I., McWilliam A., Shtetman S., Reimers D., Wisotzki L., Kirby E., 2013, *ApJ*, 778, 56
- Dalton G. et al., 2012, in McLean I. S., Ramsay S. K., Takami H., eds, *Proc. SPIE Conf. Ser. Vol. 8446, Ground-based and Airborne Instrumentation for Astronomy IV*. SPIE, Bellingham, p. 84460P
- de Jong R. S. et al., 2019, *Messenger*, 175, 3
- Demarque P., Woo J.-H., Kim Y.-C., Yi S. K., 2004, *ApJS*, 155, 667
- Deng L.-C. et al., 2012, *Res. Astron. Astrophys.*, 12, 735
- Donati J. F., Catala C., Landstreet J. D., Petit P., 2006, in Casini R., Lites B. W., eds, *ASP Conf. Ser. Vol. 358, Solar Polarization 4*. Astron. Soc. Pac., San Francisco, p. 362
- Dotter A., 2016, *ApJS*, 222, 8
- Eisenstein D. J. et al., 2011, *AJ*, 142, 72
- Fernández-Trincado J. G. et al., 2017, *ApJ*, 846, L2
- Frebel A., 2018, *Annu. Rev. Nucl. Part. Sci.*, 68, 237
- Frebel A., Norris J. E., 2015, *ARA&A*, 53, 631
- Freiburghaus C., Rosswog S., Thielemann F. K., 1999, *ApJ*, 525, L121
- Gaia Collaboration, 2016, *A&A*, 595, A1
- Gaia Collaboration, 2018, *A&A*, 616, A1
- Gaia Collaboration, 2021, *A&A*, 649, A1
- Gerber J. M., Briley M. M., Smith G. H., 2019, *AJ*, 157, 154
- Goswami P. P., Singh Rathour R., Goswami A., 2021, *A&A*, 649, A49
- Gratton R. G., Sneden C., Carretta E., Bragaglia A., 2000, *A&A*, 354, 169
- Hansen T. T., Andersen J., Nordström B., Beers T. C., Placco V. M., Yoon J., Buchhave L. A., 2016, *A&A*, 588, A3
- Hansen C. J., Hansen T. T., Koch A., Beers T. C., Nordström B., Placco V. M., Andersen J., 2019, *A&A*, 623, A128
- Heger A., Woosley S. E., 2010, *ApJ*, 724, 341
- Hill V. et al., 2019, *A&A*, 626, A15
- Hillebrandt W., Takahashi K., Kodama T., 1976, *A&A*, 52, 63
- Iben I. Jr., 1964, *ApJ*, 140, 1631
- Ivans I. L., Sneden C., James C. R., Preston G. W., Fulbright J. P., Höflich P. A., Carney B. W., Wheeler J. C., 2003, *ApJ*, 592, 906
- Jablonka P. et al., 2015, *A&A*, 583, A67
- Jacobson H. R. et al., 2015, *ApJ*, 807, 171
- Ji A. P., Simon J. D., Frebel A., Venn K. A., Hansen T. T., 2019, *ApJ*, 870, 83
- Keller S. C. et al., 2007, *Publ. Astron. Soc. Aust.*, 24, 1
- Khoperskov S., Haywood M., Snaith O., Di Matteo P., Lehnert M., Vasiliev E., Naroenkov S., Berczik P., 2021, *MNRAS*, 501, 5176
- Kielty C. L. et al., 2021, *MNRAS*, 506, 1438
- Kratz K.-L., Farouqi K., Möller P., 2014, *ApJ*, 792, 6
- Kupka F. G., Ryabchikova T. A., Piskunov N. E., Stempels H. C., Weiss W. W., 2000, *Balt. Astron.*, 9, 590
- Lattimer J. M., Schramm D. N., 1974, *ApJ*, 192, L145
- Lind K., Primas F., Charbonnel C., Grundahl F., Asplund M., 2009, *A&A*, 503, 545
- Lindgren L. et al., 2021, *A&A*, 649, A4
- Lucchesi R. et al., 2020, *A&A*, 644, A75
- Mackereth J. T. et al., 2019, *MNRAS*, 482, 3426
- Majewski S. R., APOGEE Team, APOGEE-2 Team, 2016, *Astron. Nachr.*, 337, 863
- Malhan K., Yuan Z., Ibata R., Arentsen A., Bellazzini M., Martin N. F., 2021, *ApJ*, 920, 51
- Martell S. L., Smith G. H., Briley M. M., 2008, *PASP*, 120, 7
- Mashonkina L., Jablonka P., Sitnova T., Pakhomov Y., North P., 2017, *A&A*, 608, A89
- Masseron T., Johnson J. A., Plez B., van Eck S., Primas F., Goriely S., Jorissen A., 2010, *A&A*, 509, A93
- Matsuno T., Aoki W., Suda T., Li H., 2017, *PASP*, 69, 24
- Mucciarelli A., 2013, preprint ([arXiv:1311.1403](https://arxiv.org/abs/1311.1403))
- Nishimura S., Kotake K., Hashimoto M.-a., Yamada S., Nishimura N., Fujimoto S., Sato K., 2006, *ApJ*, 642, 410
- Nissen P. E., Schuster W. J., 2010, *A&A*, 511, L10
- Norris J. E., Yong D., 2019, *ApJ*, 879, 37
- Pagel B. E. J., Cambridge Univ. Press Cambridge 1997, *Nucleosynthesis and Chemical Evolution of Galaxies*
- Paxton B., Bildsten L., Dotter A., Herwig F., Lesaffre P., Timmes F., 2011, *ApJS*, 192, 3
- Piskunov N. E., Kupka F., Ryabchikova T. A., Weiss W. W., Jeffery C. S., 1995, *A&AS*, 112, 525
- Placco V. M., Frebel A., Beers T. C., Stancliffe R. J., 2014, *ApJ*, 797, 21
- Plez B., 2012, *Astrophysics Source Code Library*, record ascl:1205.004
- Prochaska J. X., McWilliam A., 2000, *ApJ*, 537, L57
- Roederer I. U., 2013, *AJ*, 145, 26
- Roederer I. U., Preston G. W., Thompson I. B., Shtetman S. A., Sneden C., Burley G. S., Kelson D. D., 2014, *AJ*, 147, 136
- Rosswog S., Davies M. B., Thielemann F. K., Piran T., 2000, *A&A*, 360, 171
- Ryabchikova T. A., Piskunov N. E., Kupka F., Weiss W. W., 1997, *Balt. Astron.*, 6, 244
- Sakari C. M. et al., 2019, *ApJ*, 874, 148
- Schlegel D. J., Finkbeiner D. P., Davis M., 1998, *ApJ*, 500, 525
- Sestito F. et al., 2019, *MNRAS*, 484, 2166
- Sestito F. et al., 2020, *MNRAS*, 497, L7
- Shetrone M. et al., 2019, *ApJ*, 872, 137

5 Conclusions and outlooks

Analytical tools :

Hundreds of absorption lines are present in stellar spectra. When hundreds of stars are analysed, this can quickly results in a huge amount of work to provide reliable chemical abundances.

During the 4 years of this thesis, an efficient Python tool was developed to help to perform all the different steps of the chemical abundance determination.

Stellar model interpolation, stellar atmospheric parameters optimization, abundance derivation from equivalent width, abundance derivation from spectral synthesis, line inspection and selection, the objective was to make all the steps as simple and flexible as possible with this tool.

For the Milky Way sample, a code was developed to significantly improve the quality of the spectra produced by the pipeline of the echelle order CFHT/ESPaDOnS spectrograph. The spectral overlapping regions are selected and cut to keep only the highest S/N regions, significantly improving the homogeneity of the final spectra.

Dwarf galaxies :

A detailed spectroscopic chemical analysis have been carried out for a unique sample of very and extremely metal-poor stars (all with $[\text{Fe}/\text{H}] < -2.5$), observed at high resolution with very good signal to noise ratios.

The α -element plateau was confirmed at the same level as the MW halo population in the EMP regime, with a relative low dispersion. The α -plateau of Fornax and Carina, very barely explored in the EMP regime, is also better defined now.

We can conclude that most of the classical dwarfs galaxies, despite having very different star formation histories and chemical compositions in their later stages, they were sharing very similar early conditions of formation.

We saw that neutron-capture elements strontium and barium, are produced at different levels in dwarfs galaxies. When $[\text{Ba}/\text{Fe}]$ ratios are generally sub-solar at $[\text{Fe}/\text{H}] \sim -3$, ratios of $[\text{Sr}/\text{Fe}]$ are

already at the solar level (Fig. 8, 9 paper Sec. 3.3). This suggests a production site of strontium that appends earlier than for the heavier n-capture element barium. This difference in production is not observed in the ultra faint dwarf (UFD) galaxies, as seen in Figure 4 of [Ji et al. \(2019\)](#) who compiled all the Sr and Ba abundances available in UFDs. The limit of this divergence between the UFDs and the classical low-mass end Sextans-like dwarfs, is still an open question.

However this study has shown the difficulty to access the early history of these systems. At distances of the order of $\sim 10^5$ pc, only the brightest candidates can be observed at high resolution and sufficient SNR to reveal their chemical composition. This is generally only reached with the largest 8m-class telescopes, such as the VLT or SUBARU. A single star requires several hours of exposure time. Thus, only few EMPs were identified and studied in detail in dSphs, and some very informative chemical elements such as lithium or europium remain inaccessible most of the time. Larger samples are needed to fully characterise the different nucleosynthesis process involved, but also to draw some maps of the chemical distributions and better link the observations to the simulations.

The European Extremely Large Telescope (E-ELT), planned for 2025, will be the first 40-m class telescope in history, followed by the Thirty Meter Telescope (TMT) in 2027, and more projects. They should allow to probe the dwarf galaxy stellar population to a depth never reached before.

Milky Way and the *Pristine* survey :

The work presented in Chapter 4 is the largest sample of stars observed at high resolution by the *Pristine* survey and analysed in a fully homogeneous way. This analysis provided a general interesting view of the Milky Way disk and halo stellar population, on both chemical and dynamical aspects.

However, this sample of stars selected from an early version of the *Pristine* catalogue allowed to identify a probable bias during the selection process against giant carbon-enhanced stars. It will be important to identify if the bias is coming from the filter itself or from the colour-colour diagnostic (Figure 4.4) and its calibration. We however identified some CEMP-no and CEMP-s stars in this sample.

Finally, a very interesting star with unusual low strontium abundance at its metallicity has been identified. It is very likely accreted from an UFD, as seen above. The discussion is still on-going for further observations and investigations of this star.

Large photometric surveys proved their efficiency in the identification of metal-poor stars. If the selection is not reaching a 100% success rate yet, it is continuously improving. New instruments will also drastically change the identification of interesting MW targets or to confirm their membership to fainter systems. WEAVE ([Dalton et al. 2016](#)), a multi-object spectrograph will soon start observations at the 4.2m William Herschel Telescope (WHT). With 1000 fibres and a 2° field of view, it will allow the metallicity and radial velocity confirmation of hundreds of $16 < V < 20$ magnitude stars ($R \sim 5000$) per field.

The MaunaKea Spectroscopic Explorer (MSE, [The MSE Science Team et al. \(2019\)](#), expected for 2029) is also a new project that *Pristine* should benefit. MSE is a 11m telescope with a 1.5° field of view, it was designed to be the successor of the CFHT in Hawaii and aims to provide more than 4000 spectra per exposure with resolution spanning 3,000 to 40,000. With the advent of such large spectroscopic datasets, machine learning and neural networks will become crucial fields to process such large amount of data. Detailed and meticulous studies as presented in this thesis will however remain essential to extract the finest information of the rarest stars.

A Improved data reduction of CFHT/ES-PaDOnS spectra

As presented in Figure 2 of Part 4.2, the analysis of the ESPaDOnS observation have led to significant improve of the reduction of the spectra, including the development of a Python based pipeline. The list below indicate the different steps of the procedure :

- 1 Gathering of the raw data
- 2 Splitting of the echelle orders
- 3 Combination of the echelle orders
- 4 Transformation of the spectra to a resolution of $R \sim 40,000$.
- 5 Calculation of the radial velocities
- 6 Combination of the sub-exposures
- 7 Measurements of the line equivalent widths

The list of Python libraries, command languages and other software programs that are necessary to perform all the steps in the pipeline:

Software programs	DAOSPEC
	Iraf
	Python 2.7
	Python 3.x
Command languages	Pyraf
Non standard Python libraries	Matplotlib
	Numpy
	Pandas
	Specutils (Astropy package)

Table A.1 – Prerequisites for running all the scripts of the pipeline

The pipeline starts by splitting the original Libre-ESpRIT ascii files with extention **SequenceNumber*inw.s* into the different echelle orders. The script will then cut the different echelle

Appendix A. Improved data reduction of CFHT/ESPaDOnS spectra

orders to remove the overlapping wavelengths with the highest error and save the newly cut echelle orders to new ascii files. The script also allows one to visualise the combined spectrum with all the cut echelle orders and their respective errors (see A.1).

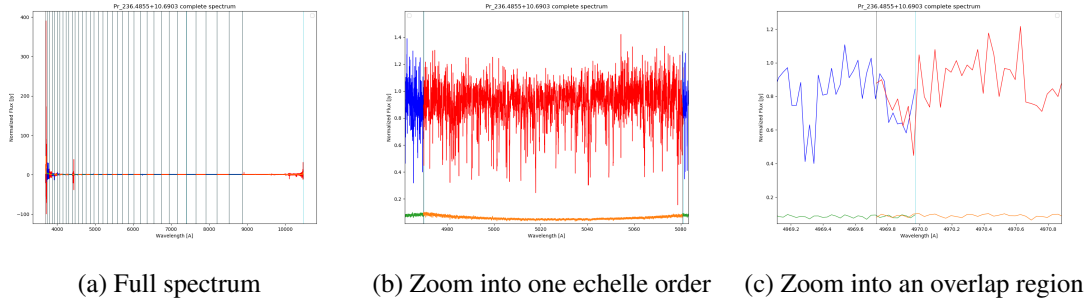


Figure A.1 – Plot returned by *Combine_ASCII_spec.py* displaying the complete spectrum in blue and red as well as the error in green and orange. The vertical blue line indicates where an echelle order ends and the black line indicates where the new echelle order begins.

All subexposures are degraded to $R \sim 40,000$, then combined to produce the final spectrum. This is done after each subexposure has been corrected for radial velocity shifts with DAOSPEC. Finally, the line equivalent width are measured with DAOSPEC.

This pipeline is made fully available to the *Pristine* consortium.

B Acronyms

AGB	Asymptotic Giant Branch
CaT	Calcium II Triplet
CEMP	Carbon Enhanced Metal-Poor
CFHT	Canada France Hawaii Telescope
CDM	Cold Dark Matter
CMB	Cosmic Microwave Background
CMD	Colour-Magnitude Diagram
DART	Dwarf Abundances and Radial velocity Team
dSph	dwarf spheroidal
EMP	Extremely Metal-Poor
ESO	European Southern Observatory
EW	Equivalent Width
FWHM	Full Width at Half Maximum
HFS	Hyperfine structure
HR	High Resolution
ISM	Interstellar Medium
LG	Local Group
M_{\odot}	Solar mass
MARCS	Model Atmospheres in Radiative and Convective Scheme
MP	Metal-Poor
MS	Main Sequence
MW	Milky Way
(N)LTE	(Non) Local Thermodynamic Equilibrium
pc	parsec

RGB	Reg Giant Branch
RV	Radial Velocity
SDSS	Sloan Digital Sky Survey
SFH	Star Formation History
SNe	Supernovae
SNeIa	Supernovae of type Ia
SNeII	Supernovae of type II
SNR	Signal to Noise Ratio
T_{eff}	Effective Temperature
UMP	Ultra metal-poor
UVES	Ultraviolet and Visual Echelle Spectrograph
VLT	Very Large Telescope
WEAVE	William Herschel Telescope Enhanced Area Explorer

Bibliography

- Abel, T., Bryan, G. L., & Norman, M. L. 2000, *ApJ*, 540, 39
- Aguado, D. S., Youakim, K., González Hernández, J. I., et al. 2019, *MNRAS*, 490, 2241
- Alonso, A., Arribas, S., & Martínez-Roger, C. 1999, *A&AS*, 140, 261
- Aoki, W., Arimoto, N., Sadakane, K., et al. 2009, *A&A*, 502, 569
- Arentsen, A., Starkenburg, E., Martin, N. F., et al. 2020a, *MNRAS*, 496, 4964
- Arentsen, A., Starkenburg, E., Martin, N. F., et al. 2020b, *MNRAS*, 491, L11
- Battaglia, G., Irwin, M., Tolstoy, E., et al. 2008, *MNRAS*, 383, 183
- Battaglia, G., Tolstoy, E., Helmi, A., et al. 2011, *VizieR Online Data Catalog*, 741
- Battaglia, G., Tolstoy, E., Helmi, A., et al. 2006, *A&A*, 459, 423
- Beers, T. C. & Christlieb, N. 2005, *ARA&A*, 43, 531
- Bettinelli, M., Hidalgo, S. L., Cassisi, S., Aparicio, A., & Piotto, G. 2018, *MNRAS*, 476, 71
- Boylan-Kolchin, M., Bullock, J. S., & Kaplinghat, M. 2011, *MNRAS*, 415, L40
- Bromm, V. & Larson, R. B. 2004, *ARA&A*, 42, 79
- Caffau, E., Bonifacio, P., François, P., et al. 2011, *Nature*, 477, 67
- Christlieb, N., Bessell, M. S., Beers, T. C., et al. 2002, *Nature*, 419, 904
- Cicuéndez, L., Battaglia, G., Irwin, M., et al. 2018, *A&A*, 609, A53
- Dalton, G., Trager, S., Abrams, D. C., et al. 2016, in *Society of Photo-Optical Instrumentation Engineers (SPIE) Conference Series*, Vol. 9908, *Ground-based and Airborne Instrumentation for Astronomy VI*, ed. C. J. Evans, L. Simard, & H. Takami, 99081G
- de Boer, T. J. L., Tolstoy, E., Hill, V., et al. 2012, *A&A*, 544, A73
- de Boer, T. J. L., Tolstoy, E., Lemasle, B., et al. 2014, *A&A*, 572, A10

Bibliography

- Gustafsson, B., Edvardsson, B., Eriksson, K., et al. 2008, *A&A*, 486, 951
- Helmi, A. 2006, *Mem. Soc. Astron. Italiana*, 77, 1111
- Helmi, A., Irwin, M. J., Tolstoy, E., et al. 2006, *ApJ*, 651, L121
- Hill, V., Skúladóttir, Á., Tolstoy, E., et al. 2019, *A&A*, 626, A15
- Hirano, S., Hosokawa, T., Yoshida, N., et al. 2014, *ApJ*, 781, 60
- Ibata, R. A., Lewis, G. F., Conn, A. R., et al. 2013, *Nature*, 493, 62
- Irwin, M. J., Bunclark, P. S., Bridgeland, M. T., & McMahon, R. G. 1990, *MNRAS*, 244, 16P
- Jablonka, P., North, P., Mashonkina, L., et al. 2015, *A&A*, 583, A67
- Ji, A. P., Simon, J. D., Frebel, A., Venn, K. A., & Hansen, T. T. 2019, *ApJ*, 870, 83
- Keller, S. C., Bessell, M. S., Frebel, A., et al. 2014, *Nature*, 506, 463
- Keller, S. C., Schmidt, B. P., Bessell, M. S., et al. 2007, *PASA*, 24, 1
- Kroupa, P., Theis, C., & Boily, C. M. 2005, *A&A*, 431, 517
- Lee, M. G., Yuk, I.-S., Park, H. S., Harris, J., & Zaritsky, D. 2009, *ApJ*, 703, 692
- Lemasle, B., Hill, V., Tolstoy, E., et al. 2012, *A&A*, 538, A100
- Letarte, B., Hill, V., Tolstoy, E., et al. 2010, *A&A*, 523, A17
- Longeard, N., Martin, N., Ibata, R. A., et al. 2021, *MNRAS*, 503, 2754
- Longeard, N., Martin, N., Starkenburg, E., et al. 2018, *MNRAS*, 480, 2609
- Lucchesi, R., Lardo, C., Jablonka, P., et al. 2022, *MNRAS*, 511, 1004
- Lucchesi, R., Lardo, C., Primas, F., et al. 2020, *A&A*, 644, A75
- Mashonkina, L., Jablonka, P., Sitnova, T., Pakhomov, Y., & North, P. 2017, *A&A*, 608, A89
- Mateo, M. L. 1998, *ARA&A*, 36, 435
- McConnachie, A. W. 2012, *AJ*, 144, 4
- Metz, M., Kroupa, P., & Jerjen, H. 2007, *MNRAS*, 374, 1125
- Mo, H., van den Bosch, F. C., & White, S. 2010, *Galaxy Formation and Evolution*
- Moore, B., Ghigna, S., Governato, F., et al. 1999, *ApJ*, 524, L19
- Norris, J. E., Yong, D., Venn, K. A., et al. 2017, *ApJS*, 230, 28
- Pawlowski, M. S. 2018, *Modern Physics Letters A*, 33, 1830004

- Placco, V. M., Frebel, A., Beers, T. C., & Stancliffe, R. J. 2014, *ApJ*, 797, 21
- Planck Collaboration, Ade, P. A. R., Aghanim, N., et al. 2014, *A&A*, 571, A16
- Planck Collaboration, Ade, P. A. R., Aghanim, N., et al. 2016, *A&A*, 594, A13
- Plez, B. 2012, *Turbospectrum: Code for spectral synthesis*, Astrophysics Source Code Library
- Revaz, Y. & Jablonka, P. 2012, *A&A*, 538, A82
- Revaz, Y. & Jablonka, P. 2018, *A&A*, 616, A96
- Robin, A. C., Reyl  , C., Derri  re, S., & Picaud, S. 2003, *A&A*, 409, 523
- Sawala, T., Frenk, C. S., Fattahi, A., et al. 2016, *MNRAS*, 457, 1931
- Sestito, F., Longeard, N., Martin, N. F., et al. 2019, *MNRAS*, 484, 2166
- Sestito, F., Martin, N. F., Starkenburg, E., et al. 2020, *MNRAS*, 497, L7
- Simon, J. D. 2019, *ARA&A*, 57, 375
- Spergel, D. N., Bean, R., Dor  , O., et al. 2007, *ApJS*, 170, 377
- Springel, V., Frenk, C. S., & White, S. D. M. 2006, *Nature*, 440, 1137
- Springel, V., Wang, J., Vogelsberger, M., et al. 2008, *MNRAS*, 391, 1685
- Starkenburg, E., Aguado, D. S., Bonifacio, P., et al. 2018, *MNRAS*, 481, 3838
- Starkenburg, E., Hill, V., Tolstoy, E., et al. 2010, *A&A*, 513, A34
- Starkenburg, E., Martin, N., Youakim, K., et al. 2017, *MNRAS*, 471, 2587
- Stetson, P. B. & Pancino, E. 2008, *PASP*, 120, 1332
- Tafelmeyer, M., Jablonka, P., Hill, V., et al. 2010, *A&A*, 524, A58
- The MSE Science Team, Babusiaux, C., Bergemann, M., et al. 2019, *arXiv e-prints*, arXiv:1904.04907
- Theler, R., Jablonka, P., Lucchesi, R., et al. 2020, *A&A*, 642, A176
- Tolstoy, E., Irwin, M. J., Helmi, A., et al. 2004, *ApJ*, 617, L119
- Tolstoy, E., Venn, K. A., Shetrone, M., et al. 2003, *AJ*, 125, 707
- Venn, K. A., Kieilty, C. L., Sestito, F., et al. 2020, *MNRAS*, 492, 3241
- Venn, K. A., Shetrone, M. D., Irwin, M. J., et al. 2012, *ApJ*, 751, 102
- White, S. D. M. & Rees, M. J. 1978, *MNRAS*, 183, 341

Bibliography

Wolf, C., Onken, C. A., Luvaul, L. C., et al. 2018, PASA, 35, e010

Yanny, B., Rockosi, C., Newberg, H. J., et al. 2009, AJ, 137, 4377

York, D. G., Adelman, J., Anderson, John E., J., et al. 2000, AJ, 120, 1579

Romain Lucchesi

Curriculum Vitæ

Laboratoire d'astrophysique
École Polytechnique Fédérale de Lausanne (EPFL)
Observatoire de Genève, 1290 Versoix, Switzerland
☎ +33 6 66 65 12 25
✉ lucchesi.romain@gmail.com
DOB: January 05, 1990, Aix-en-Provence, France
Driving licence : French cat B



Education

- 2017–2021 **PhD in Astrophysics**, *Laboratory of astrophysics*, EPFL, Switzerland, Supervisor : Prof. Pascale Jablonka.
- 2014–2016 **Master**, *Master of Astronomy Astrophysics and Space Engineering*, PSL University – Paris Observatory, France.
- 2010–2014 **Bachelor**, *Bachelor of Physics and Chemistry Sciences*, Aix-Marseille University, France.
- 2009 **Scientific Baccalaureate**, *Speciality Engineering Sciences*.

Work Experience

- 2017–present **PhD – Doctoral assistant**, *"The first generations of stars in the Local Group"*, Expertise in high and medium resolution spectroscopy, data reduction, determination of chemical abundances in stars, spectrographs and astronomical observations. This project takes place in the Pristine Survey and the ESO Large Programme DART (Dwarf galaxy Abundances and Radial-velocities Team) – under the joint supervision of Pascale Jablonka (EPFL, Switzerland) and Francesca Primas (ESO, Germany), Assistant for astrophysics tutorials at EPFL.
- 2016 **Master 2 Thesis**, *"Detection and characterisation by direct imaging of giants exoplanets with SPHERE/VLT"*, Expertise in adaptive optics imaging, integral field spectrograph, and speckles removing, Supervisor : Dr Arthur Vigan, Laboratoire d'Astrophysique de Marseille, CNRS, France.
- 2015 **Master 1 Thesis**, *"Rotation of stars in the Magellanic clouds depending on their metallicity"*, Supervisor : Dr Frederic Royer, Paris Observatory, GEPI, France.
- 2014 **Bachelor Project**, *"Femtosecond laser and material ablation"*, LP3 – Lasers, Plasmas et Procédés Photoniques, CNRS, Aix-Marseille University.

Publications

- **Lucchesi, R. et al. 2020**, *Homogeneity in the early chemical evolution of the Sextans dwarf Spheroidal galaxy*, A&A, 644, A75, [ADS Link](#).
- **Lucchesi, R. et al. 2021**, *The Pristine survey – XV. A CFHT ESPaDOnS view on the Milky Way halo and disc populations*, MNRAS, 511, 1004, [ADS Link](#).
- **Lucchesi, R. et al. in prep.**, *Extremely metal-poor stars in the Fornax and Carina dwarf spheroidal galaxies*.
- **Co-author publications**, *Detailed list attached*.

Observing Experience

- 2019–07 **Euler**, 16 nights on the 1.2m Swiss telescope, La Silla Observatory. Photometry of exoplanet transits, radial velocity monitoring of exoplanet host stars, monitoring of gravitational lenses for time delays.
VLT, 2 nights visit at Paranal Observatory, Introduction to MUSE observations.
- 2018–11 **APEX**, 10 days on the 12m ESO radio telescope, Chajnantor Observatory, Chile. Detection of molecular emission lines in distant galaxies.
VLT, 2 nights visit at Paranal Observatory.
- 2018–02 **Isaac Newton Telescope**, 8 nights on the 2.5m telescope, Roque de los Muchachos observatory, La Palma, Canary Islands. Pristine Survey – Low resolution spectroscopy in the search of extremely metal poor stars candidates.
- 2012–2015 **Observatoire de Haute Provence**, several weeks of training sessions on the 1.93m, 1.2m and 0.8m telescopes.

Technical Skills

Programming PYTHON, BASH, C++, IDL, FORTRAN, HTML
Software LATEX, IRAF, MS VISUAL STUDIO, OPENSCAD, SOLIDWORKS, MS OFFICE
Editing ADOBE PHOTOSHOP, ADOBE LIGHTROOM, DAVINCI RESOLVE

Experience as amateur astronomer, photographer, designer

- **Astrophotography since 2012**, nightscape photography, [Flickr link](#), [ESO publications](#).
- **Remote observatory**, conception of a small fully remotely operating observatory, [Youtube](#).
- **Electronics and mechanical**, design of *Arduino* based electronic devices, design of printed circuit boards (PCB), components assembly, 3D printing, camera and optical modifications, *Raspberry Pi* based weather station.

List of Publications – [ADS Library](#)

- [1] **Lucchesi, R., Lardo, C., Primas, F., et al. 2020**, *Homogeneity in the early chemical evolution of the Sextans dwarf Spheroidal galaxy*, A&A, 644, A75, [ADS Link](#).
- [2] **Lucchesi, R., Lardo, C., Jablonka, P., et al. 2021**, *The Pristine survey – XV. A CFHT ESPaDOnS view on the Milky Way halo and disc populations*, MNRAS, 511, 1004, [ADS Link](#).
- [3] **Lucchesi, R., Jablonka, P., et al. in prep.**, *Extremely metal-poor stars in the Fornax and Carina dwarf spheroidal galaxies*, .

Co-author Publications

- [4] **Longeard, N., Jablonka, P., Arentsen, A., et al. 2021**, *The Pristine Dwarf-Galaxy survey – IV. Probing the outskirts of the dwarf galaxy Boötes I*, MNRAS[arXiv:2107.10849].
- [5] **Longeard, N., Martin, N., Ibata, R., et al. 2021**, *The pristine dwarf-galaxy survey – III. Revealing the nature of the Milky Way globular cluster Sagittarius II*, MNRAS, 503, 2754.
- [6] **Theler, R., Jablonka, P., Lucchesi, R., et al. 2020**, *The chemical evolution of the dwarf spheroidal galaxy Sextans*, A&A, 642, A176.
- [7] **Sestito, F., Martin, N., Starkenburg, E., et al. 2020**, *The Pristine survey – X. A large population of low-metallicity stars permeates the Galactic disc*, MNRAS, 497, L7.
- [8] **Aguado, D., Youakim, K., González Hernández, J., et al. 2019**, *The Pristine survey – VI. The first three years of medium-resolution follow-up spectroscopy of Pristine EMP star candidates*, MNRAS, 490, 2241.